INTEGRATION AND MINIATURIZATION OF ANTENNAS FOR SYSTEM-ON-PACKAGE APPLICATIONS

A Dissertation
Presented to
The Academic Faculty

By

Nevin Altunyurt

In Partial Fulfillment
of the Requirements for the Degree
Doctor of Philosophy
in
Electrical and Computer Engineering

School of Electrical and Computer Engineering
Georgia Institute of Technology
May 2010

INTEGRATION AND MINIATURIZATION OF ANTENNAS FOR SYSTEM-ON-PACKAGE APPLICATIONS

Approved by:

Dr. Madhavan Swaminathan, Advisor
Professor, School of ECE
Georgia Institute of Technology

Dr. Farrokh Ayazi
Professor, School of ECE
Georgia Institute of Technology

Dr. Andrew F. Peterson
Professor, School of ECE
Georgia Institute of Technology

Dr. Paul A. Kohl
Professor, School of ChBE
Georgia Institute of Technology

Dr. Manos M. Tentzeris
Professor, School of ECE
Georgia Institute of Technology

Date Approved: April 2010

This thesis is dedicated to my beloved family, for their love and encouragement. To my mother, Azime, my father, Mehmet, my brother, Sabahattin, and my sisters, Nebahat and Nilgün.

ACKNOWLEDGMENT

I have always enjoyed reading the acknowledgements sections of dissertations. I remember even dreaming about writing my own one day. Finally, I can see the light at the end of the tunnel, and I could not have completed this journey unless there were people who lit my way or held my hand through this journey. Now, it is my turn to express my gratitude to these people who contributed to my research and Ph.D. life over the last five years.

I am forever grateful to Prof. Madhavan Swaminathan, my academic advisor, for the opportunity he gave me to be an EPSILON lab member. This has been a turning point both in my career and personal life. Being a member of the EPSILON group, I have worked with many gifted people and learned much from the diverse research areas that have been covered in the lab. Prof. Swaminathan, I cannot thank you enough for your continuous trust, guidance, enthusiasm and encouragement both in my Ph.D. research and my personal life.

I would like to thank my committee members Prof. Farrokh Ayazi, Prof. Paul A. Kohl, Prof. Andrew F. Peterson and Prof. Manos M. Tentzeris for taking much of their valuable time to give me invaluable advice and feedback. I owe special thanks to Prof. Andrew F. Peterson and Prof. Manos M. Tentzeris. Their computational electromagnetics classes had a major impact on my understanding of what Maxwell's story really was. The foundation I built with these classes and their invaluable discussions on my research had a strong effect on shaping my ideas.

Prof. Swaminathan has this great ability to pick the right people to make the EPSILON lab a great place to work. This is especially important for us whose families live on the other side of the ocean thousands of miles away. Special thanks go to my colleagues Krishna Bharath, Souvik Mukherjee, Subramanian Lalgudi, Wansuk Yun, Marie Solange

Milleron, Janani Chandrashekar, Abdemanaf Tambawala, Amit Bavisi, Tae Hong Kim, Rohan Mandrekar, Prathap Muthana, Krishna Srinivasan, Ranjeeth Doppalapudi, Sukruth Pattanagiri, Aswani Kurra, Vishal Laddha, Abhilash Goyal, Seughyung Hwang, Myunghyun Ha, Suzanne Huh, Narayanan Terizhandur, Nithya Sankaran, Tapo Bandhopadyay, Jae Young Choi, Jianyong Xie, and Kyuhwan Han. I would like to thank each one of you for your friendship and the fun times in the lab. I have learned a lot from your presentations and research efforts. The research faculty of the EPSILON group has also been great supporters for all of us and I would like to thank Dr. Arif E. Engin, Dr. Daehyun Chung, and Dr. Sunghwan Min for their help and constructive discussions on my research. I have also made great friends from our trusted neighboring lab. Maryam, Vishwa, Raj, Ganesh, Vidhya, Jayaram, Shyam, and Sehun, thank you for your friendship.

I was fortunate to receive help and support from several people to fabricate my designs. I am grateful to Dr. Venkatesh Sundaram and Dr. Ralf Rieske for their help with the fabrication of LCP boards. I would like to thank Dr. Raj Pulugurtha, Dr. Dashartham G. Janagama, Dr. Himani Sharma, Mr. Aditya Kumar, Mr. Vibhas Singh, Mr. Nikhilesh Natarajan, and Mr. Prashant Reddy for their collaborating efforts in the magneto-dielectrics research. I would also like to thank Dr. Vijay Nair of Intel Corporation for his support on this project.

I would like to express my gratitude to Prof. John Papapolymerou for his support on my research and letting me use the measurement facilities in his lab. I am indebted to Dr. Benjamin Lacroix and my friend Arnaud Amadjikpe for their help with the fabrication and measurement of antennas. I believe this research collaboration has been a great start for our friendship as well. I would also like to thank James Steinberg of ECE for his help with soldering some of the world's tiniest connectors on my designs.

Computer Simulation Technology's Microwave Studio (CST MWS) has been an indispensable tool during my studies. I would like to thank CST for their support in providing us with the licenses and Dr. Antonio Ciccomancini of CST for his prompt responses to my

emails and invaluable help to get the best from this great tool.

The best part of my Ph.D. life has certainly been the friends I have made all these years. I am grateful to all my friends for the cherished memories and fun times we shared. I would like to thank Krishna for his support with my research, for being the "walking wikipedia" and making me become aware of so many interesting topics. I will always appreciate Yonca's and Souvik's support especially during the first months of my life in Atlanta, when settling in was the hardest. Vishwa, thank you for being an exceptional friend with a great heart and being there whenever a strong shoulder is needed. Şafak, Esra, Selçuk, Ozan, Ahmet, Symeon, Diana, and Anya: I am grateful for your friendship and thank you for all the fun times. I cannot thank Seray, Elif, and Alper enough for having supported me all the way from Turkey. You guys are awesome.

I owe special thanks to Gence, Onur, Sabina, and the Karkin family for making Atlanta another "home" for me. I would not exaggerate it if I said that I would not be able to finish my Ph.D. if you had not supported me and lifted my spirits when I was down. Gence, especially you have been my biggest support here. Words are not enough to thank for your sistership, you never failed to be my side when I needed you. I am also grateful that you brought another brother to my life. Onur, thank you for being a great friend. Sabina, your sistership has been another gem I have found here. Thank you for all the fun you brought to our lives. Leaving Atlanta is so tough when you guys stay behind.

Michael, you definitely need to be awarded with a degree for putting up with my bitter times during my Ph.D. I thank you from the bottom of my heart for having been my guarding angel here. It meant a lot to me when you say everything was going to be all right. Thank you for being on my side through my most difficult times. Finally you are right, and everything turned out to be all right.

I owe my deepest gratitude to my family. Pages would not be enough to pen down my gratitude and love for you. Mom and dad, the toughest part of the past five years has been being away from you but you have always found ways to make me feel your unconditional

love and support despite all the distance. Whenever I need motivation to work, I remember how hard you two have worked for our education, happiness and well-being. I can never pay back your efforts but this degree is dedicated to the both of you. My brother Sabahattin and my sisters Nebahat and Nilgün, you have been, are, and will be my three heros. I have always looked up to you and I cannot thank you enough for your support throughout the stressful times during my Ph.D. I thank God everyday for being born as an Altunyurt and having you as my family. Therefore, this dissertation is dedicated to you, my beloved family.

TABLE OF CONTENTS

LIST OF TABLES

LIST OF FIGURES

SUMMARY

Wireless communications have been an indispensable aspect of everyday life, and there is an increasing consumer demand for accessing several wireless communication technologies from a single, compact, mobile device. System-on-package (SOP) technology is an advanced packaging technology that has been proven to realize the convergence of multiple functions into miniaturized, high-performance systems to meet this demand. With the advancements in the SOP technology, the miniaturization of the front-end module has been achieved using embedded passives in multilayer packages. However, the integration of the antenna directly on the module package is still the barrier to achieve a fully-integrated, high-performance RF SOP system. The main reason for this missing link is that integrating the antenna on the package requires miniaturizing the antenna, which is a difficult task.

The focus of this dissertation is to design high-performance antennas along with developing techniques for miniaturization and system-on-package (SOP) integration of these antennas to achieve fully-integrated SOP systems using advanced multilayer organic substrates and thin-film magneto-dielectric materials. The targeted spectrum for the antenna designs are 2.4/5 GHz WLAN/WiMAX and 60 GHz WPAN bands. Several novel antenna designs and configurations to integrate the antenna on the package along with the module are discussed in this dissertation. The advanced polymers used in this research are Liquid Crystalline Polymer (LCP), RXP, and thin-film magneto-dielectrics.

CHAPTER 1

INTRODUCTION

Wireless communications have been a major aspect of everyday life, making it a rapidly increasing segment of the communications industry. The evolution of wireless communications includes several indispensable technologies such as cellular communications, wireless local area networks (WLANs), and wireless personal area networks (WPANs). The consumer demand for accessing these radio technologies using hand-held mobile devices has been pushing engineers to innovate on advanced technologies to achieve the integration and miniaturization of multiple systems.

One of the key enablers of achieving this goal has been the advancements in the packaging technologies and manufacturing systems [1]. The invention and miniaturization of the transistor followed by the integration of large numbers of transistors have led to a design approach called system-on-chip (SOC). The SOC aims for the integrated circuit (IC) level integration, where the transistors, passive and mixed-signal components are all integrated into one silicon device. Although realizing this kind of integration offers the most compact, high-performance, lightweight systems that can be manufactured in high volumes, SOC has challenges and limitations, especially for wireless communications applications. Among these challenges are high costs due to the fabrication and test complexities that stem from integrating disparate silicon technologies, such as Complementary Metal Oxide Semiconductor (CMOS), bipolar, silicon germanium, with different requirements into one chip. Moreover, while the silicon technology is great for digital applications, it is not the optimal platform for integrating RF components (such as antennas, capacitors, inductors), thermal structures, power sources and packages. These prevent the SOC from achieving a system-level integration [2].

The invention of the multichip module (MCM) technology in the 1980s to overcome

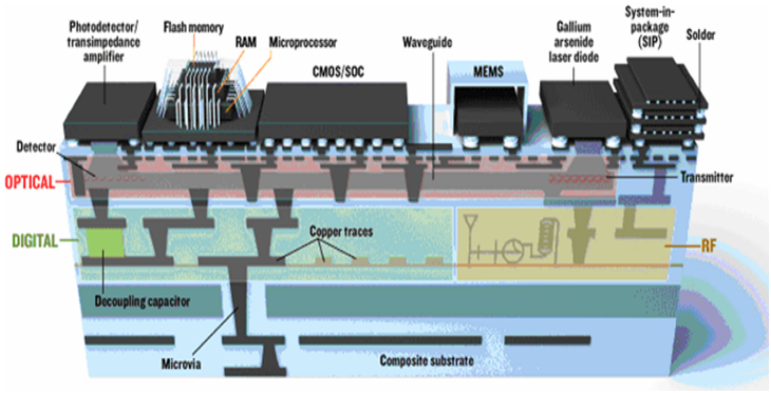

Figure 1. System on package concept (Picture courtesy of [3]).

some of these challenges has led to a module-level integration technology called system-in-package (SIP) that is based on the vertical stacking of similar and dissimilar ICs. Even though the 3D stacking of the ICs has been popular in manufacturing compact modules for the cell-phone industry, the SIP is still an IC-based module-level integration technology, leaving 80%-90% of the system integration needs unanswered. On the other hand, the system-on-package (SOP), another major paradigm introduced in the mid 1990s, combines the high electrical performance and the miniaturization capabilities of the chip- and module-level integration to achieve a system-level integration. The SOP technology uses the thin-film integration of numerous system-level functions to achieve ultra-miniaturized, high-performance systems [1]. As shown in Figure 1, SOP enables the system-level integration of the SOC, SIP, micro-electro-mechanical (MEMS), RF, digital, analog, and opto-electrical components along with the thermal structures, interconnects, and power sources into a single package [3].

The integration capabilities the SOP offers for RF applications have initiated considerable amount of research efforts to miniaturize the RF front-end modules (FEMs). As shown in Figure 2, the vertical integration of the planar RF components (such as filters, baluns, mixers) using the embedded passive technology in multilayer packages has enabled designing compact, highly-integrated FEMs compared to the ones on the conventional laminates

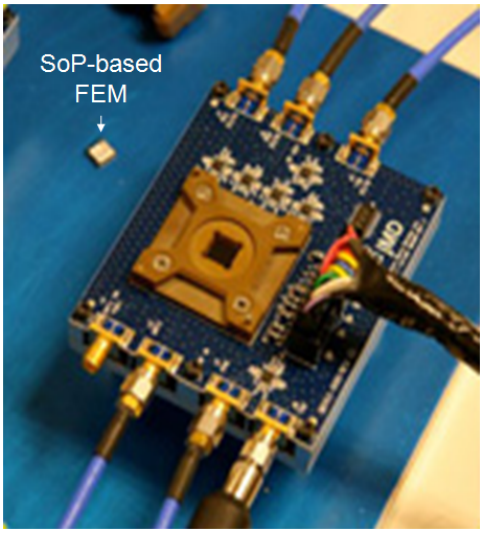

Figure 2. Comparison of a SOP-based FEM with a conventional module (Picture courtesy of Jacket Micro Devices).

fabricated with surface mount components [4]. However, the miniaturization and integration of the antennas with the front-end module, while maintaining high-performance and low-cost is still a barrier to achieve complete RF SOP integration.

Antennas have a crucial effect on the overall size and performance of wireless systems. For instance, the efficiency of the antenna plays an important role to determine the overall efficiency of the wireless system because the antenna is the first to receive the signal in the receiver and the last to send out the signal in the transmitter. Therefore, the integration of the antenna directly on the FEM package is required to optimize the size, cost and, RF performance. However, this kind of integration is a difficult task.

One reason for the difficulty in achieving the SOP integration of the antenna is the large size of the antenna compared to the compact size of the module. The size of the antenna is particularly an issue for the microwave frequency range used by most wireless mobile applications (1 GHz to 6 GHz). Hence, integrating the antenna requires miniaturizing the antenna, which is another intricate task since the gain and bandwidth of the antenna are bounded by the fundamental limits depending on the size of the antenna. Another difficulty arises because of the undesired coupling between the antenna and the module circuitry

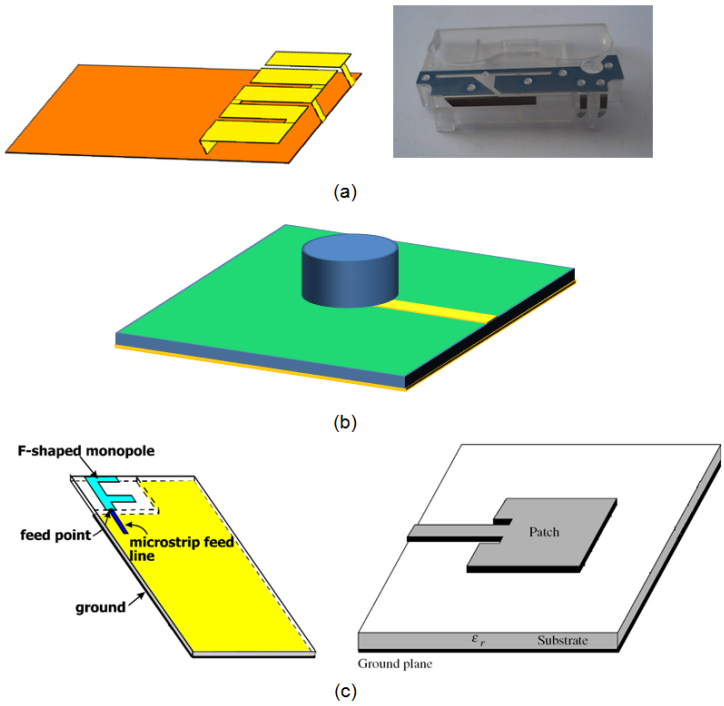

Figure 3. Examples of planar antenna designs. (a) Planar inverted F-antenna (PIFA) [7] and [8], (b) Dielectric resonator antenna (DRA), (c) Printed monopole antenna (left) and microstrip patch antenna (right) [9] [10].

as the separation between the two is reduced. This results in a need for the co-design of the antenna with the module circuitry or the package to prevent possible de-tuning of the antenna and the RF circuits after integration [5].

Planar antennas are mostly preferred in mobile devices. Some popular planar antennas are the planar inverted-F antennas (PIFA)s, the dielectric resonator antennas (DRAs) and the printed planar antennas [6], as shown in Figure 3. The conventional PIFA design is comprised of a short-circuited radiating patch that is suspended over a ground plane as shown in Figure 3a. Although the PIFAs have been used in mobile phones to successfully replace the conventional protruded whip or rod antennas, they are not suitable for SOP integration since they are thick, bulky, machined metal structures.

DRAs, as shown in Figure 3b, form another group of planar antennas. As the name implies, in a DRA the resonating structure is a dielectric disk instead of a conductor patch

or trace. Although this eliminates the conductor loss and results in low-loss antenna designs, miniaturization of a DRA requires expensive high-permittivity dielectrics. Moreover, DRAs are mostly designed as surface-mount components, making them difficult to integrate with the module.

Printed planar antennas, as shown in Figure 3c, are better candidates than PIFAs and DRAs to achieve SOP integration of the antenna since they can be fabricated on the module package using printed circuit board (PCB) processes. Moreover, these antennas can be fed easily with a printed transmission line, an aperture or a via. The microstrip patch antenna is probably the most common printed planar antenna structure that has been studied in the literature [11]. It is especially preferred when the application requires a broadside radiation pattern since the ground plane of the patch antenna offers increased front-to-back ratio. Moreover, if the patch is integrated in an SOP configuration, the ground plane provides shielding for the rest of the system when the antenna is printed on top of the FEM substrate. On the other hand, the printed monopole antennas, comprised of printed patches or traces on truncated ground planes as shown in Figure 3c, are more suitable for mobile applications that require an omni-directional radiation pattern. Moreover, the printed monopoles offer wider bandwidth than the microstrip patch antennas, making it easier to cover the required spectrum of the targeted applications.

In addition to the antenna design, the fabrication technology and the substrate material are two other critical selections that affect the performance of the RF SOP module. In an SOP architecture, the substrate not only provides the mechanical support but also becomes the medium for the electromagnetic wave propagation between the embedded/integrated components. This makes the selection of the substrate material critical since the characteristics of the wave propagation and capabilities of the technology are determined by the substrate parameters.

Low temperature co-fired ceramic (LTCC) technology has been a popular solution for

implementing RF SOP in both the microwave and V-bands to integrate the RF components and the antenna in a multilayer substrate. In an LTCC configuration, a microstrip patch antenna is integrated by printing the antenna on top of the module circuitry that is embedded in the lower layers of the substrate [5], [12], and [13]. Although the high dielectric constant and the low loss tangent of the LTCC substrate have been advantageous for the miniaturization and integration of the RF components, the LTCC substrate is not the optimal material as far as the antenna performance is concerned. This is because the efficiency and bandwidth of the antenna decreases as the permittivity of the substrate is increased. Moreover, the mismatch of the coefficient of thermal expansion (CTE) of the LTCC substrate with that of the PCB can lead to reliability issues in the highly-integrated front-end packages. Additionally, the cost of the ceramic-based package and fabrication process prevent the LTCC package to be used as the final PCB. Therefore, the LTCC may not provide a long-term effective packaging solution because of the higher processing temperature ($> 900°$C), larger manufacturing variation, bulkier substrate, and higher cost as compared to other technologies having the same integration capability such as multilayer organic (MLO) substrates.

As an alternative to the LTCC, liquid crystalline polymer (LCP) based MLO offers a low-cost, low-profile, high-performance RF SOP solution with the FR-4 compatible processes [14], [15], [16], [17], [18], and [19]. LCP is a laminate-type organic dielectric material that can be stacked to form multilayer substrates with the use of adhesive bondply layers in between the stacked LCP layers. In addition to being a low-cost dielectric suitable for a large panel area fabrication process, the LCP has a combination of good electrical and mechanical properties. It has a low dielectric constant of $\epsilon_r = 2.95$ and a low loss-tangent of 0.002 up to millimeter wave frequencies. The LCP also has favorable mechanical properties such as mechanical flexibility, a low coefficient of thermal expansion, and low moisture absorption [20].

In spite of the good RF performance and integration capability of the LCP, the LCP-based MLO technology suffers from a few limitations due to the relatively high processing temperature (290°C) compared to that of FR-4. Additionally, the need for bondply material for building stack-ups results in yield issues because of the registration errors. A new organic material, called RXP, has been introduced to overcome these limitations.

The RXP is an ultra-thin, laminate-type substrate that has been proposed to extend the micro-scale SOP to nano-scale SOP since it enables building thinner substrates and finer lines/spaces compared to the LCP technology. For instance, 30-50 μm diameter through-vias, 25-40 μm blind vias and 15 μm line/spaces can be fabricated with the RXP technology [21]. The RXP has two distinct variants. RXP-1 is a thin glass-reinforced laminate used as the core, and RXP-4 is a thin dry film used as the build-up layer. The RXP technology is more advantageous than the LCP technology in terms of preventing the registration errors since RXP-4 is one of the RXP variants, unlike the bondply layer of the LCP. Additionally, RXP-4 can be made as thin as 20 μm under a low processing temperature (220°C), which is better compatible with the standard PCB manufacturing processes.

Similar to the LCP, the RXP is a low-loss dielectric with a stable frequency response up to 110 GHz, being suitable for both microwave and millimeter wave RF applications. The dielectric constant and the loss tangent of the core RXP-1 are $\epsilon_r = 3.41 \pm 0.06$ and $tan\delta < 0.006$ up to 110 GHz. The dielectric constant and the loss tangent of the build-up RXP-4 are $\epsilon_r = 2.98 \pm 0.05$ and $tan\delta < 0.0053$ up to 110 GHz [22]. Recently, the fabrication details of the initial RXP-based MLO substrates with fine lines and low CTE capability has been presented in [23] and [21]. Moreover, high quality factor embedded inductors fabricated with the RXP technology have been reported in [24], followed by the embedded-passive filter designs presented in [25].

Another type of advanced polymer proposed for SOP applications falls under the category of magneto-dielectrics, materials with $\epsilon_r > 1$ and $\mu_r > 1$. Magneto-dielectric materials have been proposed to overcome the limitations of the dielectric substrates in effectively

miniaturizing the antenna for SOP applications [26]. However, these materials do not exist in nature and are not yet available in the market; hence, they need to be synthesized. Thin-film magneto-dielectrics based on nanoparticle inclusions have been proposed in the literature. Polymer composite thin-films based on insulator-coated nickel (Ni) and cobalt (Co) nanoparticles have been found promising to provide stable and low-loss magneto-dielectric properties. In this synthesis approach, high ϵ_r and μ_r of the material are sustained with the inclusion of the magnetic nanoparticles; whereas, the insulating shell prevents the material loss, while improving the stability with frequency [27], [28], [29].

1.1 Contributions and Dissertation Outline

The focus of this research is to design high-performance antennas along with developing the techniques to **integrate** and **miniaturize** these antennas to achieve the SOP approach using the aforementioned advanced MLO substrates and thin-film magneto-dielectrics, for the 2.4/5 GHz WLAN/WiMAX and 60 GHz WPAN applications. In this regard, the accomplished research can be listed as follows:

1. *SOP integration of antennas in the 2.4/5 GHz WLAN/WiMAX bands using conformal antennas on rigid-flex LCP-based MLO substrates*

   A conformal antenna configuration using LCP-based rigid-flex substrates has been proposed and implemented to efficiently integrate the antenna on the package of an SOP module. Monopole antennas have been used to prove the concept since the SOP integration of the monopole antennas has not been covered in the literature before although the monopoles are highly preferred in mobile devices. In the proposed configuration, the antenna is positioned on the protruding flexible portion of a rigid-flex substrate and an on-package shielding box is used to protect the possible module circuitry from the radiated fields of the antenna. Even though flexible antennas have been proposed in the literature and already employed in the state-of-the-art mobile devices, e.g. the iPhone, the integration of the flexible antenna with the rigid SOP

substrate with a single process has been shown for the first time with the proposed LCP-based rigid-flex substrates. This novel technology not only provides a solution for the antenna integration but also miniaturizes the overall size of the complete RF SOP package by folding the flexible part of the substrate on the rigid part the substrate. The configuration was implemented using single and dual-band prototypes covering the 2.4/5 GHz WLAN and WiMAX bands. The fabricated antennas were also measured and good correlation was observed between the simulation and measurement results.

2. *Characterization of thin-film magneto-dielectric substrates*

   As mentioned before, the large size of the antenna compared to the size of the FEM is a limiting factor to effectively integrate the antenna directly on the module package. This is especially an issue for the microwave range (up to 10 GHz), where the popular mobile applications are centered. Therefore, in addition to developing antenna integration techniques, the other main focus of this PhD research has been to investigate antenna miniaturization techniques. The work covered in this part of the dissertation focuses on using magneto-dielectric substrates to miniaturize the antennas. Since magneto-dielectrics do not exist in nature and are not available in the market, these materials should be synthesized with advanced techniques. Moreover, novel characterization methodologies are needed to provide feedback during the synthesis process as the conventional metrologies are mostly limited to characterizing dielectric properties. This part of the dissertation has supported the magneto-dielectric synthesis research of the material science engineers from the Packaging Research Center at Georgia Tech. Two characterization methods that are based on measuring easy-to-fabricate, -measure, and -analyze two-layer printed structures have been proposed. The methods were both verified with controlled experiments based on simulations and measurements. Theoretical analysis was also performed to explain the working principles of the methods proposed.

3. *Investigating the application of the magneto-dielectric substrates for the antenna miniaturization.*

   Magneto-dielectrics have been proposed in the literature to effectively miniaturize the antenna. However, apart from intuitive explanations based on image theory, there is not enough theoretical analysis in the literature to explain why magneto-dielectric substrates are better substrates than the conventional dielectric substrates. Moreover, the effect of increasing the permeability of the substrate on the surface wave propagation has not been highlighted in the previously published papers. Therefore, the advantages and limitations of using magneto-dielectric substrates to efficiently miniaturize the conductor-backed planar antennas were investigated in this research. The well-known analysis methods reported for the microstrip patch antennas were applied to derive the expressions for the stored electromagnetic energy and radiated power from a microstrip patch antenna on a magneto-dielectric substrate. These expressions were used to gain insight on the use of magneto-dielectric substrates. The results obtained from the theoretical analysis were verified with the simulations results. The surface wave propagation on a conductor-backed magneto-dielectric substrate was also investigated. Strong surface wave propagation on magneto-dielectric substrates has been highlighted for the first time with this analysis.

4. *Investigating the application of the magneto-dielectric substrates for the miniaturization of reactive impedance surfaces.*

   In addition to the antennas, the efficient miniaturization of the reactive impedance surfaces using magneto-dielectric substrates was investigated along with the application of these surfaces to the low-profile antennas. A reactive impedance surface composed of two-layer periodic metal islands was explored using full-wave simulations.

5. *Designing novel antennas with multiple beam directions for the 60 GHz WPAN applications*

   The size of the antenna is not an issue for the 60 GHz WPAN applications since the high carrier frequency helps to miniaturize the antenna. However, compared to the applications centered in the microwave frequencies, the constraints on the antenna design are more complicated due to the increased material loss, substrate mode propagation, and multipath reflections. Directive antennas with wide-bandwidth, high-efficiency and ability to be used in array configurations are desired. Two novel slot antenna designs satisfying these requirements have been proposed and implemented in this research. Both of the antennas are easy-to-fabricate single-layer slot antenna structures. The novelty of the designs comes from the modifications made to well-known slot antenna designs to achieve multiple beam directions in their radiation patterns. A multiple-beam radiation pattern has been proposed especially for the mobile applications, as an alternative to pattern-reconfigurable antennas, to prevent the user from being forced to orient the mobile device for successful wireless communications. Moreover, ground corrugations were used to eliminate the strong effects of the surface-waves due to the higher-order mode propagation. Design guidelines have been proposed for both antennas.

6. *Designing stacked triangular patch antenna array configurations on RXP-based MLO substrates for the 60 GHz WPAN applications*

   The RXP-based MLO substrates have been proposed to realize SOP technology around the 60 GHz band. There is no work reported in the literature on the characterization of these substrates for antenna applications. A novel stacked triangular patch antenna array configuration on the RXP-based MLO substrates has been proposed. The configuration integrates triangular patch antennas on the top and inner layers of the RXP stack-up. In addition to the multilayer RXP substrate, the novelty of the proposed stacked patch antenna array comes from the fact that triangular patch

antennas with stubs were used instead of the conventional rectangular patch antennas. The internationally available 7 GHz bandwidth centered around 60 GHz was covered by merging coupled resonances. The principles behind the radiation of the proposed antenna array and the details of the design process were investigated along with design guidelines for the antenna designers.

1.1.1 Contributions

The contributions of this research can be listed as follows:

1. System-on-package integration of single- and dual-band monopole antennas using the LCP-based rigid-flex substrates. The first demonstration of flexible antenna designs integrated with the rigid SOP substrate.

2. Characterization of thin-film magneto-dielectric substrates using simple two-metal layer microstrip structures.

3. Analysis of using magneto-dielectrics to miniaturize the microstrip patch antennas and the analysis of surface wave propagation in the magneto-dielectric antenna substrate.

4. Analysis of the miniaturization of reactive impedance surfaces using magneto-dielectric substrates along with the application of these surfaces to the low-profile patch antennas.

5. Design and optimization of single metal layer CPW-fed slot antenna designs with multi-beam directive radiation patterns.

6. The first demonstration of the stacked triangular patch antenna array on RXP-based MLO substrates.

1.1.2 Organization

The rest of this thesis is organized as follows. Chapters 2, 3, 4 and 5 focus on antenna applications in the microwave band (up to 10 GHz), where antenna miniaturization is desired along with the integration. A conformal antenna configuration proposed to enable system-on-package integration of the antenna for the 2.4/5 GHz applications is presented in Chapter 2 in addition to the application of this configuration to single- and dual-band antenna designs. Chapters 3, 4 and 5 are based on the characterization and applications of the magneto-dielectric substrates to antennas and reactive impedance surfaces. The characterization of the thin-film magneto-dielectrics are discussed in Chapter 3. The application of these novel materials for antenna miniaturization is investigated in Chapter 4 using the theory and simulation based approaches. Reactive impedance surfaces and the use of magneto-dielectrics to effectively miniaturize these surfaces are discussed in Chapter 5 along with the application of these surfaces to antennas.

Chapters 6, 7 and 8 focus on the design and SOP integration of antennas on single and multilayer organic substrates to operate in the 60 GHz WPAN band. A coplanar waveguide-fed bi-directional linear tapered slot antenna is discussed in Chapter 6. Chapter 7 presents another multi-beam directional slot antenna design called an H-shaped slot antenna. Miniaturization of the antenna as well as eliminating the effects of the surface waves on the radiation pattern are discussed in this chapter. Chapter 8 introduces a solution to the SOP integration of the antennas using RXP-based multilayer substrates in the 60 GHz WPAN band and presents a stacked triangular patch antenna array configuration.

The dissertation is concluded in Chapter 9.

CHAPTER 2

CONFORMAL ANTENNAS ON LIQUID CRYSTALLINE POLYMER BASED MULTILAYER RIGID-FLEX SUBSTRATES

The system-on-package (SOP) integration of the front-end module circuity on liquid crystalline polymer (LCP) based multilayer organic substrates has been proven to miniaturize the size of the front-end module while improving its performance. However, the compact and efficient integration of the antenna to the front-end module is still a major problem. One reason for the difficulty in this integration is the large size of the antenna because of the fundamental limits on its electrical length. The size of the antenna is particularly an issue for the microwave frequency range used by most wireless mobile applications (1 GHz to 6 GHz). Another difficulty arises because of the undesired coupling between the antenna and the module circuitry as the distance between the two is reduced. This results in a need for the co-design of the antenna with the module circuitry or the package to prevent possible de-tuning of the antenna and the RF circuits after integration [5].

Despite the difficulties mentioned above, the integration of the antenna directly on the module package has the advantages of reduced loss and size. Integrating the antenna on the module package can also eliminate the mismatch introduced by the coaxial cable connections along with the associated loss and the cost of the cable. Thus, there is a need for a novel technology to miniaturize the front-end module with the antenna integrated directly on the module package.

In this chapter, conformal antenna configurations on rigid-flex LCP-based substrates are proposed for the SOP-integration of the antenna. Section 2.1 reviews the state-of-the-art methods used for the antenna integration. Next, the proposed multilayer module concept with the integrated monopole antenna on the flexible substrate is presented in Section 2.2. Several single- and dual-band antennas are presented in Sections 2.3, 2.4, 2.5, and 2.6. The details of the design procedure for the proposed single- and dual-band antennas are

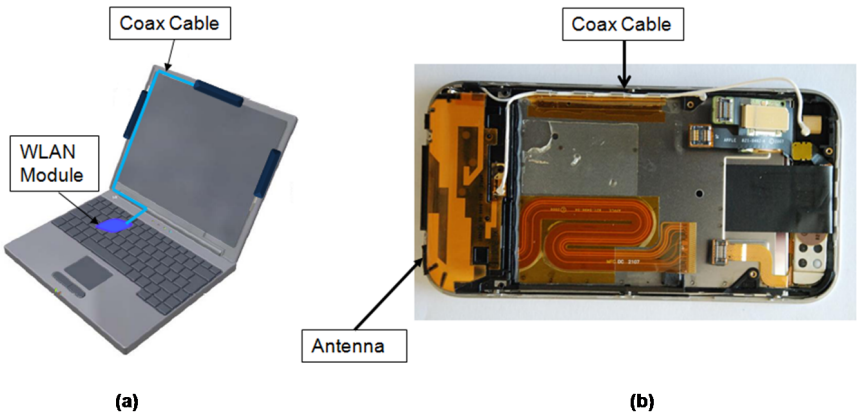

Figure 4. Examples of antenna integration in state-of-the-art mobile devices.

explained along with the details of the fabrication process. The simulation results verified with the measurement results are also provided in each section, followed by Section 2.7 which presents a comparison between the rigid-flex substrate proposed in this dissertation and a rigid substrate. The integration of multiple antennas is also discussed for the proposed configuration in Section 2.8 of this chapter. Finally, the chapter is concluded in section 2.9.

2.1 Review of Antenna Integration

The most straightforward method for integrating the antenna to the module is to place the antenna at a distant location away from the circuits and to connect the two with a coaxial cable. This method is widely utilized in the state-of-the-art mobile devices. As seen in Figure 4, the antenna or multiple antennas are usually placed along the edges of the case of the mobile device, and the RF signals are carried through a long lossy coaxial cable. Although this method is straightforward, the cable introduces mismatch and conductor losses into the system. In an application of this method to printed antennas, the antenna is printed on the package, leaving a separation with the rest of the circuitry to avoid undesired coupling. In this case, the separation needed results in unused package space, which conflicts with the miniaturization objective behind the integration.

A more compact method for the integration is to use the 3-D stacking approach of the low-temperature co-fired ceramic (LTCC) technology, where a patch antenna is printed on

top of the module circuitry [5], [12], and [13]. A dielectric resonator antenna can also be employed [30] as an alternative to the microstrip patch antenna. A metal plane or a cavity between the antenna and the circuit components can be used as a shielding mechanism in this configuration. Since vertical real estate is used in this approach, this configuration usually results in an increase in the overall height of the package.

Thin substrates or substrates with high dielectric constants can be used to decrease the thickness of the package; however, achieving wide-band operation is harder for these cases. Moreover, resonator antennas suffer from low-efficiency as the permittivity of the substrate is increased. The efficient miniaturization of conductor-backed resonator antennas is addressed in Chapter 4 and 5 of this dissertation.

The advantage of the LTCC integration method is that it is a multilayer technology. Therefore, both the module circuitry and the antenna can be integrated into the package. However, the LTCC is a more expensive solution for RF SOP applications compared to the other technologies having the same integration capability. Additionally, the mismatch of the coefficient of thermal expansion of LTCC with that of the printed circuit board (PCB) can lead to reliability issues in highly-integrated front-end packages. Moreover, the cost of the ceramic-based package and fabrication process prevent the LTCC package to be used as the final PCB.

As an alternative to LTCC, LCP-based multilayer organic technology offers a low-cost, low-profile, high-performance RF SOP solution with FR-4 compatible processes [31], [14], [15], [16], [17], [18], and [19]. In addition to being a low-cost dielectric for a large panel area fabrication process, LCP has a combination of good electrical and mechanical properties. LCP has a low dielectric constant of $\epsilon_r = 2.95$ and a low loss tangent of 0.002 up to millimeter wave frequencies. LCP also has favorable mechanical properties such as mechanical flexibility, a low coefficient of thermal expansion, and low moisture absorption [31] [14]. Furthermore, LCP has the mechanical strength and low-cost to be the final PCB, making it suitable for SOP applications.

Figure 5. Examples of conceptual phones introduced by leading phone companies as the foreseen phones of the future.

Among all these properties, the mechanical flexibility of the LCP can enable low-profile antenna solutions based on conformal configurations. Antennas on flexible substrates have been utilized in some popular commercial devices, e.g., the iPhone, as shown in Figure 4b. As seen in the figure, the antenna printed on a flexible, thin film can easily conform to the shape of the device, making the integration easier. Moreover, emergent technologies such as wearable electronics or the nanotechnology-based foldable electronics can also benefit from low-cost conformal antenna configurations. As seen in Figure 5, the vision for future phones, introduced by leading wireless phone companies such as Nokia and Samsung, is based on thin, flexible devices capable of being used as a wrist band [32] [33].

The idea of using conformal antennas on flexible substrates for consumer applications has also been investigated in [34]. In this paper, a dual-band antenna printed on a silicon suspended parylene membrane has been proposed. Although the monopole presented in [34] is on a flexible, low-profile substrate, the fabrication technique is a costly MEMS-based procedure that includes high-temperature processes. Moreover, it is not a complete solution, unlike the 3-D multilayer LCP technology, where the integration of the module circuitry can also be handled successfully.

As mentioned earlier, a mechanism is required to protect the RF circuits from the radiated fields of the antenna when the antenna is integrated in close proximity to the module. The conventional on-board shielding metal case can be replaced with an on-package shielding metal case to eliminate the need for a separation between the module circuitry and the

antenna. The on-package shielding metal case is also employed in [35], where a bent-monopole antenna is placed on the side of the shielding metal box. The antenna used in [35] is a separate metal piece soldered to a feeding line on the package. This connection method introduces mismatch into the system while adding a connection step into the integration. Moreover, integration of the antenna with the rest of the front-end circuitry still remains an issue since the antenna is not printed on the same substrate with the module circuitry.

2.2 Multilayer Module Concept with the Integrated Conformal Antenna

As shown in Figure 6, previous work on RF SOP has shown that high-performance front-end modules with significant size reduction can be designed using 3-D integration of the RF front-end functional blocks into LCP-based multilayer organic substrates. Examples of the filter, low noise amplifier (LNA), voltage controlled oscillator (VCO), and mixer designs using embedded passives in multilayer substrates can be found in the literature [14], [15], [16], [17], [18], and [19]. However, the SOP-integration of the antennas with the front-end module with high-efficiency and low-cost is still a significant problem. A novel configuration to enable high-level integration of the antenna with the front-end module is proposed in this thesis.

Conformal antennas fabricated on the LCP-based rigid-flex substrates, as proposed in [36], can provide a promising solution to the antenna integration problem in SOP applications. In such a configuration, the advantages of the multilayer substrates in miniaturizing the front-end module using embedded passives are combined with the flexibility of the LCP to provide a solution for the antenna integration problem.

The proposed multilayer module concept, including the antenna integrated on the module package, is shown in Figure 7. As seen in Figure 7, the antenna is printed on a thin, flexible LCP layer, which protrudes from a rigid multilayer stack-up. The rigid part of the

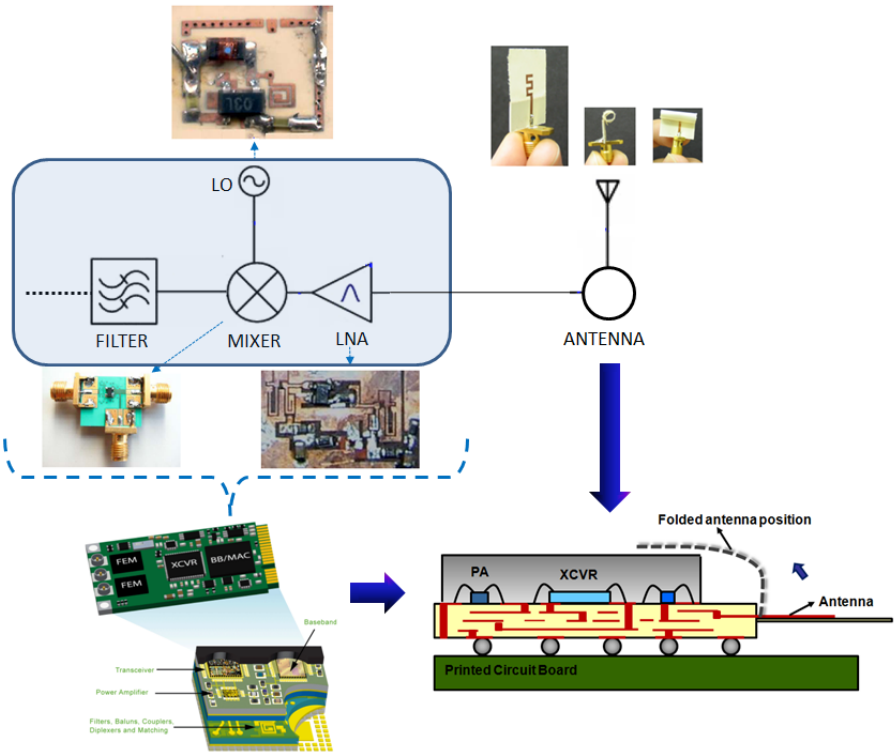

Figure 6. Extension of the RF receiver front-end on a multilayer organic-based package to include on-package antenna integration. The references for the previous work shown are as follows: Local oscillator [15], mixer [17], low-noise amplifier [19], antenna [36].

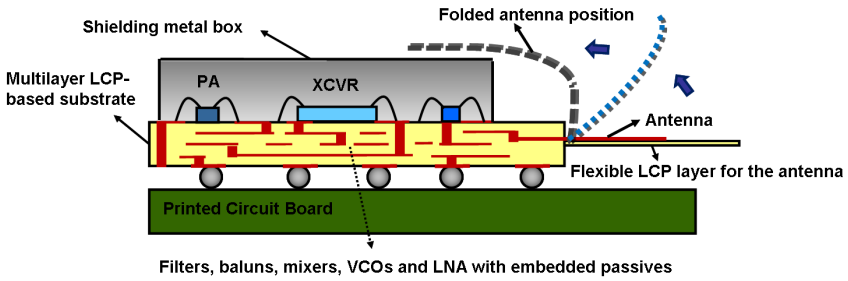

Figure 7. Proposed multilayer module concept using the conformal antenna on a flexible layer of LCP. The abbreviations used in the figure stand for power amplifier (PA) and transceiver (XCVR).

substrate includes module components such as filters, mixers, VCOs, balun, LNA, and the matching circuitries constructed with the embedded passives printed on different layers of the substrate. The power amplifier (PA) and the transceiver (XCVR) chip are placed on the top layer of the rigid substrate and enclosed by an on-package shielding metal case, which serves as a part of the front-end module package. The shielding metal case eliminates the need for a separation between the module circuitry and the antenna to protect the RF circuits from the radiated fields of the antenna. The antenna is printed on the flexible part of the substrate and folded over the metal case to result in compact integration. The possible configurations of the antenna are illustrated in Figure 7 with dashed lines.

Several antennas have been designed on LCP-based rigid-flex substrates to verify this concept. First, a single-band meander monopole antenna has been designed on a two-layer substrate. Then, this single-band meander design has been extended to a dual-band design, such that both the 2.4/5.2 GHz WLAN bands were covered. Next, an L-shaped monopole design has been proposed to increase the bandwidth for additional coverage of WiMAX bands. The single-band L-shaped monopole design has also been extended to a dual-band design similar to the meander antenna case. The details of the designed structures and the fabrication processes are explained in the following sections.

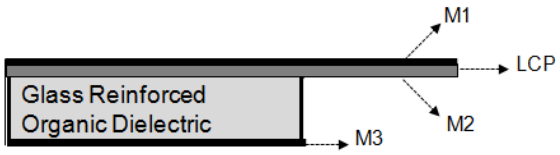

Figure 8. Cross-section of the two-layer rigid-flex substrate.

2.3 Single-band Meander Antenna on a Two-layer Rigid-flex Substrate

2.3.1 Structure Description

In this part, a single-band meander monopole antenna on a two-layer rigid-flex substrate is introduced. A meander design is preferred because of its ability to achieve the required length of the current path within a compact size.

The substrate of the antenna is composed of two layers of dielectric, as shown in Figure 8. The top layer is a 25 μm thick LCP layer with a size of 18 mm $\times$ 25 mm. The bottom layer is a 508 μm rigid, glass-reinforced organic dielectric layer (prepreg) with a size of 18 mm$\times$9 mm. The LCP layer has a dielectric constant of 2.95 and a loss tangent of 0.002. The prepreg layer has a loss tangent of 0.0037 and a dielectric constant of 3.48.

As seen in Figure 8, the protruding portion of the LCP layer is not supported by the prepreg layer; thus, the LCP layer can easily be conformed using the advantage of its mechanical flexibility. There are three metal layers available in this stack-up, labeled as M1, M2 and, M3 in Figure 8. The antenna and the feeding microstrip line are printed on M1. The antenna is positioned on the protruding part of the LCP making it possible to bend, fold and roll the antenna, leading to a compact antenna design. The ground reference for the antenna is printed on M3, and M2 is not occupied in this design.

A commercial 3-D electromagnetic simulator, High Frequency Structure Simulator (HFSS) [37] was used to optimize the dimensions of the antenna to obtain a resonant frequency of 5.9 GHz. The final dimensions of the design are shown in Figure 9. Given the width of the meander antenna, w = 3.5 mm, and the gap between the meandered sections, g = 1 mm, the total length of the antenna was found as 16.5 mm, which is equal to $0.33\lambda_0$ at the resonant frequency. The antenna is excited with a 50Ω microstrip line with length

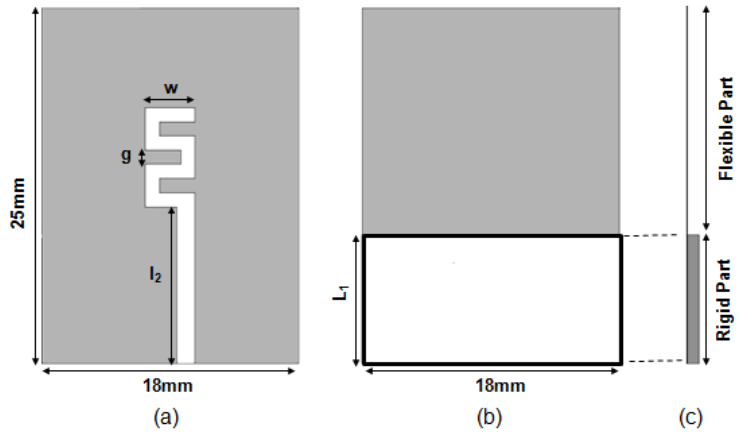

Figure 9. Details of the optimized design. (a) Top view, (b) Bottom view, (c) Side view.

$L_1 = 10$ mm, which is printed on the rigid part of the substrate. The ground plane of the signal line covers the bottom of the rigid substrate with a size of 18 mm $\times$ 9 mm.

2.3.2 Fabrication

The single-band meander antenna on a two-layer substrate was fabricated using a novel, low-cost, multilayer rigid-flex LCP process [4]. This process technology employs only low temperature FR-4 compatible processes (all $< 290\,^{\circ}$C). As mentioned earlier, the antenna and the feeding microstrip line were printed on a 25 μm thick LCP layer. Multiple layers of a low-loss glass-reinforced adhesive dielectric were bonded with the LCP to form the rigid part of the substrate. The single-band antenna was designed on a two-layer stack-up to prove the concept. A three-layer balanced stack-up is discussed in the following sections of this chapter.

The fabrication of the rigid-flex antenna substrate follows the process flow chart shown in Figure 10. The designs were fabricated on a $9'' \times 11''$ board. The first step of the process is patterning the metal layer M1 on the LCP core layer. Next, the cavities below the antenna structures were formed by the precision mechanical routing of a stack-up formed with prepreg layers and a copper layer to realize M3. The copper layer was placed at the bottom of the stack-up, followed by five layers of 101.6 μm thick prepreg and the 25 μm thick LCP layer on top. An alignment board was used throughout the process to prevent

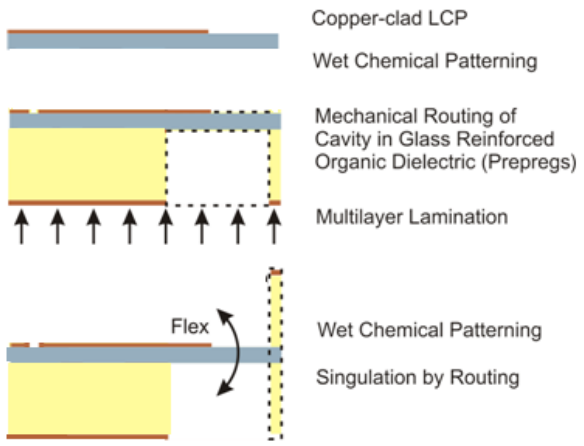

Figure 10. Steps followed during the fabrication of the conformal single-band antenna on a rigid-flex substrate.

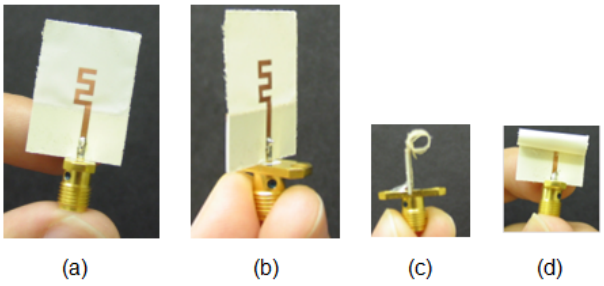

Figure 11. Photos of the fabricated single-band meander antenna prototype. (a)-(b) Straight configuration, (c)-(d) Rolled configuration.

misplacement. The alignment step was followed by the multilayer lamination ($< 290\,^{\circ}\mathrm{C}$) to bond the LCP with the adhesive prepreg layers. The metal layer M3 was patterned with wet chemical processing. Finally, the antenna elements were singulated by precision mechanical routing.

The photos of the fabricated prototype are presented in Figure 11. As seen in the photos, the 25 μm thick LCP layer is flexible enough to be rolled, showing the potential of the LCP as a conformal antenna substrate.

2.3.3 Simulation and Measurement Results

The return loss of the antenna was measured by using an Agilent E8363B vector network analyzer. An SMA connector was soldered directly onto the microstrip line without using

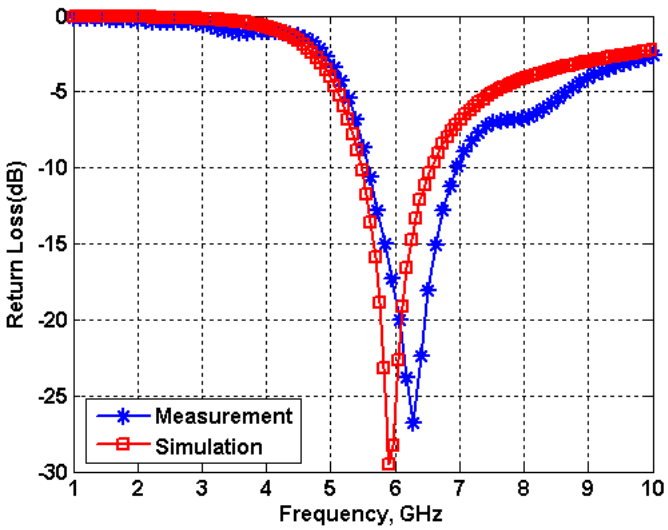

Figure 12. Simulated and measured S_{11} data of the fabricated single-band antenna.

any tuning components. During simulations, the antenna was considered in straight configuration. A comparison between the simulated and the measured return loss of the antenna for this configuration is presented in Figure 12, where good agreement is observed between simulation and measurement. The measurements were repeated for the folded and rolled cases of the antenna, and the results are shown in Figure 13. As seen in the figure, the measured return loss of the antenna does not change much for different configurations.

The simulated far field patterns of the antenna for a straight configuration are presented in Figure 14. The antenna has a nearly omni-directional pattern like that of a dipole, and the simulated peak gain of the antenna was found as 2.5 dB at a resonant frequency of 6 GHz.

2.4 Dual-band Meander Antenna Structure

In this part, the single-band operation of the meander antenna is extended to dual-band operation such that 2.4/5.2 GHz WLAN bands are both covered. The dual-band coverage is achieved by adding an extra resonator and changing the orientation of the meander antenna. The antenna is positioned on a vertical substrate, obtained by folding the flexible part of the substrate. The details of the structure as well as the measurement and simulation results

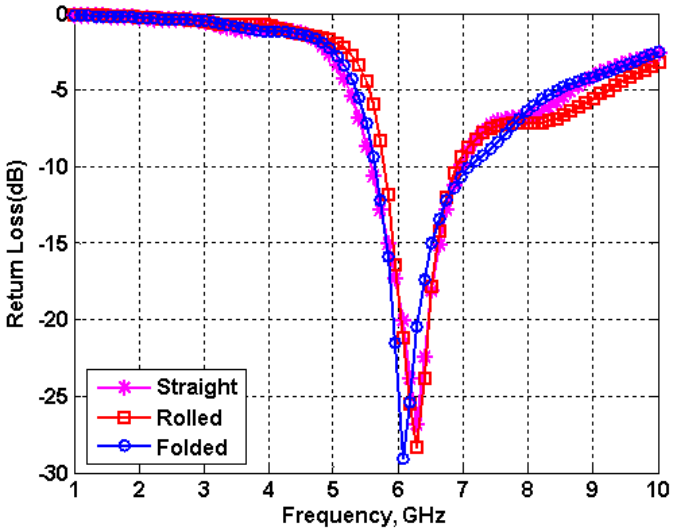

Figure 13. Measured S_{11} data of the fabricated single-band antenna for different configurations.

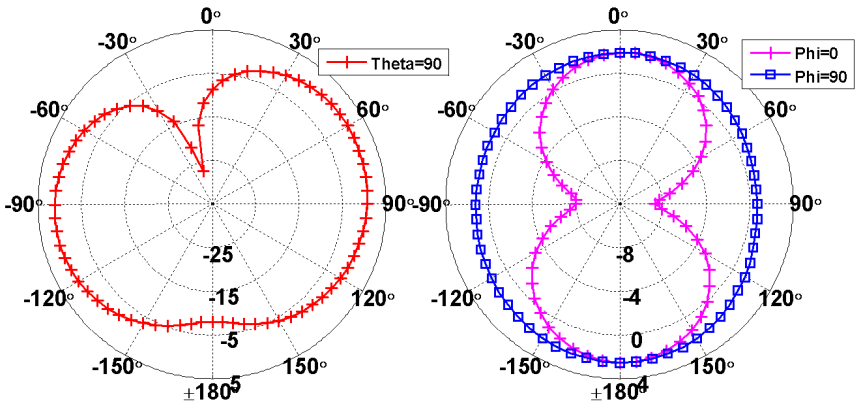

Figure 14. Simulated radiation patterns of the fabricated single-band antenna at 6 GHz.

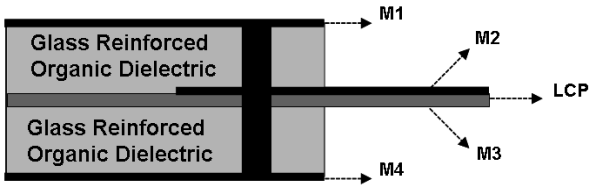

Figure 15. Cross-section of the balanced stack-up used for the dual-band meander antenna.

are presented in the following sections.

2.4.1 Structure Description

The details of the proposed dual-band meander structure are discussed in this section. Extended from the single-band antenna substrate, the substrate is a balanced rigid-flex substrate composed of three layers of low-loss dielectrics, as shown in Figure 15. In this stack-up, a 25 μm thick LCP layer is supported by 508 μm thick top and bottom prepreg layers.

The substrate consists of a flexible part for the antenna and a rigid part to house the signal lines and the module circuitry, as shown in Figure 7. The 30 mm$\times$45 mm LCP layer is between the 30 mm$\times$35 mm rigid prepreg layers. This middle LCP layer protrudes from one edge of the substrate; thus, it provides a 10 mm long flexible substrate for the antenna using the mechanical flexibility of LCP.

As seen from the cross-section of the substrate shown in Figure 15, there are four metal layers in this stack-up [M1-M4]. The antenna is fabricated on the protruded portion of M2, so that it can be bent, folded, or even rolled, resulting in a compact design. The microstrip signal lines feeding the antenna are on M1 and M2. Metal layer M4 serves as the ground reference for the signal lines and the antenna. M3 is left unused in this design.

The details of the proposed antenna structure integrated with the shielding metal case are presented in Figure 16. As shown in Figure 16b, the antenna is composed of two resonating structures to support dual-band operation. The lower band is covered by a meander line element resonating around 2.4 GHz, while the upper resonance is obtained by a quarter-wave long antenna element resonating around 5.2 GHz. Both of the resonating

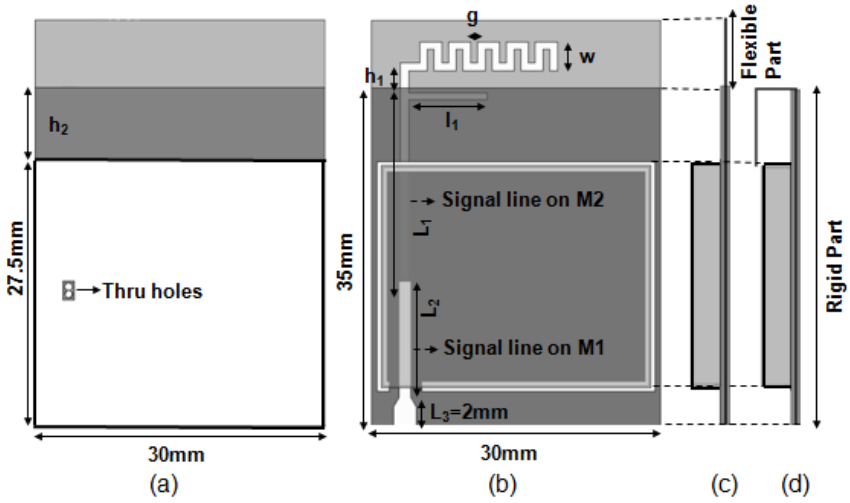

Figure 16. Details of the meander dual-band antenna. (a) Bottom view (straight), (b) Top view (straight), (c) Side view (straight), (d) Side view (folded).

elements are printed on M2. The meander line antenna element with width, $w = 3$ mm, gap, $g = 0.7$ mm, and height, $h_1 = 1$ mm, is positioned on the flexible portion of the LCP, such that it will be vertical to the substrate when the flexible portion is folded, as shown in Fig 16d. The quarter-wavelength long element with $l_1 = 8$ mm, is embedded inside the rigid part, which is not covered by the ground metal. This region is labeled as $h_2 = 7.5$ mm in Figure 16a.

The antenna is excited through a 50Ω microstrip line printed along the rigid part of M2 with length $L_1 = 22$ mm. To enable the use of an edge-mount SMA connector for the measurements, the signal line on M2 is connected to another 50Ω signal line on M1 by two through holes. The through holes are isolated from the ground plane by a rectangular clearance area, as shown in Figure 16a. The widths of the 50Ω signal lines on M1 and M2 are 1.2 mm and 0.9 mm, respectively. These values were found by considering the traces to be in stripline configurations because of the presence of the grounded metal box. A tapered transition is used at the edge of the substrate to account for the changes in the impedance in the absence of the metal box.

The shielding metal case is a hollow metal box with a size of 28 mm × 23 mm × 3 mm,

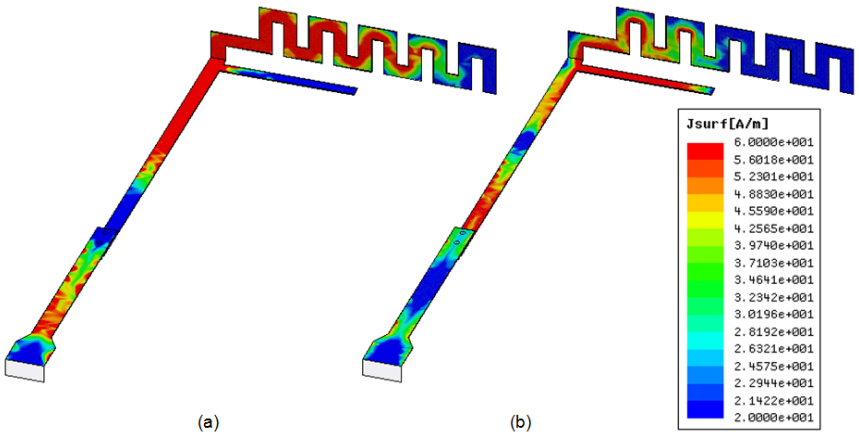

Figure 17. Simulated surface current distribution of the dual-band antenna. (a) 2.45 GHz, (b) 5.2 GHz.

and it is constructed by bending an 80 μm thick copper sheet. The metal box is electrically connected to a rectangular metal trace printed on metal layer M1, which is shorted to ground by a series of through holes. The metal box not only protects the module circuitry from the undesired coupling to the nearby conducting elements and the radiated fields of the antenna, but it also serves as a ground reference for the antenna.

2.4.2 Design Based on Simulation

HFSS [37] was used to optimize the proposed structure. The antenna was designed to be used in the folded configuration, in which the protruding flexible LCP portion is folded over the shielding metal case, as shown in Figure 16d.

The surface current graphs at 2.45 GHz and 5.2 GHz are shown in Figure 17. As seen from the figure, the meander resonator is excited at 2.45 GHz, while the quarter-wavelength element is excited at 5.2 GHz. Since the resonance frequencies are determined by the lengths of the current paths for the resonator antennas, the lengths of the structures were tuned to cover the desired bands. Other parameters affecting the resonant frequencies and the matching of the antenna were found to be the separation distance between the shielding metal case and the antenna elements, the gap between the arms of the meander resonator, the width and height of the meander resonator, and the separation distance between the ground metal and the antenna elements.

During simulations, it was found that a minimum distance of 8 mm is required between the vertical folded part and the shielding metal case to obtain the desired return loss values. This resulted in a substrate size of 30 mm × 35 mm. The final size of the ground metal on M4 was found to be 30 mm × 27.5 mm, leaving an h_2 = 7.5 mm wide part near the folded edge of the substrate without the ground metal.

2.4.3 Fabrication

The fabrication of the dual-band antenna on a three-layer rigid-flex substrate follows similar steps to the ones explained for the fabrication of the single-band antenna on a two-layer substrate. Although additional steps were required to increase the number of layers and to form via connections, the overall process is still a low-cost, FR-4 compatible, low-temperature process.

As mentioned in the structure description, the antenna signal traces and the resonating structures were printed on a 25 μm thick LCP layer. The rigid part of the substrate was formed by bonding multiple layers of a low-loss glass-reinforced adhesive dielectric with the LCP. A stack-up with only three layers of dielectrics was used in this design to prove the concept. In the case of the module integration, the number of LCP layers can be increased to create more real estate for the embedded passives realizing the module circuitry. The thickness of the substrate and the position of the ground metal can also be adjusted based on the thickness and the number of prepreg and LCP layers. If necessary, based on the application, even the rigid part of the substrate can be made more flexible by changing the number and the thicknesses of the laminate layers.

The fabrication of the rigid-flex antenna substrate follows the process flow chart shown in Figure 18. The first step is patterning the metal layer M2 on the LCP core layer. Next, the cavities above and below the antenna structures were formed by the precision mechanical routing of the prepreg layers. The prepreg layers were placed on a board with alignment pins, as shown in Figure 19a, to prevent registration errors. Five layers of 101.6 μm thick prepreg layers were used on each side of the LCP layer to realize the 508 μm thickness on

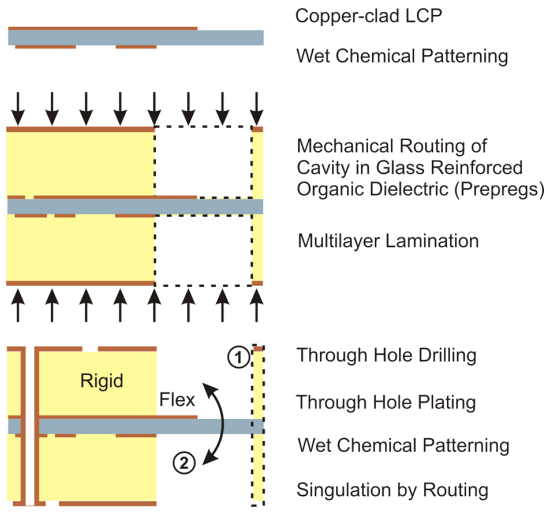

Figure 18. Steps followed during the fabrication of the antennas on the balanced stack-up.

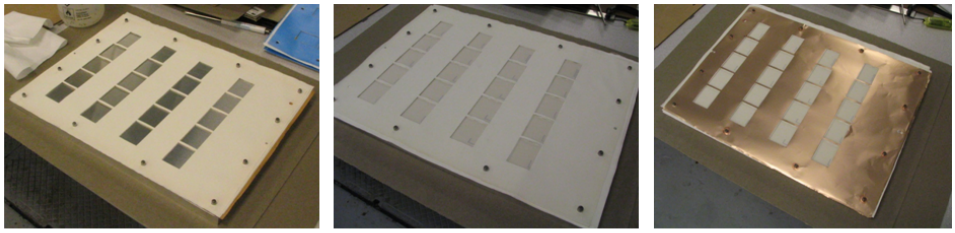

Figure 19. Photos of the alignment step during fabrication. (a) Bottom prepreg layers placed on the alignment board after forming the cavities. (b) Total stack-up including the middle LCP layer and the top prepreg layers. (c) The metal copper layer placed to form metal layer M4.

each side. The LCP layer was placed between the prepreg layers, as shown in Figures 19b and 19c. Two copper layers were also placed at the top and the bottom of the stack-up, as shown in Figure 19c, to realize the metal layers M1 and M4 in Figure 15. Cavities were drilled on these copper layers similar to the ones on the prepreg layers. The alignment step was followed by multilayer lamination ($< 290\,^{\circ}\mathrm{C}$) to bond the LCP with the adhesive prepreg layers.

After the multilayer lamination step, through holes were mechanically drilled and plated using both electroless and electrolytic copper plating to form vertical interconnections. Patterning the metal layers M1 and M4 was done by wet chemical processing. X-ray photos

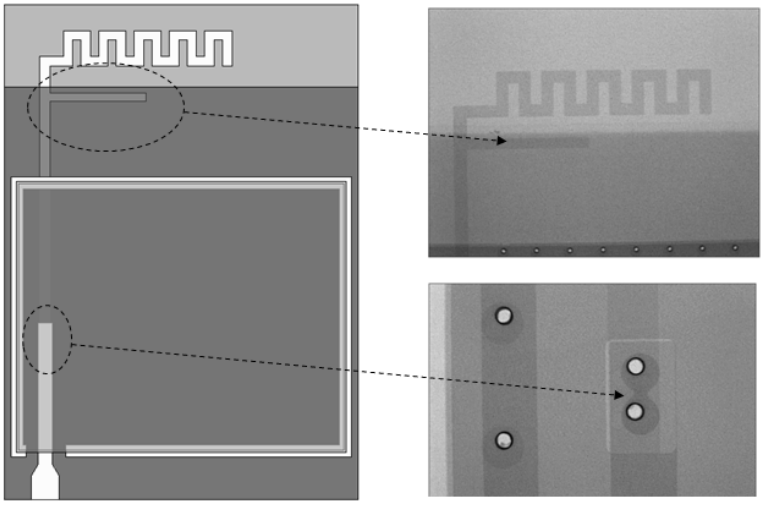

Figure 20. X-ray photos showing the critical via connections.

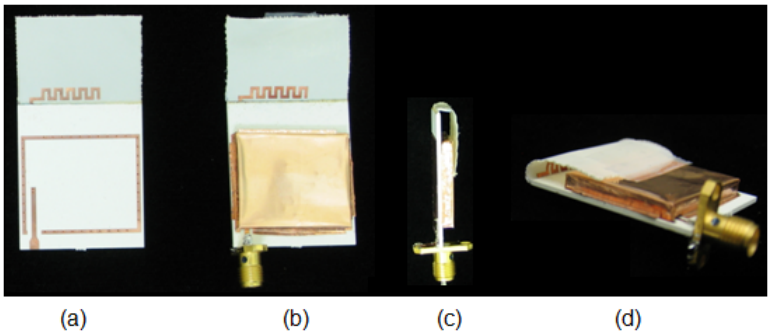

Figure 21. Photos of the fabricated dual-band meander antenna. (a) Antenna, (b) Antenna with the metal case, (c) Folded configuration, (d) Perspective view.

were taken to check the metallization of vias. As seen in Figure 20, the critical vias connecting the two signal lines were metallized properly. Finally, antenna elements were singulated by precision mechanical routing. Designs were fabricated on a $9'' \times 12''$ panel, using large-area PCB tooling, resulting in a low-cost implementation that can be easily scaled to larger panel sizes for further cost reduction.

The photos of the fabricated prototype are presented in Figure 21. The shielding metal box and an SMA connector were mounted on the substrate, as shown in Figure 21b. Then, the flexible substrate of the antenna was folded over the metal case, as seen in Figure 21c and Figure 21d.

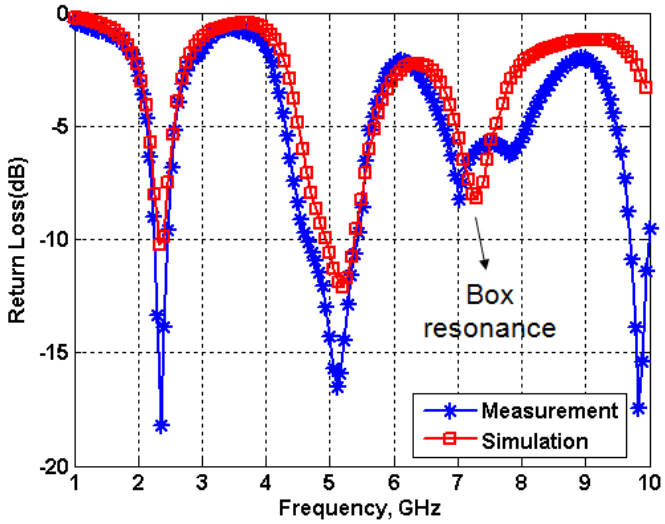

Figure 22. Simulated and measured S_{11} data of the dual-band meander antenna.

2.4.4 Simulation and Measurement Results

The simulated and measured return loss results of the fabricated antenna are shown in Figure 22. As seen in Figure 22, good agreement is observed between the measured and the simulated results. The measured 10 dB bandwidth of the antenna is 215 MHz (2248 MHz-2465 MHz) for the 2.4 GHz band and 800 MHz (4622 MHz-5423 MHz) for the 5 GHz WLAN band.

The resonance observed around 7.6 GHz in both the simulation and the measurement data is the box resonance, corresponding to the dominant TM mode of a partially-loaded rectangular cavity resonator with a size of 23 mm $\times$ 28 mm $\times$ 4 mm [38], [39]. Since the shielding metal box is shorted to ground with a series of vias, the box acts like a closed rectangular cavity partially-filled with the rigid substrate of the proposed structure. It should be noted that the box resonance frequency falls out of the band of interest as desired.

The far field of the fabricated antenna was also measured at 2.4 GHz and 5.2 GHz. The simulated and measured radiation patterns of the antenna in the x-y, y-z, and x-z planes are shown in Figures 23 and 24. As seen in the figures, the measured patterns agree well with the simulation results. The correlation between the measured and the simulated results is particularly good for the x-y plane since the effects of the SMA connector are eliminated

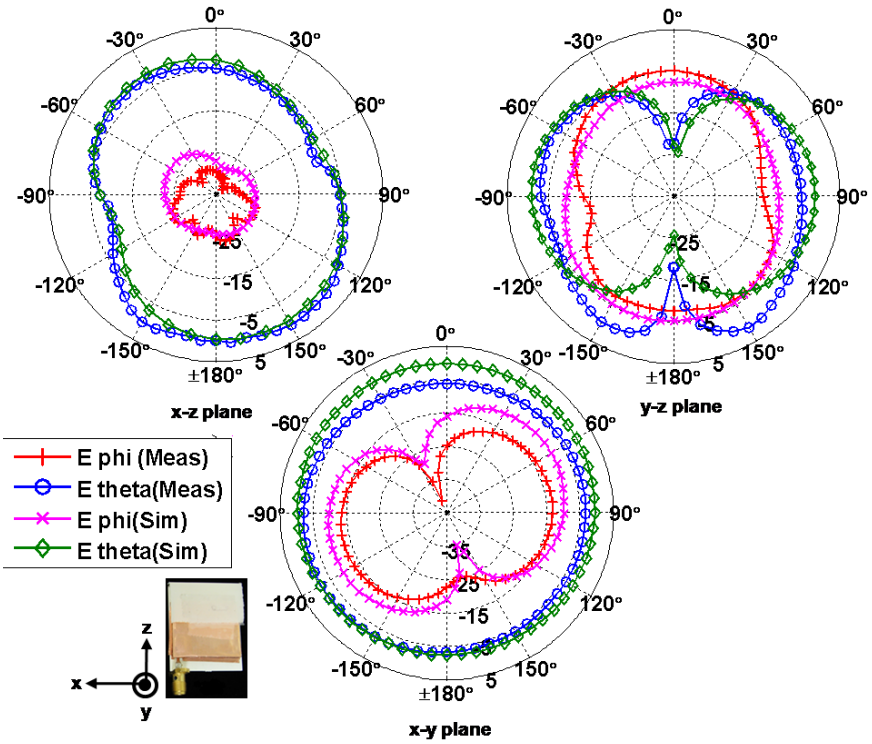

Figure 23. Simulated and measured far field patterns of the dual-band meander antenna at 2.4 GHz.

in the x-y plane. It should also be noted that the overall radiation pattern of the antenna has a nearly omni-directional pattern, which is desirable especially for mobile applications. The simulated and the measured peak gains of the antenna for 2.4 GHz and 5.2 GHz were found as 1.33 dB and 0.32 dB, and 3.4 dB and 2.42 dB, respectively. The slight difference may be attributed to the SMA connector and cable errors introduced in the measurement.

2.5 L-shaped Single-band Monopole

The single-band meander antenna structure was successfully extended into a dual-band structure, such that both the 2.4 GHz and 5.2 GHz WLAN bands were covered. However, optimization of the design required many iterations since there were many design parameters affecting the resonance frequencies and the matching of the antenna. As an alternative to the meander antenna, an inverted L-shaped monopole was chosen because it is a more compact, easy to design antenna, capable of providing wide bandwidth. First, a single-band antenna was designed to cover the 5 GHz WLAN and WiMAX bands. Then, the design

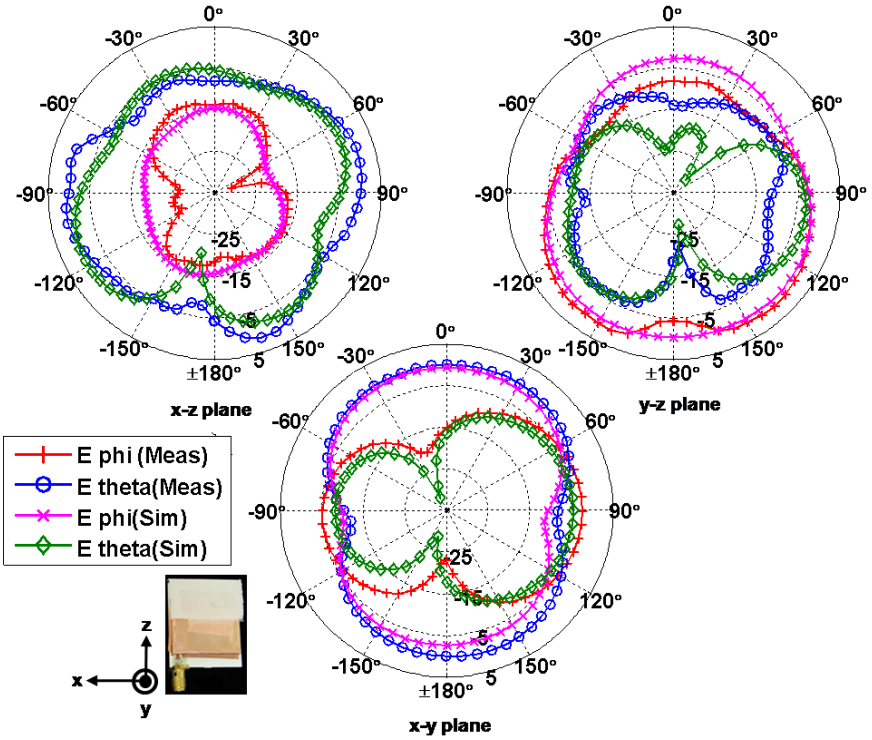

Figure 24. Simulated and measured far field patterns of the dual-band meander antenna at 5.2 GHz.

was transformed into a dual-band antenna to include the 2.4 GHz WLAN band as well. In this section, the details and the measurement and simulation results of the single-band inverted L-shaped antenna are discussed.

2.5.1 Structure Description

The antenna substrate has the same stack-up with that of the dual-band meander antenna, as shown in Figure 8. The 30 mm × 45 mm LCP layer is between the 30 mm × 33 mm rigid prepreg layers. The 12 mm long protruding portion of the LCP layer provides a flexible substrate for the antenna.

The antenna structure used in this design is an inverted L-shaped monopole since it can provide wide bandwidth with a relatively small size. The details of the proposed antenna structure integrated with the shielding metal case are presented in Figure 25. As shown in the figure, the antenna consists of an L-shaped structure with width, w = 1 mm, length, l_1 = 8.5 mm, height, h_1 = 2.3 mm, and an embedded part, h_2 = 4 mm. This embedded part

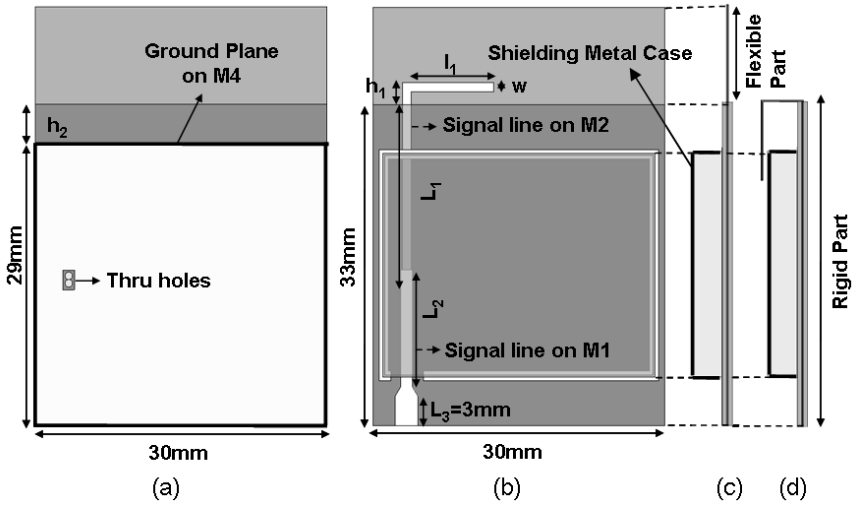

Figure 25. Details of the fabricated single-band L-shaped antenna. (a) Bottom view (straight), (b) Top view (straight), (c) Side view (straight), (d) Side view (folded).

is the portion of the signal line on metal layer M2 that is not covered by the bottom ground plane. The layout of the feed lines is similar to the layout in the meander antenna design. The microstrip lines are on M1 and M2, with lengths $L_1 = 19$ mm and $L_2 = 12$ mm, and they are connected with two through holes. The shielding metal case was also modeled as a part of the module package.

2.5.2 Design Based on Simulation

HFSS [37] was used during the optimization of the design. The antenna was optimized to be used in the folded configuration, in which the protruding flexible LCP portion is folded over the shielding metal case, as shown in Figure 25d.

During the design process, it was found that the primary parameters affecting the matching and the resonant frequency of the antenna are the length of the antenna, l_1, the height of the antenna, h_1, and the distance of the bottom ground plane to the antenna, h_2. A series of parametric sweep simulations was performed to study the effect of these parameters on the matching of the antenna.

The simulated return loss data obtained for three different values of antenna length $l_1 =$ 7.5 mm, 8.5 mm and 9.5 mm with $h_1 = 2.3$ mm and $h_2 = 4$ mm are shown in Figure 26.

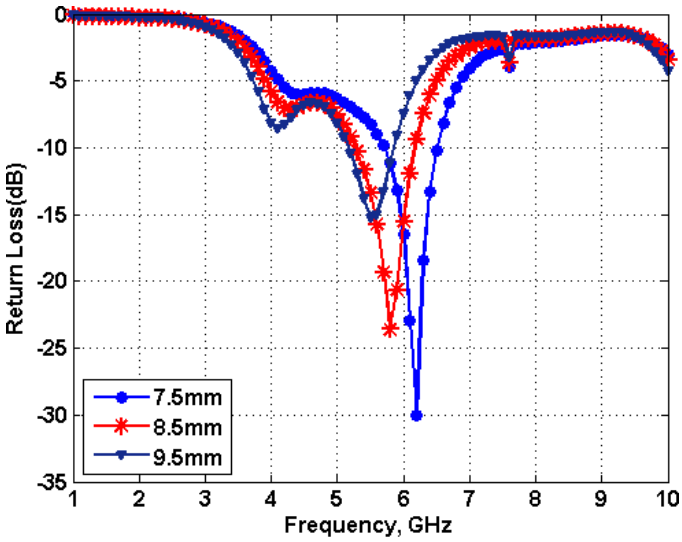

Figure 26. Simulated S_{11} data for different values of l_1 (h_1 = 2.3 mm and h_2 = 4 mm).

The resonance frequency of the antenna decreases as the length of the L-shaped radiating structure, l_1, is increased. This is expected because of the increase in the electrical length of the antenna as l_1 is increased. Furthermore, the bandwidth and the matching level of the antenna are also affected as l_1 is changed. This may be because of the change in the capacitive coupling of the antenna to the vertical ground provided by the metal box.

For the fixed value of l_1 = 8.5 mm, the effect of the antenna height, h_1, was studied by simulating the structure for h_1 = 2.3 mm, 4 mm and 5 mm. The distance from the ground, h_2, was kept as 2.5 mm for these simulations. As seen in Figure 27, the antenna resonance frequency shifts to upper frequencies as h_1 is decreased.

Finally, the effects of the distance from the ground, h_2, was studied by simulating the structure for h_2 = 2.5 mm, 3 mm, and 4 mm with l_1 = 8.5 mm and h_1 = 2.3 mm. As shown in Figure 28, h_2 affects the bandwidth and the resonance frequency of the antenna. Final values for the fabricated structure were chosen as l_1 = 8.5 mm, h_1 = 2.3 mm, and h_2 = 4 mm to cover 5 GHz WLAN and WiMAX bands. It was found from the parametric sweeps for h_1 and h_2 that both h_1 and h_2 change the resonance frequency of the antenna. In other words, both h_1 and h_2 contribute to the resonance electrical length of the antenna. The total length, $L = l_1 + h_1 + h_2$, of the optimized design was found to be approximately

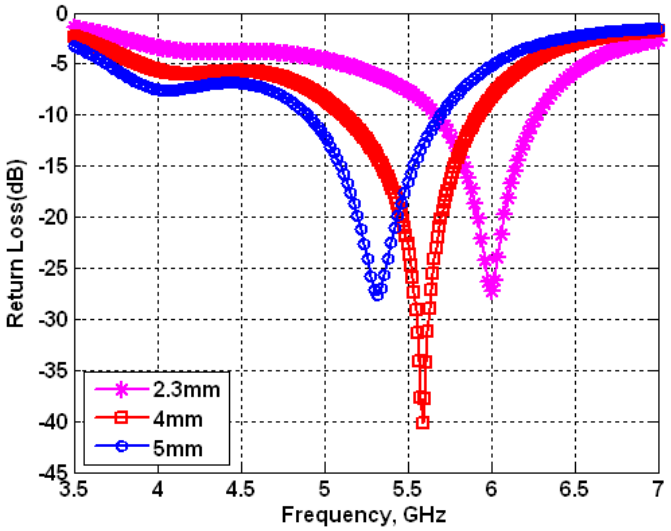

Figure 27. Simulated S_{11} data for different values of h_1 (h_2 = 2.5 mm and l_1 = 8.5 mm).

$0.28\lambda_0$ at a resonant frequency of 5.8 GHz.

2.5.3 Fabrication

A prototype of the antenna was fabricated in the same board with the dual-band meander antenna. Therefore, the fabrication follows the same steps explained for the dual-band meander antenna. The photos of the fabricated prototype are shown in Figure 29.

2.5.4 Simulation and Measurement Results

Figure 30 shows the simulated and measured results for the S_{11} of the fabricated prototype. As seen in Figure 30, good agreement is observed between the measured and the simulated results. The measured 10 dB bandwidth of the antenna is 1070 MHz (4710 MHz-5780 MHz) covering most of the 5 GHz WLAN (5150 MHz-5825 MHz) and WiMAX band (5250 MHz-5850 MHz). The return loss value at the upper frequency of the WiMAX band is measured to be -8.5 dB, which is an acceptable value for wireless applications. As mentioned for the previous designs explained in this chapter, the resonance observed around 7.6 GHz in both the simulation and the measurement data in Figure 30 is the box resonance corresponding to the dominant TM mode of a partially loaded rectangular cavity resonator with a size of 23 mm × 28 mm × 4 mm [20], [21].

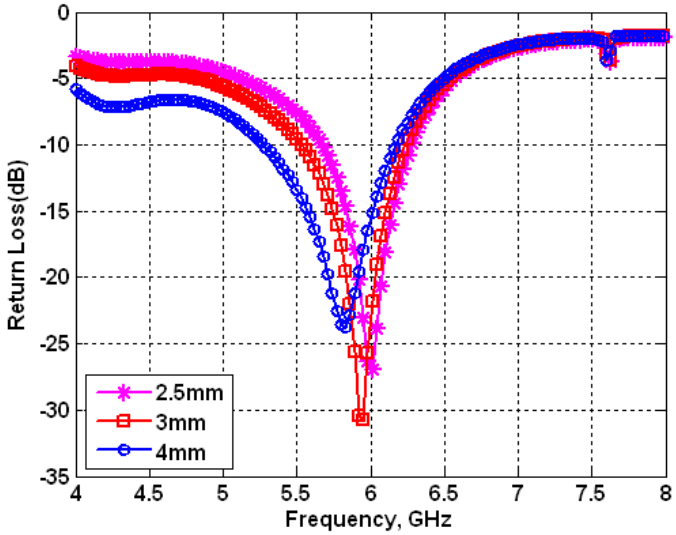

Figure 28. Simulated S_{11} data for different values of h_2 (h_1 = 2.3 mm and l_1 = 8.5 mm).

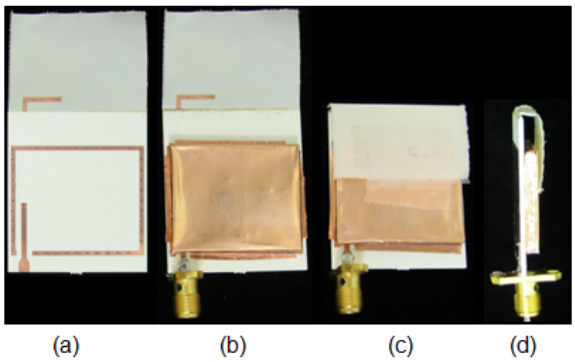

Figure 29. Photos of the fabricated prototype. (a) Antenna, (b) Antenna with the metal case, (c) Folded configuration, (d) Side view.

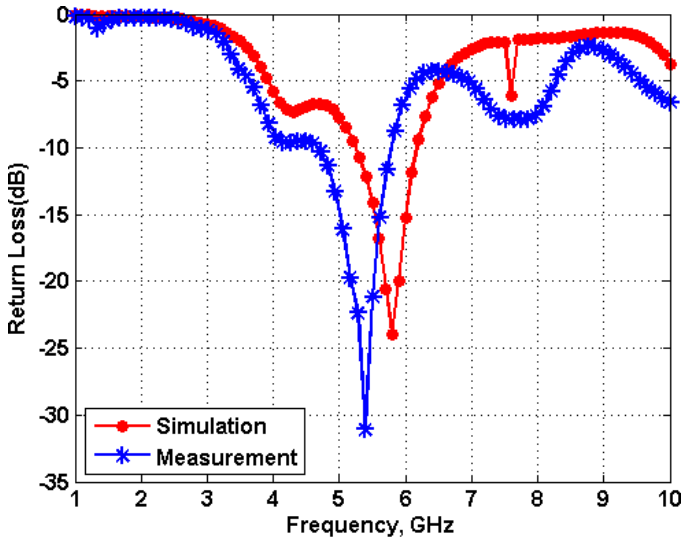

Figure 30. Simulated and measured S_{11} data of the single-band L-shaped antenna.

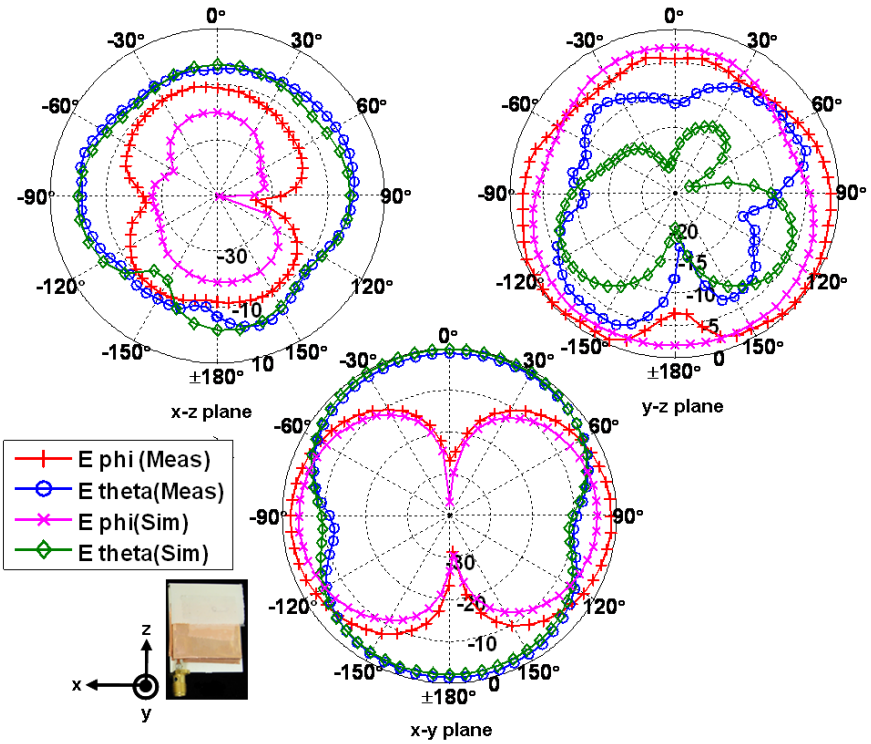

Figure 31. Simulated and measured radiation patterns of the single-band L-shaped antenna at 5.2 GHz.

The far field of the fabricated antenna was also measured at 5.2 GHz. The simulated and measured radiation patterns of the antenna on the x-y, y-z, and x-z planes are shown in Figure 31. As seen in Figure 31, the measured patterns agree well with the simulation results. The correlation between the measured and the simulated results is particularly good for the x-y plane since the effects of the SMA connector are eliminated in the x-y plane. It should also be noted that, the overall radiation pattern of the antenna has a nearly omni-directional pattern, which is desirable for mobile applications. The radiation pattern has two slight nulls approximately on the $\phi = 45^\circ$ and $\phi = 135^\circ$ planes owing to the fact that the radiating structure is composed of three orthogonal resonators, labeled as l_1, h_1 and h_2 in Figure 25. The measured and simulated peak gains of the antenna at 5.2 GHz are 1.74 dB and 2.75 dB, respectively. The slight difference may be attributed to the SMA connection and the cable errors introduced in the measurement.

2.6 Dual-band L-shaped Antenna for 2.4/5.2 GHz WLAN and WiMAX Applications

2.6.1 Structure Description

The single-band L-shaped antenna was transformed to a dual-band antenna such that the operation frequency covers both the 2.4 GHz and 5 GHz WLAN/WiMAX bands. This was achieved by including an additional radiating structure resonating at 2.4 GHz. The compactness of the design was preserved by choosing the second radiator as a meandered structure. The meandered line was embedded in the rigid part of the substrate, using the unoccupied separation area between the antenna and the ground, which is labeled as h_2 in Figure 25. This way, a dual-band antenna was designed with only a 2 mm size increase in one of the dimensions compared to the single-band structure.

The details of the final dual-band antenna are shown in Figure 32. The dual-band antenna was printed using the same stack-up with the single-band antenna, as shown in Figure 15. The meandered structure was printed on the same metal layer, M2, with the inverse L-shaped monopole, as shown in Figure 32b.

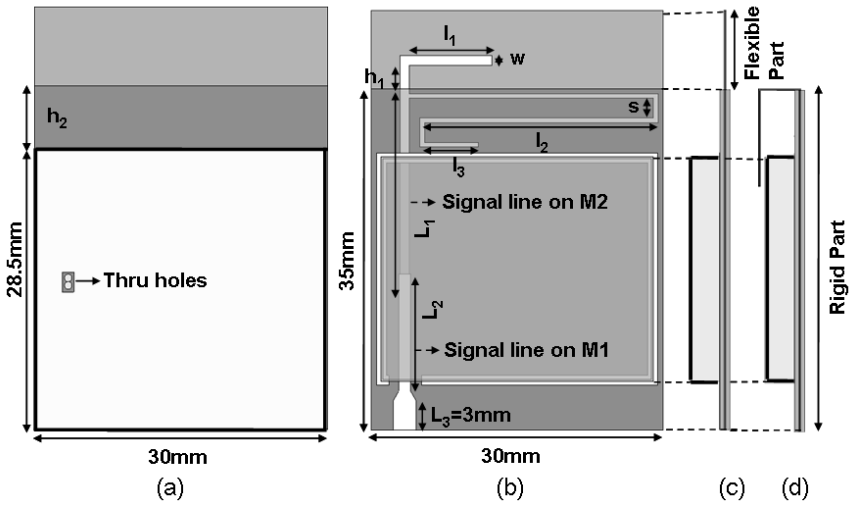

Figure 32. Details of the proposed dual-band antenna structure integrated with the module case. (a) Bottom view (straight), (b) Top view (straight), (c) Side view (straight), (d) Side view (folded).

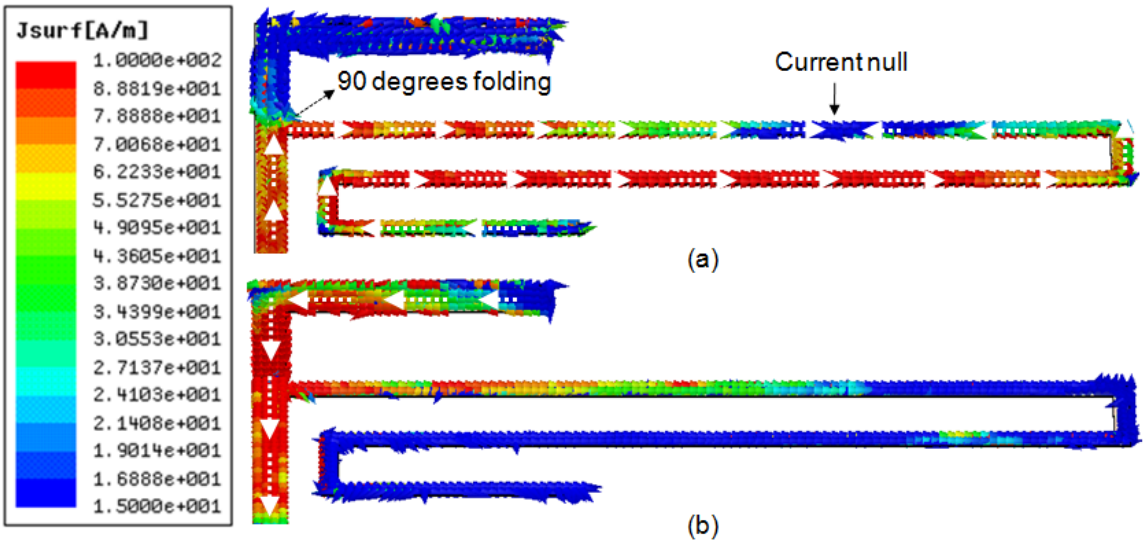

Figure 33. Simulated surface current distribution of the proposed dual-band antenna in folded configuration at (a) 2.4 GHz and (b) 5.2 GHz.

2.6.2 Design Based on Simulation

Similar to the single-band L-shaped antenna, the optimization of the dual-band antenna performance for the folded configuration was achieved using HFSS. Figure 33 shows the surface current distributions of the antenna in the folded configuration at 2.4 GHz and 5.2 GHz. The substrate layers are made invisible in the plots to make the current distribution on the embedded meander resonator visible. As seen in Figure 33, the currents on the L-shaped resonator are stronger at 5.2 GHz; whereas, the meander resonator has stronger currents at 2.4 GHz. The current distribution in Figure 33b implies that the meander is a full-guided-wavelength long (λ_g) resonator at 2.4 GHz with a current null separating two $\lambda_g/2$ long sections.

Although a half-wavelength structure can also provide the desired resonance, a full-wavelength resonator was preferred to achieve the necessary 10 dB bandwidth in the 2.4 GHz band. As seen from the Smith chart shown in Figure 34, the real part of the input impedance of the half-wavelength long resonator antenna is lower than the full-wavelength long structure, resulting in poor matching. The matching of the half-wavelength structure can be improved by increasing the separation from the ground plane, labeled as h_2 in Figure

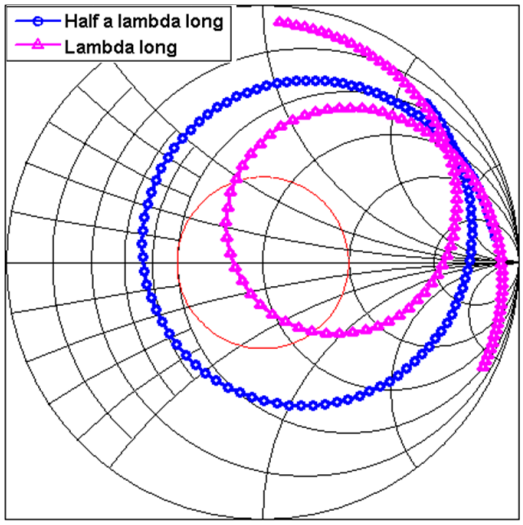

Figure 34. S_{11} **comparison of a** λ_g **long and a** $\lambda_g/2$ **long structures on Smith chart.**

32. However, this conflicts with the aim of the miniaturization. An elegant solution for a fully-integrated system, such as one shown in Figure 7, is replacing the conventional 50 Ohm matching impedance with another impedance value such that both the antenna and the duplexer are optimized simultaneously. This can be achieved in an SOP architecture since embedded components can be co-designed based on optimized impedance values without being limited to 50 Ohm standard. The antenna size can be further decreased with this approach while improving the performance.

A 50 Ohm matching was followed in the design of the antenna prototype since a 50 Ohm edge-mount SMA connector was used during measurements. As seen in Figure 34, the full-wavelength resonator can be well-matched to 50 Ohms in the VSWR$\leqslant$2:1 circle. The optimization of the antenna for the 2.4 GHz band was done by tuning the separation between the arms of the meander and the total length of the meandered structure while the design rules obtained for the single-band L-shaped antenna were applied to optimize the antenna operation in the 5 GHz band. The final values of the parameters shown in Figure 17 can be listed as follows: l_1 = 8.5 mm, h_1 = 2.5 mm, h_2 = 6.5 mm, w = 1 mm, s = 2 mm, l_2 = 24 mm, l_3 = 5.5 mm, $L1$ = 21 mm, $L2$ = 12 mm, and the width of the meandered line is 0.5 mm. The full wavelength aspect of the antenna can be verified by calculating the

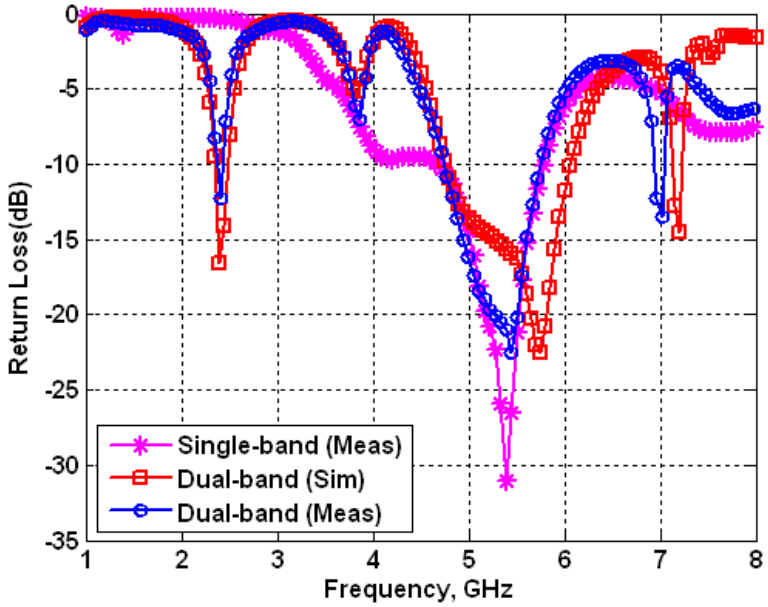

Figure 35. Simulated and measured return loss data for 2.4/5 GHz L-shaped dual-band antenna.

length of the current-path as $L = h_2 + l_2 + 2s + l_3 = 64$ mm, which is equal to $0.98\lambda_g$ at 2.45 GHz.

2.6.3 Simulation and Measurement Results

The simulated and measured return loss results of the conformal dual-band antenna are shown in Figure 35. The measured return loss of the single-band antenna is also included in Figure 35 for comparison. The 2.4 GHz band created by the meandered resonator is clearly seen in the figure. The measured 10 dB bandwidths of the dual-band antenna are 90 MHz (2435 MHz-2445 MHz) for the 2.4 GHz band and 1000 MHz (4750 MHz-5750 MHz) for the 5 GHz WLAN band. The bandwidth of the antenna in the 2.4 GHz band can be improved by slightly decreasing the end length, l_3, or increasing the separation between the arms of the meander, s. As in the case of single-band antenna, a slight shift in the resonance frequency is observed in the 5 GHz band due to the enlargement of the prepreg layers, affecting the folding of the antenna.

The reason for the small shift in the measured resonance frequency of the antenna for the 5 GHz band was investigated using a series of simulations, where the fabrication

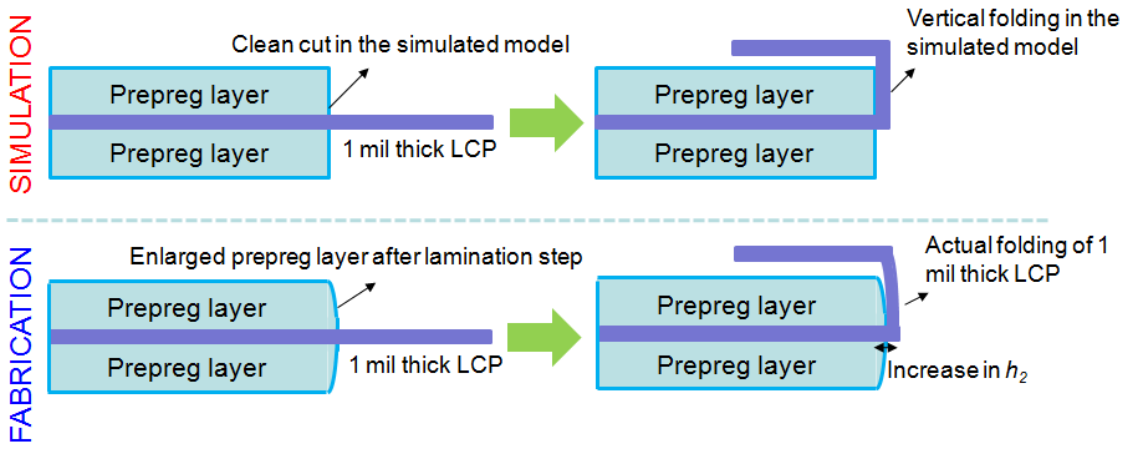

Figure 36. Comparison of the cross-sections of the stack-up in the simulation model and the fabricated prototype. The pressure and the heat applied in the lamination step result in the enlargement of the prepreg layers toward the cavities. This enlargement affects the folding of the flexible substrate.

tolerances for the via misplacement and the signal misalignment were modeled. It was found from these simulations that the S_{11} of the antenna is not affected considerably from the misalignment of the signal lines on metal layers M1 and M2 or the misplacement of the critical via connections between these signal lines.

Another possibility investigated as the reason of the shift in the measured resonance frequency of the antenna was the difference between the folding of the flexible substrate in the fabricated prototype and in the HFSS model. The difference in the folding can be explained as a result of the enlargement of the prepreg layers toward the cavities, as shown in Figure 36, because of the pressure and the heat applied during the multilayer lamination step of the fabrication. When the prepreg layers expand, the separation between the antenna and the ground plane, labeled as h_2 in Figure 32a, increases and the height of the L-shaped resonator, labeled as h_1 in Figure 32b, decreases. The deviation from the optimized values of the final design, in turn, changes the capacitive coupling of the antenna to the ground plane and the shielding metal box, which is observed as a shift in the resonance frequency of the antenna. The change in the resonance frequency can be avoided by compensating for the enlargement of the prepreg layers when mechanically routing the cavities before lamination.

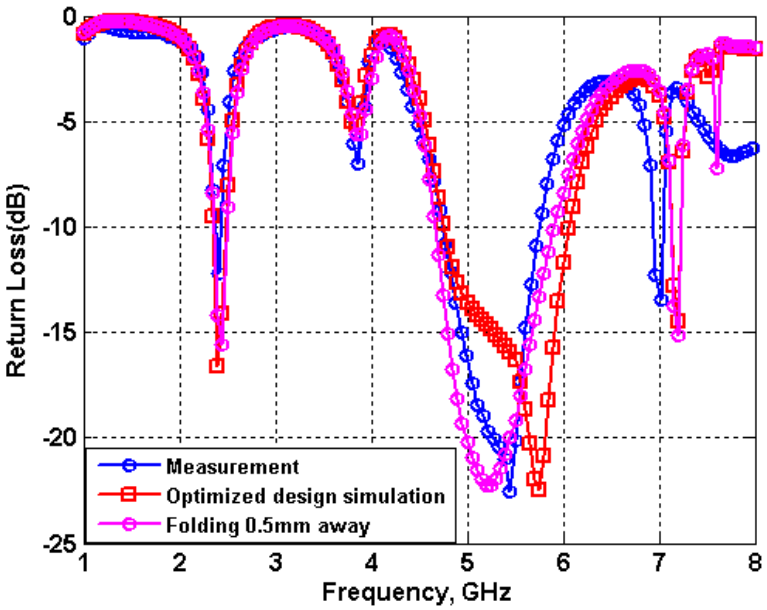

Figure 37. S_{11} **comparison of the antenna to observe the effect of the enlargement of the prepreg layer.**

The effect of the enlarged prepreg layers was captured with an HFSS simulation, where the width of the rigid part of the substrate was increased by 0.5 mm to model the enlargement of the prepreg layers. In this simulation, the $h_1 + h_2$ summation was kept the same with the value in the optimized design. The comparison of the S_{11} data is shown in Figure 37. As seen in the figure, when the folding is further away by 0.5 mm, the resonance frequency of the antenna decreases similar to the measured S_{11}. This result supports the idea that the shift in the measured resonance frequency of the antenna is due to the enlargement of the prepreg layers during the multilayer lamination step.

Furthermore, the additional resonances seen in Figure 35 at 3.7 GHz and 7 GHz were also studied. These frequencies correspond to the harmonic resonances of the meander structure when it is $1.5\lambda_g$ and $2.5\lambda_g$ long. This can be verified by analyzing the surface current distributions of the meander structure at 3.7 GHz and 7 GHz, as shown in Figure 38. As seen in Figure 38a, there are two current nulls separating three $\lambda_g/2$ long sections at 3.7 GHz. The resonance at 7 GHz is supported with the currents on both the L-shaped resonator and the meander, and there are four current nulls on the meander structure. The resonance at 3.7 GHz can be avoided by replacing the full-wavelength long meander resonator with

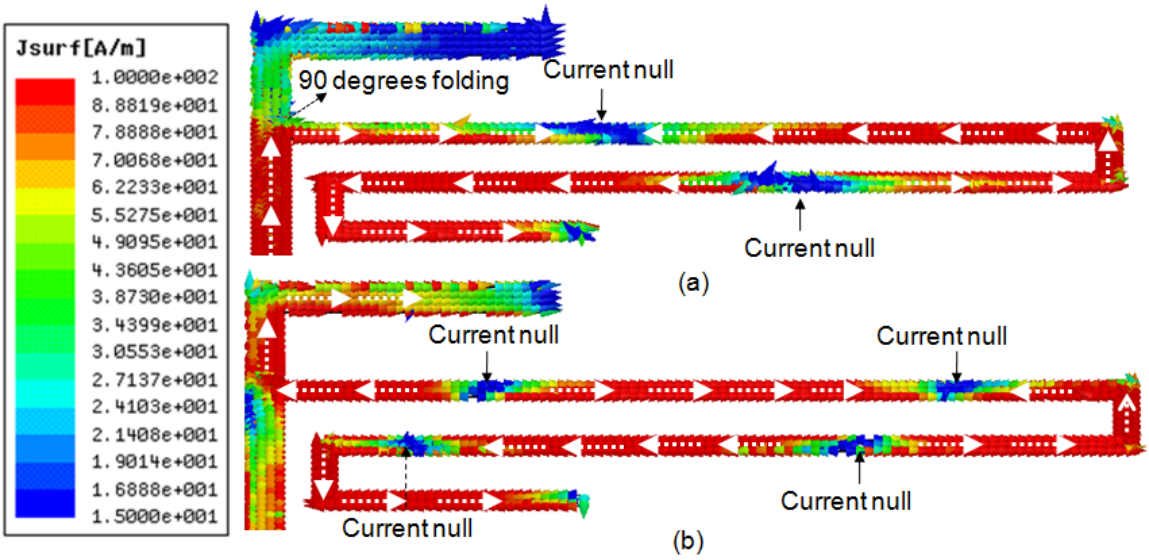

Figure 38. Simulated surface current distribution of the proposed dual-band antenna at (a) 3.7 GHz and (b) 7 GHz.

a half-wavelength long resonator; however, this was not possible due to the limitations in the matching of the antenna, as mentioned earlier. A resonance around 7 GHz is observed even when a half-wavelength long resonator is used.

The radiation patterns of the dual-band antenna were also measured at 2.4 GHz and 5.2 GHz. The results are presented in Figures 39 and 40. Good correlation between the simulation and the measurement results is observed similar to the single-band antenna. The simulated and measured peak gains of the antenna were found as 1.47 dB and 0.52 dB for 2.4 GHz, while the values were 3.9 dB and 2.92 dB for 5.2 GHz, respectively. The radiation pattern at 2.4 GHz is a dipole like pattern with a null along z-axis since only the vertical current elements, labeled as s and h_2 in Figure 32, contribute to the radiation, while the fields of the horizontal components, labeled as l_2 and l_3, cancel each other. On the other hand, the pattern at 5.2 GHz has two nulls approximately along the $\phi = 45°$ and $\phi = 135°$ axes due to the existence of orthogonal resonators for the 5 GHz band.

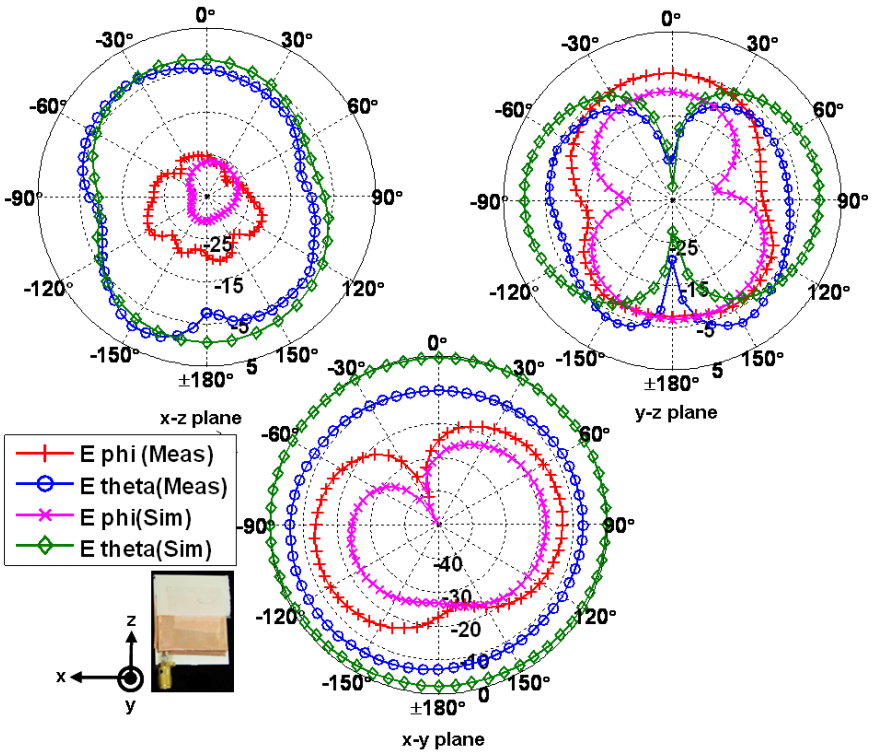

Figure 39. Simulated and measured radiation patterns of the dual-band antenna at 2.4 GHz.

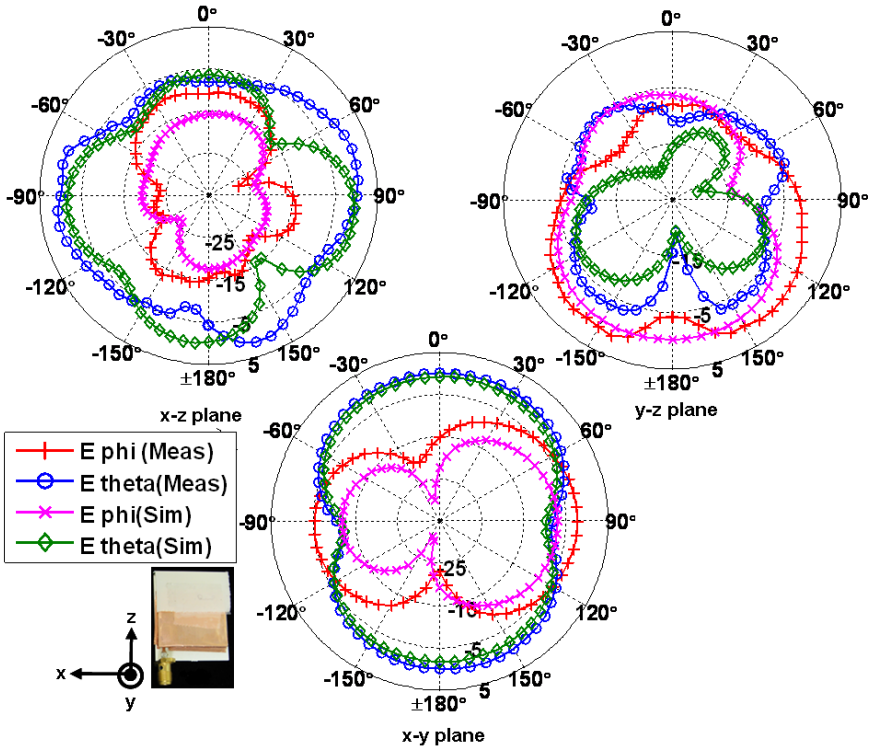

Figure 40. Simulated and measured radiation patterns of the dual-band antenna at 5.2 GHz.

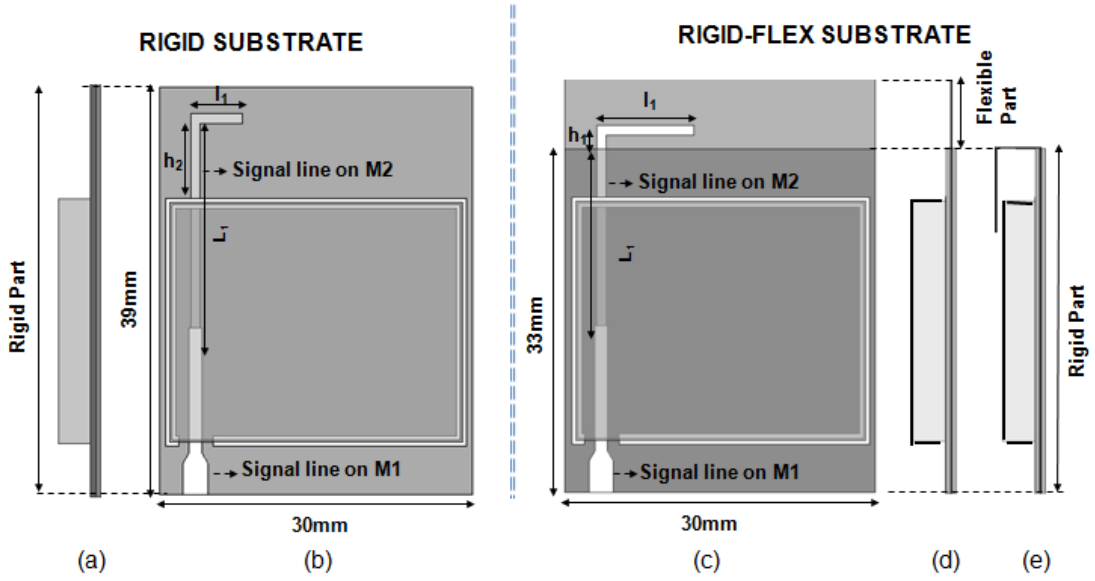

Figure 41. Comparison of the single-band L-shaped antenna designs on rigid and rigid-flex substrates. (a) Side view (rigid), (b)Top view (rigid), (c) Top view, straight (rigid-flex), (d) Side view, straight (rigid-flex), e) Side view, folded (rigid-flex).

2.7 Comparison with a Rigid Substrate

The single-band L-shaped antenna was redesigned on a totally rigid substrate to observe the advantages of the conformal configuration proposed in this research. The stack-up in Figure 15 was used as the rigid substrate without the protruding part. Figure 41 shows the details of the both antenna designs on rigid-flex and totally rigid substrates side-by-side. The antenna is on the metal layer M2 in both designs. However, the antenna is embedded in the substrate for the rigid substrate case; whereas, it is positioned on the flexible portion for the rigid-flex substrate. The dimensions of the signal lines and the metal box are the same with the values provided for the designs explained previously.

The final dimensions of the antenna on the rigid substrate were found as $l_1 = 5$ mm, $L_1 = 22.5$ mm and $h_2 = 6.5$ mm with a substrate area of 30 mm $\times$ 39 mm. Since the conformal antenna on the rigid-flex substrate is designed to be used in the folded configuration as in Figure 41e, the final size of the rigid-flex structure is determined only with the size of the rigid part of the substrate, which is 33 mm $\times$ 30 mm. These values show that a 6 mm decrease in the width of the substrate can be achieved by using the flexibility of the LCP

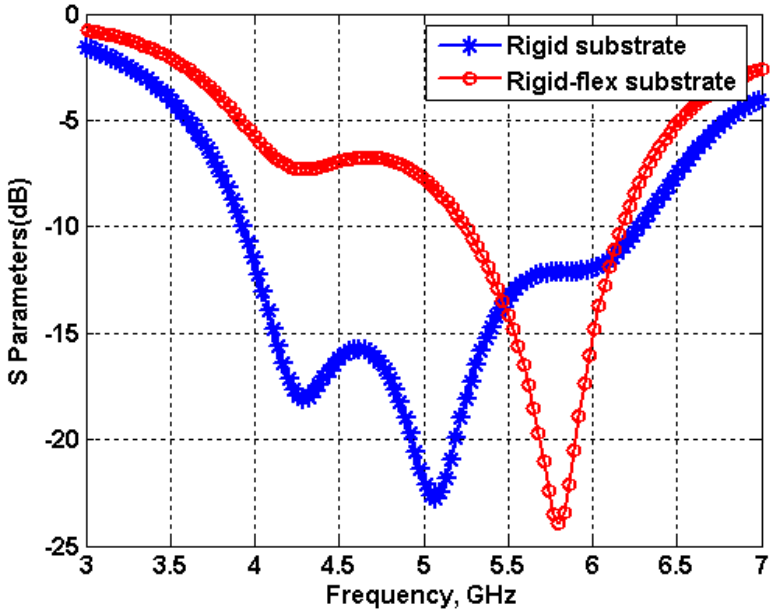

Figure 42. S_{11} **comparison of the single-band L-shaped antenna designs on rigid and rigid-flex substrates.**

substrate.

The comparison of the simulated S_{11} data of both antennas is presented in Figure 42. As seen in the figure, the antenna on the rigid substrate has a wider bandwidth than that of the conformal antenna on the rigid-flex substrate. The wider bandwidth is a result of merging two resonances, created by the parts of the antenna labeled as l_1 and h_2 in Figure 41b. The part labeled as h_2 in Figure 41b represents the part that is not covered with the ground plane. Therefore, this part also acts like a $\lambda/4$ long monopole antenna and creates a resonance close to that of the part labeled as l_1 in Figure 41b.

The far field of the antenna on the rigid substrate was also simulated. It was found that both designs have similar far field patterns. The simulated peak gain of the antenna on the rigid substrate at 5.5 GHz was found as 3.2 dB compared to 2.9 dB gain of the conformal antenna.

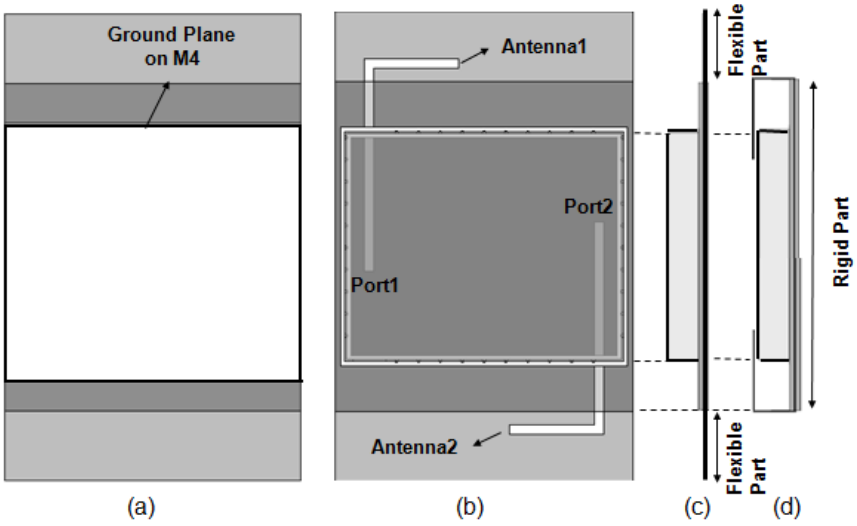

Figure 43. First configuration enabling integration of two conformal antennas. (a) Bottom view (straight), (b) Top view (straight), (c) Side view (straight), (d) Side view (folded).

2.8 Integration of Two Antennas

The integration of two conformal antennas has also been investigated by extending the flexible LCP substrates on multiple edges. Figure 43 and Figure 44 show two configurations, where two single-band L-shaped antennas are placed on flexible substrates protruding from two different edges of the rigid substrate.

The simulated S-parameters of the first configuration presented in Figure 43 are shown in Figure 45. As seen in Figure 45, mutual coupling (S_{12}) between the antenna ports is high since the antennas are coupled through common ground plane currents, and they are in the close proximity of each other. The interaction between the antennas can be decreased by using electromagnetic band-gap structures that prevent the surface-wave propagation. Similar results were obtained for the second configuration in Figure 44.

2.9 Conclusions

In this chapter, a novel conformal antenna configuration has been proposed to integrate the antenna directly on the module package. This configuration complements the previous work on the miniaturization of the front-end module by enabling the SOP integration of

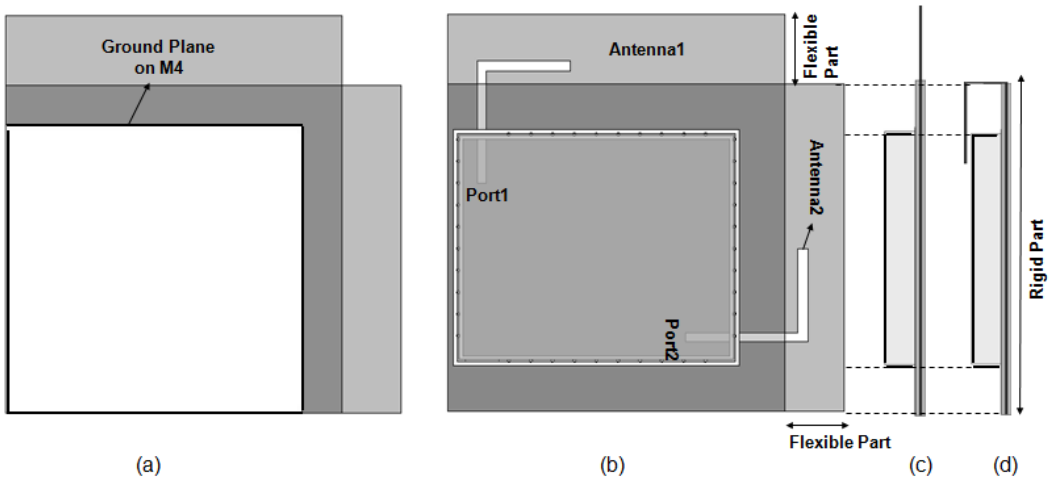

Figure 44. Second configuration enabling integration of two conformal antennas. (a) Bottom view (straight), (b) Top view (straight), (c) Side view (straight), (d) Side view (folded).

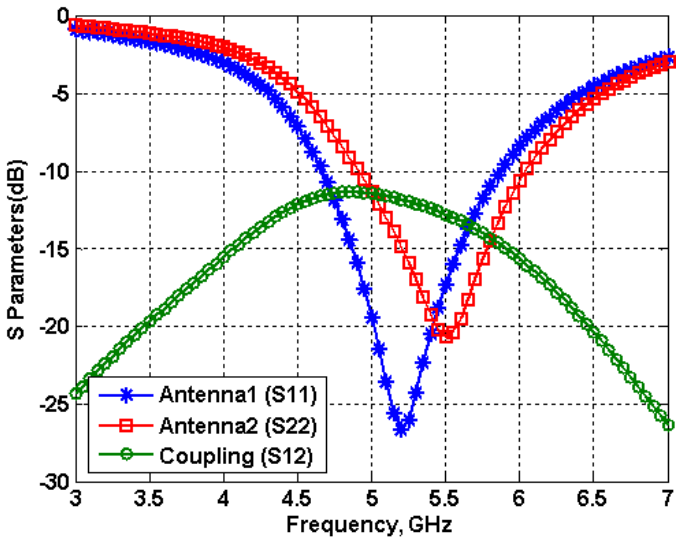

Figure 45. Simulated S-parameters of the first configuration shown in Figure 43.

Table 1. Summary of the designs covered in this chapter.

Substrate	Antenna	Size	Bandwidth	Peak Gain
Rigid-flex	Single-Band Meander Antenna	18mm × 25mm	5500-7000 MHz	2.5 dB at 6 GHz
Rigid-flex	Dual-Band Meander Antenna	30mm × 27.5mm	2248-2465 MHz 4622-5423 MHz	1.33 dB at 2.4 GHz 3.4 dB at 5.2 GHz
Rigid-flex	Single-Band L-shaped Antenna	30mm × 33mm	4710-5780 MHz	2.75 dB at 5.2 GHz
Rigid-flex	Dual-Band L-shaped Antenna	30mm × 35mm	2435-2445 MHz	1.47 dB at 2.4 GHz 3.9 dB at 5.2 GHz
Rigid	Single-Band L-shaped Antenna	30mm × 39mm	3600-6750 MHz	3.2 dB at 5.5 GHz

the antenna to achieve a complete RF SOP solution. The configuration was designed and implemented for the 2.4/5 GHz WLAN and WiMAX bands. The proposed configuration is based on a multilayer rigid-flex LCP substrate, where the advantages of the mechanical flexibility of the LCP are combined with its superior electrical performance compared to the ceramic-based SOP solutions. Even though flexible antennas have been proposed in the literature and already employed in the state-of-the-art mobile devices, e.g. the iPhone, the integration of the flexible antenna with the rigid SOP substrate has been shown for the first time with the proposed LCP-based rigid-flex substrates.

The proposed configuration was applied to several single- and dual-band monopole antennas since the SOP integration of the monopole antennas has not been covered in the literature before although the monopoles are highly preferred in mobile devices. Meander-shaped and L-shaped monopole antennas were integrated successfully to cover the required bands for the desired WLAN and WiMAX applications with a single antenna element. The properties and design parameters of the antennas covered in this chapter are summarized in Table 2.9.

The details of the fabrication process have also been presented. The proposed configuration is based on low-cost, low-temperature, FR-4 compatible processes. Moreover,

the overall fabrication process is suitable for a large-panel area fabrication for further cost reduction. The simulated and measured return loss and the far field data of the fabricated prototypes were compared and have also been included in this chapter. Good correlations were observed for all of the fabricated designs. The reasons for the slight mismatches between the measured and simulated results have also been analyzed in this chapter.

This novel technology not only provides a solution for the antenna integration but also miniaturizes the overall size of the complete RF SOP package by folding the flexible part of the substrate on the rigid part the substrate. The comparison of the proposed antenna configuration on a rigid-flex substrate with the corresponding rigid substrate verified a 6 mm size reduction in the overall size of the package integrated with the antenna. Although the fabricated prototypes were single antenna elements, the integration of multiple antennas have been investigated using the full-wave electromagnetic simulations. Configurations enabling multiple antenna integration have also been proposed in this chapter.

CHAPTER 3

CHARACTERIZATION OF MAGNETO-DIELECTRIC SUBSTRATES

Future generation modules for mobile and wireless systems are expected to have increased functionality and better performance in a more compact size. System-on-package (SOP) technology promises low-cost and high-performance system solutions by integrating high-speed digital, RF, and passive components in a compact package. Therefore, in an SOP architecture, the package substrate not only provides the mechanical support but also becomes the medium for the electromagnetic wave propagation between the embedded components. This makes the selection of the substrate material critical since, as a well-known fact, the characteristics of wave propagation is based on parameters such as the permittivity, the permeability and the loss in the medium. Hence, these parameters have a crucial role in determining the performance and the size of the embedded/integrated components such as inductors, capacitors, antennas, etc.

The importance of selecting or even synthesizing substrate materials with desired parameters creates interdisciplinary research problems that bring the electrical and the material-science engineers together to work for a solution. As an example, magneto-dielectrics, materials with $\epsilon_r > 1$ and $\mu_r > 1$, form a novel category of materials that do not exist in nature. It has been proposed in the literature and also elaborated in Chapters 4 and 5 of this thesis that the magneto-dielectrics can be used to efficiently miniaturize the antennas and other electromagnetic structures such as reactive impedance surfaces. However, the absence of the magneto-dielectric materials in nature makes it necessary to synthesize these materials.

The accurate characterization of the magneto-dielectric samples is a crucial and an indispensable step during the material synthesis of these materials. On the other hand, the characterization of the magneto-dielectrics is a challenging problem since the number of parameters to be characterized is increased to four by the inclusion of the magnetic

properties; whereas, there are only two parameters to be characterized for the dielectric materials. It is required to find novel metrologies that can separate ϵ' from μ' and ϵ'' from μ'' accurately.

Two rigorous extraction algorithms that were developed to extract the ϵ', ϵ'', μ' and μ'' from the measured S-parameter data of easy-to-fabricate two metal-layer structures on thin-film magneto-dielectric materials are presented in this chapter. This chapter first starts with reviewing the state-of-the-art material synthesis techniques for the magneto-dielectric materials in Section 3.1. Then, the conventional characterization techniques are summarized in Section 3.2. Next, the first proposed method based on using measured responses of a two-port parallel plate resonator and a one-port inductor is explained in Section 3.3. The accuracy of the method is verified with a controlled study. An example case is also presented based on the measured data. In Section 3.4, the second method is explained, based on using two-port impedance and admittance measurements to characterize the desired substrate properties. Finally, the chapter is summarized in Section 3.5.

3.1 Review of Magneto-dielectric Material Synthesis

Recent advances in the material synthesis technology have increased the hope for the synthesis of the magneto-dielectric materials to be used in the effective miniaturization of the antennas and other electromagnetic structures. The magneto-dielectric substrates to be used for the antenna miniaturization are desired to have low-loss and stable permeability and permittivity values in the GHz frequencies. Additionally, it is preferable that these materials can be fabricated in a range of thicknesses.

One group of materials, named as artificial magneto-dielectric substrates, have been proposed to emulate the characteristics of the magneto-dielectric materials [40], [41], [42], and [43]. These materials are constructed by the stacking and periodic placement of embedded circuits in a dielectric host medium. For instance, the embedded-circuit building

blocks proposed in [42] are periodic spiral inductors while similar behavior has been reported in [40] by using stacked ring resonators and in [43] using fractal Hilbert cells as the embedded circuits.

The idea behind the artificial magneto-dielectric materials is to emulate the magnetic energy storage mechanism of the atoms in natural magnetic materials by the magnetic energy storage capability of the embedded circuits. The magnetic energy storage is higher close to the resonance of the embedded circuits, resulting in a higher μ_r value. In addition, the relative permittivity and the relative permeability of these engineered materials can be altered by the geometric control of these embedded-circuits.

Although the magneto-dielectric characteristics and the antenna miniaturization can be achieved with the usage of such engineered substrates, several issues related to these substrates were reported in [44] that will limit their application to antennas for mobile devices. These limitations can be summarized as follows:

1. The loss of the dielectric host medium combined with the conductor losses of the embedded circuits result in an overall lossy substrate.

2. The size and weight of these materials are not suitable for mobile applications. As an example, the engineered material proposed in [42] is 24 cm $\times$ 24 cm $\times$ 2 cm with a weight of approximately 3.5 lbs.

3. These materials show anisotropic behavior which would limit their application to antennas and other electromagnetic structures. The orientation-dependent permeability and permittivity values are determined with the stacking direction, in which the magnetic field would be enhanced by the embedded circuits.

4. The permeability of these substrates shows strong dispersive behavior since high μ_r values are obtained close to the resonance frequency of the embedded circuits.

Table 2. Summary of the literature review for the magneto-dielectric material synthesis. N/A means no information is provided in the paper.

Affiliation	Year	Frequency	μ_r	ϵ_r	Thickness	Application	Synthesis method
Nanjing Uni.	2004 [28]	up to 1GHz	9	N/A	N/A	Power transmission in AC devices	Insulating coating of NiSiO2 nanocomposites
Nanjing Uni.	2004 [45]	up to 1GHz	4 composites: 22, 11, 16, 14	N/A	N/A	Power transmission in AC devices	Wet chemistry coating of Fe particles with alumina
Trans-Tech	2005 [42]	up to 500MHz	16	16	N/A	Antenna	Z-phase hexaferrite
Samsung (Semco)	2005 [46]	182MHz	9 at 50MHz 3.5 at 1GHz	5.3 between 100MHz-1GHz	1mm 2mm	Antenna for VHF band	Ni-Zn ferrite with dielectric resin
Nanjing Uni.	2005 [27]	up to 1GHz	6.5-8	N/A	N/A	Power transmission in AC devices	Insulating coating of CoSiO2 nanocomposites
Nanjing Uni.	2005 [47]	up to 1GHz	10.5	N/A	N/A	Power transmission in AC devices	Insulating coating of FeSiO2 nanocomposites
Georgia Tech (Prof. Zhong)	2008 [48]	20-30GHz	68	1.19	300nm	Inductors for CMOS	Multiple nanoparticle layer deposition
Georgia Tech (Prof Wong)	2008 [49]	400MHz	3-5 between 20-200MHz	7	1.6mm	RFID	NiZn and BaCo ferrite composites
Human Uni	2008 [50]	up to 1GHz	18	N/A	N/A	N/A	Insulating coating of $NiSiO_2$ nanocomposites
Uni. of Electronic Sci. Tech. of China	2008 [51]	1-8GHz	56.87	N/A	N/A	N/A	Ferromagnetic thin film

A more promising way to realize the magneto-dielectric materials is to synthesize thin-films with natural magnetic inclusions and nano-magnetic composite materials. Table 2 summarizes the work published in literature on the synthesis of the magneto-dielectrics. Ferrites are the most common method to achieve the magneto-dielectric behavior. The magneto-dielectrics based on ferrite composites have been reported in [42], [46], and [49] to be used in the microwave and antenna applications at very high frequency (VHF) range. Although high permeability values can be achieved with the ferrites, the process requires very high magnetic fields to be applied during the synthesis to achieve high permeability values. Moreover, the ferrites show strong dispersive characteristics and require a magnetic field excitation.

Another synthesis technology is based on the deposition of multiple nanoparticle layers. Although high permeability values, around 60-100, can be achieved with this method, the thickness of the film is limited to several hundred nanometers up to a micrometer [48], [51]. These thin film substrates have been proposed for miniaturizing the inductors and coplanar waveguide lines used in CMOS technology; however these substrates are not suitable for antenna applications because of their limited thickness.

Transitional metals and alloys (such as Fe, Ni, Co, FeNi, etc.) are more promising soft magnetic materials with both high-permeability and low-coercivity. However, the eddy current generation because of their metallic characteristics severely limits their applications at high frequencies. The affinity of the nanoparticles of the transition metals to oxygen introduces additional limitations since they may ignite spontaneously in air. Recent publications have shown that this problem can be solved by coating the surfaces of the soft magnetic nanoparticles with insulating shells [47], [28], and [27]. Insulator coating may also provide a protective shell to enhance the resistance of the core materials to oxidation. Furthermore, the protective shell prevents the interactions between the neighboring magnetic particles as well as the grain-growth and agglomeration during the heat treatment resulting in stable permeability values. Stable high permeability values have been shown up to 1 GHz for the

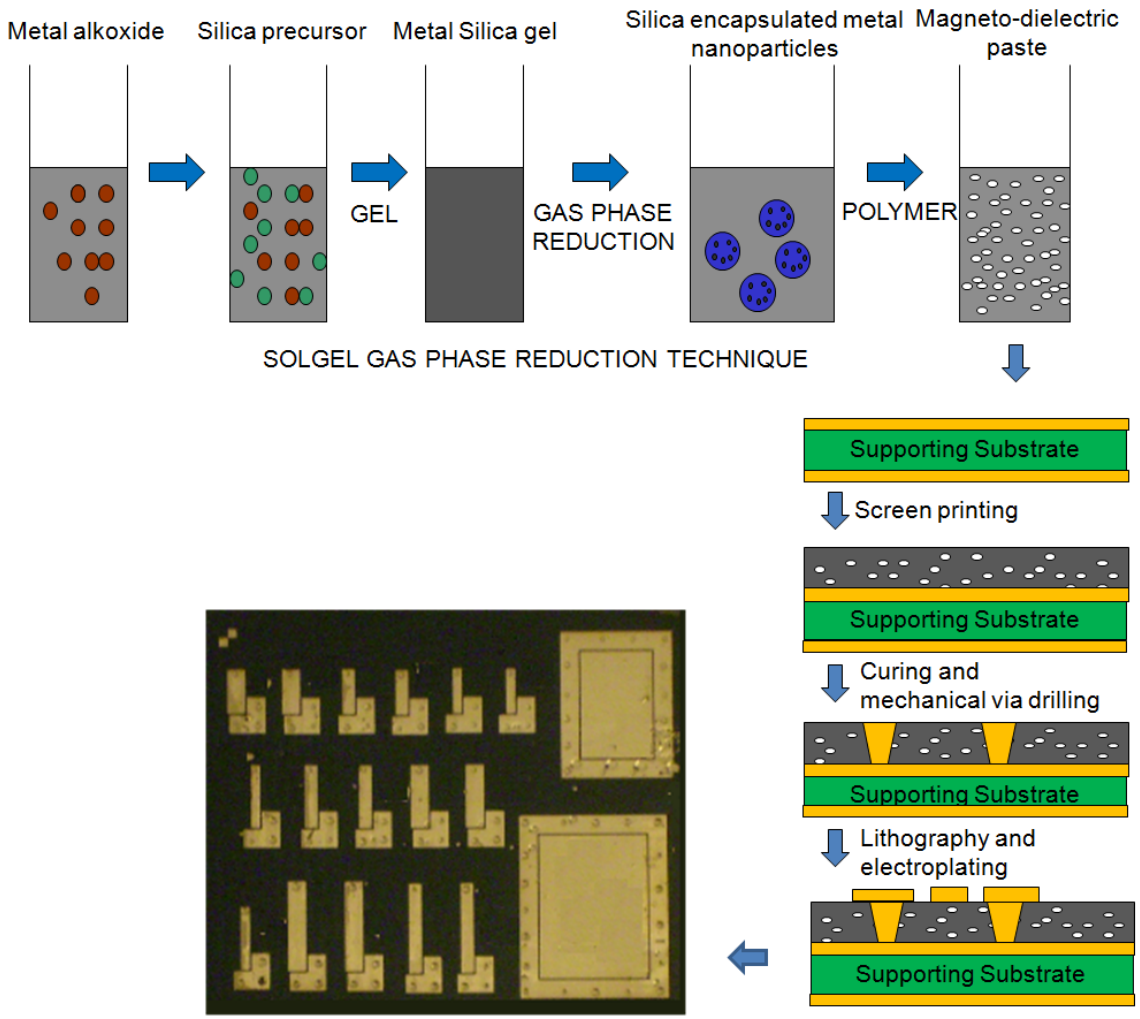

Figure 46. Process steps to fabricate the test vehicle used for the characterization.

Ni, Co and Fe alloys in [47], [28], and [27]. The magneto-dielectric materials employed in this thesis have been synthesized with the extension of the techniques in these references to higher frequencies and the details of the synthesis process are explained in the next section.

3.1.1 Material Synthesis and Test Vehicle Fabrication

The magneto-dielectric substrates investigated in this thesis are the nano-magnetic composites that have been synthesized by the Packaging Research Center (PRC) at Georgia Tech. The method followed in this research was based on encapsulating Ni and Co nanoparticles with polymer to reduce magnetic losses due to interaction between neighboring magnetic particles and also to prevent oxidation.

The synthesis process followed in this research was based on a sol-gel process where silica coated nanoparticles were milled with polymer composite to create a paste. Figure 46 shows a flow chart of the material synthesis and device fabrication processes and the steps can be summarized as follows [29]:

1. Nickel precursors and tetraethyl orthosilicate (TEOS) are uniformly dispersed in methoxy ethanol at low molar concentrations. The volume ratio of nickel to silica is chosen to get adequate silica encapsulation.

2. The solution is then gelled by slowly hydrolyzing it in air. The resulting Ni-O-Silica gel contains nickel ions bonded with oxygen and silicon with covalent bonds as a gel network.

3. Gas phase reduction of the gel is done in a reducing atmosphere to nucleate silica-coated nickel nanoparticles. The reduction of nickel in silica gels, within the temperature range $550 - 700°C$, leads to the formation of metallic nickel nanoparticles homogeneously dispersed in this amorphous matrix.

4. The sample obtained from the reduction of the gel is then dispersed in PGMEA (propylene glycol methyl ether acetate) mixed with the Epoxy, Ciba LMB 7081 (supplied by Vantico Corporation) to create a paste.

5. The magneto-dielectric paste is used to fabricate magneto-dielectric thin-film substrates using screen printing techniques followed with curing of the polymer.

6. Vias are mechanically drilled and the metallization on the film is patterned using conventional wet chemical processing steps.

Several batches have been fabricated and characterized to verify the material synthesis process. The characterization methods used to extract the material properties are summarized in the following sections.

3.2 Review of Common Characterization Methods

Conventional techniques for characterizing the permittivity, $\epsilon = \epsilon' - j\epsilon''$, and the permeability, $\mu = \mu' - j\mu''$, of the magneto-dielectric substrates are based on processing the measured impedance and admittance data. Therefore, the most common method is using a commercially available impedance analyzer connected with material fixtures, such as the Agilent E4991A connected with the Agilent 16454A for μ characterization and connected with the Agilent E1643A for ϵ characterization [52]. In this method, the impedance properties of the material-under-test (MUT) are measured using the material fixtures, where the disk-shaped samples are sandwiched with the properly-shaped electrodes. As shown in Figure 47a, circular disks are used for the ϵ characterization while toroid-shaped disks are used for the μ characterization. Although frequency-dependent material characteristics can be obtained from the impedance measurements, this method is limited to machinable materials and the frequency range from a few MHz to 1 GHz.

Another common method is based on the S-parameter measurements of a loaded waveguide. As shown in Figure 47b, a rectangular or a circular waveguide is loaded with a sample of MUT, and the S_{11} and S_{21} are used to determine the reflection coefficient, Γ, and the complex propagation constant, γ. Using these two parameters both the ϵ and μ can be characterized [53]. This method is suitable for high-frequency characterization; however, it is also limited to machinable materials.

The cavity perturbation method applied to a cylindrical resonator is another common method used for material characterization. In this method, a small sample is inserted into a resonant cavity, and the intrinsic properties of the material are extracted by processing the measured complex frequency shift and quality factor of the resonator. The measurement setup is shown in Figure 47c. Although this method has been reported to be successful for the characterization of both isotropic and anisotropic dielectric materials [54], [55], the application of this method on ferrimagnetic samples was reported to extract anomalous dispersion of the permeability data. Therefore, this method may not be reliable for the

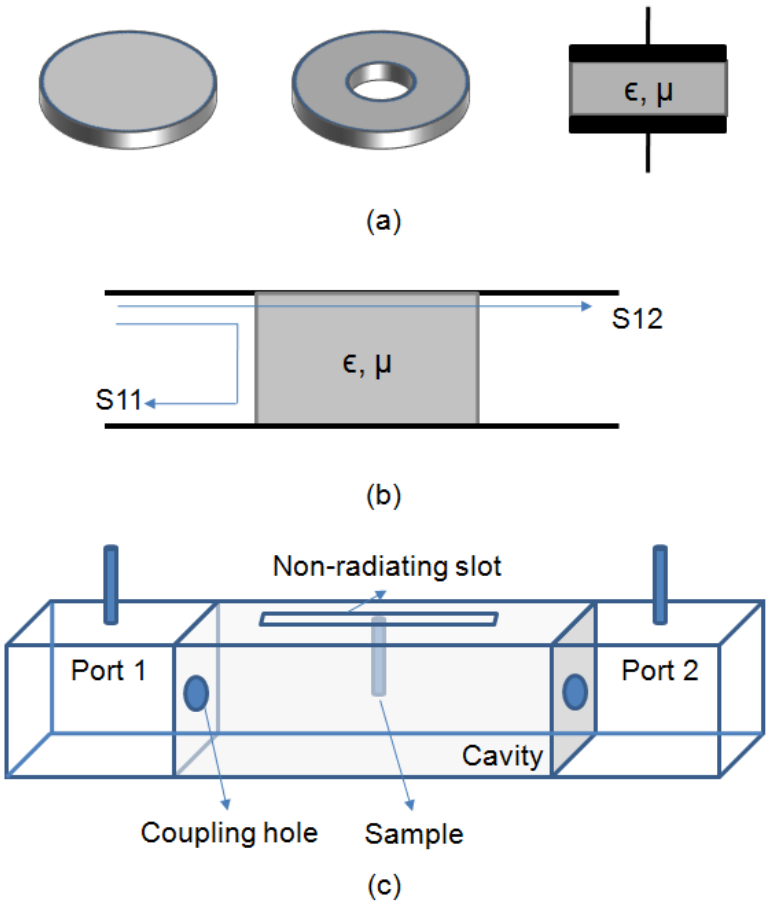

Figure 47. Examples of conventional characterization methods. (a) Impedance analyzer method, (b) Waveguide method (c) Cavity method.

characterization of magneto-dielectric materials.

The transmission line method is more suitable for the characterization of thin-film magneto-dielectric materials. In this method, multiple coplanar waveguide or microstrip transmission lines are printed on the thin-film MUT. Using the multiline thru-line-reflect (TRL) algorithm, the complex propagation constant γ_{eff} and the characteristic impedance Z_0 of the line are found, and this data is processed to characterize the intrinsic properties of the MUT [51].

The magneto-dielectric substrates investigated in this thesis are the nano-magnetic composites that have been synthesized by the Packaging Research Center (PRC) at Georgia Tech. Since the material synthesis process has been on-going with the material characterization process, easy-to-fabricate methods that can give quick and accurate results have been employed for material characterization. This has enabled the continuous synthesis of multiple batches depending on the feedback from material characterization.

In the first method used for the characterization, two electromagnetic structures are used to characterize the permittivity and the permeability of the synthesized samples. This is achieved by using two structures, one of which is mostly sensitive to the changes in permittivity, while the other one is sensitive to the changes in permeability. In the second method, two-port impedance and admittance data of simple microstrip structures are used to characterize the permittivity and permeability.

3.3 Characterization Algorithm Based on Parallel Plate Resonator and Strip Inductor

3.3.1 Parallel Plate Resonator

The resonator structures have been extensively used for material characterization since the resonance frequencies are highly sensitive to the changes in the permittivity and permeability of the loading material that is to be characterized. Compared to the machined resonators, the printed resonators are more suitable for extracting the frequency-dependent characteristics of the thin film nano-magnetic composites. Therefore, printed parallel-plate cavity

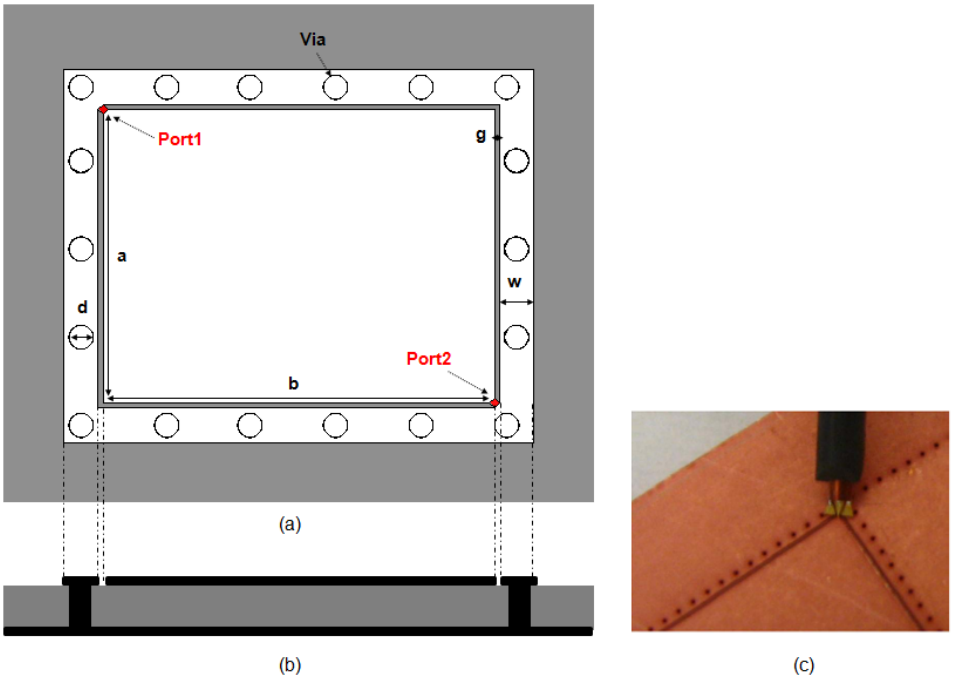

Figure 48. Details of the parallel plate resonator used with the corner-to-corner probing method. (a) Top view, (b) Side view (c) Probe position in the corner-to-corner probing.

resonators were used in this research combined with the corner-to-corner probing method. The corner-to-corner probing method has been proven to be successful for the frequency-dependent characterization of thin-film high-permittivity materials [56]. In this thesis, this work is extended for the characterization of thin-film magneto-dielectric materials.

The top and the cross-sectional views of the parallel plate resonator are shown in Figure 48. The structure is composed of two metal layers printed on the top and bottom of the substrate to be characterized. As seen in Figure 48, the top metal is framed with another metal layer, which is shorted to the bottom metal with a series of vias with diameters d = 0.5 mm. The gap between the framing metal and the top metal is g = 0.1 mm, and the width of the framing metal is w = 0.7 mm. Three different sizes of the parallel plate resonator were used during the material characterization process: a × b = 8 mm × 8 mm, 8 mm × 6 mm, and 6 mm × 4 mm.

The electric wall created by the series of vias shorting the frame metal transforms the parallel plate resonator into a box resonator created by printed board technology. As shown

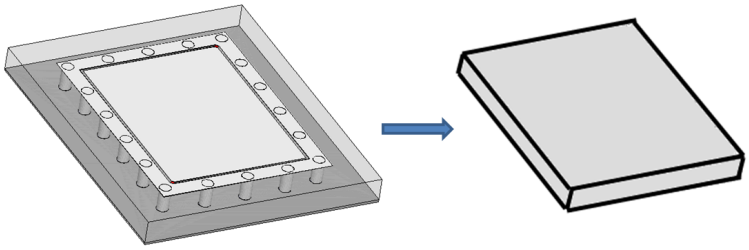

Figure 49. Analogy between the parallel plate resonator and the box resonator.

in Figure 49, the parallel plate structure acts like a box resonator filled with the substrate, which emulates the resonator method for the characterization of thin film substrates. Moreover, the response of the resonator can be measured using the ground-signal-ground (GSG) air probes. The resonator is excited by probing the structure at the corners such that the signal tip of the probe lands on the top metal, while the ground tips land on the frame, as shown in Figure 48c.

The sensitivity of the parallel plate structure to the changes in the material properties of the thin-film magneto-dielectrics were studied using full-wave electromagnetic simulations, where the responses of the parallel plate resonator for different combinations of the material parameters were compared. In this study, the parallel plate structure was simulated using parameter sweeps, where either the relative permittivity or the relative permeability of the substrate was swept while the other parameter was kept constant at 4. It was found from this study that the resonance frequencies and the amplitude of Z_{12} are sensitive to changes in ϵ_r and μ_r.

In the case of dielectric substrates, since it is known that $\mu_r = 1$, fitting the amplitude and the resonance frequencies of Z_{12} can result in the accurate characterization of ϵ_r [56]. In the case of magneto-dielectric substrates; however, the parallel plate resonator is useful only in the frequency range up to the first anti-resonance in the transmission impedance response, Z_{12}. In this range of frequencies, because of the inherent capacitive behavior of the parallel plate resonator, the impedance response is more sensitive to the changes in the permittivity, making it possible to characterize ϵ' and ϵ'' almost independently from the

values of μ' and μ''. Therefore, the frequency-dependent data can be extracted by assuming an approximate value for μ_r and by fitting the simulated $Im(Z_{12})$ and $Re(Z_{12})$ values to the measured values to extract the relative permittivity and dielectric loss, respectively. Although Z_{11} and Z_{22} are also sensitive to the changes in permittivity at low frequency, they were not employed since one-port impedance measurements are not as accurate as the transfer impedance measurements due to the probe impedance and the contact resistance that cannot be calibrated out.

Similar to the Z_{12} data, the Y_{12} data can be used to characterize μ_r and magnetic loss tangent. However, it was found through simulations that the accuracy of the Y_{12} data is small due to the low-inductance value obtained from the wide top-metal of the resonator. Instead, one-port inductors can be used to characterize the permeability of the thin-film materials. These inductors are explained in the next section.

3.3.2 Strip Inductors

It was found through the analysis of the parallel plate resonator that the Z_{12} response of the resonator is insensitive to the changes in μ_r at low frequencies up to the first antiresonance because of the inherent capacitive behavior of the parallel plate structure. To solve this problem and complement the results obtained from the parallel plate resonators, a set of planar inductors were used to extract the μ of the substrate.

Spiral inductors and strip inductors have been considered for characterizing the permeability of the substrate. It was found through experiments that the strip inductors are more suitable to characterize the permeability of the lossy substrates since the dominating parasitic resistance of the spiral inductors makes it harder to measure the inductance. Therefore, strip inductors designed based on shorted microstrip lines were used during the characterization.

Figure 50 shows the details of the strip inductors used in the characterization process. As seen in the figure, a microstrip line with length L, and width W, is shorted to the ground with a via connection. 3.5 mm, 5 mm and 7.5 mm long lines were used with 0.5 mm and

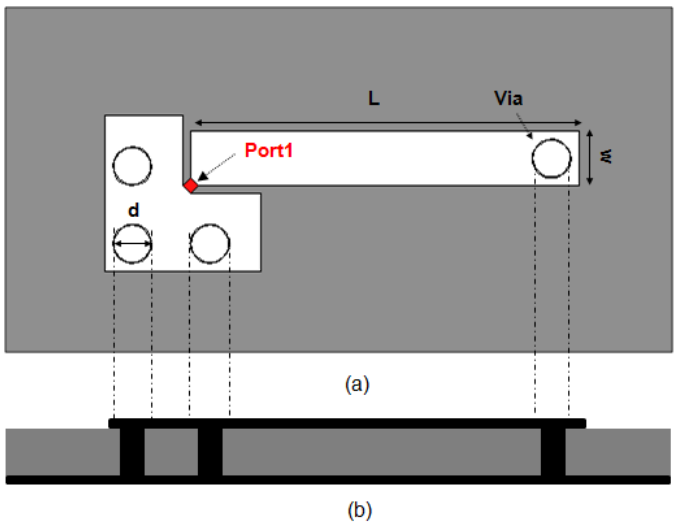

Figure 50. Details of the strip inductor structure used for characterizing the permeability. a) Top view, b) Side view.

0.7 mm width values. The ground pad is placed at the corner so that the response can be measured with a GSG probe as in the corner-to-corner probing method for the parallel plate resonator.

The principle behind this method can be explained by analyzing the impedance characteristics of a shorted microstrip line. Assuming all the conductors are lossless, the input impedance of a shorted microstrip line on a lossy magneto-dielectric substrate with the permittivity ϵ and permeability μ can be approximated as:

$$Z_{in} = Z_0 \tanh(\gamma \ell) \tag{1}$$

where γ is the complex propagation constant, Z_0 is the characteristic impedance of the line, and ℓ is the length of the line [39]. γ and Z_0 can be expressed in terms of the per-unit length resistance R, inductance L, conductance G, and capacitance C, of the microstrip line.

$$\gamma = \alpha + j\beta = \sqrt{(R + j\omega L)(G + j\omega C)} \tag{2}$$

$$Z_0 = \sqrt{\frac{(R + j\omega L)}{(G + j\omega C)}} \tag{3}$$

For a short microstrip line, the *tanh* function can be approximated as $tanh(\gamma\ell) \approx \gamma\ell$.

Using this approximation and substituting (2) and (3) in (1) yields

$$Z_{in} = Z_0 \tanh(\gamma\ell) \approx Z_0\gamma\ell \tag{4}$$

$$Z_{in} = \sqrt{\frac{(R + j\omega L)}{(G + j\omega C)}}\sqrt{(R + j\omega L)(G + j\omega C)}\ell \tag{5}$$

$$Z_{in} = (R + j\omega L)\ell \tag{6}$$

The derivation of the per-unit length parameters for a microstrip line with a lossy magneto-dielectric substrate can be found in Appendix A of this thesis, and the expressions for R and L are repeated here as follows:

$$R = \frac{\omega\mu''_{eff}h}{W} \tag{7}$$

$$L = \frac{\mu'_{eff}h}{W} \tag{8}$$

Substituting these expressions for R and L in (6) one can find

$$Z_{in} = \frac{\omega\mu''_{eff}h\ell}{W} + j\omega\frac{\mu'_{eff}h\ell}{W} \tag{9}$$

where W is the width of the line, h is the height of the substrate, and μ'_{eff} and μ''_{eff} are the real and the imaginary part of the effective permeability.

A close look at Eq. (9) reveals that for frequencies where $\ell \ll \lambda_g/4$ the real part of the input impedance of the strip inductor can be used to characterize the magnetic loss while the imaginary part of the input impedance can be used to extract the relative permeability. The input impedance can be obtained from the Z_{11} data. Moreover, the effect of the air medium above the strip inductor can be modeled through full-wave electromagnetic simulations.

The sensitivity of the inductors has also been studied using electromagnetic simulations, where the parameter sweeps of the relative permeability and the relative permittivity of the substrate were performed. The results support the theoretical analysis as expected. It was found from the results of the μ_r sweep that the simulated Z_{11} curves can be distinguished for different values of the μ_r of the substrate. On the other hand, the ϵ_r sweep revealed that the simulated Z_{11} of the structure is not sensitive to the changes in ϵ_r of the substrate, especially

at low frequencies, where the response is inductive. This is desired and complements the results from the parallel plate method such that the strip inductors can be used to extract the μ of the substrate, while the parallel plate resonator can be used to extract ϵ of the substrate.

This method can be used up to the first resonance of the resonator and the inductor, whichever happens first. Different sizes of the parallel plate resonator and strip inductor can be used to adjust the frequency range.

3.3.3 Characterization Process

The flow chart in Figure 51 summarizes the steps of the characterization process. These steps can be listed as follows:

1. The parallel plate structure and strip inductors were measured with a vector network analyzer (VNA) using the corner-probing method.

2. The measured S-parameter data were converted to the Z-parameter data.

3. The thickness of the film was measured at several positions on the substrate.

4. Using the measured thickness, the parallel plate resonator was simulated with an electromagnetic solver at the first frequency point with an initial guess for ϵ_r. In this research, Sonnet was used as the electromagnetic solver [57]. The substrate can be assumed as a non-magnetic lossless substrate at this initial step.

5. Z_{12} data obtained from the simulation was compared with the measured Z_{12} data. The simulation process is repeated while sweeping ϵ_r of the substrate until the imaginary part of the simulated Z_{12} is matched to the imaginary part of the measured Z_{12}. The real parts of the simulated and the measured Z_{12} are also matched by altering the dielectric loss tangent.

6. Using the measured thickness and the approximated value for the permittivity and dielectric loss tangent of the substrate, the strip inductor was simulated with an electromagnetic solver at the first frequency point.

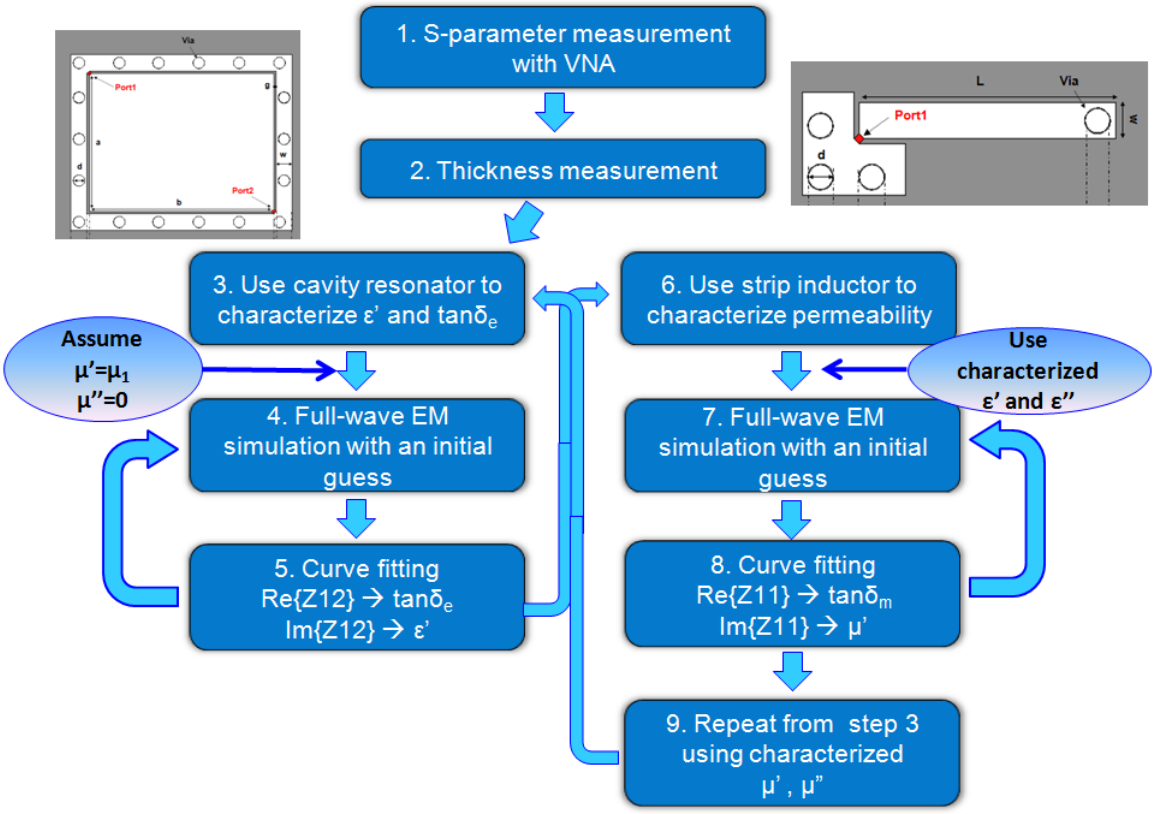

Figure 51. Flow graph of the characterization process using the parallel plate cavity resonator and the strip inductor.

7. Z_{11} data obtained from the simulation was compared with the measured Z_{11} data. The simulation process was repeated while sweeping μ_r of the substrate until the imaginary part of the simulated Z_{11} is matched to the imaginary part of the measured Z_{11}. The real parts of the simulated and measured Z_{11} were also matched by altering the magnetic loss tangent.

8. Starting from step 4, the process was repeated for the same frequency point but this time using the extracted μ_r, ϵ_r, and loss tangent values as the initial values. Once a convergence was achieved such that the extracted values do not change considerably between passes, the process was started for the next frequency point from step 4.

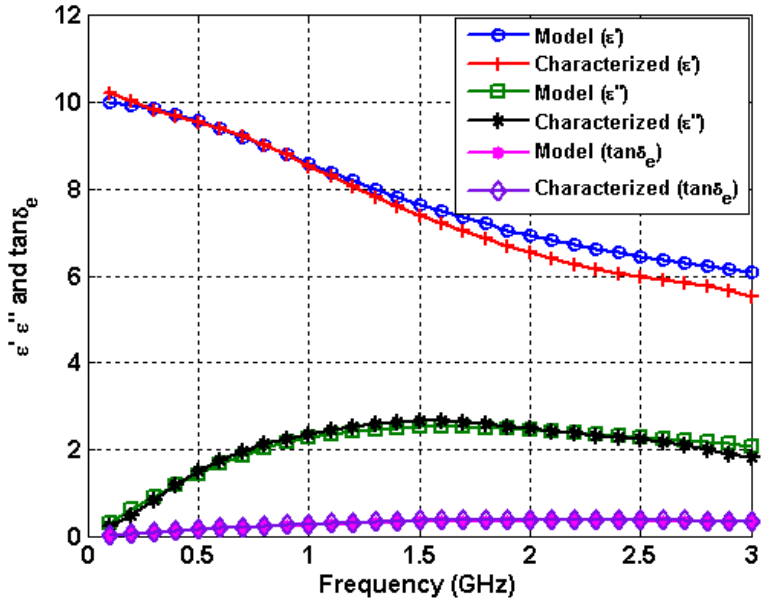

Figure 52. Characterized ϵ', ϵ'' and dielectric loss tangent. It should be noted that the model material is a fictitious material used to verify the characterization technique.

3.3.4 Controlled Characterization Study Based on Simulation

A controlled experiment based on the full-wave electromagnetic simulations was performed to verify the accuracy of the method. In this experiment, first, the impedance responses of a parallel plate resonator and a strip inductor on a dispersive substrate were obtained by simulating these structures in a commercially available full-wave electromagnetic solver, Microwave Studio by Computer Simulation Technology (CST MWS) [58]. In the simulations, a highly-dispersive fictitious substrate was modeled using a first order Debye model for the permittivity of the substrate and a second order general dispersion model for the permeability of the substrate. The assumed models for the ϵ', ϵ'', μ' and μ'' are shown in Figures 52 and 53, with curves labeled as "model". During the simulation of the strip inductor, the ground pad was also included in the simulation model as in the case of real prototypes.

Next, the simulation results were exported from the CST MWS to be used as if they were measured responses. These data were characterized using Sonnet, following the characterization steps summarized in Figure 51 and the previous section. The ground pad of the

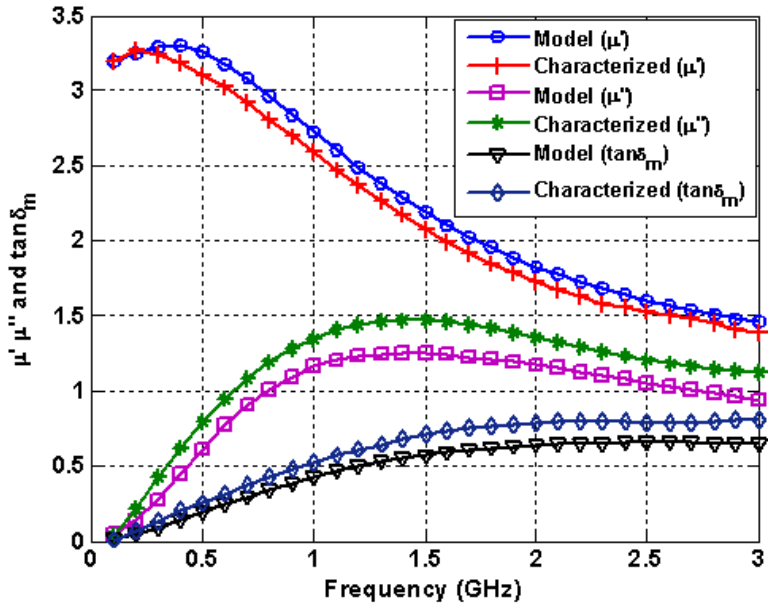

Figure 53. Characterized μ', μ'' and magnetic loss tangent. It should be noted that the model material is a fictitious material used to verify the characterization technique.

strip inductor and the framing structure around the parallel plate cavity resonator were not included in the Sonnet simulation models to decrease the simulation time for each iteration.

The characterized values for the permittivity and the permeability are also shown in Figures 52 and 53. As seen in the figures, both the permittivity and the permeability values were extracted with acceptable accuracy. The accuracy of the characterization can be improved by repeating the steps with the extracted values one more time. Also, the simulation models in Sonnet can be improved including the measurement pads in the strip inductor model and the framing ground metal in the parallel plate resonator model. It should also be noted that as the frequency increases and becomes closer to the resonance of the structures, more iterations are required to increase the accuracy of the method.

3.3.5 Characterization Example Based on Measured Data

Several batches have been fabricated and characterized to verify the material synthesis process. A sample test vehicle including the characterization structures is displayed in Figure

46. The main challenge during the magneto-dielectric thin-film synthesis has been to obtain stable high-permeability values with low magnetic and dielectric loss. The permeability values ranging from 1.3-1.9 have been characterized for several batches. In this section, the results obtained for a sample board that gave approximately $\epsilon_r = 7.5$ and $\mu_r = 1.9$ are presented.

After the structures on the sample were measured, the characterization steps explained in Figure 51 were followed using a 7.5 mm long strip inductor and a 6 mm $\times$ 8 mm parallel plate resonator. The permittivity and the permeability values were characterized at several frequency points between 400 MHz and 3 GHz. Then, the characterized values were fitted using the automatic fitting scheme built in the CST MWS. A second order Debye model was used which is defined as

$$\varepsilon(\omega) = \varepsilon_\infty + \frac{\beta_0 + j\omega\beta_1}{\alpha_0 + j\omega\alpha_1 - \omega^2} \tag{10}$$

Figure 54a shows the real and the imaginary parts of the characterized and the fitted ϵ values. In Figure 54a, the characterized values are shown as single points whereas the fitted curves are represented with continuous lines. The characterized and fitted dielectric loss tangent are shown in Figure 54b. As seen in both graphs, a good fit to the Debye model was achieved.

Similarly, the permeability values were characterized at single frequency points and then fitted to the Debye models using the built in tool in the CST. Figure 55a displays the real and the imaginary parts of the characterized permeability values, while the magnetic loss tangent values are shown in Figure 55b. It can be concluded from the characterized parameters shown in Figures 54 and 55 that the material is quite lossy with high dielectric and magnetic losses. Although the substrate is not suitable for the antenna applications due to high loss values, the stable permeability and permittivity values are promising. The loss of the substrate can be decreased using more advanced synthesis techniques.

After characterizing the sample and creating a model for the parameters of the substrate, the inductor and the parallel plate resonator models were simulated in the CST MWS using

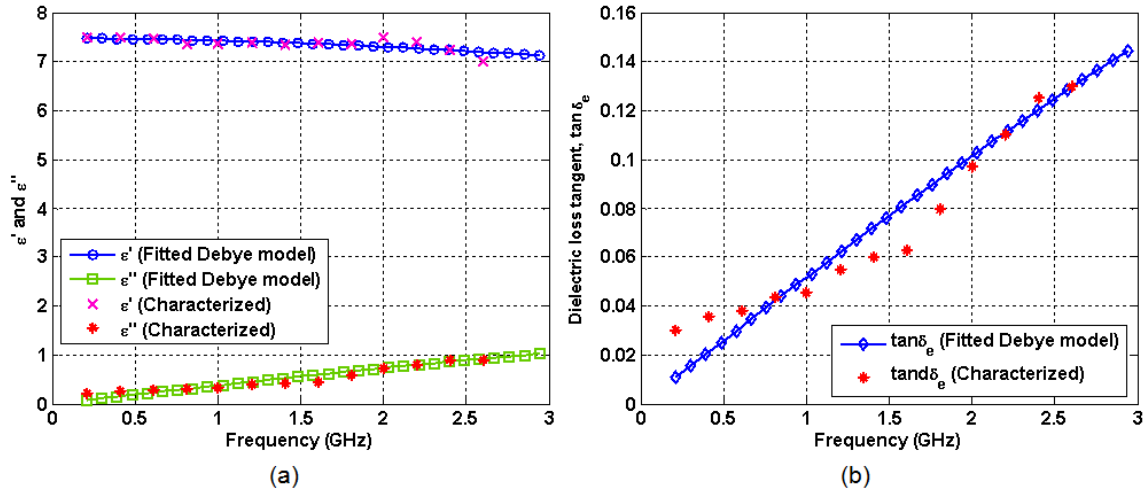

Figure 54. Characterized permittivity values with the fitted Debye models. (a) ϵ' and ϵ'', (b) Dielectric loss tangent.

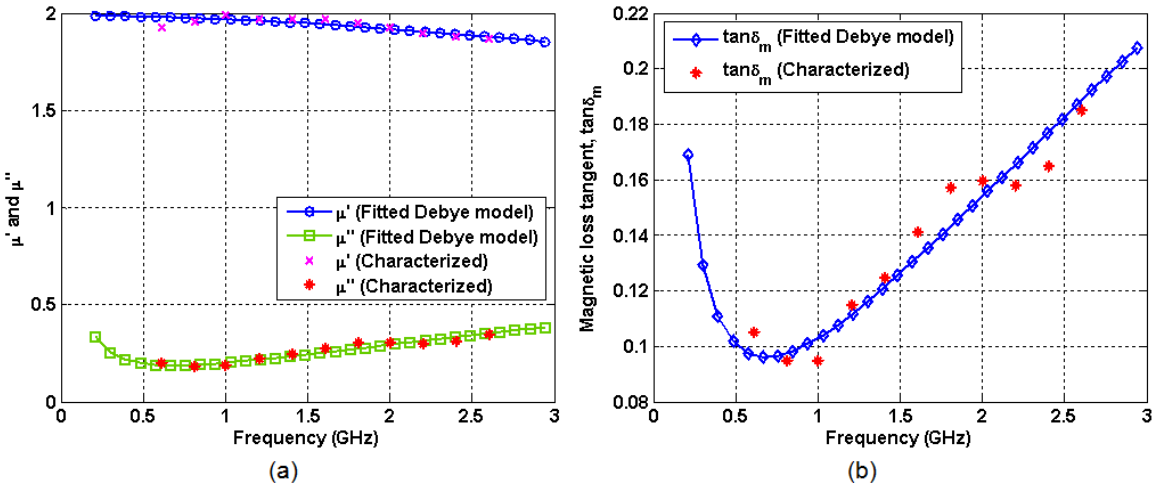

Figure 55. Characterized permeability values with fitted Debye models. (a) μ' and μ'', (b) Magnetic loss tangent.

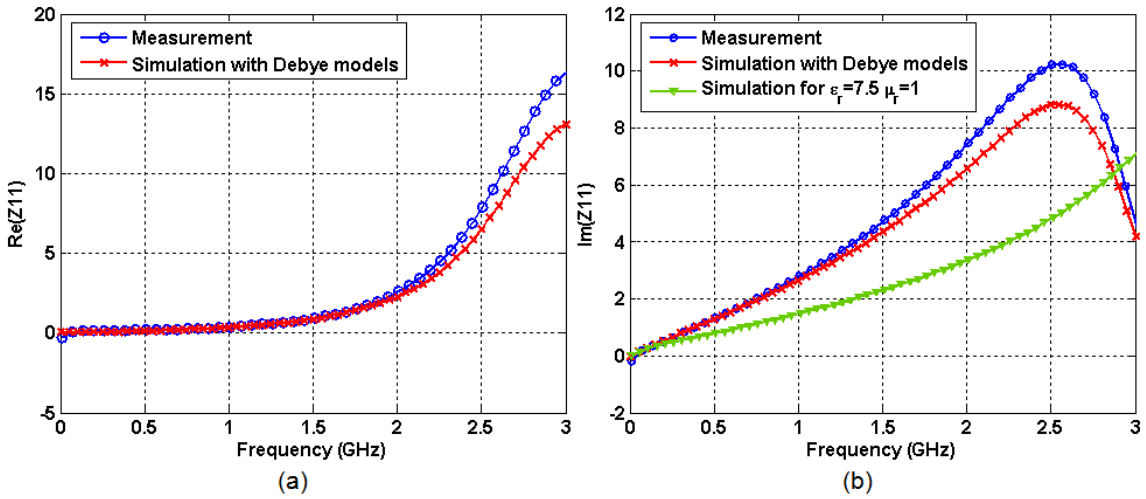

Figure 56. Comparison of the measured and simulated data of the strip inductor. (a) Re{Z_{11}}, (b) Im{Z_{11}}.

the created substrate model. The results obtained from the inductor simulations are compared with the measured response in Figure 56. In this simulation, the ground pad was also modeled to account for its effects in the measurements. As seen in Figure 56, the simulation results obtained from the fitted models agree well with the measurements up to 2 GHz and the error increases after 2 GHz. The error can be attributed to the difference between the simulated values of CST and Sonnet. The $\mu_r = 1$ case is also included in Figure 56b to present a comparison. As seen in the graph, there is a considerable difference with the non-magnetic case. The results obtained from the simulation of the parallel plate resonator are also shown in Figure 57. Good correlation was observed between the simulated and the measured results.

In addition to the samples that show magnetic properties, samples with nonmagnetic properties were also characterized during this research. Figure 58 shows the simulated and measured data from a characterization sample that showed nonmagnetic properties. The extracted properties for this board were found to be $\epsilon_r = 3$, $\mu_r = 1$, and $tan\delta_e = 0.2$. The fact that not every batch of the materials synthesized in this project showed magnetic properties points to the difficulty of synthesizing magneto-dielectric materials. The reason for the instability in the results of consecutive batches may be attributed to improper alignment

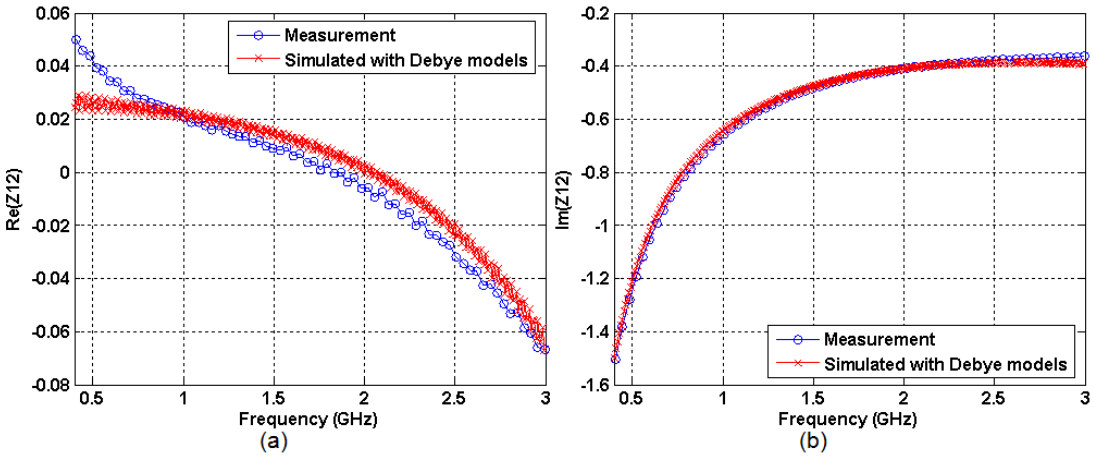

Figure 57. Comparison of the measured and simulated data of the parallel plate resonator. (a) Re{Z_{12}}, (b) Im{Z_{12}}

of the magnetic dipoles in the synthesized material, oxidation, agglomeration and improper encapsulation of nanoparticles. Although magneto-dielectric films with magnetic properties in the low GHz frequencies have been synthesized with the chosen material synthesis process, advanced synthesis techniques and alternative routes are required to reduce the loss of the substrates and guarantee the consistency and repeatability of the parameters for every fabricated batch.

Although the strip inductors have been used successfully for the characterization of the permeability values, the accuracy of this method is limited especially at low frequencies because of the difficulty in the one-port measurement of the ultra-low impedance values. This problem in the one-port measurements arises because S_{11} is close to 1 for the ultra-low impedance values, which means almost all of the signal is reflected. Therefore, impedances less than about 0.1 Ohms are difficult to measure using a one-port technique [59]. Additionally, even after the calibration, the flexing or the over-travel of the microprobe introduces an uncompensated, residual inductance of the probe. Furthermore, depending on the metallization of the probe tip and the surface of the pads there can be a residual, uncompensated resistance term on the order of 10 to 100 milliOhms due to the contact resistance.

These uncompensated inductance and the resistance values contribute to a probe series

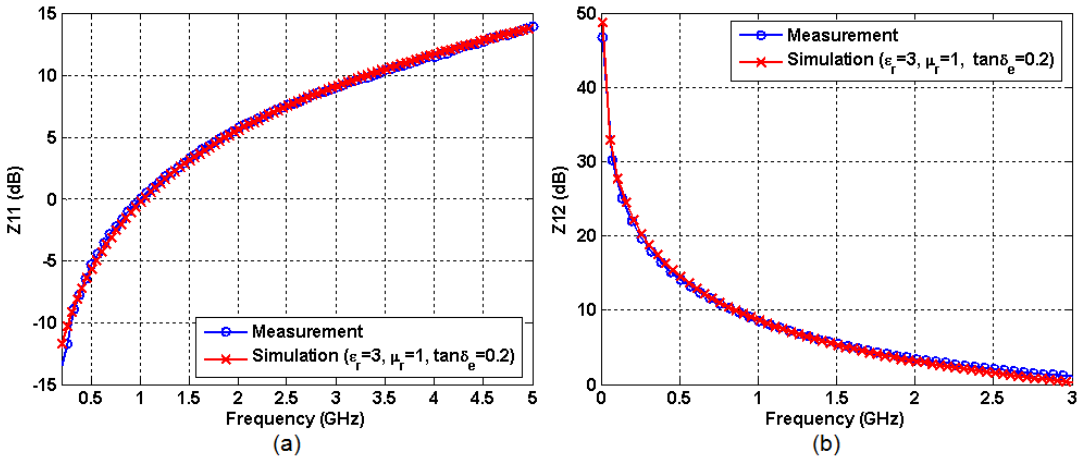

Figure 58. Comparison of the measured and simulated data of a sample board with $\mu_r = 1$. (a) Z_{11} of a 3.5 mm × 0.7 mm **strip inductor on** 21 μm **thick substrate, (b) Z_{12} of a** 6 mm × 8 mm **parallel plate resonator on** 23 μm **thick substrate.**

impedance on the order of 0.1 Ohms and 100 pH. Since this impedance cannot be calibrated out, it limits the reliability of the one-port measurements. This limitation is avoided in a two-port measurement setup due to the symmetry of the probes. Therefore, the characterization methods based on two-port measurements are expected to give more accurate results. A two-port algorithm is proposed in the next section.

3.4 Characterization Algorithm Based on Two-port Microstrip Structures

As mentioned in the previous section, the first characterization method introduced has limitations mainly because of the difficulty in measuring the one-port S_{11} data accurately for ultra-low-impedance values. Moreover, the residual probe inductance due to over-travel of the probe and the contact resistance add an uncompensated impedance on the measured data. These limitations can be eliminated by using a two-port structure instead of the one-port inductor. As an added advantage, using this methodology both the permittivity and the permeability of the substrate can be characterized with a single structure.

Figure 59 displays the details of the two-port strip structure used in the characterization process. As seen in the figure, the structure is nothing but a short microstrip line with length

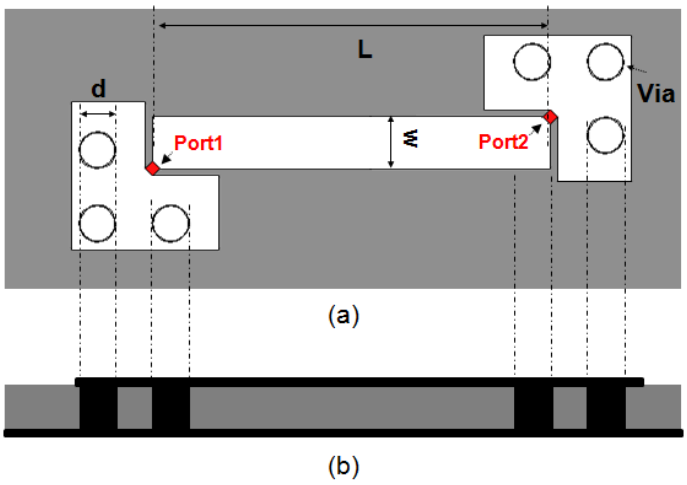

Figure 59. Details of the two-port microstrip line structure used for characterizing the permeability and the permittivity. (a) Top view, (b) Side view.

L and width W. Two ground pads are placed at two opposite corners so that the response can be measured with two GSG probes as in the corner-to-corner probing method for the parallel plate resonator. A meander line can also be used instead of the straight line, as displayed in Figure 60. The meander line has a higher inductance value and; therefore, a higher impedance.

The characterization process is based on processing the measured Y_{12} and Z_{12} data of the two-port microstrip line structure. To explain how this method works one can look at the analytical expressions for the Z_{12} and Y_{12} derived from the ABCD parameters of a lossy microstrip line on a substrate with ϵ_{eff} and μ_{eff}, as shown in Figure 61. The thickness of the substrate and the width of the line are labeled as h and W, respectively. The microstrip line can be assumed to be embedded in a medium that has the same parameters as the magneto-dielectric substrate. Also, the conductor loss is assumed zero in this analysis.

The ABCD parameters of a microstrip line with length ℓ and characteristic impedance Z_0 can be expressed as

$$\begin{bmatrix} A & B \\ C & D \end{bmatrix} = \begin{bmatrix} \cosh\gamma\ell & Z_0 \sinh\gamma\ell \\ \sinh\gamma\ell/Z_0 & \cosh\gamma\ell \end{bmatrix} \tag{11}$$

In Eq. (11), γ is the complex propagation constant as defined in Eq. (2). Z_{12} can be

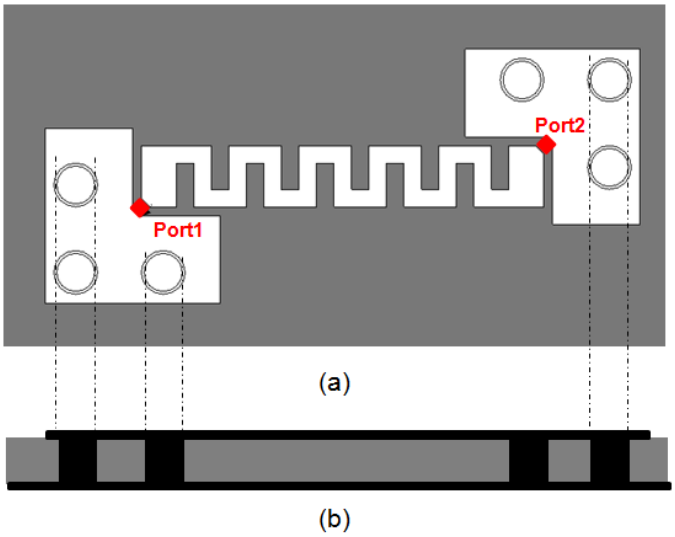

Figure 60. Details of the two-port meander line structure used for characterizing the permeability and the permittivity. (a) Top view, (b) Side view.

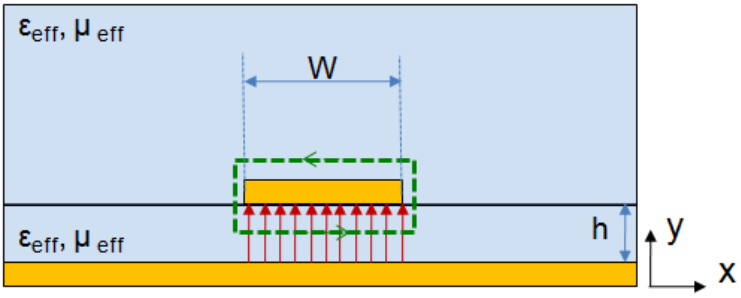

Figure 61. Geometry of the microstrip line on a magneto-dielectric substrate.

calculated from the ABCD parameters as follows:

$$Z_{12} = \frac{V_1}{I_2} \mid_{I_1=0} = \frac{AD - BC}{C} = \frac{1}{C} \tag{12}$$

$$Z_{12} = \frac{Z_0}{\sinh \gamma \ell} \tag{13}$$

For a short microstrip line for frequencies where $\gamma\ell \ll \lambda_g/2$, $\sinh \gamma\ell$ can be approximated as $\sinh \gamma\ell \approx \gamma\ell$. Using this approximation, Eq. (13) can be reduced to the following form:

$$Z_{12} = \frac{Z_0}{\sinh \gamma \ell} \approx \frac{Z_0}{\gamma \ell} \tag{14}$$

$$\frac{Z_0}{\gamma\ell} = \sqrt{\frac{(R + j\omega L)}{(G + j\omega C)}} \frac{1}{\sqrt{(R + j\omega L)(G + j\omega C)}\ell} \tag{15}$$

$$Z_{12} \approx \frac{1}{(G + j\omega C)\ell} \tag{16}$$

A similar analysis can be carried out using Y_{12} to find

$$Y_{12} \approx \frac{1}{(R + j\omega L)\ell} \tag{17}$$

The expressions for the per unit length parameters for a microstrip line with a lossy magneto-dielectric substrate can be found in Appendix A. The expressions for the R and L were repeated in this chapter in (7) and (8), and the expressions for the G and C can be repeated as follows:

$$G = \frac{\omega \epsilon''_{eff} W}{h} \tag{18}$$

$$C = \frac{\epsilon'_{eff} W}{h} \tag{19}$$

Equations (7), (8), (18), and (19) show that the per-unit length parameters R and L are dependent on the real and imaginary parts of the permeability, while the per-unit parameters G and C are dependent on the real and imaginary parts of the permittivity. Therefore, as can be concluded from (16), Z_{12} can be used to characterize the permittivity, and Y_{12} can be used to characterize the permeability of the substrate. Full-wave electromagnetic simulations should be used to take into account the effect of the air medium on ϵ_{eff} and μ_{eff}.

3.4.1 Characterization Process

The flow chart in Figure 62 summarizes the steps of the characterization process. These steps can be listed as follows:

1. The two-port microstrip structure is measured with a vector network analyzer (VNA) using the corner-to-corner probing method.

2. Measured S-parameter data are converted to Z- and Y-parameter data.

3. The thickness of the film is measured at several positions on the substrate.

4. Using the measured thickness, the structure is simulated with an electromagnetic solver at the first frequency point with an initial guess for ϵ_r, μ_r, magnetic and dielectric loss tangents. In this research, Sonnet was used as the electromagnetic solver.

5. The Z_{12} and Y_{12} data obtained from the simulation are compared with the measured Z_{12} and Y_{12}.

6. Simulation process is repeated while sweeping the ϵ_r to match the imaginary part of the Z_{12}, sweeping the dielectric loss tangent to match the real part of the Z_{12}, sweeping the μ_r to match the imaginary part of Y_{12}, and sweeping the magnetic loss tangent to match the real part of Y_{12}. Once a convergence is achieved such that the approximated values do not change considerably between iterations, the process can be repeated for the next frequency point starting from step 4.

3.4.2 Characterization Example Based on Simulation

The same fictitious material used to verify the previous method was used to test the accuracy of the characterization method using the two-port microstrip structure measurements. The material was characterized with both the microstrip line and the meander line structures.

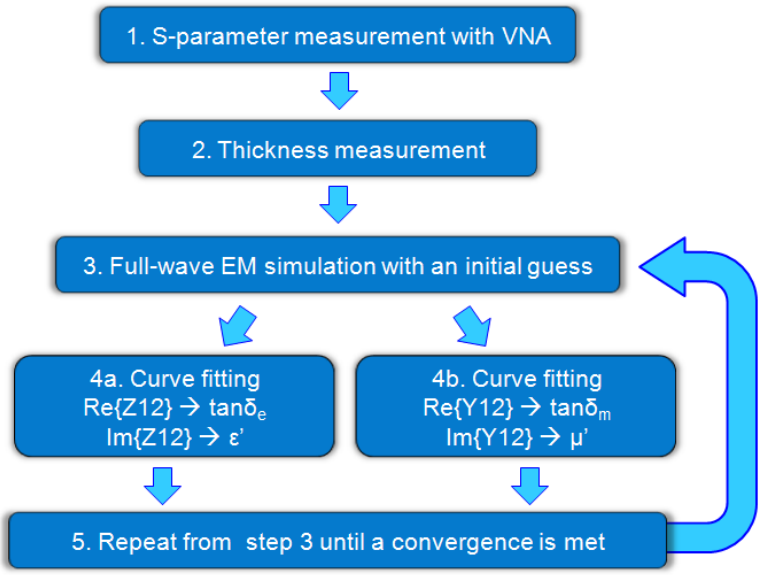

Figure 62. Flow graph of the characterization process using two-port microstrip structure.

First, the two-port structures were simulated separately on a 50 μm thick fictitious substrate using the CST MWS. Ground pads were also included in the simulation models as in the case of real prototypes. The permittivity of the fictitious substrate material was modeled with a first order Debye model, while a second order general dispersion model was used for the permeability of the substrate. After exporting the simulation results from CST MWS, the simulated Y_{12} and Z_{12} responses were used as if they are the measurement responses, and they were characterized using Sonnet, following the characterization steps summarized in Figure 62. The material was characterized using both the microstrip line and the two-port meander line to compare the accuracy obtained from these structures. During the characterization process the microstrip line was modeled with the measurement pads whereas the meander inductor was simulated without the pads to decrease the simulation time.

The results obtained from this study are compared in Figures 63, 64, 65, and 66. In all of these figures, the curves labeled as "model" correspond to the characteristics of the fictitious substrate material. Characterized values for several frequencies are also included in the graphs as single data points along with the curves corresponding to the Debye models fitted using these characterized data points. Figure 63 shows the results obtained for the

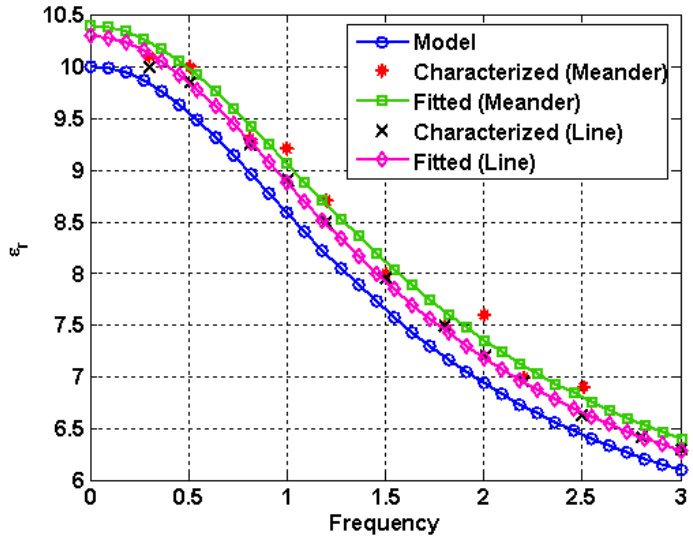

Figure 63. Characterized ϵ' using the two-port microstrip and the meander lines. It should be noted that the model material is a fictitious material used to verify the characterization technique.

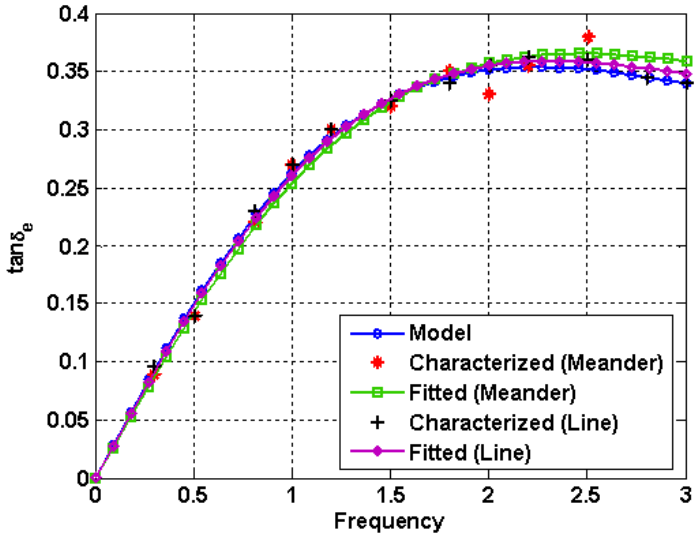

Figure 64. Characterized dielectric loss tangent using the two-port microstrip and the meander lines. It should be noted that the model material is a fictitious material used to verify the characterization technique.

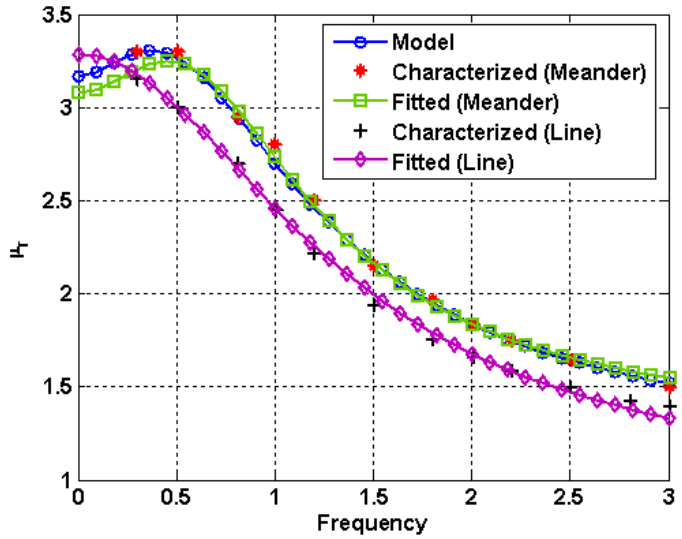

Figure 65. Characterized μ' using the two-port microstrip and the meander lines. It should be noted that the model material is a fictitious material used to verify the characterization technique.

permittivity. Although the accuracy of the method is low compared to the parallel plate resonator, acceptable accuracy is obtained using two-port microstrip line measurements. The error is higher for the values extracted using the meander line, which might be because of the additional capacitance between the meander arms. Characterized results for the dielectric loss tangent are shown in Figure 64. As seen in the figure, the accuracy is better up to 1.5 GHz compared to the higher frequencies.

Figure 65 displays the characterized relative permeability values. As seen in the figure, two-port meander can extract the modeled permeability values with high accuracy; whereas, the line can be used with an acceptable accuracy. Finally, the results obtained for the magnetic loss tangent are shown in Figure 66. Two-port meander can be used to characterize the magnetic loss tangent accurately up to 1.5 GHz but the error increases for higher frequencies.

It can be concluded that the meander structure is more suitable to characterize the permeability values with high accuracy; whereas, the straight line should be preferred to characterize the permittivity values. However, as can be seen from Figures 63 to 66, both of the

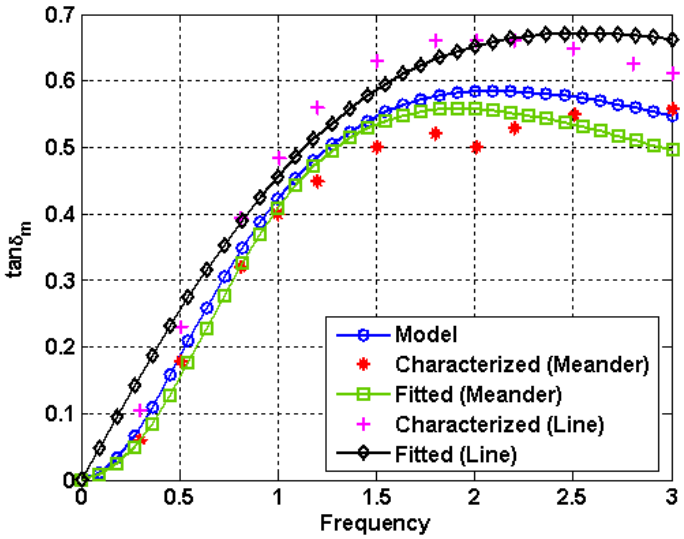

Figure 66. Characterized magnetic loss tangent using the two-port microstrip and meander lines. It should be noted that the model material is a fictitious material used to verify the characterization technique.

structures can be used to characterize thin-film magneto-dielectric materials with acceptable accuracy.

3.5 Conclusions

In highly-integrated packaging technologies, the parameters of the materials used in the package have an important role in determining the quality of the performance and the size of the system since these parameters determine the characteristics of the wave propagation in the substrate. Therefore, there is a growing effort to synthesize novel materials with desired characteristics. The thin-film magneto-dielectrics is an example of these materials, which have been proposed to achieve the effective miniaturization of the antennas and other electromagnetic structures. However, these materials need to be synthesized artificially due to their absence in nature. There has been research efforts at the Packaging Research Center at Georgia Tech to synthesize low-loss thin-film magneto-dielectric substrates. The method followed in this research was based on encapsulating Ni and Co nanoparticles with polymer to reduce magnetic losses due to interaction between neighboring magnetic particles and

also to prevent oxidation. The work covered in this chapter has supported this magneto-dielectric material synthesis project in terms of characterization of synthesized materials.

One crucial step in the material synthesis process is the accurate characterization of the samples to extract the permeability and the permittivity of the substrate. However, the characterization of the magneto-dielectric materials is a difficult task since it is necessary to separate the effects of the ϵ' from μ' and ϵ'' from μ'', accurately. Moreover, it is preferred that the test vehicles needed for the characterization are easy-to-fabricate and easy-to-measure structures so that long turn around times between samples are avoided.

Two characterization methodologies have been proposed in this chapter for the characterization of the thin-film magneto-dielectric materials. Both of the methods use samples that can be fabricated with the standard printed circuit board technology and that can be measured with the standard coplanar air probes.

The first method is based on using two-port measurement of a parallel plate resonator to characterize the permittivity, while using one-port measurement of strip inductors to characterize the permeability of the substrate. It has been shown both analytically and experimentally that this method can be used to characterize the frequency-dependent properties of the thin-film magneto-dielectric substrates. The method can be used in a frequency range from 600 MHz to approximately 3 GHz. The upper bound of the frequency range depends on the resonance frequency of the inductors and the resonators, and it can be increased by adjusting the size of the structures. The lower bound is limited with the accuracy of the VNA measurements.

The second method proposed is based on using two-port measurements of simple microstrip structures. The principles of this method have also been explained theoretically and experimentally in this chapter. This method is expected to be more accurate in the extraction of the permeability compared to the first method. This is because the accuracy limitations of the one-port measurements are avoided in the second method by using two-port structures. Similar to the first method, the frequency range is determined by the

resonance frequencies of the structures. Both of the characterization methodologies presented in this chapter can be used separately or together for the accurate extraction of the permeability and the permittivity of the magneto-dielectric substrates.

Several batches have been fabricated and characterized to verify the material synthesis process. The main challenge during the magneto-dielectric thin-film synthesis has been to obtain stable high-permeability values with low magnetic and dielectric loss. As presented in this chapter, one of the fabricated batches was characterized to have $\mu_r \sim 1.9$ in the low GHz band. Although this substrate was found to be too lossy for antenna and other electromagnetic applications, stable high permeability value extracted in the GHz range was found promising for the chosen material synthesis process.

However, in addition to the materials characterized to have magnetic attributes with μ_r values ranging from 1.3 to 1.9, several batches with nonmagnetic attributes were also characterized. The fact that not every batch of the materials synthesized in this project showed magnetic properties points to the difficulty of synthesizing magneto-dielectric materials. The reason for the inconsistency in the characterized values of consecutive batches may be attributed to improper alignment of the magnetic dipoles in the synthesized material, oxidation, agglomeration and improper encapsulation of nanoparticles. Advanced synthesis techniques and alternative routes are required to reduce the loss of the substrates and guarantee the consistency and repeatability of the parameters for every fabricated batch.

CHAPTER 4

MINIATURIZATION OF ANTENNAS USING MAGNETO-DIELECTRIC SUBSTRATES

Increasing demand for smaller size in mobile devices results in a need for the effective antenna miniaturization, since the antenna size is an important factor determining the overall size of a mobile device. Planar antennas are highly preferred in mobile systems because of their characteristics such as ease of fabrication and integration, compactness, and low profile. Moreover, backing the planar antenna with a ground plane, as in the case of a microstrip patch antenna, offers increased front-to-back ratio, while shielding the rest of the system from the fields of the antenna in a multilayer substrate.

Antenna miniaturization is a difficult problem since the gain and the bandwidth of the antenna are bounded with fundamental limits depending on the size of the antenna. The techniques proposed in the literature to miniaturize the antenna can be categorized into two groups. One method is to alter the geometry of the antenna to achieve a compact design. The techniques in this group are based on using meandered structures, cuts, arms and slots on the radiating conductor to fit the necessary electrical length of the current path in a compact size. Although modifying the geometry can result in miniaturization, these techniques require many iterations and long design periods.

Antenna miniaturization techniques in the second category are more straightforward and based on the material loading using the effect of the electromagnetic parameters of the substrate or the superstrate. These techniques are applied especially to the planar resonant antennas printed on a substrate backed with a conductor, such as microstrip patch antennas. Since the resonant length of an antenna scales with the guided wavelength ($\lambda_g = \lambda_0/\sqrt{\epsilon_r \mu_r}$), the values of the ϵ_r and μ_r of the substrate play an important role in determining the size of the antenna for a certain resonance frequency.

There are two types of materials that can be used as the substrate or the superstrate of

the antenna. The first type is the conventional dielectric materials with $\epsilon_r > 1$ and $\mu_r = 1$. Dielectric materials can be found in nature or synthesized in the laboratories, and they have been commonly used as RF substrates. The second type is the magneto-dielectric materials with $\epsilon_r > 1$ and $\mu_r > 1$. Although these novel materials do not exist in nature and must be synthesized, these materials provide advantages over the conventional dielectric substrates.

In this chapter, the application of magneto-dielectric substrates towards the effective antenna miniaturization is presented along with evidence that the magneto-dielectrics are better candidates as the antenna substrates compared to the conventional dielectrics. The results of theoretical and experimental analysis based on full-wave electromagnetic simulations are presented in this chapter. Moreover, a discussions of surface wave propagation in the conductor-backed magneto-dielectric substrates has also been included in this chapter since the surface wave propagation has a considerable impact on the radiation properties of planar antennas.

4.1 Review of Antenna Miniaturization Using Material Loading

As mentioned before, the resonant length of an antenna scales with the guided wavelength, λ_g, which is determined with the values of the ϵ_r and μ_r of the substrate. Therefore, substrate parameters play an important role in determining the size of the antenna for a certain resonance frequency.

For this reason, using high-permittivity materials as the antenna substrate has been proposed in the literature to reduce the size of the antenna. Although, miniaturization can be achieved using low-loss, high-permittivity materials as the substrate of the antenna [60] [61], the antenna usually suffers from low-efficiency and narrow-bandwidth in this method. This problem stems from the fact that the radiated field from the image of the antenna's electric current tends to cancel out the radiated field from the antenna current, since the image of the horizontal current on a ground plane is in close proximity and opposite to the direction of the current itself. The cancelation of the radiated fields results in increased stored

electromagnetic energy, which causes narrow-bandwidth and low-efficiency. Increased permittivity of the substrate contributes to the stored electromagnetic energy, deteriorating the bandwidth and the efficiency of the antenna and making the situation worse.

Thicker substrates can be used to increase the bandwidth at the expense of the increased energy trapped in the substrate in the form of surface waves. Moreover, increasing the thickness is not consistent with the aim of miniaturization. It has been proposed in [60] that using a superstrate with higher dielectric constant can compensate for the decrease in the antenna gain. However, this method introduces additional fabrication steps, while increasing the thickness of the antenna.

The concept of using magneto-dielectrics as the antenna substrate was introduced by Hansen and Burke in [26], where the bandwidth of a microstrip patch antenna on a magneto-dielectric substrate was analyzed using transmission line theory. In this paper, the authors derived the zero-order bandwidth for a microstrip patch antenna and analyzed three cases: $\mu_r < \epsilon_r$, $\mu_r = \epsilon_r$ and $\mu_r >> \epsilon_r$ for a constant miniaturization factor of $\sqrt{\mu_r \epsilon_r}$. It was concluded in [26] that by properly increasing the relative permeability of the substrate, the antenna can be miniaturized without deteriorating the bandwidth of the antenna compared to the $\mu_r = 1$ case. In this chapter, a more thorough analysis is presented to explain why magneto-dielectrics are better substrates than the dielectric counterparts.

Following Hansen and Burke's analysis in [26], developing and characterizing artificial magneto-dielectric substrates have gained increasing attention because of the absence of low loss magneto-dielectric materials in nature. Artificial magneto-dielectric substrates constructed of embedded circuits in a dielectric host medium have been reported in [40], [41], [42], [62], and [43]. A detailed review on these material can be found in Chapter 3 of this thesis.

Artificial magneto-dielectric substrates were also used as the antenna substrate. According to the results reported in [42], miniaturization factors of 4-7 have been obtained for microstrip patch antennas that are designed around 200 MHz-250 MHz. Although

magneto-dielectric characteristics and antenna miniaturization can be achieved with the usage of such engineered substrates, the substrates reported so far were lossy and bulky; hence, not suitable for the mobile applications. Moreover, the substrates were reported to show highly-dispersive anisotropic behavior, which is another limitation for their application to the antenna miniaturization.

It was suggested in [63] that the magneto-dielectric substrates with natural magnetic inclusions, e.g. ferromagnetic films, can provide higher relative permeability values such that the effect of the dispersion can be compensated. Composites of nickel [49], [46] and cobalt [49] have been used to synthesize low-loss magnetic materials. Applications of these magnetic composite substrates to the antenna miniaturization problem have also been published in the literature recently [46], [49], [64]. However, the research that has been conducted so far is mostly focused on the MHz frequency range, and there is still a need to have low-loss magnetic materials in the GHz frequencies. Although size reduction is a more critical issue for MHz frequencies, most mobile applications can benefit from the efficient miniaturization of antennas with the use of magneto-dielectric materials at GHz frequencies.

There have been intuitive explanations in the aforementioned papers on why the magneto-dielectrics are expected to provide effective antenna miniaturization. However, there is not enough theoretical analysis in the literature to support these intuitive explanations. Moreover, since most of the previous analysis on the planar antennas assume dielectric substrates, the previous theoretical analysis also fails to provide direct insight to answer this question. Therefore, in this chapter the well-known analysis methods, such as cavity theory for the microstrip patch antenna, are revisited and applied for the magneto-dielectric substrates. The details of the analysis are presented in the next section.

4.2 Why are Magneto-dielectrics Better Substrates?

In this section, the advantages of the magneto-dielectric substrates for the planar antennas are explained by analyzing the bandwidth, the radiated power, and the stored electromagnetic energy of a microstrip patch antenna on a magneto-dielectric substrate. Although a preliminary analysis was reported in [26], a more detailed analysis is provided here to explain how the stored energy and the radiated power of the antenna are also affected from increasing the permeability of the substrate.

A microstrip patch antenna can be considered as a lossy cavity; therefore, the well-known cavity model has been proposed to analyze the patch antenna [65]. In the cavity model, the volume beneath the patch is treated as a rectangular cavity loaded with the antenna substrate with the relative permittivity ϵ_r and the relative permeability μ_r. The substrate is assumed to be truncated and not extended beyond the edges of the patch, as shown in Figure 67. Moreover, the cavity is assumed to be bounded by electric walls on the top and bottom, and magnetic walls along the periphery. This assumption is based on the following observations for thin substrates ($h \ll \lambda_0$) [65]:

1. The fields in the interior region do not vary with z due to the thin substrate ($\frac{\partial}{\partial z} \equiv 0$).
2. The electric field is z directed only, E_z, and the magnetic field has only the transverse components in the interior region, H_x and H_y.
3. The electric current on the patch has no component normal to the edge of the patch metallization, which implies the tangential magnetic field along the edge is negligible.

The field distribution of the patch antenna can be divided into two regions: the interior fields, $\bar{E}^i$ and $\bar{H}^i$, and the exterior fields, $\bar{E}^e$ and $\bar{H}^e$. As mentioned before, there are only three components of the interior fields, E_z, H_x and H_y, since the substrate is thin. The dielectric loss, conductor loss, and surface wave loss are all assumed to be zero in this analysis.

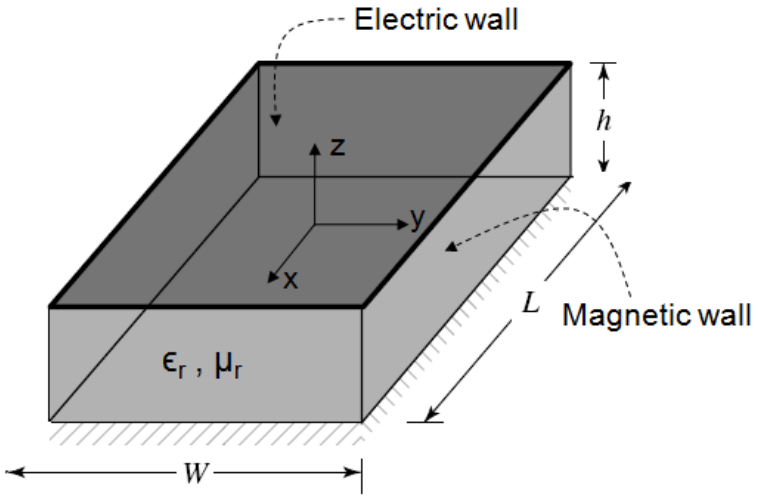

Figure 67. Cavity model with magnetic walls for analyzing microstrip patch antenna on a magneto-dielectric substrate.

The interior electric field must satisfy the inhomogeneous wave equation that can be derived from Maxwell's equations

$$(\nabla_t)^2 E_z + k^2 E_z = j\omega\mu_r\mu_0\hat{z}\cdot\bar{J} \tag{20}$$

where $k^2 = \omega^2\mu_0\mu_r\epsilon_0\epsilon_r$, $\bar{J}$ is the excitation current density either due to coaxial feed or the microstrip feed, $\hat{z}$ is a unit vector normal to the plane of the patch, and $(\nabla_t)^2$is the transverse del operator with respect to the z axis.

The fields should also satisfy the following boundary conditions:

$$\begin{aligned} \hat{n}\times\bar{E}^i &= 0 \text{ on the electric walls} \\ \hat{n}\times\bar{E}^e &= \hat{n}\times\bar{E}^i \text{ on the magnetic walls} \\ \hat{n}\times\bar{H}^e &= \hat{n}\times\bar{H}^i = 0 \text{ on the magnetic walls} \end{aligned} \tag{21}$$

where $\hat{n}$ is the unit outward normal to the walls.

The interior electric field distribution can be obtained in terms of the eigenfunctions of

the cavity by solving the inhomogeneous wave equation in (20) with the boundary conditions in (21). The electric field in the patch cavity can be expressed as

$$E_z(x,y) = \sum_m \sum_n A_{mn}\psi_{mn}(x,y) \tag{22}$$

where A_{mn} are the amplitude coefficients of the eigenfunctions, ψ_{mn}. The eigenfunctions are solutions of

$$(\nabla_t^2 + k_{mn}^2)\psi_{mn} = 0. \tag{23}$$

Substituting (22) for E_z in (20), and multiplying both sides by ψ_{mn}^* ,and integrating over the patch, the amplitude coefficients, A_{mn}, in (22) can be obtained as

$$A_{mn} = \frac{j\omega\mu_r\mu_0}{k^2 - k_{mn}^2} \frac{\iint J_z\psi_{mn}^* dS}{\iint \psi_{mn}\psi_{mn}^* dS}. \tag{24}$$

Substituting A_{mn} in (22) gives

$$E_z = j\omega\mu_r\mu_0 \sum_m \sum_n \frac{1}{k^2 - k_{mn}^2} \frac{\iint J_z\psi_{mn}^* dS}{\iint \psi_{mn}\psi_{mn}^* dS} \tag{25}$$

where k_{mn} is defined as

$$k_{mn} = \sqrt{\left(\frac{m\pi}{L}\right)^2 + \left(\frac{n\pi}{W}\right)^2} \tag{26}$$

The magnetic field can be obtained using

$$\vec{H} = \frac{1}{j\omega\mu_r\mu_0}\hat{z} \times \nabla E_z \tag{27}$$

The eigenfunctions, ψ_{mn} depend on the shape and size of patch of the antenna, and not on substrate parameters. The eigenfunctions for the rectangular patch shown in Figure 67 are given as [65]

$$\psi_{mn} = \cos\left(\frac{m\pi x}{L}\right)\cos\left(\frac{m\pi y}{W}\right). \tag{28}$$

At this point, the analysis is carried out with two different excitation cases. First, a constant amplitude coaxial excitation is assumed. Next, a constant voltage excitation is assumed. The fields obtained for both excitations are further analyzed to calculate the radiated field and the stored electromagnetic energy. The results are compared for a dielectric and a magnetic substrate to explain why increasing the permeability of the substrate increases the bandwidth of the antenna.

4.2.1 Constant Current Excitation

Assuming a coaxial feed, the excitation current, J_z, at the feed point (x_0, y_0) can be defined as

$$J_z = I_0 \delta(x - x_0)\delta(y - y_0). \tag{29}$$

Substituting (28) and (29) in (25), the expression for the E-field can be rewritten as follows for the TM_{10} mode

$$E_z = j\omega\mu_r\mu_0 I_0 \frac{2}{WL}\frac{1}{(k^2 - k_{10}^2)}\cos\left(\frac{\pi x_0}{L}\right)\cos\left(\frac{\pi x}{L}\right). \tag{30}$$

Using (27), the magnetic field can also be calculated as

$$H_y = -I_0 \frac{2}{WL}\frac{\pi}{L}\frac{1}{(k^2 - k_{10}^2)}\cos\left(\frac{\pi x_0}{L}\right)\sin\left(\frac{\pi x}{L}\right). \tag{31}$$

(30) and (31) can be rewritten as follows by collecting the common terms

$$E_z = j\omega\mu_r\mu_0 B_0 \cos\left(\frac{\pi x}{L}\right) \tag{32}$$

$$H_y = -\frac{\pi}{L} B_0 \sin\left(\frac{\pi x}{L}\right) \tag{33}$$

where

$$B_0 = I_0 \frac{2}{WL}\frac{1}{(k^2 - k_{10}^2)}\cos\left(\frac{\pi x_0}{L}\right). \tag{34}$$

The electromagnetic energy stored under the patch can be determined by integrating the fields under the patch. The total stored electromagnetic energy W_t is defined as:

$$W_T = W_e + W_m = \frac{1}{4}\iiint_V (\epsilon|E|^2 + \mu|H|^2)\, dV. \tag{35}$$

Since the electric and magnetic energies are equal at the resonance, (35) can be simplified to

$$W_t = W_e + W_m = \frac{1}{2}\iiint_V (\epsilon|E|^2)\, dV \tag{36}$$

$$\simeq \frac{1}{2}\epsilon h \iint_S (|E|^2\, dS) \text{ for thin substrates.} \tag{37}$$

Substituting the expression for E_z, in (37) yields

$$W_t = \frac{1}{2}\epsilon_r\epsilon_0 h \int_{-W/2}^{W/2}\int_{-L/2}^{L/2}(\omega\mu_r\mu_0|B_0|)^2\cos\left(\frac{\pi x}{L}\right)dx\,dy$$
$$= \frac{1}{4}\omega^2\mu_r^2\mu_0^2|B_0|^2\epsilon_r\epsilon_0 hWL \tag{38}$$

Calculating the radiated power using the interior fields defined in (32) and (33) is not possible since there was no loss mechanism in the cavity modeling the radiation. The radiated power of the antenna, P_r, can be determined by integrating the radiated fields over the hemisphere above the patch, which is given as

$$P_r = \frac{1}{2\eta_0}\int_0^{2\pi}\int_0^{\pi/2}(|E_\theta|^2 + |E_\phi|^2)r^2\sin\theta\,d\theta\,d\phi. \tag{39}$$

E_θ and E_ϕ are the θ and ϕ components of the radiated E-field. The expressions for E_θ and E_ϕ are complicated functions of θ, ϕ, and the substrate parameters.

While calculating the far-fields of the patch antenna, both the electric and magnetic current densities of the antenna should be considered. The electric current density, J_s, occurs due to the presence of the conducting patch and distributed on the radiating patch of the antenna. The magnetic current density, M_s, is a result of the strong E-field under the antenna and is distributed along the side periphery of the cavity. M_s is the main radiating current since the image of the horizontal magnetic current with respect to the ground plane is in the same direction with the original magnetic current; whereas, the radiated fields of the horizontal electric current are mostly cancelled with the fields of the image current. Although usually the power radiated J_s is neglected in the literature [10], the power radiated by both current densities are calculated here for the sake of completeness.

4.2.1.1 Radiated power by the electric patch current

It was proposed in [66] that the radiated fields of the patch antenna can be approximated using the radiated fields of a horizontal Hertzian electric dipole placed on top of a grounded substrate. In this method, the conductor-backed substrate is modeled with a transmission line analogy and the radiated fields of the Hertzian dipole are found including the effect of

the substrate on the radiated fields. The details of this analysis can be found in [66] and [67].

Once the expressions for the radiated fields are known, the radiated power can be calculated using (39). In [66], the following expression is derived for the radiated power from a Hertzian electric dipole on top of a thin magneto-dielectric substrate:

$$P_r^h = \frac{1}{\lambda_0^2}(k_0 h)^2 \left[80\pi^2 \mu_r^2 \left(1 - \frac{1}{\epsilon_r \mu_r} + \frac{2/5}{\epsilon_r^2 \mu_r^2} \right) \right]. \tag{40}$$

Next, the radiated power by the electric current distribution on the patch antenna can be approximated with the radiated power from an equivalent Hertzian dipole of the same current moment. The electric current distribution on the patch can be found from the H-field expression as

$$J_s = B_0 \left(\frac{\pi}{L} \right) \sin\left(\frac{\pi x}{L} \right) \tag{41}$$

Using J_s, the current moment for the patch current can be obtained as

$$m_{eq} = \iint_S J_s \, dx \, dy \tag{42}$$

$$= \int_0^W \int_0^L B_0 \left(\frac{\pi}{L} \right) \sin\left(\frac{\pi x}{L} \right) dx \, dy \tag{43}$$

$$= 2 B_0 W \tag{44}$$

The radiated power by the electric current density of the patch antenna is then equal to [66]

$$\begin{aligned} P_r^e &= m_{eq}^2 P_r^h \\ &= 4 B_0^2 W^2 \frac{1}{\lambda_0^2}(k_0 h)^2 \left[80\pi^2 \mu_r^2 \left(1 - \frac{1}{\epsilon_r \mu_r} + \frac{2/5}{\epsilon_r^2 \mu_r^2} \right) \right]. \end{aligned} \tag{45}$$

Although it was claimed in [66] that the radiated power expression derived in this paper is the total radiated power of the patch antenna, it only includes the contribution of the electric current of the patch antenna.

4.2.1.2 Radiated power by the magnetic current

The equivalent magnetic currents are distributed along the periphery of the patch antenna. Although there are four slots along the periphery of the antenna, two of these slots are

non-radiating slots and their contribution can be neglected for the approximate expressions [10]. Therefore, the patch antenna can be modeled as a combination of two parallel slots of length W, height h and a distance L apart. The magnetic current distribution on the slots can be calculated from the E-field under the patch antenna and using the image theory as

$$M_s = \begin{cases} 2\omega\mu_r\mu_0 B_0, & -\frac{W}{2} \le y \le \frac{W}{2} and -\frac{h}{2} \le z \le \frac{h}{2} \\ 0, & \text{elsewhere} \end{cases} \tag{46}$$

The radiated fields calculated using the equivalent magnetic currents result in complicated expressions of θ, ϕ and substrate parameters. Approximate expressions for the thin substrates can be derived, and the total radiated power can be calculated using (39) and a closed-form expression was obtained for thin substrates by Thouroude et. al. in [68]. The expression is repeated here as follows:

$$P_r^m = \frac{(\omega\mu_r\mu_0 B_0 h)^2 A\pi^4}{23040}\left[(1-B)(1-\frac{A}{15}+\frac{A^2}{420})+\frac{B^2}{5}(2-\frac{A}{7}+\frac{A^2}{189})\right] \tag{47}$$

where $A = (\pi W/\lambda_0)^2$ and $B = (2L/\lambda_0)^2$.

The total radiated power of the patch antenna is the sum of the power radiated by the equivalent electric current and magnetic current densities.

$$P_r = P_r^e + P_r^m \tag{48}$$

where P_r^e and P_r^m are given in Equations (45) and (47), respectively.

Now that the expression for the stored electromagnetic energy and the radiated power are known, the quality factor Q, of the antennas can also be calculated. The quality factor can be defined as

$$Q = \frac{\omega_r W_t}{P_r}. \tag{49}$$

The quality factor of the antenna is a useful parameter since the VSWR 2:1 bandwidth of the antenna can be approximated using

$$BW = \frac{1}{Q\sqrt{2}} \times 100. \tag{50}$$

The effect of increasing the permeability of the substrate can be studied comparing the W_T, P_r, and, Q of two patch antennas with same dimensions but on two different substrates. One of the substrates is chosen as a dielectric substrate with $\epsilon_r = K$, $\mu_r = 1$ while the other one is a magnetic substrate with $\epsilon_r = 1$, $\mu_r = K$. Patch antennas on these substrates are assumed to have the same resonance frequency ω since $\epsilon_r \mu_r = K$ for both cases, and they are excited with the same current I_0.

4.2.1.3 Dielectric substrate with $\epsilon_r = K$, $\mu_r = 1$

Let us assume the fields of the patch antenna on this dielectric substrate are labeled as E_1 and H_1. Substituting the substrate parameters in (32) and (33) yields

$$E_1 = j\omega\mu_0 B_0 \cos\left(\frac{\pi x}{L}\right) \tag{51}$$

$$H_1 = -\frac{\pi}{L} B_0 \sin\left(\frac{\pi x}{L}\right). \tag{52}$$

It should be noted that B_0 does not depend on substrate parameters, as expressed in (34). By substituting the substrate parameters in (37), the total stored electromagnetic energy W_{t1} is given as

$$W_{t1} = \frac{1}{4}\omega^2 \mu_0^2 |B_0|^2 K \epsilon_0 h W L \tag{53}$$

Using (45), the radiated power of the patch current J_s on the dielectric substrate can be found as

$$P_{r1}^e = 4B_0^2 W^2 \frac{1}{\lambda_0^2}(k_0 h)^2 \left[80\pi^2 \left(1 - \frac{1}{K} + \frac{2/5}{K^2}\right)\right] \tag{54}$$

Similarly, the radiated power of the equivalent magnetic currents can be found using (47) as

$$P_{r1}^m = \frac{(\omega\mu_0 B_0 h)^2 A \pi^4}{23040}\left[(1-B)(1 - \frac{A}{15} + \frac{A^2}{420}) + \frac{B^2}{5}(2 - \frac{A}{7} + \frac{A^2}{189})\right] \tag{55}$$

Then the total radiated power of the patch is found as

$$P_{r1} = (P_{r1}^e + P_{r1}^m). \tag{56}$$

4.2.1.4 *Magnetic substrate with $\epsilon_r = 1$, $\mu_r = K$*

Assuming the fields of the patch antenna on this magnetic substrate are E_2 and H_2, the expression for the fields can be obtained from (32) and (33) as

$$E_2 = j\omega\mu_0 K B_0 \cos\left(\frac{\pi x}{L}\right) \tag{57}$$

$$H_2 = -\frac{\pi}{L} B_0 \sin\left(\frac{\pi x}{L}\right). \tag{58}$$

Total stored energy, W_{t2} can be calculated using (37) and it is given as

$$W_{t2} = \frac{1}{4}\omega^2 K^2 \mu_0^2 |B_0|^2 \epsilon_0 h W L. \tag{59}$$

Using (45), the radiated power of the patch current can be found as

$$P^e_{r2} = 4B_0^2 W^2 \frac{1}{\lambda_0^2}(k_0 h)^2 \left[80\pi^2 K^2 \left(1 - \frac{1}{K} + \frac{2/5}{K^2}\right)\right]. \tag{60}$$

Similarly, using (47), the radiated power of the equivalent magnetic currents can be found as

$$P^m_{r2} = \frac{(\omega K \mu_0 B_0 h)^2 A \pi^4}{23040}\left[(1-B)(1 - \frac{A}{15} + \frac{A^2}{420}) + \frac{B^2}{5}(2 - \frac{A}{7} + \frac{A^2}{189})\right]. \tag{61}$$

Then, the total radiated power of the patch antenna is found as

$$P_{r2} = P^e_{r2} + P^m_{r2} = K^2(P^e_{r1} + P^m_{r1}). \tag{62}$$

4.2.1.5 *Summary of the Constant Current Analysis*

When two identical patch antennas printed on separate magnetic and dielectric substrates, satisfying $\epsilon_r \mu_r = K$, are excited with the same coaxial current, the following observations can be made

1. The electric field amplitude of the patch antenna on the magnetic substrate is stronger than the amplitude of the electric field of the patch antenna on the dielectric substrate.

$$E_2 = K E_1 \tag{63}$$

2. The amplitude of the magnetic field is the same for both cases.

$$H_2 = H_1 \tag{64}$$

3. The total stored electromagnetic energy is increased by K in the magnetic substrate since amplitude of the electric field is stronger compared to the dielectric substrate.

$$W_{t2} = KW_{t1} \tag{65}$$

4. Similar to the stored electromagnetic energy, the radiated power from the patch on the magnetic substrate is greater than the power radiated from the patch on the dielectric substrate.

$$P_{r2} = K^2 P_{r1} \tag{66}$$

5. Since the radiated power from the patch on magnetic substrate increases with K^2 while the stored energy increases only by K, the quality factor of the antenna decreases by K compared to the Q of the dielectric substrate. Using (65) and (66), the ratio of the quality factors of these two cases can also be obtained as

$$Q_2 = \frac{Q_1}{K} \tag{67}$$

6. The lower quality factor obtained from the patch on the magnetic substrate translates to a higher impedance bandwidth.

It can be concluded from this analysis that increasing the permeability of the substrate is more advantageous than increasing the permittivity of the substrate to miniaturize the antenna since the bandwidth of the antenna can be improved, while miniaturizing the antenna simultaneously. The results obtained from the constant current analysis are summarized in Figure 68.

4.2.2 Constant Voltage Excitation

The analysis can be repeated for the constant voltage excitation case as well. The electric and magnetic fields can be expressed in the following forms when the antenna is excited with constant voltage between the patch and the ground plane. If the amplitude of the voltage phasor is V_0,

$$E_z = -\frac{V_0}{h}\cos\left(\frac{\pi x}{L}\right) \tag{68}$$

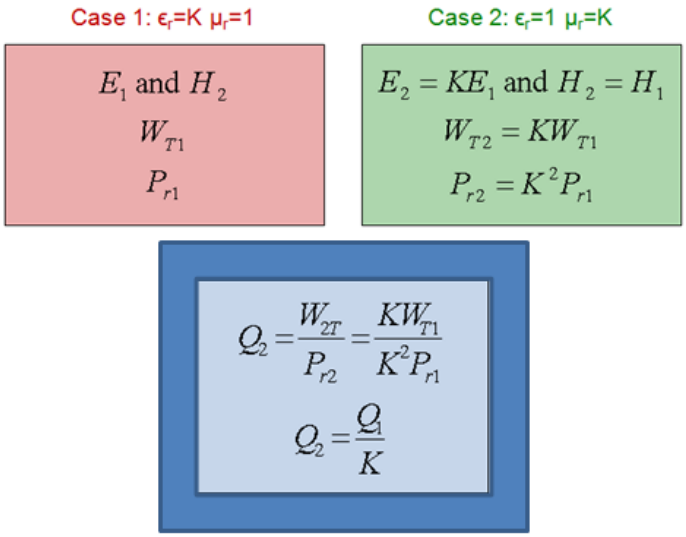

Figure 68. Summary of the constant current analysis

$$H_y = -\frac{V_0}{j\omega\mu_r\mu_0 h}\frac{\pi}{L}\sin\left(\frac{\pi x}{L}\right) \tag{69}$$

Substituting these field expressions in (37) the stored electromagnetic energy can be obtained as

$$W_T = \frac{1}{2}\epsilon h \iint_S (|E|^2\, dS) = \frac{1}{4}\epsilon_r\epsilon_0 WL\frac{(V_0)^2}{h} \tag{70}$$

The expressions for the radiated powers by the electric and magnetic current densities were derived for the constant current excitation analysis. The expressions in Equations (45) and (47) can be rewritten here for the constant voltage excitation.

$$P_R^E = 4W^2(V_0^2\frac{\epsilon_0}{\mu_0\lambda_0^2}\left[80\pi^2\left(1 - \frac{1}{\epsilon_r\mu_r} + \frac{2/5}{\epsilon_r^2\mu_r^2}\right)\right]. \tag{71}$$

$$P_R^M = \frac{(V_0)^2 A\pi^4}{23040}\left[(1-B)(1 - \frac{A}{15} + \frac{A^2}{420}) + \frac{B^2}{5}(2 - \frac{A}{7} + \frac{A^2}{189})\right] \tag{72}$$

where $A = (\pi W/\lambda_0)^2$ and $B = (2L/\lambda_0)^2$. A close look in (72) reveals that on the contrary to the radiated power expression calculated with the Hertzian electric dipole in (71), the radiated power expression using the magnetic Hertzian dipole is not dependant on the substrate parameters ϵ_r and μ_r for thin substrates. The reason is explained in Appendix B using a transmission line analogy.

The total radiated power of the antenna is the sum of the power radiated by the equivalent electric current and magnetic current densities.

$$P_R = P_R^E + P_R^M \tag{73}$$

where P_R^E and P_R^M are given in Equations (71) and (72), respectively.

Similar to the analysis with the constant current excitation, the effect of increasing the permeability of the substrate can be studied comparing the W_T, P_r, and Q of two patch antennas with the same dimensions but on two different substrates. One of the substrates is chosen as a dielectric substrate with $\epsilon_r = K$, $\mu_r = 1$, while the other one is a magnetic substrate with $\epsilon_r = 1$, $\mu_r = K$. Patch antennas on these substrates are assumed to have the same resonance frequency ω since $\epsilon_r\mu_r = K$ for both cases. Both antennas are excited with the same voltage V_0 between the patch and the ground plane.

4.2.2.1 Dielectric Substrate with $\epsilon_r = K$, $\mu_r = 1$

Let us assume the fields of the patch antenna on this dielectric substrate are labeled as E_1 and H_1. The expressions can be obtained as follows using (68) and (69)

$$E_1 = -\frac{V_0}{h}\cos\left(\frac{\pi x}{L}\right) \tag{74}$$

$$H_1 = -\frac{V_0}{j\omega\mu_0 h}\frac{\pi}{L}\sin\left(\frac{\pi x}{L}\right) \tag{75}$$

The stored electromagnetic energy of the substrate for the patch on the dielectric substrate can also be found using (70) as

$$W_{T1} = \frac{1}{4}K\epsilon_0 WL\frac{(V_0)^2}{h} \tag{76}$$

The radiated powers by equivalent electric and magnetic current densities of the antenna on the dielectric substrate can be calculated using Equations (71) and (72) as

$$P_{R1}^E = 4W^2(V_0^2\frac{\epsilon_0}{\mu_0\lambda_0^2}\left[80\pi^2\left(1 - \frac{1}{K} + \frac{2/5}{K^2}\right)\right]. \tag{77}$$

$$P_{R1}^M = \frac{(V_0)^2 A\pi^4}{23040}\left[(1-B)(1 - \frac{A}{15} + \frac{A^2}{420}) + \frac{B^2}{5}(2 - \frac{A}{7} + \frac{A^2}{189})\right]. \tag{78}$$

The total radiated power of the antenna can then be calculated as

$$P_{R1} = P_{R1}^{E} + P_{R1}^{M}. \tag{79}$$

4.2.2.2 Magnetic Substrate with $\epsilon_r = 1$, $\mu_r = K$

Similar to the dielectric case, substituting the substrate parameters in the corresponding formulas for the interior fields, the stored electromagnetic energy and the radiated power yields

$$E_2 = -\frac{V_0}{h}\cos\left(\frac{\pi x}{L}\right) \tag{80}$$

$$H_2 = -\frac{V_0}{j\omega\mu_0 K h}\frac{\pi}{L}\sin\left(\frac{\pi x}{L}\right) \tag{81}$$

$$W_{T2} = \frac{1}{4}\epsilon_0 WL\frac{(V_0)^2}{h} \tag{82}$$

The radiated powers by equivalent current densities of the antenna on the magnetic substrate can be calculated using Equations (71) and (72) as

$$P_{R2}^{E} = P_{R1}^{E} = 4W^2(V_0^2\frac{\epsilon_0}{\mu_0\lambda_0^2}\left[80\pi^2\left(1 - \frac{1}{K} + \frac{2/5}{K^2}\right)\right] \tag{83}$$

$$P_{R2}^{M} = P_{R1}^{M}\frac{(V_0)^2 A\pi^4}{23040}\left[(1-B)(1 - \frac{A}{15} + \frac{A^2}{420}) + \frac{B^2}{5}(2 - \frac{A}{7} + \frac{A^2}{189})\right] \tag{84}$$

The total radiated power of the antenna on the magnetic substrate can then be calculated as

$$P_{R2} = P_{R2}^{E} + P_{R2}^{M} = P_{R1}. \tag{85}$$

4.2.2.3 Summary of the Constant Voltage Analysis

When two identical patch antennas printed on separate magnetic and dielectric substrates, satisfying $\epsilon_r\mu_r = K$, are excited with the same voltage between the patch and the ground plane, the following observations can be made

1. The electric field amplitudes are equal for both substrates since the excitation voltage has the same amplitude.

$$E_2 = E_1 \tag{86}$$

2. The magnetic field amplitude of the patch antenna on the magnetic substrate is smaller by K compared to the field under the patch on the dielectric substrate.

$$H_2 = \frac{H_1}{K} \tag{87}$$

3. Similar to the magnetic field, the total stored electromagnetic energy is decreased by K in the magnetic substrate.

$$W_{T2} = \frac{W_{T1}}{K} \tag{88}$$

4. The radiated power from the patch is the same for both substrates since the amplitude of the electric field is the same for both cases.

$$P_{R2} = P_{R1} \tag{89}$$

5. Since the radiated power from the patches are the same while the the stored energy decreases by K, the quality factor of the antenna decreases by K compared to that of the patch on the dielectric substrate. Using (88) and (89), the ratio of the quality factors of these two cases can also be obtained as

$$Q_2 = \frac{Q_1}{K} \tag{90}$$

6. The lower quality factor obtained from the patch on the magnetic substrate translates to a higher impedance bandwidth.

The results obtained from the constant voltage analysis is summarized in Figure 69.

As expected, the same Q-factor ratio is found from both cases using the constant current excitation and the constant voltage excitation. It was found that when the antennas are excited with the same current, the amplitude of the E-field in the magnetic substrate is stronger than that of the E-field in the corresponding dielectric substrate. This translates to an increase in both the stored electromagnetic energy and the radiated power of the antenna when the magnetic substrate is used. However, detailed calculations revealed that since

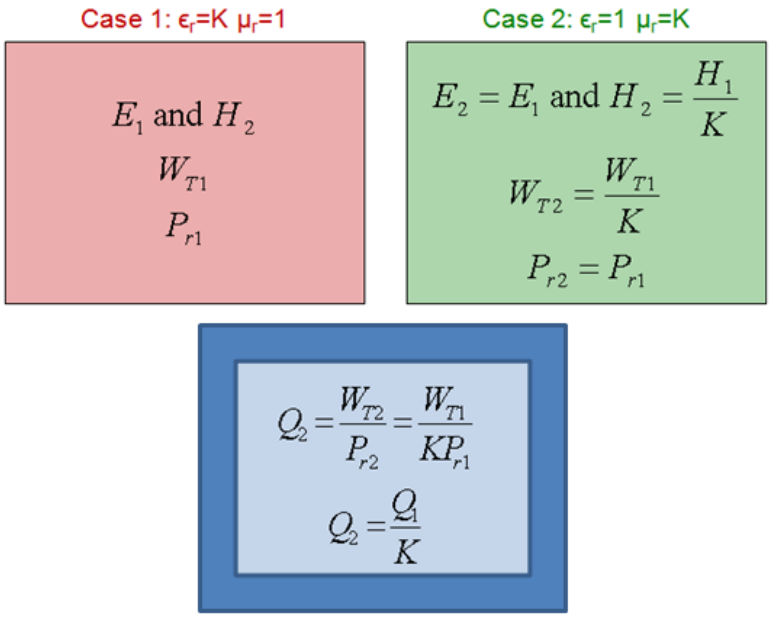

Figure 69. Summary of the constant voltage excitation analysis

the increase in the radiated power is more than the increase in the stored electromagnetic energy, the quality factor of the antenna on the magnetic substrate decreases despite the increase in the stored electromagnetic energy.

The situation is a little different when both antennas are excited with the same voltage. In this case, since the voltage is the same for both antennas the E-field is the same for both antennas. However, it was found that the amplitude of the H-field in the magnetic substrate is smaller than the amplitude of the H-field in the corresponding dielectric substrate. Smaller H-field translates to a smaller stored electromagnetic energy in the magnetic substrate. Since the radiated power is the same for both cases due to the identical E-field strength, the Q of the antenna is smaller for the magnetic substrate.

4.3 Simulations of Microstrip Patch Antennas on Magneto-dielectric Substrates

In addition to the theoretical analysis presented in the previous section, an experimental study based on the simulations of the microstrip patch antennas on finite magneto-dielectric

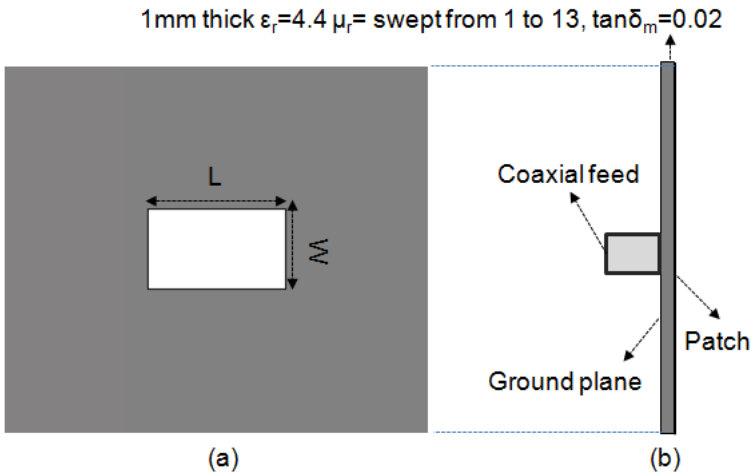

Figure 70. Details of the microstrip patch antenna used in the simulations. (a) Top view, (b) Side view.

substrates has been performed. The simulated results of the peak gain, the percentage bandwidth, the radiation efficiency, and the size of the patch antennas on 1 mm thick substrates with $\epsilon_r = 4.4$ and μ_r ranging from 1 to 13 were compared to investigate the effects of increasing μ_r on the antenna performance. In all cases, the microstrip patch antenna was designed such that only the dominant TM_{10} mode was excited, and the resonance frequency was set at 2.5 GHz. A 50Ω coaxial feed was used for all designs. The ground plane was extended 15 mm beyond each side of the patch for all cases. The details of an example structure is shown in Figure 70.

The results of the simulations for the patch area, percentage bandwidth, the radiation efficiency, and peak gain are presented in Figures 71, 72, 73, and 74 respectively. The values obtained for these parameters for different μ_r of the substrate are also included as a table in each figure. In agreement with the findings of the theoretical analysis explained in the previous section, it was found from the simulations that the effective antenna miniaturization is possible with the use of magneto-dielectric substrates. It was observed that increasing the μ_r of the substrate increases the radiation efficiency, the percentage bandwidth, and the peak gain while decreasing the patch size. As seen in Figure 71, the patch size can be decreased by 90% by increasing the μ_r of the substrate from 1 to 13.

As seen in Figure 72, the percentage bandwidth increases from 2% to 7.3% as μ_r of the

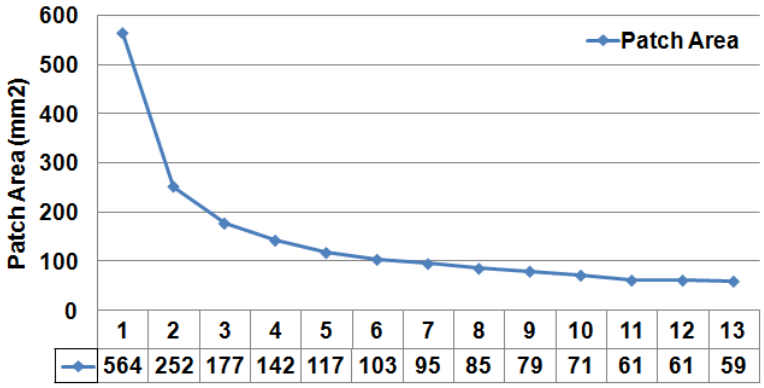

Figure 71. Patch area comparison of the microstrip patch antennas simulated on substrates with ϵ_r = 4.4 and μ_r is swept from 1 to 13.

substrate is increased from 1 to 13. The fundamental limit for the bandwidth calculated by using the minimum achievable quality factor formula derived by McLean [69] is also shown in Figure 72. McLean derived the minimum attainable radiation Q of a linearly polarized antenna in [69] by calculating the radiation Q associated with the TM_{10} or TE_{10} spherical modes. The equation for the minimum attainable Q is modified as follows to account for the losses in the system:

$$Q = \left(\frac{1}{(ka)^3} + \frac{1}{(ka)} \right) \times \eta, \tag{91}$$

where k is the wavenumber in vacuum, a is the radius of the smallest sphere enclosing the antenna, and η is the total efficiency. Using this minimum Q value, an approximation for the maximum VSWR=2:1 (~-10 dB) bandwidth can be found using (50).

While calculating the fundamental limit, the radius of the smallest sphere enclosing the antenna, a, was calculated using two different assumptions. In the first assumption, a was taken as the diagonal length of the patch, and the values are labeled as "Fundamental Bandwidth (1)" in Figure 72 for this assumption. When this assumption is used, the results show that the magneto-dielectric substrates can help to abrogate the fundamental limits on the electrically small antennas, as seen in Figure 72.

In the second assumption, a was calculated by assuming that the diameter of the radiansphere is equal to one third of the diagonal of the ground plane. This assumption is based

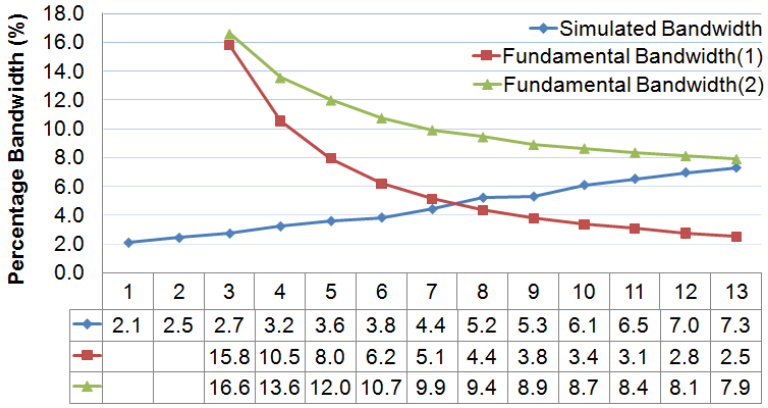

	1	2	3	4	5	6	7	8	9	10	11	12	13
Simulated Bandwidth	2.1	2.5	2.7	3.2	3.6	3.8	4.4	5.2	5.3	6.1	6.5	7.0	7.3
Fundamental Bandwidth(1)			15.8	10.5	8.0	6.2	5.1	4.4	3.8	3.4	3.1	2.8	2.5
Fundamental Bandwidth(2)			16.6	13.6	12.0	10.7	9.9	9.4	8.9	8.7	8.4	8.1	7.9

Figure 72. Percentage bandwidth comparison of the microstrip patch antennas simulated on substrates with $\epsilon_r = 4.4$ and μ_r is swept from 1 to 13. Please note that the fundamental values for $\mu_r = 1$ and $\mu_r = 2$ are not included in the graph since the equations give impractical values for these cases.

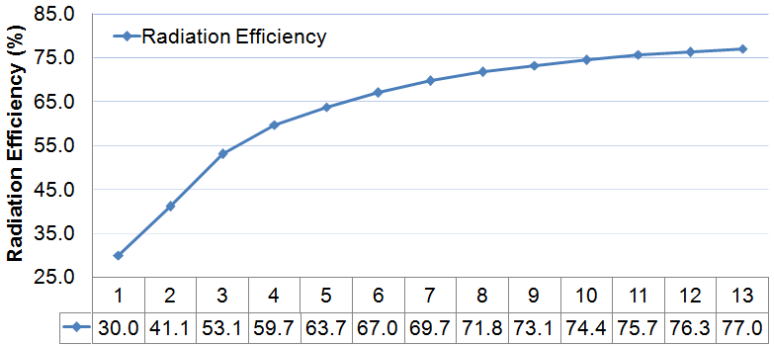

	1	2	3	4	5	6	7	8	9	10	11	12	13
Radiation Efficiency	30.0	41.1	53.1	59.7	63.7	67.0	69.7	71.8	73.1	74.4	75.7	76.3	77.0

Figure 73. Radiation efficiency comparison of the microstrip patch antennas simulated on substrates with $\epsilon_r = 4.4$ and μ_r is swept from 1 to 13.

on the fact that the currents on the ground plane are also contributing to the radiation and they should also be included when determining the size of the antenna. As seen in Figure 72, the simulated values converge to the values calculated with this assumption, labeled as "Fundamental Bandwidth (2)" in the figure. This is a more reliable comparison since the fundamental limits should not be dependent on the permeability of the substrate. It should also be mentioned that as the permeability is increased beyond 13, the bandwidth keeps the increasing trend. However, it was observed that higher order TM_{20} mode also gets excited and the comparison with the fundamental limits is not possible for these multi-mode cases.

The radiation efficiency of the antenna was also studied, and it was observed that the radiation efficiency increases as μ_r of the substrate increases.

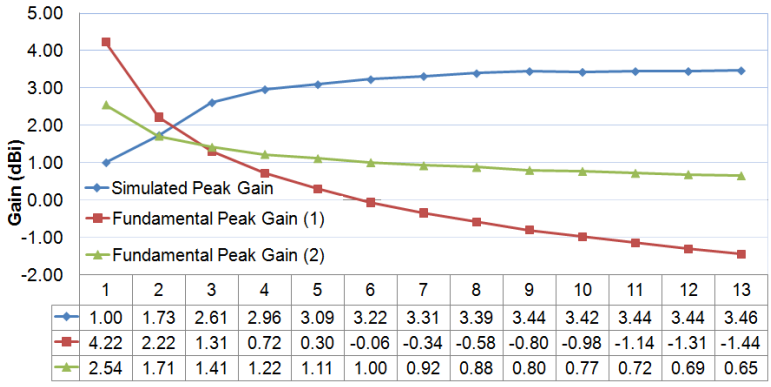

	1	2	3	4	5	6	7	8	9	10	11	12	13
Simulated Peak Gain	1.00	1.73	2.61	2.96	3.09	3.22	3.31	3.39	3.44	3.42	3.44	3.44	3.46
Fundamental Peak Gain (1)	4.22	2.22	1.31	0.72	0.30	-0.06	-0.34	-0.58	-0.80	-0.98	-1.14	-1.31	-1.44
Fundamental Peak Gain (2)	2.54	1.71	1.41	1.22	1.11	1.00	0.92	0.88	0.80	0.77	0.72	0.69	0.65

Figure 74. Peak gain comparison of the microstrip patch antennas simulated on substrates with $\epsilon_r = 4.4$ and μ_r is swept from 1 to 13.

Similar to the bandwidth, the antenna gain was also compared with the fundamental limit calculated using the normalized gain formula derived by Harrington [70], repeated as follows:

$$G = (ka)^2 + 2ka, \tag{92}$$

where k and a are defined as in (50). The same assumptions employed for the bandwidth case were used to estimate the radius of the radiansphere. As seen in Figure 74, the simulated gain values exceed the fundamental gain values calculated using (92). However, it should be noted that the normal gain defined in (92) provides an absolute upper limit to the gain of the antenna for the antennas with moderate Q values. The antennas compared in this study have high Q values which may invalidate the applicability of (92).

As seen from the table in Figure 74, the peak gain of the antenna increases and nearly converges to 3.45dBi as the μ_r of the substrate is increased. Although it is not shown in Figure 74, the peak gain starts to decrease as μ_r is increased beyond 15. This decrease in the gain can be explained considering the radiation pattern comparison of the antennas, shown in Figure 75. As seen from the radiation patterns, in addition to the broadside peak gain, the back-scattering of the antenna also increases as μ_r of the substrate is increased. This shows that the surface wave propagation becomes stronger with increasing μ_r. The analysis of surface wave propagation on conductor-backed magneto-dielectric substrates is discussed in the next section.

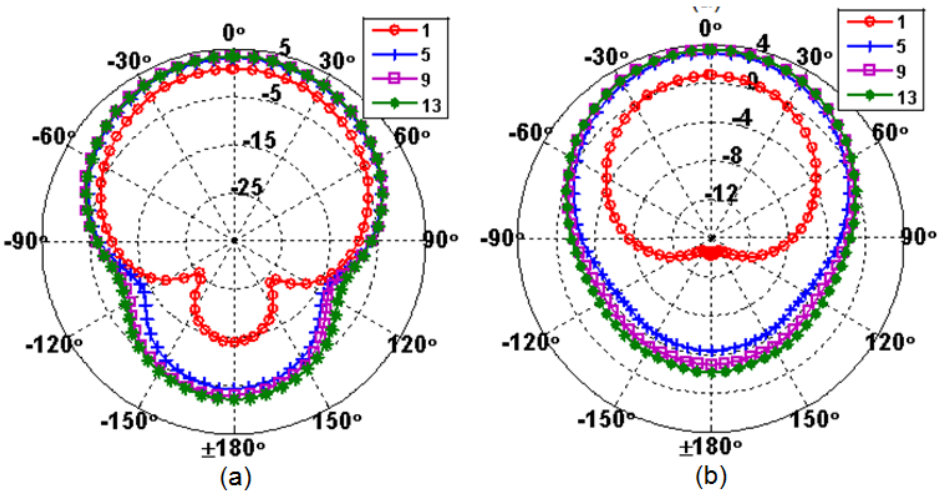

Figure 75. Radiation pattern comparison of the microstrip patch antennas simulated on substrates with $\epsilon_r = 4.4$ and μ_r is swept from 1 to 13. (a) E plane, (b) H plane.

4.4 Surface Wave Analysis of Conductor-backed Magneto-dielectric Substrates

Printed antennas excite surface waves which can be defined as the wave propagation along the boundary of the conductor-backed substrate and the air medium. It is critical to characterize the surface wave propagation and the power carried with these waves since it constitutes a significant amount of the loss in an antenna. Moreover, surface wave propagation is the main cause of the undesired coupling between the neighboring RF components. Surface waves are also responsible for deteriorating the far field pattern of the antenna since they diffract as they reach the edges of the substrate.

Although full-wave electromagnetic simulations include the effect of the surface waves in the solved fields, it is useful to analyze the surface wave propagation analytically since the analytical expressions can provide more insight. Conductor-backed dielectric substrates have been studied before and approximate expressions for the surface wave power can be found in [71], [72], and [65]. In this section, the analysis of the surface wave power in a conductor-backed magneto-dielectric substrate is presented. The analysis presented in this section follows the derivation in [71], and the results are obtained from the exact Green's function for the conductor-backed magneto-dielectric substrate.

4.4.1 Surface Wave Power of a Hertzian Dipole on a Conductor-backed Magneto-dielectric Substrate

The spectral domain Green's functions for the microstrip geometries have been derived and presented in the literature to analyze the surface wave modes excited in the substrates. For instance, the surface wave power due to a horizontal electric dipole on top of a conductor-backed dielectric was analyzed in [71], using the spectral-domain Green's function to derive the exact and approximate expressions depending on the substrate parameters. A similar analysis is presented in this section for the conductor-backed magneto-dielectric substrates.

The derivation of the spectral Green's function for a conductor-backed magneto-dielectric substrate is presented in Appendix C. The x-directed electric field at (x, y, h) on the surface of a conductor-backed magneto-dielectric slab caused by a Hertzian electric dipole current at (0, 0, h) can be expressed as (Eq. (201) in Appendix C)

$$E_{xx} = \frac{1}{4\pi^2} \int_{-\infty}^{\infty} \int_{-\infty}^{\infty} \tilde{Z}_{xx} e^{jk_x x} e^{jk_y y}\, dk_x\, dk_y \tag{93}$$

where

$$\tilde{Z}_{xx} = \frac{-jZ_0 \sin(k_1 h)}{k_0 \beta^2} \left[\frac{k_x^2 k_1 k_2}{T_m} + \frac{\mu_r^2 k_0^2 k_y^2}{T_e} \right] \tag{94}$$

$$T_m = \epsilon_r k_2 \cos(k_1 h) + j k_1 \sin(k_1 h) \tag{95}$$

$$T_e = k_1 \cos(k_1 h) + j \mu_r k_2 \sin(k_1 h) \tag{96}$$

$$k_1^2 = \epsilon_r \mu_r k_0^2 - \beta^2 \tag{97}$$

$$k_2^2 = k_0^2 - \beta^2 \tag{98}$$

$$\beta^2 = k_x^2 + k_y^2 \tag{99}$$

$$Z_0 = \sqrt{\mu_0 / \epsilon_0} \tag{100}$$

E_{xx} denotes the x component of the E-field caused by an x-directed Hertzian dipole on the $z = h$ plane. There is no loss of generality by choosing the x-directed current. It should be noted that the integral in Eq. (93) is defined over the entire spectral domain, and

it is critical to pay attention to the singular points, where T_m and T_e functions forming the denominator of the Green's function have zeros. As defined in Equations 96 and 95, T_m and T_e are functions of β, and their zeros represent the transverse magnetic (TM) and transverse electric (TE) surface wave poles [73]. For the lossless substrates, as the one considered in this analysis, the surface wave poles occur for real $\beta = \beta_0$ values and positioned in the $k_0 \leq \beta_0 < \sqrt{\epsilon_r \mu_r} k_0$ interval on the real β axis.

The first TM surface wave mode, designated as TM_0 mode, has a zero cutoff frequency so it is always excited when $\epsilon_r > 1$. Therefore, there is at least one surface wave pole associated with this mode. The cutoff frequencies for the first TE mode and higher order TM modes are usually in the millimeter wave range and are neglected in this analysis for simplicity.

The power carried by the E-field can be found as follows:

$$P_T = -Re\left\{\int_S E_{xx} J_s \, dS\right\} \tag{101}$$

where J_s is the infinitesimal current of the Hertzian dipole at (0, 0, h)

$$J_s = \delta(x)\delta(y) \tag{102}$$

Substituting (93) in (101) yields

$$P_T = \frac{-1}{4\pi^2} Re\left\{\int\int Z_{xx}(k_x, k_y)\, dk_x\, dk_y\right\}. \tag{103}$$

Applying the following transformation:

$$k_x = \beta \cos\phi \tag{104}$$

$$k_y = \beta \sin\phi$$

to the integral in (103) gives

$$P_T = \frac{-1}{4\pi^2} Re\left\{\int_{\phi=0}^{2\pi}\int_{\beta=0}^{\infty} Z_{xx}(\phi, \beta)\beta \, d\beta \, d\phi\right\} \tag{105}$$

The limits for the β integral in (105) is $0 < \beta < \infty$. Since this range includes the surface wave pole for the TM_0 mode, some adjustments are needed to calculate the integral. First, assuming the pole corresponding to the TM_0 mode occurs for β_0, the integration in (105) can be divided into three integrals as follows [73]:

$$\int_{\phi=0}^{2\pi}\int_{\beta=0}^{\infty}(\,)\,d\beta\,d\phi = \int_{\phi=0}^{2\pi}\left\{\int_{0}^{\beta_0-\delta}(\,)\,d\beta + \int_{\beta_0-\delta}^{\beta_0+\delta}(\,)\,d\beta + \int_{\beta_0+\delta}^{\infty}(\,)\,d\beta\right\}d\phi. \tag{106}$$

Applying this method to (105) results in three integrals. The first integral with limits $0 \le \beta < \beta_0 - \delta$ corresponds to the power carried by the space waves, i.e. radiated power. The second integral gives the surface wave power since the limits for this integral is in the vicinity of β_0. Since the aim of this analysis is to find the surface wave power, the second integral is calculated in Appendix D to yield the following expression for surface wave power, assuming the surface wave pole occurs at $\beta_0 = x_0 k_0$:

$$P_{sw} = \frac{Z_0 k_0^2}{4}\frac{\epsilon_r(x_0^2-1)}{(k_0h)\left[1+\dfrac{\epsilon_r^2(x_0^2-1)}{(\epsilon_r\mu_r - x_0^2)}\right] + \epsilon_r\left[\dfrac{\sqrt{x_0^2-1}}{(x_0^2-\epsilon_r\mu_r)} + \dfrac{1}{\sqrt{x_0^2-1}}\right]} \tag{107}$$

The result obtained for P_{sw} is exact if x_0 is the exact value. The exact value can be obtained through a root finding algorithm which usually requires an iterative approach and an initial value. A close approximation can be obtained using a Taylor series expansion for T_m.

If the substrate is electrically thin and lossless, it is expected that $\beta_0/k_0 = x_0 \approx 1$. The value of x_0 can then be approximated as $x_0 = 1 + \delta$. Substituting x_0 into $T_m = 0$ yields

$$T_m = \epsilon_r k_2 + jk_1\tan(k_1h) = 0 \tag{108}$$

$$= \epsilon_r\sqrt{2\delta+\delta^2} - \sum_{n=0}^{\infty}\alpha_n\delta^n = 0 \tag{109}$$

where the infinite sum is a Taylor series representation for $k_1\tan(k_1h)$ around the point

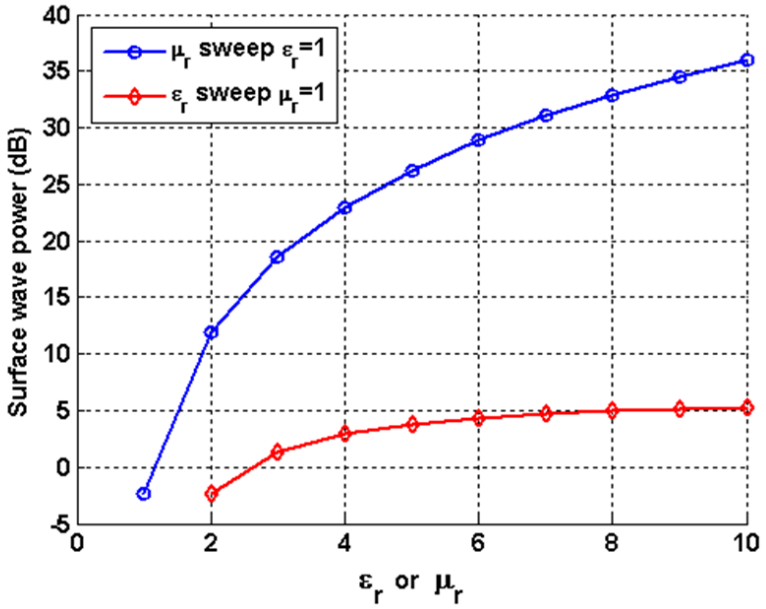

Figure 76. Calculated surface wave power for dielectric and magnetic substrates.

$x_0 = 1$. The first few coefficients of the infinite sum can be defined as

$$\alpha_0 = s\tan(k_0 hs) \tag{110}$$

$$\alpha_1 = -\frac{1}{s}\left[\tan(k_o hs) + \frac{k_0 hs}{\cos^2(k_0 hs)}\right] \tag{111}$$

$$s = \sqrt{\epsilon_r \mu_r - 1} \tag{112}$$

Using two-term expansion yields

$$x_0 = 1 + \frac{\alpha_0\alpha_1 - \epsilon_r^2 + \epsilon_r\sqrt{\epsilon_r^2 - 2\alpha_0\alpha_1 + \alpha_0^2}}{\epsilon_r^2 - \alpha_1^2} \tag{113}$$

Substituting Eq. (113) in (107) the surface wave power was calculated for different dielectric and magnetic substrates, where ϵ_r and μ_r were swept. Figure 76 shows the calculated results for 0.5 mm thick substrates at 2.5 GHz. The thickness value was chosen so that the approximation for x_0 is valid for the ranges of ϵ_r and μ_r sweeps.

As expected, surface wave power increases when either the permeability or the permittivity is increased. This can be explained intuitively with the increase in the electrical thickness of the substrate as ϵ_r or μ_r is increased. A more interesting observation that can

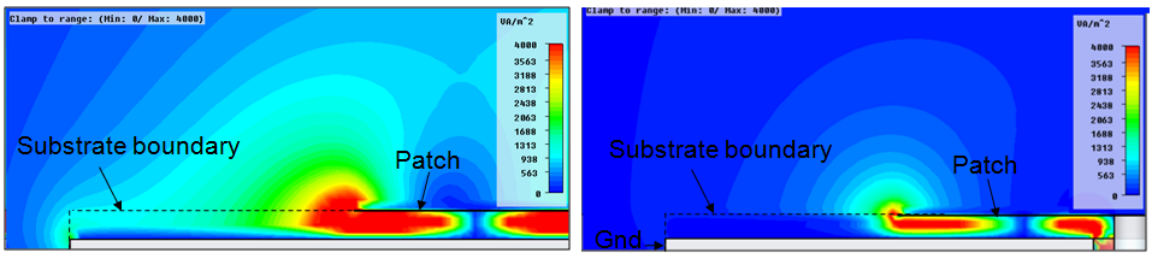

Figure 77. Power flow graph of the surface waves excited by patch antennas on a magnetic ($\epsilon_r = 1$ $\mu_r = 12$) **and a dielectric substrate** ($\epsilon_r = 9$ $\mu_r = 1$)**. The graphs are plotted on the cross-sections of the substrates, and the substrates are truncated in the figure for a closer view. (a) Magnetic substrate, (b) Dielectric substrate.**

be made from Figure 76 is that the surface wave power increases faster with increasing permeability than the increasing permittivity. This can be explained by considering the surface wave impedance of the substrate. Surface wave impedance of a lossless conductor-backed substrate can be approximated with

$$Z_s = j\eta \tan(\beta h) \tag{114}$$

where $\eta = \sqrt{(\mu_r \mu_0)/(\epsilon_r \epsilon_0)}$ is the wave impedance in the substrate, β is the propagation constant, and h is the thickness of the substrate. As permeability is increased both $tan(\beta h)$ and η increases; whereas, when permittivity is increased only $tan(\beta h)$ term increases while η decreases. TM mode surface waves require an inductive surface wave impedance [74]. Therefore, they propagate further into the substrate carrying more power as the surface wave impedance becomes more inductive with increasing permeability.

Figure 77 shows the power flow graphs of two patch antennas designed on 1 mm thick dielectric ($\epsilon_r = 9$ $\mu_r = 1$) and the corresponding magnetic ($\epsilon_r = 1$ $\mu_r = 12$) substrates. The permittivity and the permeability of the substrates are chosen such that both antennas resonate at 3 GHz with the same patch size. The simulations were done using the CST. As seen from the power flow plots on the cross-sections of the substrate, the power flow is stronger even inside the magnetic substrate; whereas, it is confined only to the surface of the dielectric substrate, supporting the conclusions drawn earlier.

Power flow graphs were also compared along the substrate and Figure 78 displays the

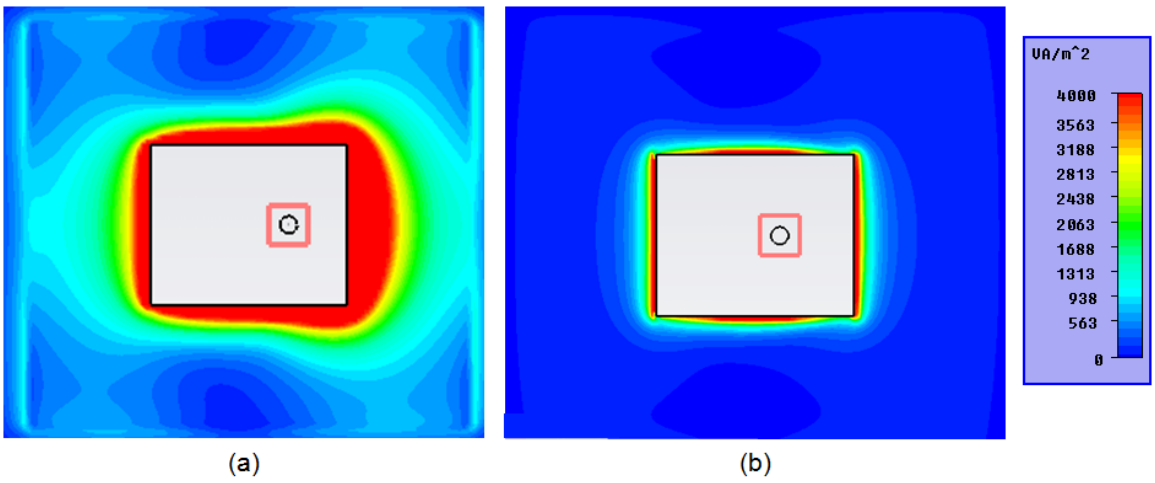

Figure 78. Power flow graph of the surface waves excited by patch antennas on a magnetic ($\epsilon_r = 1$ $\mu_r = 12$) and a dielectric substrate ($\epsilon_r = 9$ $\mu_r = 1$). The graphs are plotted on the along the substrates. (a) Magnetic substrate, (b) Dielectric substrate.

power flow graphs plotted on $z = h/2$ planes. The difference between the magnetic and the dielectric substrates can be clearly seen in the figure. Power flow along the magnetic substrate is much stronger compared to the dielectric cases where most of the fields are confined under the patch antenna.

Increased surface wave power due to the increasing permeability of the substrate is critical and should be handled carefully while using the magneto-dielectric substrates. The radiation of the surface waves from the edges causes back-radiation, which can be considered to emulate a monopole-like radiation pattern as in the case of a surface wave antenna [75]. Moreover, when the ground plane size is properly adjusted, the diffracted surface waves can contribute to the antenna radiation, which can improve the overall gain of the antenna. This can be a way to compensate for the expected decrease in the gain of the antenna as the antenna size is miniaturized. On the other hand, if the size of the ground plane is not adjusted properly, the diffracted surface waves can add onto the radiated fields of the antenna destructively, resulting in a poor radiation. Moreover, surface waves can increase the coupling between the antenna and the other antenna elements or the circuitry integrated on the same substrate. Surface-wave mitigation techniques may be required to prevent undesired coupling.

4.5 Conclusions

Magneto-dielectric substrates have been proposed for the efficient miniaturization of antennas. In this chapter, the question why magneto-dielectric substrates are better substrates than the dielectric substrates has been answered through theoretical and experimental analyses. The limitations of these substrates have also been discussed in this chapter. The conclusions drawn from the presented analyses are summarized in this section.

The theoretical analysis on microstrip patch antennas printed on a dielectric and the corresponding magnetic substrate that gives the same miniaturization factor revealed that increasing the permeability of the substrate is more advantageous to miniaturize the antenna instead of increasing the permittivity of the substrate. It was found that increased permeability helps to improve the bandwidth of the antenna while miniaturizing the antenna. This is especially valid for the conductor-backed resonator type antennas since the fields are confined mostly in the substrate for these antennas, making the near-fields of the antenna depend strongly on the substrate parameters. However, increasing permeability or the permittivity of the substrate is not as effective of a solution for miniaturizing printed monopole antennas without backing ground conductor since the substrate is usually thin compared to surrounding air substrate, resulting in low effective permittivity and permeability.

As expected, similar results were obtained from the experimental study based on the full-wave electromagnetic simulations of microstrip patch antennas on magneto-dielectric substrates. In the simulations, several antennas were designed on substrates with the same permittivity but different permeability. In addition to the supporting evidence on the improved bandwidth of the antenna, the full-wave simulations revealed that the back radiation of the antenna increases as the permeability of the substrate is increased. It was also found interestingly that increasing permeability of the substrate helped to increase the peak gain of the antenna although the patch size was miniaturized at the same time.

The reason for this observation has been explained in this chapter with the surface

wave power that becomes stronger as the permeability of the substrate is increased. Although this is similar to the case with the dielectric substrates, it was found through further theoretical analysis that surface wave power increases at a faster rate with the increased permeability than with the increased permittivity. This is a critical characteristic of the magneto-dielectric substrates which should be handled properly when these substrates are used for antenna applications.

The increased surface wave of the antenna can be advantageous or disastrous as far as the far field of the antenna is considered. This is because if the size of the ground plane is adjusted properly, the increased surface wave radiation can be diffracted from the edges of the substrate to add constructively with the radiation of the antenna, resulting in a higher gain of the antenna. Moreover, increased back-radiation can be used to emulate the radiation pattern of a monopole antenna. However, if the ground size is not adjusted properly, the diffracted surface wave radiation may cancel the antenna fields, resulting in low gain values. Surface wave propagation can also limit the integration of the multiple antennas on the same substrate due to the increased coupling through surface waves. The diffraction of the surface waves from the edges of the truncated conductor-backed magneto-dielectric substrates may be studied in more detail as a part of future work. Finding design guidelines on the size and shape of the ground plane (circular, rectangular etc.) to optimize the radiation parameters of the antenna can also be targeted as a part of future work.

In conclusion, the advantages and limitations of the magneto-dielectric substrates can be listed as follows:

1. Increasing the permeability of the substrate is more advantageous than increasing the permittivity of the substrate since the antenna can be miniaturized without deteriorating the bandwidth of the antenna.

2. Using magneto-dielectric substrates for effective miniaturization of the antenna is only valid for resonant type antennas with a backing ground plane. This method is not as effective for printed monopole antennas without a backing conductor.

3. Although magneto-dielectrics are effective in antenna miniaturization, synthesizing materials with low magnetic loss is difficult. The simulations on patch antennas have showed that the total loss of the substrate should be on the order of a loss tangent around 0.02 to ensure effective radiation of the antenna.

4. Strong surface wave propagation in magneto-dielectric substrates can be advantageous or disadvantageous. The effect of the surface waves on the radiation pattern of the antenna should be optimized by selecting the size and the shape of the ground plane carefully.

5. Strong surface wave propagation may limit multiple antenna integration or integration of the antenna on the module package due to increased coupling between the components. Co-design of the antenna along with other components is indispensable for these cases.

CHAPTER 5

MINIATURIZATION OF REACTIVE IMPEDANCE SURFACES WITH MAGNETO-DIELECTRIC SUBSTRATES

Printed planar antennas are highly preferred in mobile systems because of their characteristics such as ease of fabrication and integration, compactness and low profile. Moreover, backing the planar antenna with a ground plane, as in the case of a microstrip patch antenna, offers increased front-to-back ratio, while shielding the rest of the system from the fields of the antenna. On the other hand, planar antennas printed on metal-backed substrates have limited bandwidth and efficiency. This is because of the cancelation of the radiated fields of the antenna with the fields of the image current that is in close proximity and opposite to the antenna current. This results in increased stored electromagnetic energy which causes narrow bandwidth and low efficiency.

High impedance surfaces and reactive impedance surfaces (RIS) have been extensively studied to alleviate the image cancelation problem of the low-profile antennas [76], [74]. This method has been especially applied to the antennas on high permittivity substrates since the miniaturization of the antenna and the RIS can be achieved simultaneously. However, it was shown in [77] that miniaturizing these surfaces with the high-permittivity substrates results in narrow reflection phase bandwidth, limiting the application of these surfaces.

Magneto-dielectric materials, defined as materials with $\epsilon_r > 1$ and $\mu_r > 1$, have been introduced and raised hope to overcome the difficulties encountered in the miniaturization of electromagnetic structures with the high-permittivity dielectrics [78]. Although these materials do not exist in nature, recent developments in material synthesis technologies have shown promising results based on nano-magnetic compounds, as discussed in Chapter 3 of this thesis.

In this chapter, the application of the magneto-dielectric substrates to miniaturize the

reactive impedance surfaces is investigated conceptually with the advantages of these materials over the high-permittivity materials. The reflection phase comparison of a planar reactive impedance surface with the well-known mushroom type high impedance surface [74] on a low-profile substrate is also included in the chapter. Additionally, the application of the miniaturized reactive impedance surfaces to the low-profile microstrip patch antenna designs is investigated in this chapter.

5.1 Reactive Surface Impedance Concept

Conductor-backed planar antennas are preferable in highly-integrated advanced packaging technologies to achieve the compact integration with the rest of the circuitry due to their advantages such as low-profile, low-cost, ease of fabrication and integration. Although conductor-backed substrates for planar antennas help to achieve the desired front-to-back ratio values, they are also responsible for the limited bandwidth and efficiency of the antennas. This problem is a result of the cancellation of the antenna fields with the fields of the image which is in close proximity and opposite in direction to the antenna's electric current. This strong coupling between the antenna and its image in turn results in an increased stored electromagnetic energy leading to low-efficiency and narrow-bandwidth of the antenna [76].

In efforts to alleviate this problem, high-impedance surfaces and artificial perfectly magnetic conductors (PMC) have been developed [74]. Since the image of the horizontal electric current in close proximity of the PMC surface is in-phase and parallel to the original electric current, the radiated fields from both of these sources add constructively resulting in the desired radiation characteristics. Moreover, the input impedance of the antenna increases making it easier to match the antenna resulting in a wider bandwidth. However, since the coupling between the antenna and the image is strong as in the case of perfect electric conductor (PEC) surfaces, the stored electromagnetic energy is still considerably high for PMC ground planes [76].

Another alternative to the conventional conductor ground plane of an antenna is called a reactive impedance surface (RIS). The work by Mosallaei and Sarabandi in [76] has showed that the interaction between the antenna current and the image current can be optimized when the surface impedance of the substrate is adjusted to a certain imaginary impedance. The work in [76] is based on the findings of an earlier publication by Sarabandi [79] where the fields of the horizontal and vertical dipole antennas placed on top of a surface with an arbitrary impedance have been derived using the exact image formulation. It has been shown in this paper that, if the surface has a moderate value of purely reactive surface impedance, the interaction between the image and the original antenna current is considerably reduced since the image current has a sinusoidal form and instead of being focused at point $-z'$ close to the source, it is distributed along the line $-z' + j\xi$, assuming the antenna current is placed at z'.

Another work on RIS by Yang et.al in [77] supported these findings and showed that replacing the metal ground plane with an RIS helps to improve the gain and the bandwidth of the low-profile antenna, when the frequency band of the antenna coincides with the reflection phase band of the RIS. The reflection phase bandwidth is defined as the frequency band, where the phase of the reflected E field for normal incidence on the surface is between -45° to $+45^\circ$.

Since the most fundamental structure with a reactive surface impedance is a conductor-backed substrate, the reflection phase characteristics of the conductor-backed magneto-dielectric substrates are analyzed in the next section. Another way to emulate the effects of the reactive impedance surfaces is to use periodic surfaces with resonating equivalent circuits. An example of these surfaces and their miniaturization with magneto-dielectric substrates is covered in the following sections.

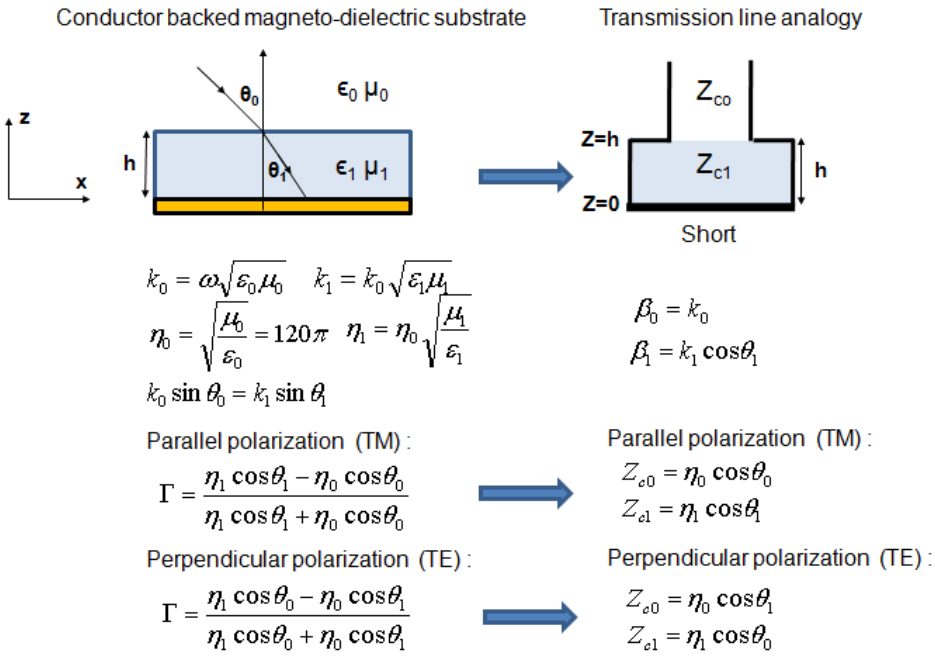

Figure 79. Transmission line analogy used to find the frequency characteristics of a conductor-backed magneto-dielectric substrate.

5.2 Conductor-backed Magneto-dielectric Substrate

Although a conductor-backed dielectric substrate has a reactive surface impedance, the thickness of the substrate needs to be at least one quarter-wavelength, $\lambda_g/4$, to observe the constructive radiation from the image of the antenna current. This results in impractical thicknesses with the preferred low-permittivity substrates especially at the low GHz frequencies that are of interest for most mobile applications.

On the other hand, the conductor-backed magneto-dielectric substrates can provide the desired reactive impedance characteristics with moderate thickness values, even at low GHz frequencies, as a result of the increase in the surface impedance as the relative permeability of the substrate is increased. This can be explained considering the reflection phase characteristics of magneto-dielectric substrates using a transmission line analogy as shown in Figure 79. In this analogy, the substrate medium and the air medium are both modeled as cascaded transmission lines loaded with a $Z_L = 0$ short-circuit load modeling the backing conductor.

In Figure 79, the TE and TM cases represent two different polarizations of the E-field, where the E-field is normal and parallel to the x-z plane, respectively. Using the analogy in Figure 79, the reflection phase response of the magneto-dielectric substrate can be derived for oblique incidence, where the angle of the incident field with the normal is denoted as θ_0. The reflection coefficient at $z = h$ can be derived as follows by calculating the input impedance of a shorted transmission line:

$$Z_{in}^{TE,TM} = jZ_{c1}^{TE,TM} \tan(\beta_1 h) \tag{115}$$

$$\Gamma^{TE,TM} = \frac{Z_{in}^{TE,TM} - Z_{c0}^{TE,TM}}{Z_{in}^{TE,TM} + Z_{c0}^{TE,TM}} = \rho \exp(j\Phi), \tag{116}$$

where Z_{c0}, Z_{c1}, β_1, and h are defined in Figure 79. Once the corresponding Z_{c0} and Z_{c1} for TE and TM polarizations are substituted in Eq. (115) and Eq. (116) from Figure 79, the reflection phase of the magneto-dielectric substrate is equal to the argument of the reflection coefficient ,Φ.

The case of normal incidence is more critical for antenna applications. $Z_{c0}^{TE,TM}$, $Z_{c1}^{TE,TM}$ and $Z_{in}^{TE,TM}$ can be simplified to the following for normal incidence, where $\theta_0 = \theta_1 = 0$:

$$Z_{c0}^{TE,TM} = \eta_0 \tag{117}$$

$$Z_{c1}^{TE,TM} = \eta_1 \tag{118}$$

$$Z_{in}^{TE,TM} = j\eta_1 \tan(\beta_1 h). \tag{119}$$

In these equations, η_0 and η_1 are the wave impedances of the vacuum and the magneto-dielectric substrate as defined in Figure 79. Substituting these values into Eq. (116) reduces that equation to

$$\Gamma_{nor}^{TE,TM} = \frac{j\eta_1 \tan(\beta_1 h) - \eta_0}{j\eta_1 \tan(\beta_1 h) + \eta_0} = \rho_{nor} \exp(j\Phi_{nor}), \tag{120}$$

where Φ_{nor} is equal to the reflection phase for the normal incidence. The reflection phase responses of the magneto-dielectric substrates with $\epsilon_r = 4.4$ and $\mu_r = 5, 9$, and 13 were compared with that of the dielectric substrate with $\epsilon_r = 4.4$ by calculating Φ_{nor} in Eq. (120). As

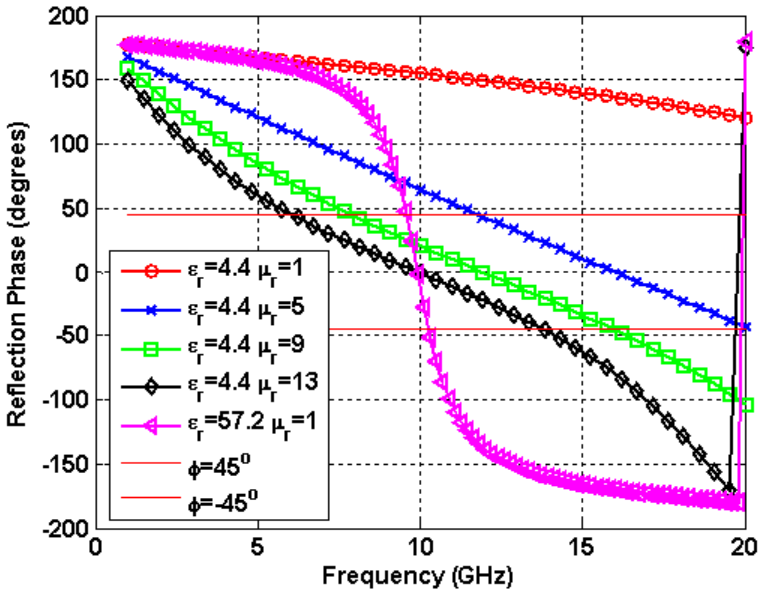

Figure 80. Reflection phase curves for several magneto-dielectric and dielectric substrates.

seen in Figure 80, the percentage reflection phase bandwidth of the substrate increases with increasing permeability. The reflection phase bandwidth was accepted as the frequencies corresponding to the angles between $+/-45^\circ$ [77]. In addition, the zero-reflection-phase frequency decreases as μ_r is increased since the guided wavelength decreases. The zero-reflection-phase frequency can be defined as the frequency at which the substrate acts like a PMC when thickness of the substrate, h, is equal to a quarter of the guided wavelength.

The reflection phase curve of the dielectric with $\epsilon_r = 13 \times 4.4 = 57.2$ was also calculated and is shown in Figure 80 for comparison. The zero-reflection-phase frequency of this dielectric is the same with that of the magneto-dielectric with $\epsilon_r = 4.4$ and $\mu_r = 13$ since the guided wavelength is the same for these two cases. As seen in the figure, the magneto-dielectric substrate provides a wider bandwidth compared to the high permittivity substrate with $\epsilon_r = 57.2$.

It can be concluded that conductor-backed magneto-dielectrics make better substrates for the planar antennas compared to the dielectrics due to their high reactive surface impedance. It is expected that the efficiency, bandwidth, and gain of a planar antenna on a magneto-dielectric substrate are higher than those of an antenna on a dielectric substrate

since the mutual coupling between the antenna current and the image with respect to the ground plane is optimized, resulting in decreased stored electromagnetic energy. These results agree with the results from Chapter 4 of this thesis.

5.3 Reactive Impedance Surfaces with Periodic Unit Cells

The advances in material synthesis technology may allow us to control the ϵ_r and μ_r of the materials in the future. If this becomes possible, these values can be adjusted for each antenna design, such that the preferred reactive impedance surface behavior can be obtained within the bandwidth of the antenna. Until this becomes possible, reactive impedance behavior can be emulated using periodic surfaces.

5.3.1 Structure Description

Two surfaces with reactive surface impedance were studied in this research. The first design, labeled as Design 1, is composed of two metal layers, as shown in Figure 81a. The top layer is comprised of metal patch islands, whereas the bottom layer is a solid metal plane. This structure was first proposed in [74], and it was further analyzed in [76], where its application to a microstrip patch antenna design was discussed. In [76], a high-permittivity substrate was used to miniaturize this reactive surface. However, as discussed in the previous section, using the high-permittivity substrates results in narrow reflection phase bandwidths, limiting the application of these surfaces.

Design 2 is the well-known mushroom type electromagnetic band-gap structure, which is similar to Design 1 with additional vias connecting the top and bottom metal layers, as shown in Figure 81b. This structure has been analyzed in [74]. Although the vertical via connections are essential to prevent surface wave propagation, the fabrication of this structure is more complicated as a result.

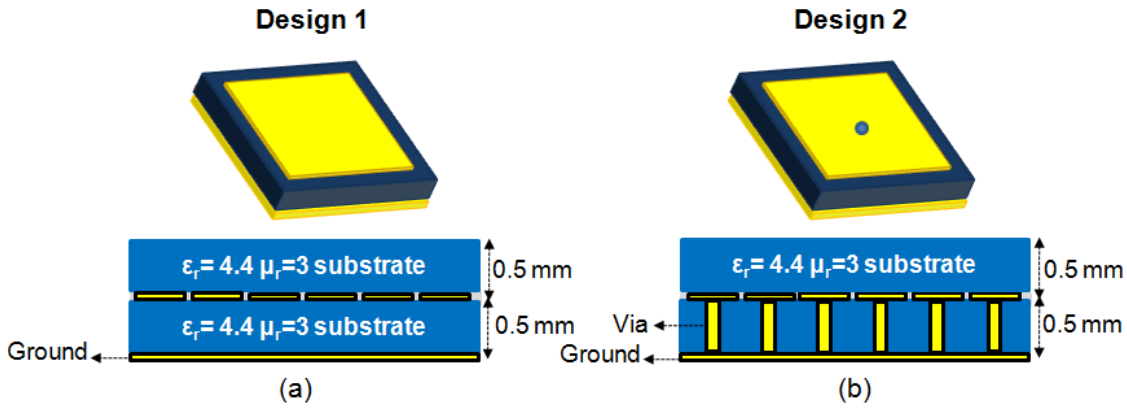

Figure 81. Periodic reactive impedance surfaces investigated in this research. (a) Design 1, (b) Design 2.

5.3.2 Simulating the Reflection Phase Characteristics

The reflection phase characteristics of the high impedance surface was simulated using the unit cell model in CST MWS. The simulation model is shown in Figure 82a. As shown in the figure, the four vertical walls of the air box are set as the unit cell boundary, which replicates the unit cell vertically and horizontally. The top wall boundary was set as a Floquet port, where only the first fundamental mode propagation is excited to model the plane wave incidence. The bottom boundary was set as the PEC boundary to model the bottom layer of the simulated unit cell. The effect of a superstrate, to model the effect of a possible antenna substrate, was also taken into account in the simulations by including the superstrate on the top metal layer.

The reflection phase data was calculated from the post-processing of the simulated S-parameter data. In this setup, the phase of the simulated S_{11} is equal to the phase of the reflected E-field since the phase of the incident field is set to 0°. Next, the structure is calibrated using the reflection from a PEC surface with the same incident field from the same port location, d, as shown in Figure 82a. The reflected phase of a PEC surface can be calculated by using Eq. (121):

$$\Phi_{pec} = 180^\circ - 2\frac{d}{\lambda}360^\circ, \tag{121}$$

where d is determined from the simulation setup. Calibrating the reflected phase from the

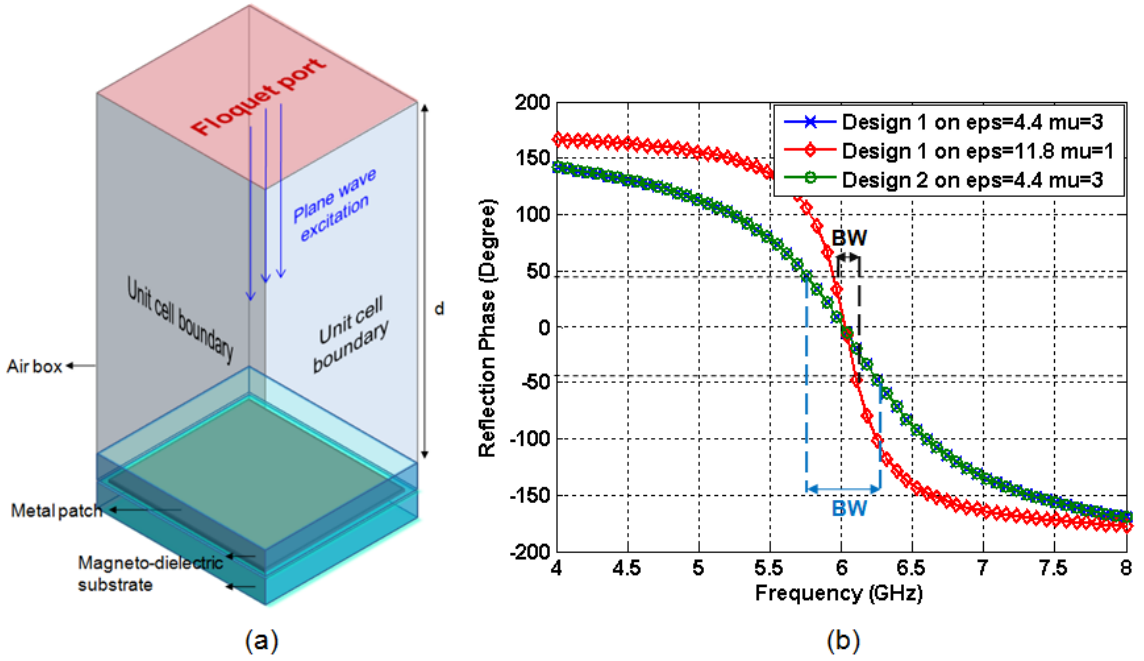

Figure 82. (a) Unit cell simulation setup in CST MWS used to obtain the reflection phase response of the reactive surfaces. (b) The reflection phase response for Design 1 and Design 2 with a=b=4mm on different substrates.

unit cell with the reflected phase of the PEC surface removes the phase difference added while the field propagates through the air box.

5.3.3 Miniaturization of the RIS

The efficient miniaturization of the reactive impedance surfaces means achieving larger reflection phase bandwidth with smaller unit cells printed on thin substrates. The reason that increasing the permeability of the substrate helps to achieve this goal can be explained by considering the equivalent unit circuit of the structure. As displayed in Figure 83, the equivalent circuit of Design 1 is comprised of a parallel tank circuit, where the coupling through the gap between patches is modeled as a capacitance, and the impedance of the grounded substrate is modeled as an inductor. The unit circuit of Design 2 has additional inductance introduced by the via connection [74]. The reflection phase bandwidth of the parallel tank circuit can be found to be proportional to the ratio $\sqrt{L/C}$, where L denotes

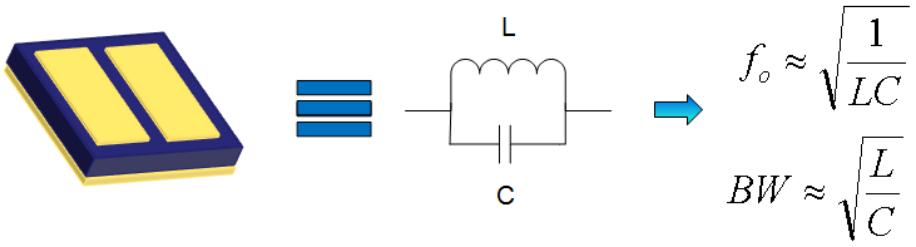

Figure 83. Equivalent circuit of the unit cell of Design 1.

the equivalent inductance, and C denotes the equivalent capacitance. The equivalent inductance value, hence the reflection phase bandwidth, can be increased by increasing the thickness and/or the μ_r of the substrate. However, increasing the thickness conflicts with the aim of miniaturization. Thus, magneto-dielectric substrates can be used for efficient miniaturization.

To verify this concept both designs were simulated with dimensions of a = b = 4 mm and g=0.15 mm on both the magneto-dielectric and dielectric substrates. The material properties of the magneto-dielectric substrate were assumed to be ϵ_r = 4.4 and μ_r = 3 with a magnetic loss tangent of 0.01. The permittivity of the dielectric material was found as ϵ_r = 11.8 with a dielectric loss tangent of 0.01 to obtain the same zero-reflection frequency with the magneto-dielectric case. The superstrate effects of a possible antenna substrate were also included in the simulations. The reflection phase responses obtained for these substrates are shown in Figure 82b. As seen in the figure, miniaturizing Design 1 with the magneto-dielectric substrate results in a larger reflection phase bandwidth compared to the high-permittivity substrate. Moreover, Design 2 does not have any additional advantage for this substrate since the additional inductance from the via is negligible due to thin substrate.

5.4 Microstrip Patch Antenna Design on a Miniaturized RIS

Several low-profile microstrip patch antennas were designed on the magneto-dielectric and high-permittivity substrates with RIS and PEC ground planes. The bandwidth, peak gain

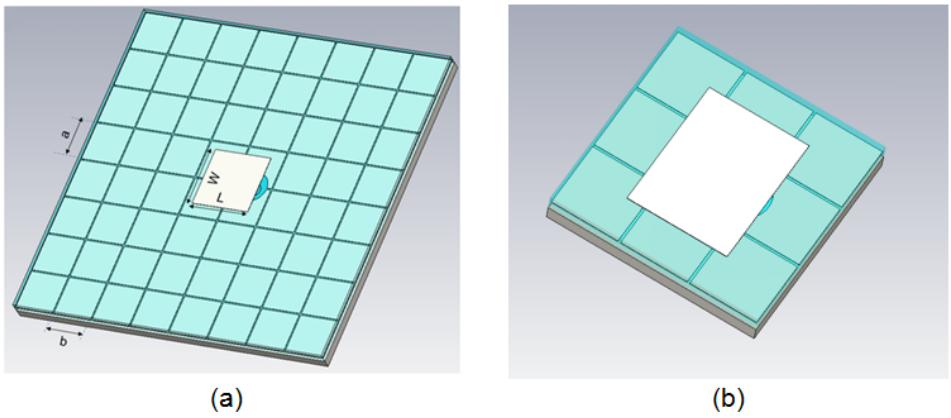

Figure 84. Patch antenna designs on 8×8 and 3×3 RIS of unit cell in Design 1.

Table 3. Summary of the microstrip patch antenna performance on RIS and PEC ground planes.

		Magneto-dielectric			Dielectric		
	Size (mm^2)	Bandwidth (%)	Peak Gain (dB)	F/B Ratio (dB)	Bandwidth (%)	Peak Gain (dB)	F/B Ratio (dB)
RIS	8×8	9	5.6	21.4	2.34	5.08	21.3
	3×3	2.9	2.8	6.2	1.26	0.9	3.8
PEC	8×8	4.4	4.9	18.6	2.17	2.5	16
	3×3	3.1	2.3	5.5	2.15	0.8	3.3

and front-to-back ratio of these antennas were compared to study the effects of these substrates. The results are summarized in Table 1 for two different sizes of RIS planes corresponding to 8×8 and 3×3 unit cells to study the effect of the size of the ground plane.

The dimensions of the patch antenna optimized on the magneto-dielectric substrate with RIS was found to be L=6 mm and W=8 mm with the probe offset x_p=1.5 mm from the center of the patch. As seen in Figure 85a and Table 5.4, the bandwidth of the antenna is improved from 4.4% to 9% by replacing the PEC ground plane of the antenna with an 8×8 RIS. Similarly, by using the RIS the peak gain of the antenna at 5.6 GHz is increased from 4.9 dB to 5.6 dB with an increased front-to-back ratio. The far field pattern of the antenna on 33.2 mm $\times$ 33.2 mm (8×8) RIS and PEC ground planes is presented in Figure 86a.

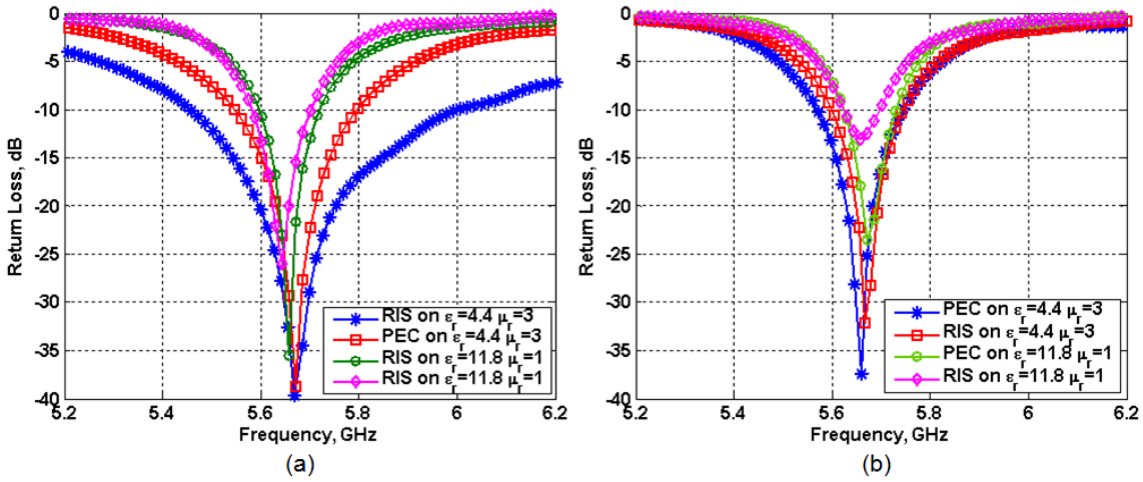

Figure 85. Comparison of simulated S_{11} data for the microstrip patch antennas on magneto-dielectric and high permittivity substrates with RIS and PEC ground planes. (a) 8×8**, (b)** 3×3**.**

The same antenna was also optimized with the RIS that is miniaturized with the high-permittivity substrate. As summarized in Table 5.4, when a high-permittivity dielectric substrate is used, the bandwidth of the antenna is almost the same for the RIS and PEC cases, without any improvement obtained with the RIS. However, similar to the magneto-dielectric case, the gain of the antenna at 5.6 GHz improves from 2.5 dB to 5.1 dB with an increased front-to-back ratio. The increase in the gain is a result of the alleviation of the undesired coupling of the image current with the inclusion of RIS [76].

The same study with the magneto-dielectric and high-permittivity dielectric substrates was repeated for a smaller PEC and RIS plane with a size of 12.45 mm $\times$ 12.45 mm corresponding to 3×3 RIS. As summarized in Table 5.4, it was found that the improvements obtained for the 8×8 RIS cannot be achieved with the 3×3 RIS. Although similar bandwidth and gain values were obtained both from the RIS and the PEC for the magneto-dielectric substrates, the antenna response deteriorated when the PEC was replaced with the RIS on the dielectric substrate. This is because the number of unit cells in the RIS is too small to emulate the desired reactive impedance. Therefore, it is important to optimize the number of the unit cells in the RIS to obtain an improvement in the antenna response.

The simulated S_{11} of the antennas on the 12.45 mm $\times$ 12.45 mm substrate is shown in

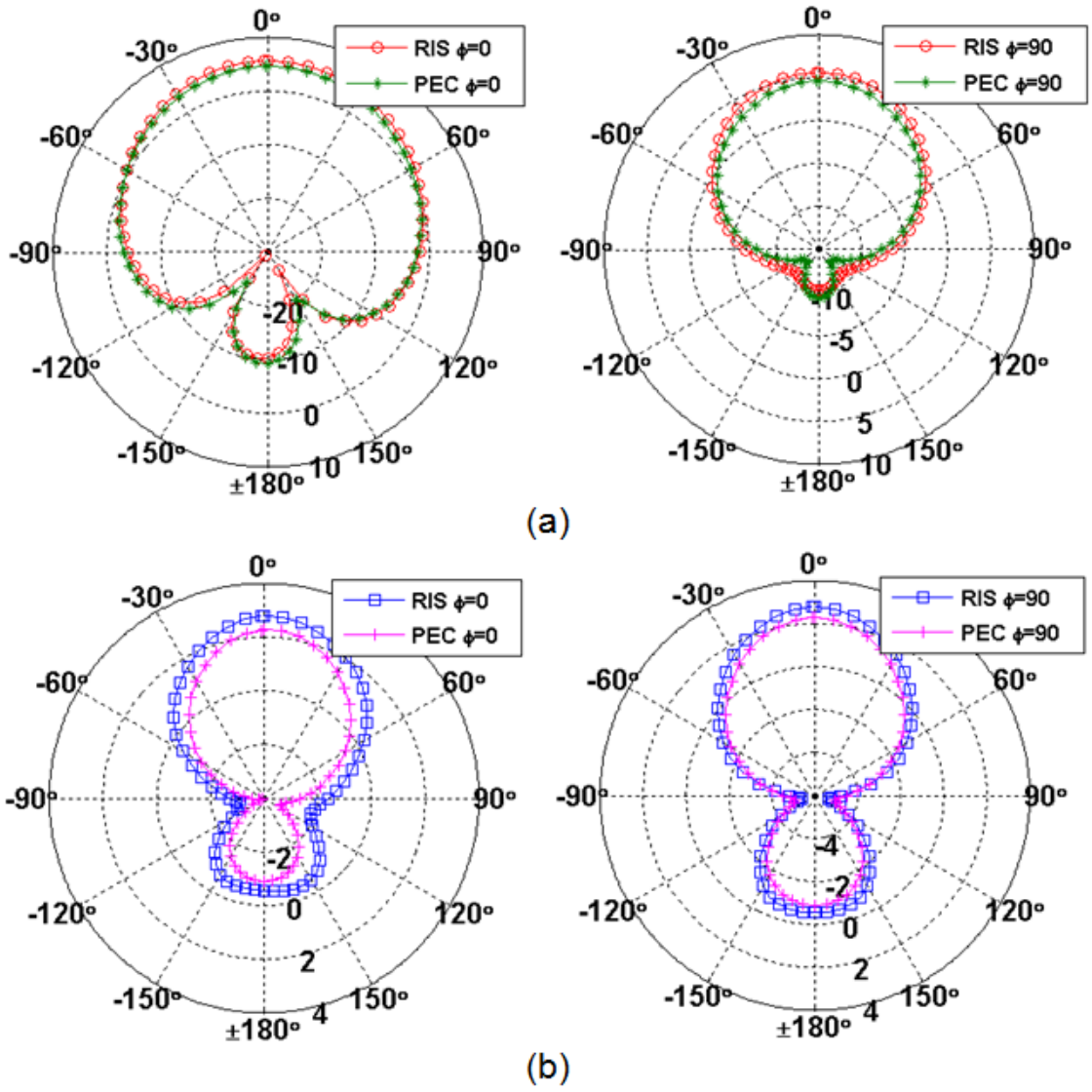

Figure 86. Comparison of far field pattern for the microstrip patch antennas on magneto-dielectric substrate with RIS and PEC ground planes. (a) 8×8**, (b)** 3×3**.**

Figure 85b. It can be seen from the figure as well that the RIS with only three unit cells does not improve the bandwidth of the antenna as promised even when the magneto-dielectric substrates are used for miniaturization. The far field pattern of the antenna for the magneto-dielectric substrate is shown in Figure 86b. Although the RIS substrate helps to improve the peak gain slightly, the antenna pattern indicates poor radiation because of the small size of the ground plane.

5.5 Conclusions

Reactive impedance surfaces have been proposed as an alternative to the conductor ground plane of planar antennas. It has been shown in the literature that the interaction between the antenna current and its image can be optimized when the surface impedance of the substrate is a certain purely reactive value. To design the RIS for this particular value of the impedance, the reflection phase bandwidth of the RIS should coincide with the operational bandwidth of the antenna.

A fundamental structure with a reactive surface impedance is the conductor-backed substrate. The analysis of the reflection phase characteristics of conductor-backed magneto-dielectric substrates revealed that increasing the permeability of the substrate can help to increase the reflection phase bandwidth. Therefore, it was concluded that conductor-backed magneto-dielectric substrates are expected to provide better antenna substrates than the conductor-backed dielectric substrates. These results support the findings of Chapter 4 of this thesis.

Surfaces with periodic unit cells can also emulate the desired reactive impedance surface characteristics. Moreover, the bandwidth of these surfaces can be tuned by changing the dimensions of the unit-cells. Miniaturization of these reactive impedance surfaces with the magneto-dielectric substrates have also been investigated in this chapter with their comparison to the high-permittivity substrates. It has been found that magneto-dielectrics can provide wider reflection phase bandwidth while providing the same miniaturization with

the high permittivity substrates.

The application of these miniaturized surfaces to the low-profile microstrip patch antenna designs has also been included in this chapter. It has been shown that the reactive impedance surfaces miniaturized with the magneto-dielectric materials provide better improvement in the bandwidth of the antenna compared to the reactive impedance surfaces miniaturized with the high permittivity substrates. It has also been found that the gain and the front-to-back ratio of the antennas on both type of substrates can be improved with the inclusion of an RIS. Moreover, it has been observed that the RIS performance is highly-dependent on the number of the unit cells; therefore, the size of the RIS should be optimized.

Following chapters present designs for an emerging technology operating around 60 GHz. This technology is proposed for the short-range high-speed wireless communications and wireless personal area network (WPAN) applications. The high operational frequency of this technology helps to overcome the problem associated with the large size of the antenna, eliminating the need for miniaturization of the antenna and using advanced conformal configurations for compact integration. However, the high carrier frequency is also responsible for new design challenges regarding the antenna. Several 60 GHz antenna designs are proposed in the forthcoming chapters to overcome these challenges.

CHAPTER 6

CPW-FED BI-DIRECTIONAL LINEAR TAPERED SLOT ANTENNA WITH GROUND CORRUGATIONS

The unlicensed spectrum around 60 GHz can provide miniaturized systems and high-throughput wireless communications. The miniaturization factors that can be achieved at 60 GHz are especially attractive compared to those that can be achieved at WLAN/WiMAX frequencies. However, in addition to the advantages regarding the size and the throughput of the system, the high carrier frequency around 60 GHz brings several challenges such as increased path-loss, indoor material attenuation, and multipath interference due to the reflections from small objects. This brings importance on the antenna selection for the short-range wireless communications at 60 GHz. Although the characterization of the channel for the short-range communications has not been fully achieved, preliminary results show that directional antennas are advantageous to reduce the multipath contributions [80].

Even though increasing the directivity of the antenna in a certain direction improves the quality of the communication, doing so also limits the high-quality communication to the line-of-sight of this particular beam. This may not be preferable when the optimum operation of a mobile device is concerned since limiting the radiation to a single direction will require the user to orient the device in a certain way to achieve successful wireless communication. In such a scenario, pattern-reconfigurable antennas can provide the optimized coverage since the radiation can be aimed at the desired direction, always maximizing the quality of the wireless communication. However, achieving pattern-reconfigurability requires using smart antenna systems that include a large number of antennas and complicated control circuitry [10], making these antenna systems expensive and large in size to be implemented in mobile devices. The ultimate desired solution to meet the need for the adaptive antenna pattern would be to achieve pattern-reconfigurability with a single antenna element. However, this is a difficult design problem that has not been fully implemented

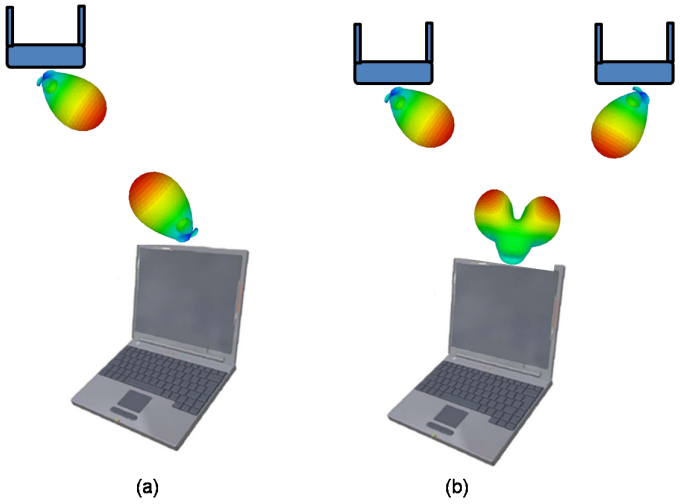

Figure 87. Comparison of single-beam antenna with dual-beam antenna.

even for the applications in the microwave band. Moreover, high-quality, low-loss, compact RF switches are needed to configure such an antenna; whereas, the switches available in the market today for millimeter wave applications are expensive and lossy.

Therefore, multi-beam antennas that can radiate and receive signals in multiple directions at the same time are proposed in this dissertation as an alternative to pattern-reconfigurable antennas. In this chapter, a coplanar waveguide (CPW-) fed bi-directional linear tapered slot antenna (LTSA) is presented. The proposed antenna has a radiation pattern with two symmetric beams, created by splitting the radiated power equally in two directions. As shown in Figure 87, the bi-directional LTSA antenna is more suitable for mobile devices than the conventional single-beam LTSA since two directions are covered at the same time. The bi-directional antenna presented in this chapter can also be an initial design step for a more advanced pattern-reconfigurable antenna, where the radiation is switched among multiple beams using switches.

The rest of this chapter is organized as follows: Section 6.1 reviews the previous work on tapered slot antennas, followed by the explanation of the proposed CPW-fed bi-directional LTSA in Section 6.2. Next, the simulation based design process is presented

in Section 6.3 with a detailed analysis of the effects of main design variables. The fabrication of the optimized designs is discussed in Section 6.4, while the model-to-hardware correlation is presented in Section 6.5. Measurement and simulation results obtained from two different measurement setups, a probe-based setup and a connector-based setup, are presented in this section. Finally, the chapter is summarized in Section 6.6.

6.1 Review of the Tapered Slot Antennas

A tapered slot antenna (TSA) was proposed by both Gibson [81], and Prasad and Mahapatra [82] in the same conference in 1979. As the name implies, a typical TSA includes a tapered slot that is etched on the ground plane such that the wider part of the slot is terminated at the edge of the ground plane, as shown in Figure 88. The tapered slot structure supports a surface wave that propagates until the end of the structure and radiates at the termination [65]. This makes the TSA an end-fire radiator with moderately high gain and narrow beamwidth.

The TSA has been preferred for many applications since it can be fabricated with easy, low-cost processes using photolithographic or screen-printing techniques. It can also be integrated with a simple feed transition. Moreover, end-fire radiation pattern of the TSA combined with these advantages make it an excellent choice to achieve the direct integration of the antenna on the same substrate with the other active and passive circuitries, as presented in Figure 88. This is possible because the antenna radiates away from the substrate and the circuitry, preventing the undesired mutual coupling and eliminating the need for a large clearance area.

However, the larger size of the TSA compared to that of the patch antenna makes it harder to realize this simple configuration for wireless applications centered at the lower GHz band. Therefore, TSAs have found a wider area of acceptance at millimeter wave frequencies. Moreover, TSAs are less sensitive to the manufacturing tolerances at the millimeter wave frequencies compared to the patch antennas, which is another reason why

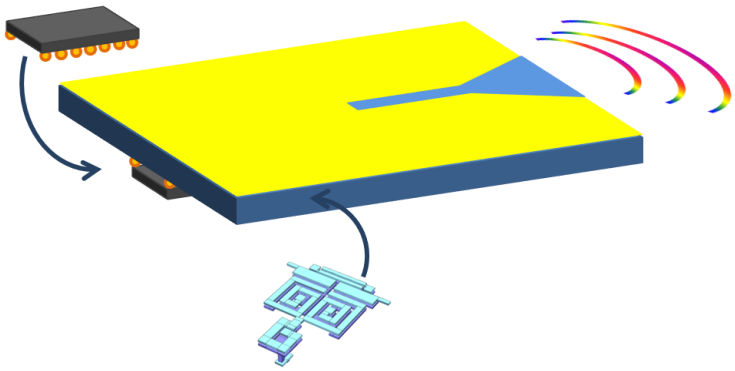

Figure 88. Proposed integration using the LTSA antenna on the same substrate with the rest of the active or passive circuitries.

TSAs are particularly well-suited for millimeter wave applications [83], [84], [85].

TSAs have been explored with different taper shapes, such as the Vivaldi antenna (exponential taper), the linear taper slot antenna, and the constant-width slot antenna. The common method to feed a TSA is to use a microstrip line (ML) to slotline (SL) transition realized by simply passing an orthogonal ML under the SL that feeds the tapered part [65]. As an alternative feed method, a CPW to SL transition was proposed in [86]. Although this feed method makes the antenna an easy-to-fabricate/integrate, single metal layer structure, the LTSA presented in [86] is still excited with a SL leading to a single-beam directive pattern.

The LTSA proposed in this dissertation is fed directly with a CPW line, eliminating the transition to the conventional slotline excitation. Additionally, the even mode excitation obtained with the CPW line was further exploited to transform the radiation pattern of the antenna from a single-beam pattern to a dual-beam pattern. The novelty of the proposed LTSA is this dual-beam pattern since the LTSAs proposed in the literature so far have been single-beam directive antennas. The details of the proposed LTSA and the design process are presented in the following sections of this chapter.

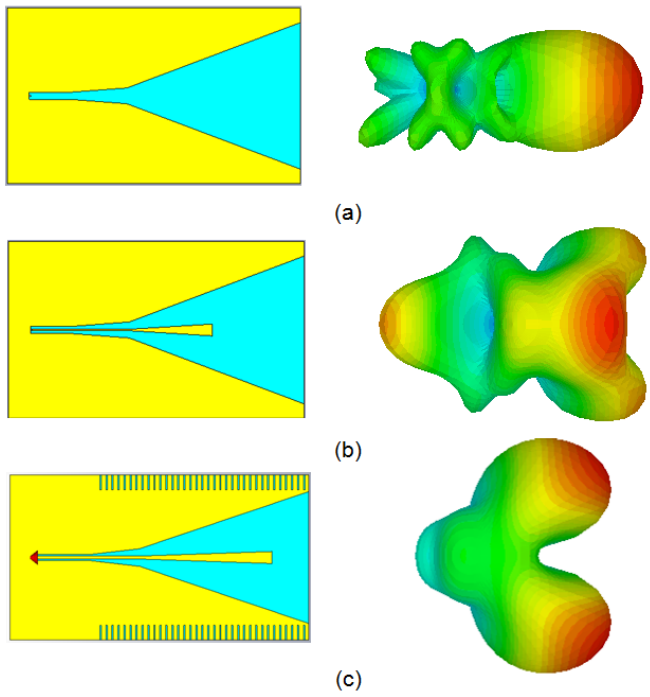

Figure 89. Evolution of the proposed CPW-fed bi-directional LTSA from a conventional LTSA structure. (a) Conventional ML-to-SL-fed LTSA. (b) Proposed CPW-fed bi-directional LTSA without ground corrugations. (c) Proposed CPW-fed bi-directional LTSA with ground corrugations.

6.2 CPW-fed Bi-directional Linear Tapered Slot Antenna

A linear tapered slot antenna has been used to prove the proposed concept since the accurate simulation of the LTSA requires shorter time and less memory compared to that of the slot antennas with curved tapers. However, the proposed idea to create dual-beam radiation pattern can be easily applied to a TSA with a curved taper.

The evolution of the proposed antenna from the well-known LTSA structure is shown in Figure 89. As seen in Figure 89b, the conventional SL-fed LTSA is first converted to a CPW-fed LTSA, where the main beam is split into two symmetric beams simply by extending the signal line and dividing the radiated power equally between the slots. Figure 90 displays the magnitude plots of the simulated peak Poynting vector at 60 GHz obtained for the conventional ML-to-SL-fed LTSA and the proposed CPW-fed bi-directional LTSA. The comparison of the plots clearly shows how the power flow is divided into two paths by simply extending the signal line of the CPW line in the proposed design.

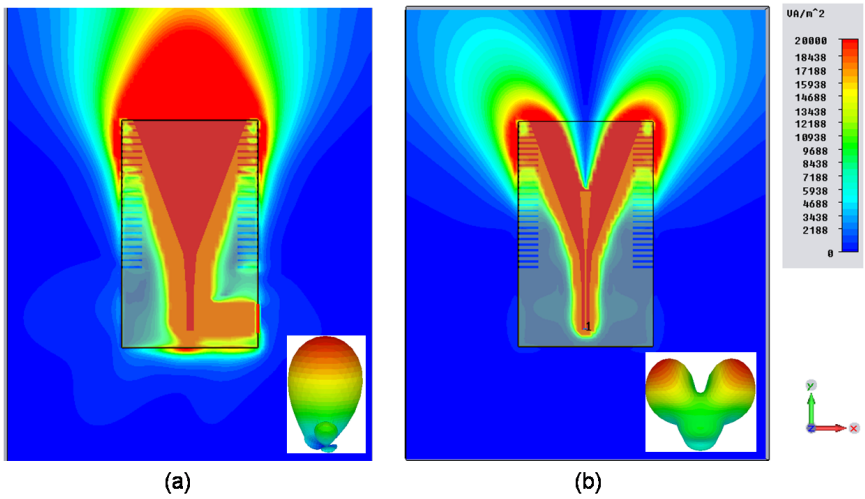

Figure 90. Comparison of the magnitude plots of the total peak Poynting vector at 60 GHz. (a) Common LTSA fed with an ML-to-SL transition (b) Proposed CPW-fed bi-directional LTSA.

As seen in Figure 89a and b, the radiation patterns of the LTSAs are distorted with back lobes and side lobes due to the high-order surface wave propagation. Surface waves can be defined as the field propagation along the boundary of the conductor-backed substrate and the air medium. Surface waves are guided along the substrate and diffracted from the edges giving rise to a deterioration in the far field pattern of the antenna. It has been reported in [86] that the substrate thickness and dielectric constant should satisfy the following constraint to prevent the deterioration in the radiation pattern due to the high-order substrate modes:

$$0.005\lambda_o < t_o \sqrt{\epsilon_r - 1} < 0.03\lambda_o \tag{122}$$

The antennas presented in Figure 89 were designed as single metal layer structures backed with an 8 mil thick liquid crystalline polymer (LCP) substrate to assure sturdy prototype fabrication. LCP is an organic, laminate-type packaging material that has been proven to have desired electrical and mechanical characteristics from DC to millimeter wave frequencies. The dielectric constant and the loss tangent of LCP at 60 GHz have been characterized as 3.15 and 0.004, respectively [20]. Substituting the permittivity of the LCP

at 60 GHz into Eq. (122) yields the thickness of the substrate to be

$$17\mu m < t_o < 102\mu m. \tag{123}$$

Although the LCP is available in 25 μm, 50 μm and 100 μm thick layers, these values are impractical as far as the sturdiness and the measurement of the prototypes are concerned. The LCP provides a flexible substrate with these thickness values which makes it difficult to mount the edge connector on the substrate. Therefore, instead of using a thinner substrate, an adjustment should be made in the design to prevent the effects of surface wave propagation.

Several solutions have been proposed in the literature to alleviate this problem. Popular methods aim to decrease the effective dielectric constant of the substrate by incorporating cavities in the substrate with the partial removal of the substrate [87], by integrating photonic band gap structures into the substrate [88], and by using air cavity backing substrates [89]. A more straightforward, easy-to-implement approach was proposed in [90] for microstrip antennas, where the finite ground plane of a microstrip patch antenna was designed using edge serragations to eliminate the radiation of the surface waves from the edges. A version of this approach was implemented in [86] to a W-band LTSA antenna by using rectangular slits to create corrugations along the edges of the ground plane. Improved side lobe level (SLL) and front-to-back (F/B) ratio of the LTSA antenna was reported in this paper.

As shown in Figure 89c, the rectangular corrugations were also applied to the edges of the proposed CPW-fed antenna. The improvement in the radiation pattern of the antenna can be clearly seen by comparing the far field patterns of the design with the corrugations in Figure 89c and without the corrugations in Figure 89b.

The details of the design process are discussed in the following sections.

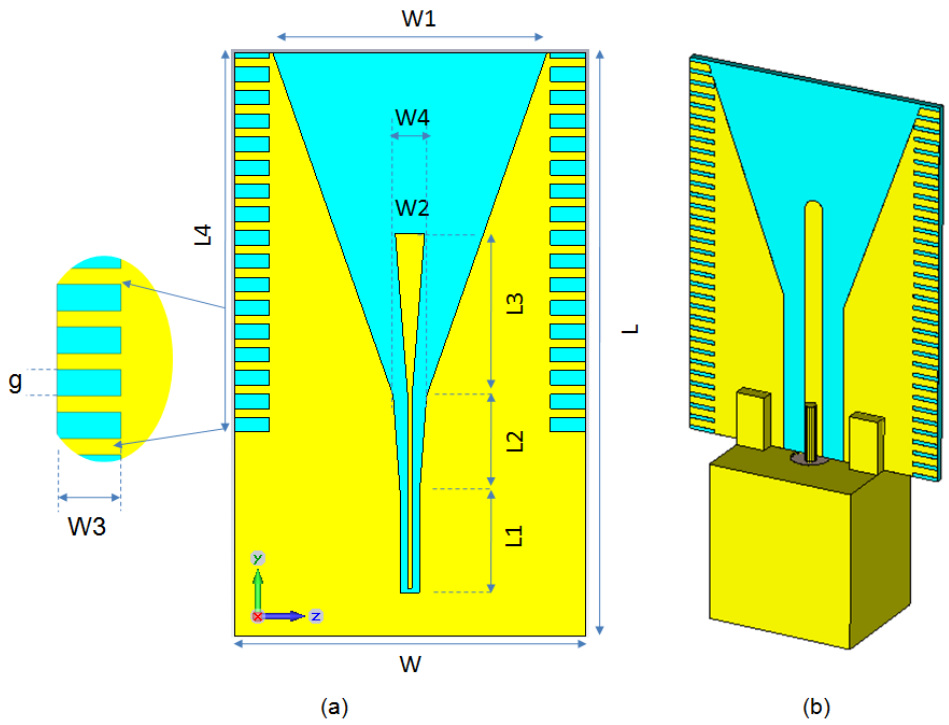

Figure 91. Details of the LTSA designed for the two measurement scenarios. (a) Design for the probe-based setup. (b) Design for the GPPO-connector based setup.

6.3 Simulation Based Design

The proposed CPW-fed bi-directional LTSA antenna was designed according to two measurement scenarios: one depending on using the probe-based setup and the other one based on using the edge-mount GPPO connectors, particularly B010-L13-01 from Corning Gilbert [91]. The LTSA designed for the probe-based measurement setup was optimized to use the GBB Probe Industry's Model 67A GSG 250 air coplanar waveguide probes [92]. The structure designed for the probe-based measurement setup is shown in Figure 91a. A tapered CPW line transition was included to improve the matching of the antenna.

The LTSA to be measured with the GPPO connector was designed with the connector model included in the simulations, as shown in Figure 91b. During the design process, the dimensions of the feeding CPW line were adjusted to ensure the proper fitting of the connector. The connector model used in the simulations was implemented according to the dimensions given in the datasheet [91]. It was modeled as a 50Ω coaxial line with a teflon

substrate and a gold metal body.

Several design variables were studied to find their effects on the matching and the directivity of the proposed antenna. These main variables were found to be the taper width $W1$, the length of the extended signal line $L3$, the taper length $L2$, the length of the corrugated portion of the edge of the ground plane $L4$, the width of the corrugations $W3$, and the gap between the corrugations g, as shown in Figure 91a. The same variables except $L2$ were used to optimize the LTSA designed for the connector-based measurement setup. Instead of $L2$, the gap between the signal and the ground planes of the CPW line was used as an additional variable to match the antenna. For both the probe-based and the connector-based LTSA designs, the width, W, and the length of the substrate, L, were kept constant at 6 mm and 10 mm, respectively.

A series of parametric sweeps was performed to analyze the effect of each design variable on S_{11} and the far field characteristics of the proposed LTSA. The directivity patterns of the antennas were compared instead of the gain patterns to eliminate the effect of the impedance matching on the far field characteristics of the antenna. The following sections summarize the results and the guidelines obtained from this study.

6.3.1 Taper width, $W1$

Figure 92 shows the effect of the taper width, $W1$, on the matching of the antenna. As seen in the figure, the matching of the antenna improves as the taper width is increased. This can be explained with the increase in the characteristic impedance of the SL that guides the surface waves to the edge of the substrate. Increased impedance matches better with the 377Ω free space wave impedance.

Similarly, increasing the taper width improves the directivity of the antenna, as presented in Figure 93. The radiation efficiency of the antenna also improves from 83% to 90% as $W1$ is increased from $W1 = 1500\,\mu$m to $W1 = 2500\,\mu$m. The improvement in the radiation characteristics can also be explained with the better match in the wave impedances.

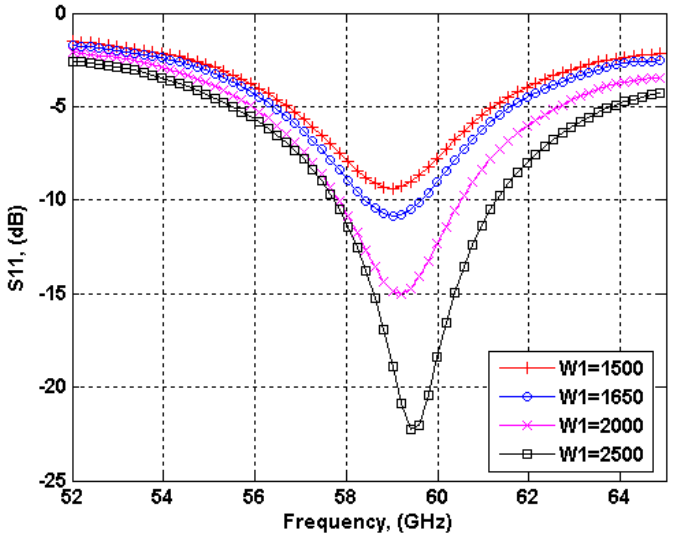

Figure 92. Simulated S_{11} data for different values of $W1$.

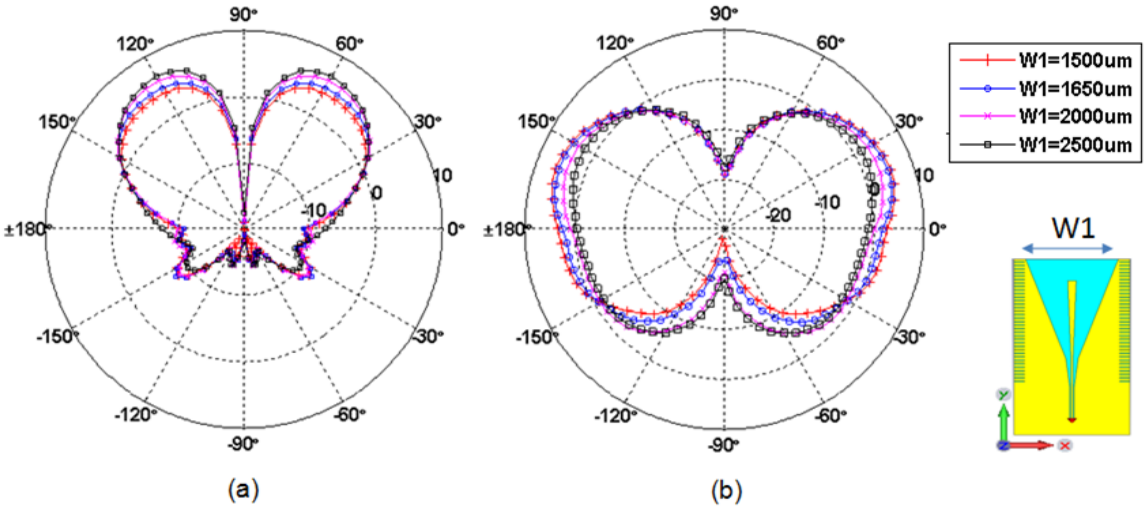

Figure 93. Simulated total directivity pattern for different values of $W1$. (a) E-plane (θ = 90°), (b) H-plane (ϕ = 90°).

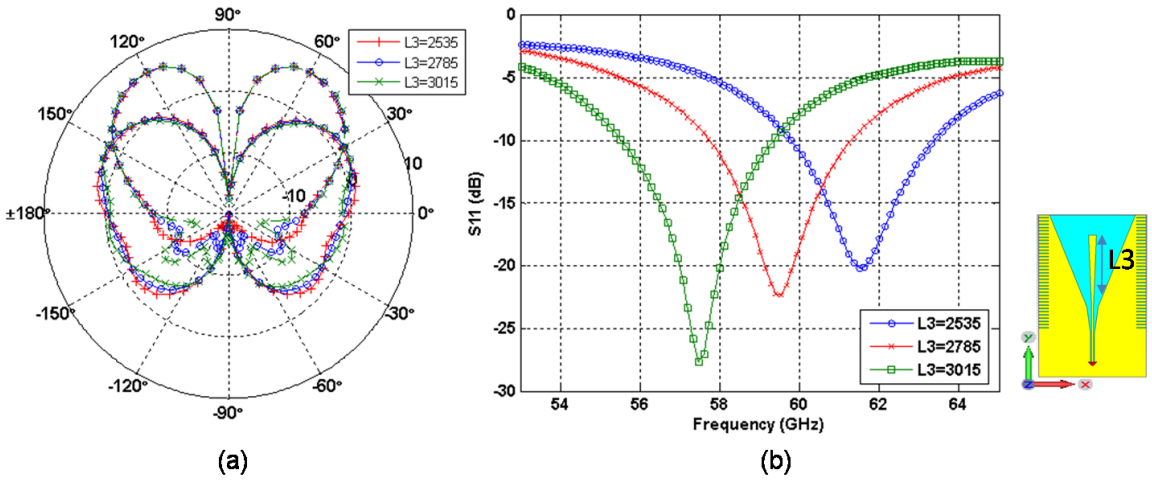

Figure 94. Simulated results for different values of $L3$. (a) Directivity patterns on the E-plane ($\theta = 90°$) and the H-plane ($\phi = 90°$), (b) S_{11}.

6.3.2 The length of the extended signal line, $L3$

The simulation results obtained by altering the extended signal line length are shown in Figure 94. As seen in the figure, the peak directivity of the antenna is not affected considerably when changing $L3$; however, the back-radiation toward the feed line increases as the signal line is extended longer. Similar to the peak directivity of the antenna the radiation efficiency of the antenna is not affected, and it is approximately 90% for all the simulated values of $L3$.

The main design parameter that $L3$ affects is the resonance frequency of the antenna, as shown in Figure 94b. As expected, increasing $L3$ decreases the resonance frequency of the antenna. It was also found from simulations that the matching level can be improved further by using a round termination at the open end of the extended signal line instead of the straight termination shown in Figure 91a.

6.3.3 Taper length, $L2$

It was mentioned earlier for the $W1$ sweep that the matching and the directivity of the antenna improve as the impedance of the CPW feed is increased to match the free space wave impedance. Therefore, to increase the impedance of the CPW line the gap between the ground planes and the signal line was widened gradually using a linear-tapered CPW

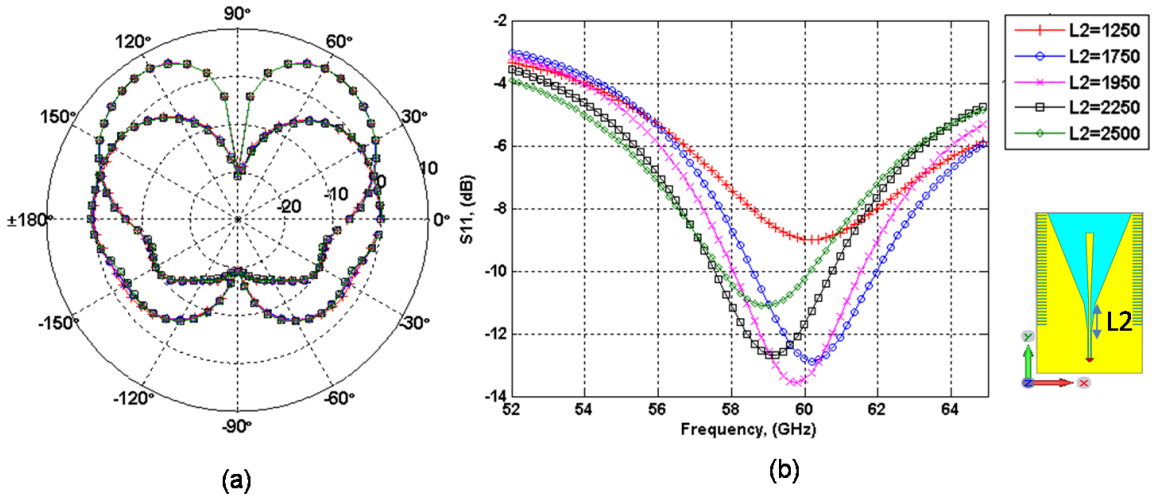

Figure 95. Simulated results for different values of $L2$. (a) Directivity patterns on the E-plane ($\theta = 90°$) and the H-plane ($\phi = 90°$), (b) S_{11}.

line section, as shown in Figure 91a. The length of this transition is labeled as $L2$ in Figure 91a.

Figure 95 displays the effects of altering the length of this tapered section on the radiation pattern and the matching of the antenna. As seen from the figure, the radiation pattern of the antenna is insensitive to the changes in the taper length; whereas, the matching of the antenna is affected considerably. Similar to the peak directivity, the radiation efficiency of the antenna was found to be insensitive to the changes in $L2$; however, the total efficiency of the antenna changes since it includes the effect of the matching as well. The optimized taper length was found to be $L2 = 1950\ \mu$m.

6.3.4 Distance between the grounds, $W4$

One of the main parameters to determine the characteristic impedance of the CPW line is the distance between the grounds. Therefore, $W4$ affects both the matching and the peak directivity of the antenna. The simulation results obtained by altering $W4$ are shown in Figure 96. As seen in the S_{11} graph, both the matching level and the resonance frequency of the antenna changes such that the resonance frequency of the antenna increases, as $W4$ is increased. The peak directivity of the antenna also slightly increases with an increased

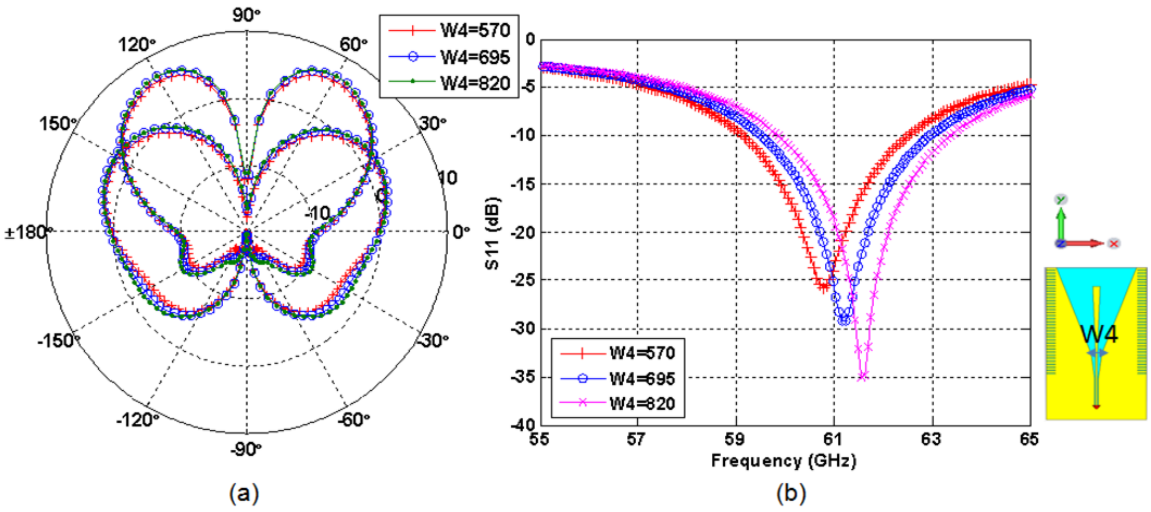

Figure 96. Simulated results for different values of $W4$. (a) Directivity patterns on the E-plane ($\theta = 90°$) and the H-plane ($\phi = 90°$), (b) S_{11}.

back-radiation towards the feed line, when $W4$ is increased. The radiation efficiency of the antenna is not affected, and it is approximately 90% for all the simulated values of $W4$.

6.3.5 The width of the corrugations, $W3$

The edges of the ground plane were corrugated to eliminate the deterioration of the radiation pattern due to the high-order surface wave propagation. There are three parameters associated with these corrugations: the width of the corrugations $W3$, the gap between the corrugations g, and the length of the corrugated part $L4$. These parameters are used to optimize the effects of the corrugations mainly on the radiation characteristics.

Figure 97 shows the effect of the width of the corrugations on the directivity of the antenna on both the E-plane ($\theta = 90°$) and the H-plane ($\phi = 90°$). As seen in the figure, the far field pattern of the LTSA is highly dependent on the width of the corrugations. It is clearly seen from the E-field plots that, increasing $W3$ eliminates the side-lobes directed towards the feed line of the antenna. The minimum value of $W3$ for successful elimination of the surface wave radiation was found to be 600 μm. However, the pattern can be improved further with wider slits, especially on the H-plane, as seen in Figure 97b. The effect of $W3$ on the radiation efficiency was also studied, and the radiation efficiency was found to be

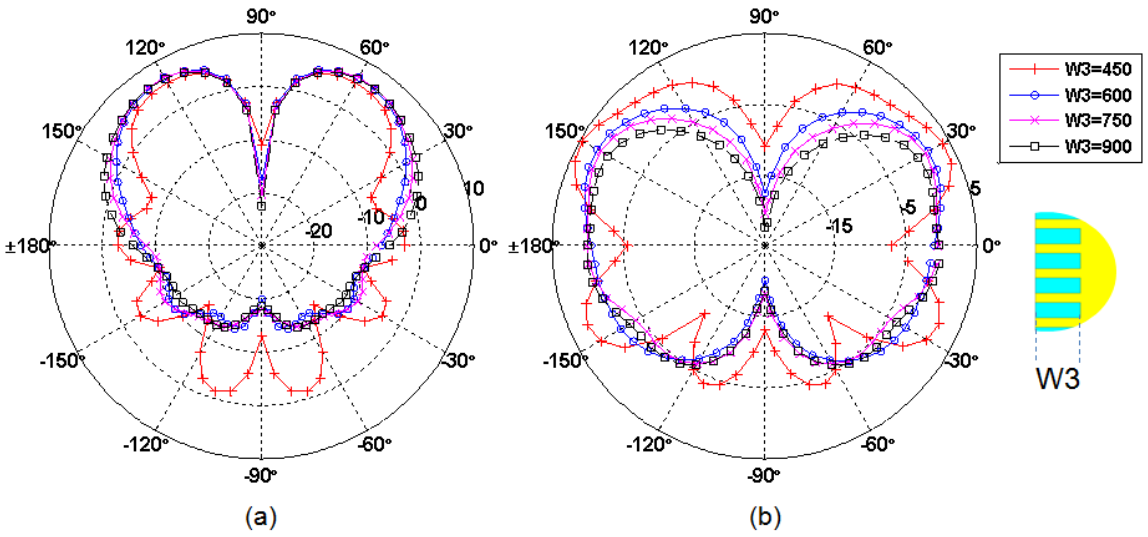

Figure 97. Simulated total directivity pattern for different values of $W3$. (a) E-plane ($\theta = 90°$), (b) H-plane ($\phi = 90°$).

approximately 90% for all simulated values of $W3$.

The S_{11} of the antenna was found to be insensitive to the changes in $W3$ since LTSA is a traveling wave antenna, and the corrugations do not affect the forward propagating wave in the tapered slot considerably.

6.3.6 The gap between the corrugations, g

Another parameter associated with the edge corrugations is the gap between the consecutive corrugations, labeled as g, in Figure 91a. Figure 98 shows the effect of altering the gap on the far field pattern of the antenna. The change in the pattern for the values below 500 μm ($\lambda_0/10$) was found to be negligible; therefore, these values are not presented in the figure. As seen in the figure, the peak directivity is almost insensitive to the changes in the gap as long as g is smaller than $\sim$ 1300 μm ($\lambda_0/4$); however, it is recommended to increase the density of the corrugations to decrease the side-lobe-level (SLL) on the E-plane. Decreasing the gap also helps to improve the pattern on the H-plane since the beams start merging each other as the gap between the corrugations is increased. Similar to the width of the corrugations, altering the gap value has negligible effect on the S_{11} of the antenna.

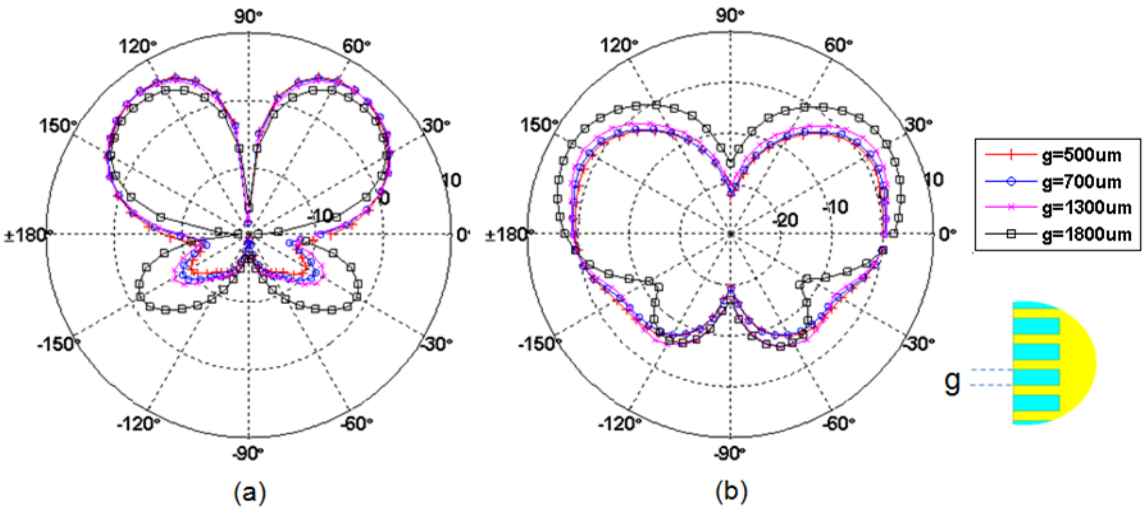

Figure 98. Simulated total directivity pattern for different values of g. (a) E-plane ($\theta = 90°$), (b) H-plane ($\phi = 90°$)

6.3.7 The length of the corrugated part of the edge, $L4$

Figure 99 shows the effect of the length of the corrugated region $L4$, on the radiation pattern. As seen in the figure, radiation pattern improves with a decreased SLL and increased front-to-back (F/B) ratio as the number of corrugations increases, i.e., $L4$ increases. Comparing the patterns for different values reveals that a minimum value for $L4$ to obtain acceptable SLL and F/B is $L4 = 6000\,\mu$m. However, corrugating the edge completely improves the pattern further.

Figure 100 shows the effect of $L4$ on the S_{11} of the antenna. As the edge started to be corrugated, the matching and the bandwidth of the antenna deteriorates compared to the case with no ground corrugations. This is because the corrugations are close to the edge of the open-end of the radiating taper, changing the current distribution. S_{11} becomes insensitive to the changes in the length of the corrugated part after $L4 \geq 4000\,\mu$m. Matching of the antenna can be improved by optimizing the taper length $L2$ and/or terminating the open-end of the extended signal line with a circular shape; however, the bandwidth of the antenna does not improve with these adjustments. The bandwidth can be improved using a curved taper such as the exponential taper in a Vivaldi antenna.

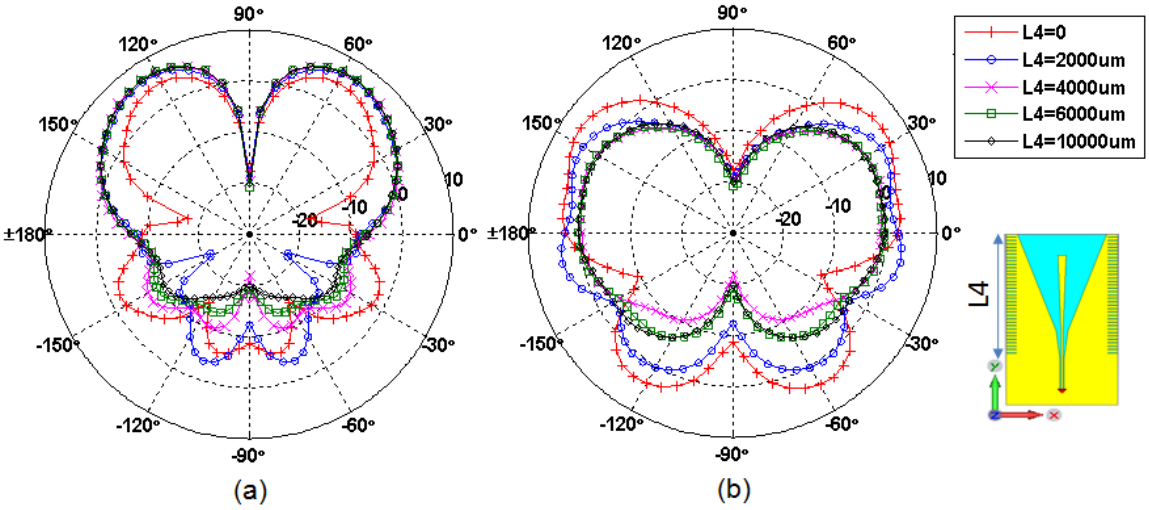

Figure 99. Simulated total directivity pattern for different values of *L*4. (a) E-plane (θ = 90°), (b) H-plane (ϕ = 90°)

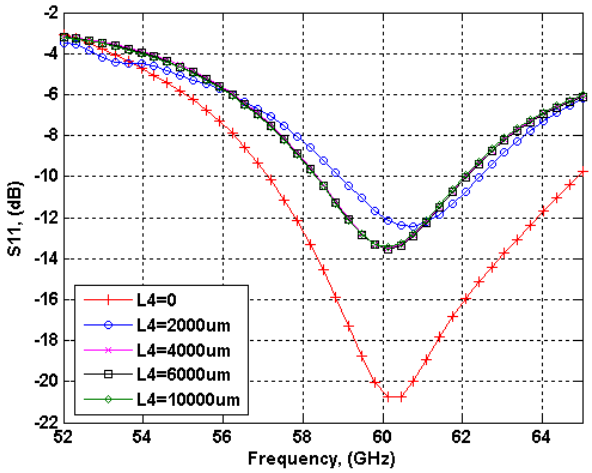

Figure 100. Simulated S_{11} data for different values of *L*4.

Table 4. Summary of the design variables for the CPW-fed bi-directional LTSA.

	W1	L3	L2	W4	W3	g	L4
S_{11}	✓	✓	✓	✓	×	×	✓
Directivity	✓	×	×	✓	✓	✓	✓

6.3.8 Summary of design guidelines

The variables studied can be grouped into two categories according to the design parameter they affect. The effects of the design variables are summarized in Table 4. It was found that the width of the termination of the taper $W1$, the length of the extended signal line $L3$, the length of transition taper $L2$ and the width of the CPW line $W4$ are the main parameters that affect the S_{11} and the impedance matching of the antenna.

The variables determining the dimensions of the corrugations along the edges of the ground planes are the main parameters that affect the far field pattern. These variables are the width of the slits $W3$ and the gap between the corrugations g. The length of the corrugated portion of the edge of the ground plane $L4$ also mainly affects the far field pattern of the antenna. However, when the corrugated portion is small and close to the open-end of the taper, $L4$ also affects the S_{11} of the antenna. Similarly, $W1$ and $W4$ affect the peak directivity and the far field pattern of the antenna in addition to S_{11} of the antenna. This is because these parameters determine the characteristic impedance of the CPW line and the tapered slot and; hence, the matching with the free-space wave impedance.

When designing the proposed CPW-fed bi-directional LTSA, it is recommended to first tune the S_{11} of the antenna to the desired frequency band using the corresponding variables shown in Table 4 along with the length of the radiating taper. Next, the ground corrugations can be added and their dimensions can be tuned to optimize the far field pattern of the antenna. The width and gap of the feeding CPW lines can be used to match the antenna.

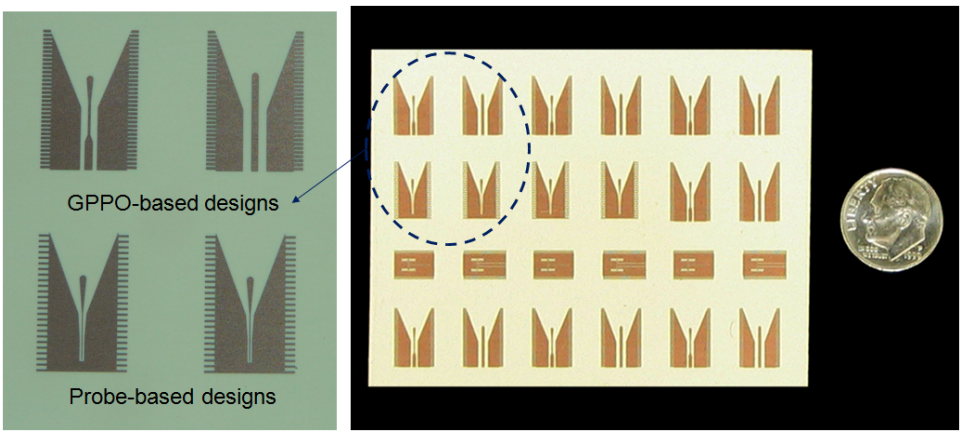

Figure 101. Photos of the fabricated LTSA antennas compared with 10 cents.

6.4 Fabrication

Using the results of the parametric sweeps summarized in the previous section, two types of CPW-fed bi-directional LTSAs were designed. As shown in Figure 91, one of the antennas was designed for the probe-based measurement setup, and the other one was designed based on the connector based measurement setup. Since the proposed designs are single metal layer structures without any via connections, the fabrication process was easy, and the antennas were patterned using conventional lithography and etching processes. The fabrication steps can be summarized as follows:

First, a 200 nm Ti and 2 μm Cu layers were deposited on an 8 mil thick bare LCP substrate with a CVC DC sputterer. Then, a Shipley S1828 photoresist was deposited and patterned using a Karl Suss MA-6 mask aligner. Next, the Cu layer was etched with FeCl, and the Ti layer was etched with an HF-based solution to pattern the antennas. Finally, the photoresist was removed using an acetone solution.

The photos of the fabricated designs are shown in Figure 101, compared with a dime. There were two different CPW-fed bi-directional LTSA designs optimized for the GPPO-based measurement setup. The antennas were fabricated along with the miniaturized H-shaped antennas explained in Chapter 7. The size of the board shown in Figure 101 is 7.5 cm $\times$ 5.5 cm.

6.5 Simulation and Measurement Results

The antennas were singulated by cutting the board with scissors. Probe-based and connector-based measurements were performed using an Agilent PNA E8361C. The Short Open Load (SOL) calibration was used for both measurement setups.

6.5.1 Probe-based Measurement Setup

Figure 102 shows the setup used for the probe-based measurements. As seen in the photos, the antenna to be measured was placed on a foam substrate since the proposed LTSAs radiate in both the azimuth and elevation planes. Two different foam thicknesses were used and, as expected, thicker foam was found to give better results. The measured S_{11} is shown in Figure 103 along with the simulated data. As seen in the figure, the measured and simulated results are almost on top of each other. The measured 10 dB bandwidth of the antenna was found to be from 58.8 GHz to 62.3 GHz. Although, the internationally available 7 GHz wide spectrum cannot be covered with this antenna, the bandwidth can be improved using a curved taper instead of the linear taper [93].

Figure 104a shows the simulated 3D gain patterns of the CPW-fed bi-directional LTSA at 61 GHz. The two beams created with the extension of the signal line can be clearly seen in the front view of the antenna. The simulated directivity patterns of the probe-based antenna at different frequencies are shown in Figure 105. As seen in the figure, the antenna pattern is stable over the frequency band. Table 6.5.1 summarizes the simulated radiation parameters. The average peak directivity of the antenna is 6.5 dBi over the spectrum from 57 GHz to 64 GHz. The simulated radiation efficiency was found to be around 90% in the whole band. As expected, total efficiency, which includes the effect of the matching of the antenna in addition to the radiation efficiency, is lower for the frequencies outside the 10 dB bandwidth of the antenna. However, within the band the antenna is matched, the average efficiency is 85% with an average peak gain of 5.7 dB. It should be noted that the gain of the antenna can be increased easily by using multiple antennas in an array configuration.

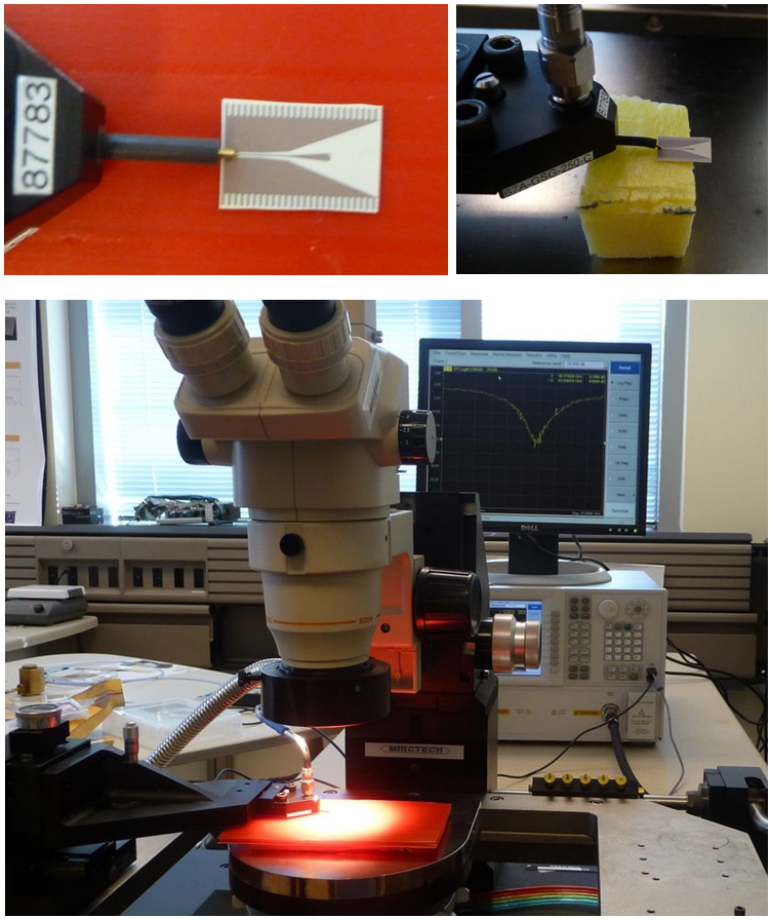

Figure 102. Photos of the probe-based measurement setup.

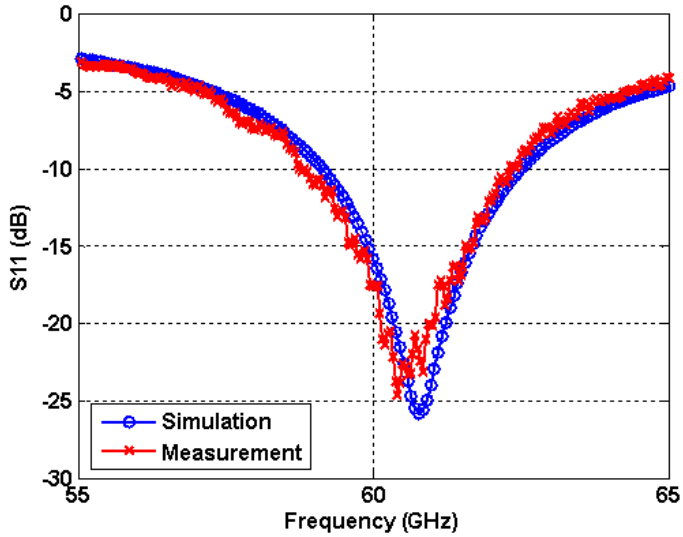

Figure 103. Simulated and measured S_{11} data of the CPW-fed bi-directional LTSA designed for the probe-based measurement setup.

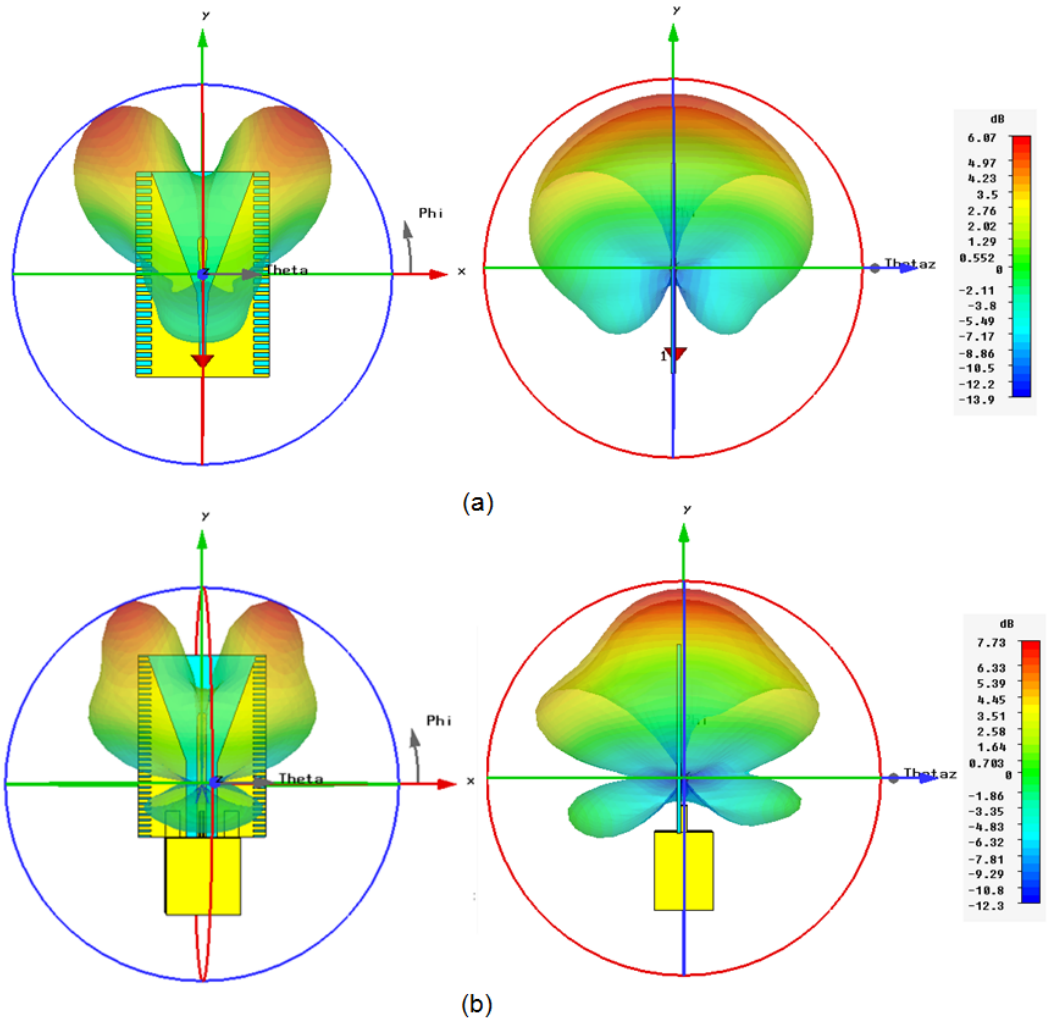

Figure 104. Simulated 3D gain patterns of the CPW-fed bi-directional LTSA at 61 GHz. (a) Probe-fed antenna, (b) GPPO-fed antenna.

Table 5. Summary of the simulated radiation parameters for the probe-fed bi-directional LTSA.

Frequency	Peak directivity	Radiation efficiency	Total efficiency	Peak gain
57 GHz	6.42 dBi	-0.49 dB (89%)	-2.31 dB (59%)	4.12 dB
58 GHz	6.38 dBi	-0.46 dB (90%)	-1.6 dB (69%)	4.8 dB
59 GHz	6.53 dBi	-0.47 dB (90%)	-1 dB (80%)	5.53 dB
60 GHz	6.5 dBi	-0.48 dB (89%)	-0.6 dB (87%)	5.9 dB
61 GHz	6.58 dBi	-0.48 dB (89%)	-0.5 dB (89%)	6.08 dB
62 GHz	6.5 dBi	-0.48 dB (89%)	-0.72 dB (85%)	5.92 dB
63 GHz	6.72 dBi	-0.47 dB (90%)	-1.17 dB (76%)	5.55 dB
64 GHz	6.79 dBi	-0.45 dB (90%)	-1. 71 dB (67%)	5.08 dB

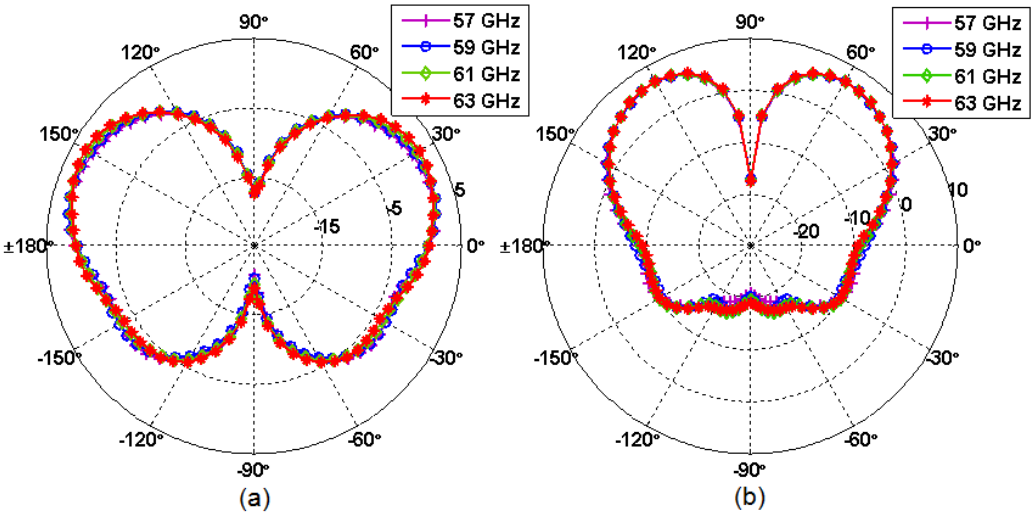

Figure 105. Simulated far field patterns of the CPW-fed bi-directional LTSA for different frequencies. (a)ϕ = 90°, (b) θ = 0°.

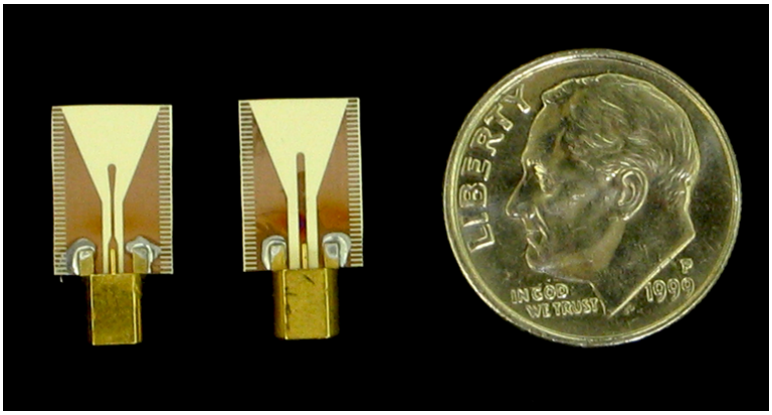

Figure 106. Photo of the singulated CPW-fed LTSAs with the GPPO connectors.

6.5.2 Connector-based Measurement Setup

The antennas were also measured with edge-mount millimeter wave connectors, called GPPO connectors [91]. The photos of the antennas fabricated for the connector-based measurement setup are shown in Figures 101 and 106. The GPPO connectors were soldered onto the CPW line feeding the antenna using copper flux. The connectors were soldered only on the ground pads, while the signal pin was left unsoldered to prevent the parasitics due to the solder.

Figure 107 shows the simulated and measured S_{11} of the LTSA designed for the connector-based measurement setup. As seen in the figure, the results do not agree as well as the

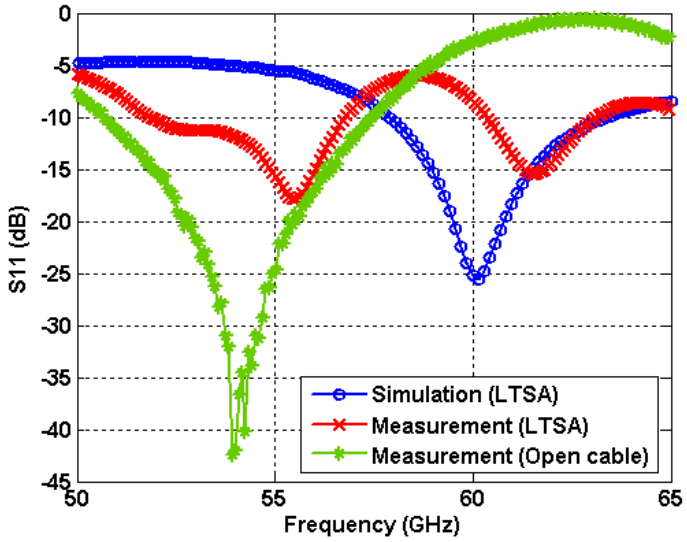

Figure 107. Simulated and measured S_{11} data of the CPW-fed bi-directional LTSA designed for the GPPO-based measurement setup.

results obtained with the probe measurements. In the figure, the measured S_{11} of the air-loaded cable, i.e. when the cable is not terminated with any structure, is also included. It can be seen from the S_{11} of the cable that even after the SOL calibration there is a resonance around 55 GHz due to the parasitics of the cable. This resonance is also observed in the antenna S_{11} as an extra resonance. It was also found through simulations that the connector should be flushed to the side of the substrate without any gap and also the signal pin should be touching the signal line to ensure proper connection. Given the tiny size of the connectors, the proper mounting of the connector is difficult to achieve and the disagreement between the measured and simulated results can be attributed to the aforementioned problems. Moreover, an adapter is used to connect the GPPO connectors to the PNA cables. Since the adapter cannot be calibrated out, the measurement data includes the effect of the adapter as well, which might be another reason for the disagreement between the measured and simulated results.

The far-field pattern of the proposed LTSA was also measured using the GPPO-based design. Although probe-based measurement setup is more suitable for S_{11} measurements, designs with the GPPO connectors were used to measure the far-field pattern of the antenna

since the proposed LTSA radiates mainly in the azimuth plane. As seen from the S_{11} graph in Figure 107, the antenna with the GPPO connector was well-matched to 50 Ohms in a narrow frequency band from 60 GHz to 62 GHz. Therefore, the far-field pattern of the antenna was measured in this frequency band with a simple measurement setup.

Figure 108 shows the setup used to measure the far-field pattern. As seen in the figure, the radiation pattern of the antenna was measured in a room, which is a measurement lab, without any absorbers surrounding the antenna. The setup includes a two-port PNA, a V-band horn antenna, a rotating disk at which the horn antenna is attached. As shown in Figure 108, the antenna was connected to Port2 of the PNA while the transmitting horn antenna was connected to Port1. The LTSA was fixed on a stack of foam substrates such that the pattern on the E-plane of the antenna (*theta* = 90° plane) can be measured using the horn antenna. The horn antenna was fixed on a disk which was rotated manually as shown in Figure 108. The radiation pattern of the antenna was plotted by measuring the S_{21} of the system for every 10° shift on the E-plane. The angle values were approximated using the holes on the rotating disk.

The measured S_{21} values were plotted on a polar plot and normalized with the maximum measured S_{21} value. Figure 109 shows the simulated and measured far-field patterns of the GPPO-based antenna. As seen in the figure, the measured pattern shows good correlation with the simulated pattern and both patterns have two beams with the null at $\phi = 90°$. It should be noted that the setup was not yet optimized for gain measurements; therefore, only the radiation patterns of the fabricated and simulated antennas were compared.

The simulated 3D gain pattern of the antenna with the GPPO connector at 61 GHz is also shown in Figure 104b. Comparing the pattern with the pattern of the probe-based antenna in Figure 104a reveals that there is a slight distortion in the far field of the antenna and also a stronger back-radiation towards the feed of the antenna. Figure 110 shows the directivity patterns of the antenna at different frequencies. As seen in the figure, although

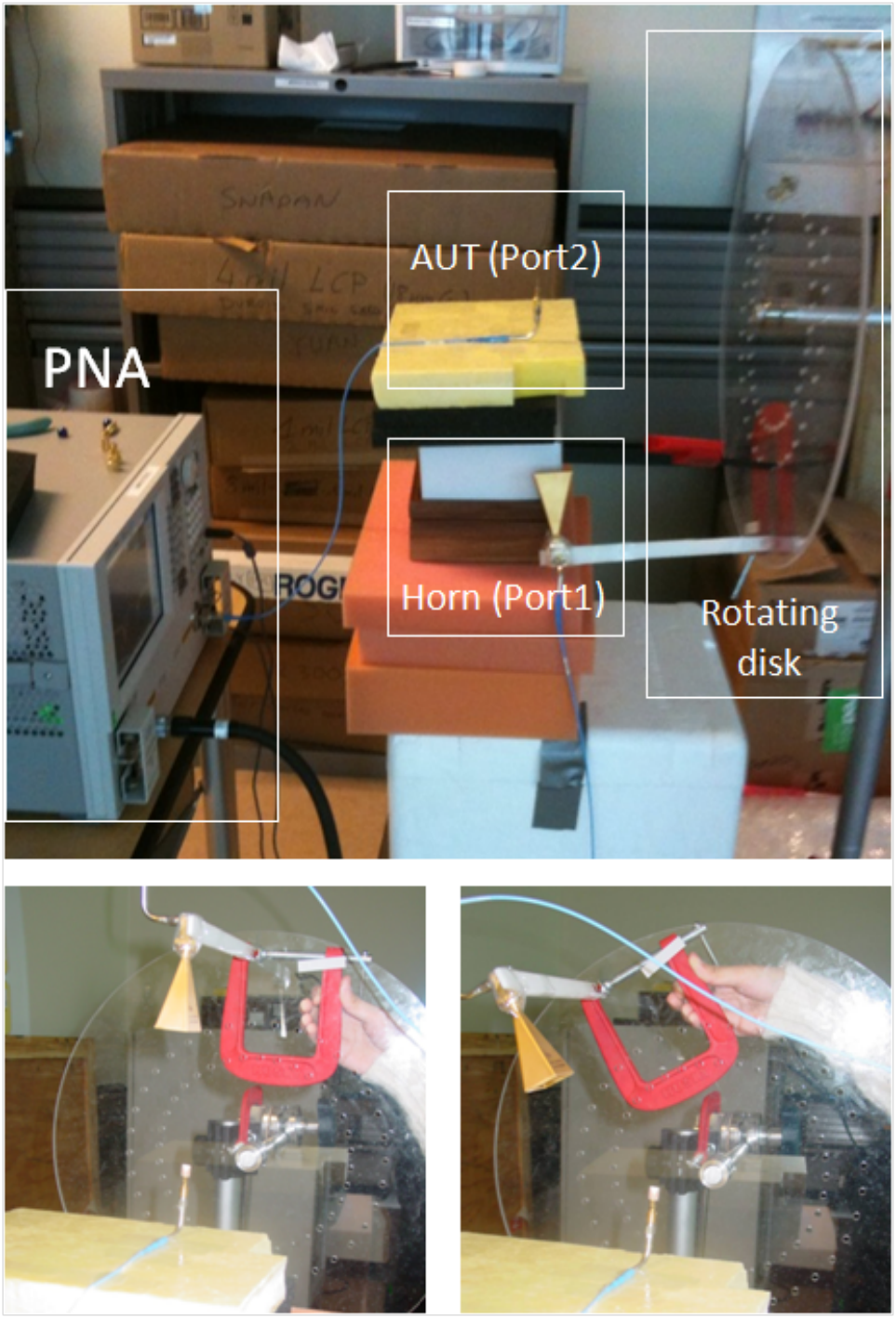

Figure 108. Photos of the far field measurement setup using the designs with the GPPO connectors.

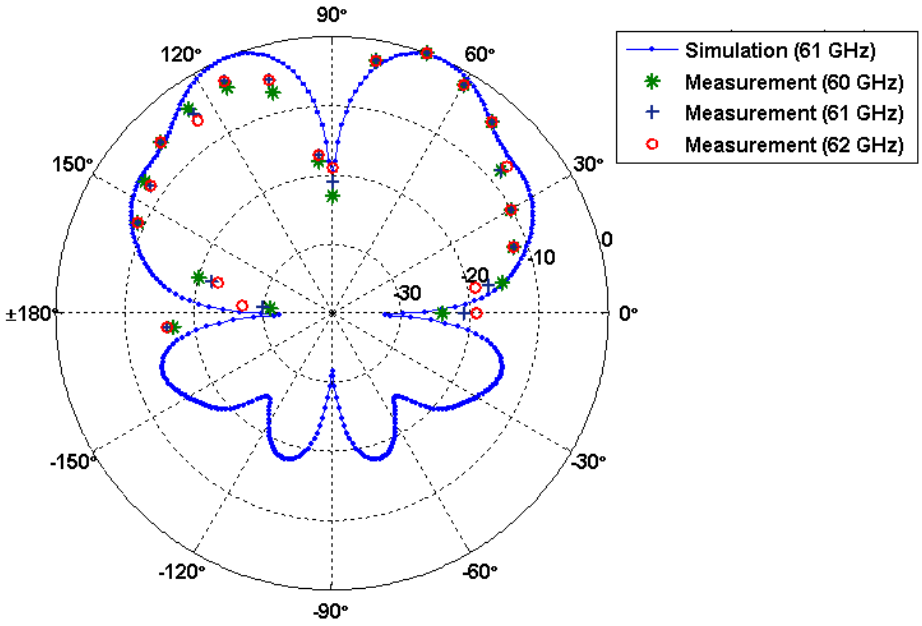

Figure 109. Comparison of the simulated and measured far-field pattern of the GPPO-based antenna.

the dual-beam pattern is preserved through the whole band, the pattern is frequency dependent and not as clean as the pattern of the antenna designed for the probe-based setup. This shows that the connector interferes with the radiated fields of the antenna.

The simulated radiation parameters are summarized in Table 6.5.2. Comparing the parameters in Table 6.5.2 with Table 6.5.1 reveals that the LTSA optimized for the connector-based setup has slightly higher gain and efficiency values, which may be attributed to the effect of the connector.

6.6 Conclusions

Due to the increased path loss, directive antennas are required for the 60 GHz applications in contrast to the omni-directional antennas required for wireless mobile applications centered in the microwave band. However, when a single-beam directive antenna is used, the wireless communication is limited to a single direction. Therefore, antennas covering multiple directions simultaneously can be more advantageous, especially for mobile

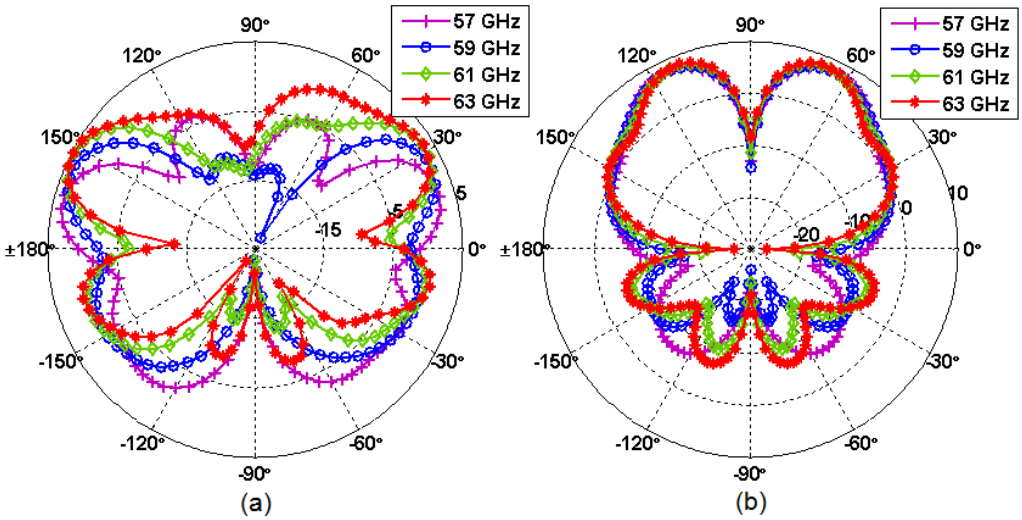

Figure 110. Simulated far field patterns of the CPW-fed bi-directional LTSA designed for the GPPO-based measurement setup. (a) $\phi = 90°$**, (b)** $\theta = 0°$**.**

Table 6. Summary of the simulated radiation parameters for the GPPO-fed bi-directional LTSA.

Frequency	Peak directivity	Radiation efficiency	Total efficiency	Peak gain
57 GHz	7.77 dBi	-0.19 dB (96%)	-0.97 dB (80%)	6.8 dB
58 GHz	7.66 dBi	-0.21 dB (95%)	-0.61 dB (87%)	7.1 dB
59 GHz	7.62 dBi	-0.21 dB (95%)	-0.34 dB (93%)	7.4 dB
60 GHz	7.98 dBi	-0.19 dB (96%)	-0.21 dB (95%)	7.8 dB
61 GHz	8 dBi	-0.19 dB (96%)	-0.26 dB (94%)	7.7 dB
62 GHz	8.1 dBi	-0.18 dB (96%)	-0.41 dB (91%)	7.7 dB
63 GHz	8.1 dBi	-0.18 dB (96%)	-0.56 dB (88%)	7.5 dB
64 GHz	8 dBi	-0.17 dB (96%)	-0.7 dB (85%)	7.3 dB

applications.

A novel CPW-fed LTSA has been presented in this chapter. The novelty of the design comes from the fact that the single-beam radiation pattern of the conventional LTSA is transformed to a dual-beam radiation pattern. This is achieved by dividing the radiated power into two directions by simply extending the signal line of the feeding CPW line. Moreover, by feeding the antenna with a CPW line the antenna is transformed into a single-metal layer device, making the fabrication easy and low-cost. The details of the design process have been presented in this chapter along with the detailed effects of the design variables on the matching and the radiation pattern of the antenna.

The deterioration in the radiation pattern because of the diffracted the higher-order surface waves has been eliminated by incorporating corrugations along the sides of the ground plane. The side-lobes in the radiation pattern were mostly suppressed this way.

One disadvantage of directing the radiated power into two directions compared to the single-beam radiation of the conventional LTSA is a decrease in the peak gain of the antenna by $\sim$ 3 dB. Approximately 6.5 dB gain of the proposed antenna may be enough for most short-range communications; however, if higher gain values are needed, the proposed antenna can easily be used in an array configuration to improve the gain of the antenna.

The proposed antenna structure has been designed to be measured with a probe-based and a connector-based setup to compare the results obtained from these setups. It was found that the probe-based measurement setup is more suitable for S_{11} measurements since using GPPO connectors require using adapters, whose effect cannot be removed with SOL calibration. Moreover, the SOL calibration was found to be ineffective to eliminate the effects of the cable when the connector-based setup is used. A de-embedding method may be required to de-embed the effect of the connectors and the cable, which was not covered in this chapter.

Although probe-based measurement setup is more suitable for S_{11} measurements, designs with the GPPO connectors were required to measure the far-field pattern of the antenna. Since the proposed LTSA radiates mainly in the azimuth plane, probe-based setup is not suitable for far-field pattern measurements. It was observed from GPPO-based S_{11} measurements that the antenna was well-matched to 50 Ohms in a narrow frequency band from 60 GHz to 62 GHz. Therefore, the far-field pattern of the antenna was measured in this frequency band with a simple measurement setup. Good correlation was observed with the simulated pattern. The bi-directional nature of the pattern was measured clearly with the null separating the symmetric beams.

CHAPTER 7

MINIATURIZED CPW-FED H-SHAPED SLOT ANTENNA WITH CORRUGATIONS

Wireless personal area (WPAN) applications proposed for the internationally available unlicensed spectrum around 60 GHz promise miniaturized, high-throughput wireless systems. The miniaturization factors achieved along with the high operation frequency prevent antenna miniaturization from being an issue, which can lead to fully-integrated systems with efficiently integrated antennas. However, the constraints on antenna design become complicated since the high carrier frequency also brings increased path-loss, material attenuation, and multipath interference due to reflections from small objects.

Several antenna types have been explored and proposed in the literature for 60 GHz WPAN applications. Dipole antennas and patch antennas are two popular categories investigated for this band. Microstrip patch antennas have been shown to provide highly-directive gain values; however, their limited bandwidth makes it difficult to cover the entire 7 GHz spectrum. As proposed in Chapter 8, stacked patch antenna configurations can be used to overcome the narrow bandwidth problem; nevertheless, stacked patch designs require multilayer substrates and a complex design process. On the other hand, dipole antennas have been demonstrated to provide efficient wide-bandwidth operation [94]. However, baluns are required to measure the dipoles with single-ended transmission lines, which makes the design process complicated.

Slot antennas can be used to overcome these limitations [65]. Slot antennas are low-profile, easy-to-fabricate antennas that can be fed with microstrip (ML) to slotline (SL) transitions or directly with coplanar waveguide (CPW) lines. They are also highly-tolerant to fabrication variances, which makes them especially suitable for the millimeter wave applications. Furthermore, slot antennas can provide wide bandwidth and directional radiation patterns.

As explained in Chapter 6, a directional radiation pattern is advantageous at 60 GHz to reduce the multipath contributions [80]. Increasing the directivity of the antenna in a certain direction improves the quality of the communication at the expense of limiting the high-quality communication in other directions from this particular beam. Although smart antenna systems can orient the beam of the antenna to always maximize the quality of wireless communication, these antenna solutions are expensive and large in size to be implemented in mobile devices [10]. A more elegant solution to meet the need for adaptive antenna systems would be to achieve pattern-reconfigurability with a single antenna element. However, this is a difficult design problem that requires high-quality, low-cost, compact RF switches to configure such an antenna. Multi-beam antennas that can radiate and receive signals in multiple directions at the same time are proposed in this dissertation as an alternative to pattern-reconfigurable antennas.

In Chapter 6 of this dissertation, a CPW-fed bi-directional linear tapered antenna has been presented as one of the multi-beam antennas proposed for 60 GHz WPAN applications. In this chapter, a multi-beam CPW-fed H-shaped slot antenna is proposed. First, a review of the previous work on slot antennas is presented in Section 7.1. Next, the details of the proposed H-shaped slot antenna and the methods to miniaturize the antenna are discussed in Section 7.2. Then, methods to eliminate the effect of the surface wave propagation are presented in Section 7.3. The design process of the proposed miniaturized H-shaped slot antenna is explained in Section 7.4, followed by the fabrication process summarized in Section 7.5. Section 7.6 presents the simulation and measurement results obtained by using probe-based and connector-based measurement setups. Finally, the chapter is summarized in Section 7.7.

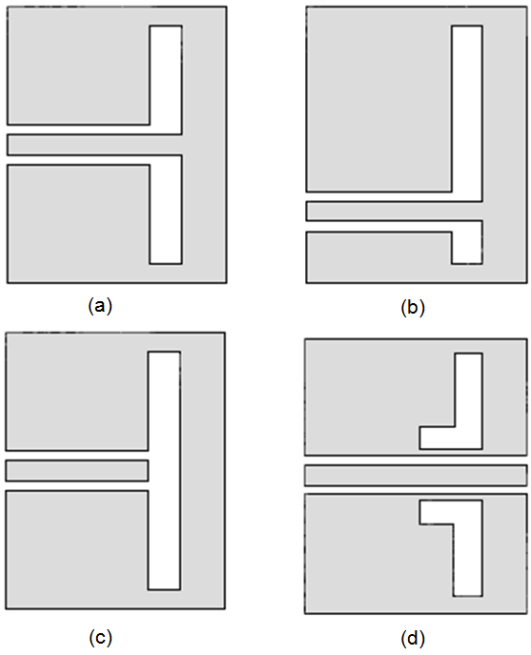

Figure 111. CPW-fed slot antennas. (a) Center-fed slot antenna, (b) Offset-fed slot antenna, (c) Capacitively-coupled slot antenna, and (d) Inductively-coupled slot antenna. Figure is reproduced from Figure 7.14 of [65].

7.1 Review of Slot Antennas

Slot antennas can be of traveling-wave-type or resonating-type [65]. An example of the traveling-type slot antennas is analyzed in Chapter 6 of this thesis. Although the traveling-type slot antennas can provide wide-bandwidth coverage and directive radiation patterns with high-efficiency, they usually have a larger size compared to the resonating-type slot antennas. Figure 111 shows some examples of the CPW-fed resonating-type slot antennas. As seen in the figure, resonating-type slot antennas are composed of closed slots etched on the ground plane. In a CPW-fed slot antenna, the electric fields in the CPW apertures excite the respective slots of the antenna by creating horizontal magnetic currents. A microstrip line printed on the back of the substrate can also be used to excite the slot antenna etched on the ground plane [65]; however, CPW-feed is more preferable since the antenna can be designed as a single metal layer structure.

Most papers published in the literature on resonating slot antennas have focused on ultra wide band (UWB) and wireless personal area (WLAN) applications because of the wide

band operation of slot antennas [95], [96]. Moreover, since the shape of the radiating slot is one of the main design variables to determine the radiation and matching characteristics of the slot antenna, several slot shapes have been explored in the literature, e.g. bow-tie, annular, and fractal, etc. [97], [98], [99], [100], and [101]. In addition to UWB and WLAN applications, a CPW-fed shorted slot antenna tuned with inductive matching elements was reported in [102] for the 60 GHz WPAN applications.

Even though slot antennas have been extensively studied in the literature and applied for several wireless technologies, the antennas proposed so far have been designed either with uni-directional or bi-directional radiation patterns. In this chapter, a multi-beam H-shaped slot antenna is proposed along with a miniaturization technique that can be applied to other slot shapes as well. The details of the antenna are explained in the following sections.

7.2 Miniaturized H-shaped Slot Antenna

The proposed H-shaped slot antenna was created by connecting two back-to-back CPW-fed shorted slot antennas and feeding them in the middle, as presented in Figure 112. Connecting two shorted slot antennas in this way transforms the bi-directional radiation pattern of the slot antenna into a multi-lobe bi-directional radiation pattern, as shown in Figure 113. H-shaped slot antennas have been reported before in [100], and [101]; however, these antennas were designed with bi-directional [101] and uni-directional [100] radiation patterns without having multi-lobe characteristics. As mentioned before, multi-lobe patterns can be more advantageous compared to single-beam directive antennas when mobile applications are considered.

H-shaped slot antenna presented in Figure 112 was designed as a single metal layer structure backed with an 8 mil thick LCP substrate to ensure mechanical rigidity. The size of the substrate was chosen as $a = 7000\ \mu$m, $b = 5000\ \mu$m. During the design process, the dielectric constant and the loss tangent of the LCP at 60 GHz were assumed as 3.15 and 0.004, respectively based on [20].

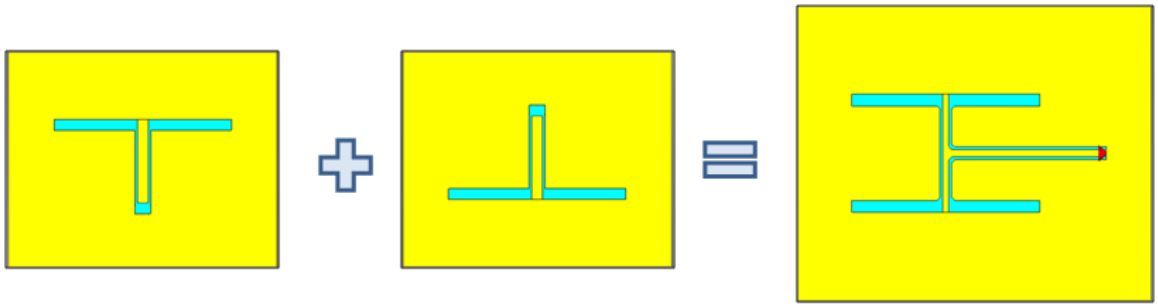

Figure 112. Transformation of H-shaped slot antenna from CPW-fed slot antenna.

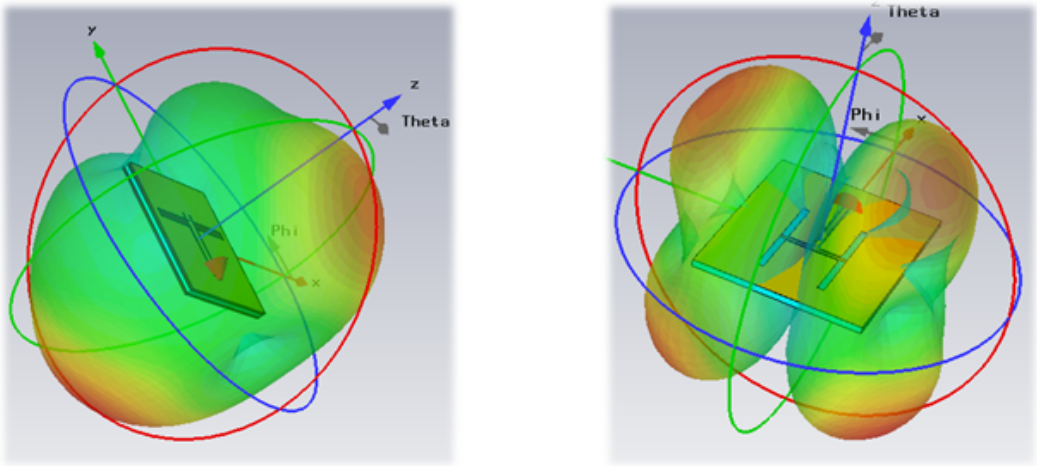

Figure 113. Transformation of radiation pattern from a single bidirectional lobe to multi bidirectional lobe. (a) Pattern of the center-fed slot antenna, (b) Pattern of the H-shaped slot antenna.

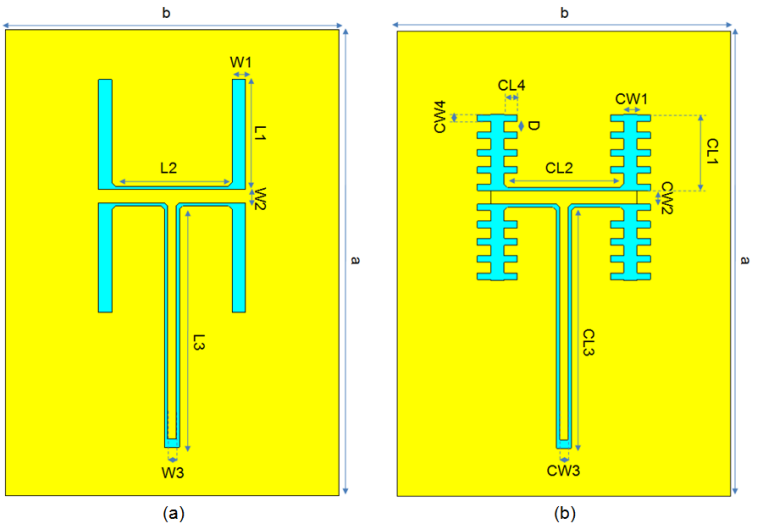

Figure 114. CPW-fed H-shaped slot antenna with and without corrugations on the slots. (a) Without corrugations, (b) With corrugations.

The details of the proposed H-shaped slot antenna are shown in Figure 114a. Tuning the dimensions of the slots and the CPW lines, the H-shaped slot antenna was optimized with the following values: $W1 = 200\,\mu$m, $L1 = 1650\,\mu$m, $W2 = 200\,\mu$m, $L2 = 1700\,\mu$m, $L3 = 3575\,\mu$m, and $W3 = 125\,\mu$m. It was found during the design process that each center-fed shorted slot antenna comprising the H-shaped slot antenna should be designed as a λ_g-long resonator, with $L1 \approx \lambda_g/2$ long slots, to achieve broadband matching in the desired frequency band. This can be explained considering that the slot antenna is the complementary structure of a dipole antenna. Therefore, it is expected that increasing the length of the slot decreases the input impedance of the antenna, providing a better match. Moreover, the gain of the antenna is increased as the length of the slot is increased.

Rectangular slits were included along the edges of the slots, as presented in Figure 114b, to shorten the slots. By corrugating the slots with rectangular slits, the length of the slots was decreased from $L1 = 1650\,\mu$m to $CL1 = 1150\,\mu$m. The optimized values for the miniaturized H-shaped slot antenna with the corrugations were found as follows: $CW1 = 200\,\mu$m, $CL1 = 1150\,\mu$m, $CW2 = 200\,\mu$m, $CL2 = 1700\,\mu$m, $CL3 = 3575\,\mu$m, $CW4 = 100\,\mu$m, $CL4 = 200\,\mu$m, $D = 160\,\mu$m and $CW3 = 125\,\mu$m.

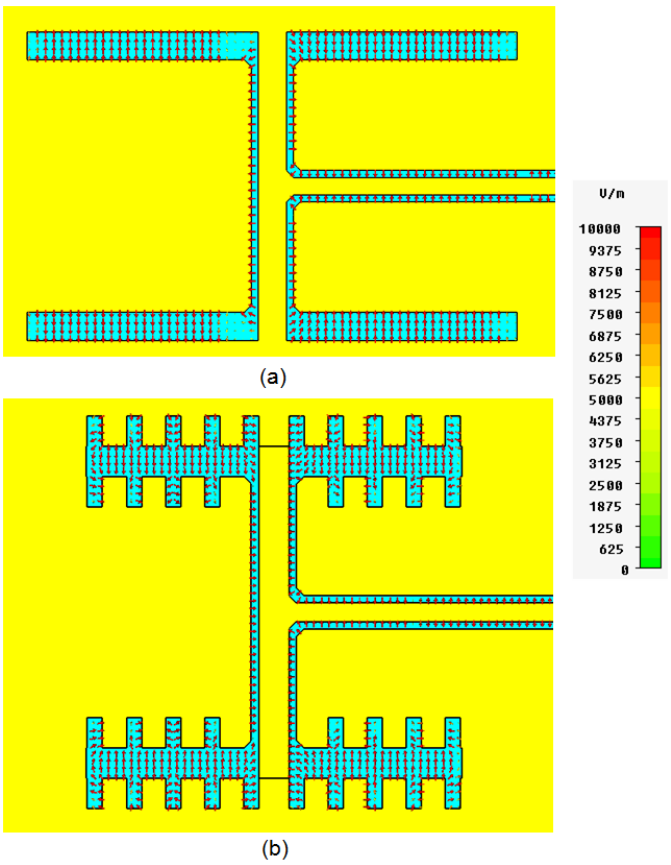

Figure 115. Vector magnetic current distribution (tangential E-field) in the slots. (a) Without corrugations, (b) With corrugations.

Figure 115 shows the magnetic current distribution, i.e., tangential electric field distribution, on the slots of the antennas with and without the corrugations. A comparison of the electric current distribution is also shown in Figure 116. As seen in these figures, corrugations help to achieve the required electrical length with a shorter slot length.

The simulated S_{11} of the H-shaped slot antennas with and without the corrugations are compared in Figure 117. Although the bandwidth slightly decreases when the antenna is miniaturized with the corrugations on the slots, the bandwidth is still wide enough to cover the desired 11.6% bandwidth.

The radiation patterns of the H-shaped slot antennas with and without the corrugations are also compared in Figure 118. As seen in the figure, the far field pattern of the miniaturized antenna has a decreased back-radiation on the $\theta = 90^\circ$ plane compared to the antenna

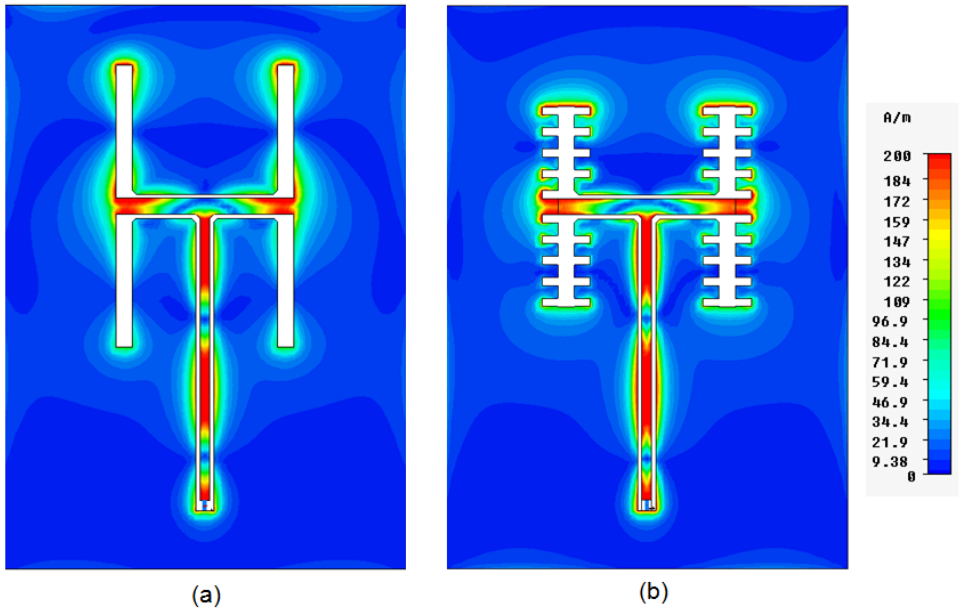

Figure 116. Magnitude of electric current distribution on the ground plane. (a) Without corrugations, (b) With corrugations.

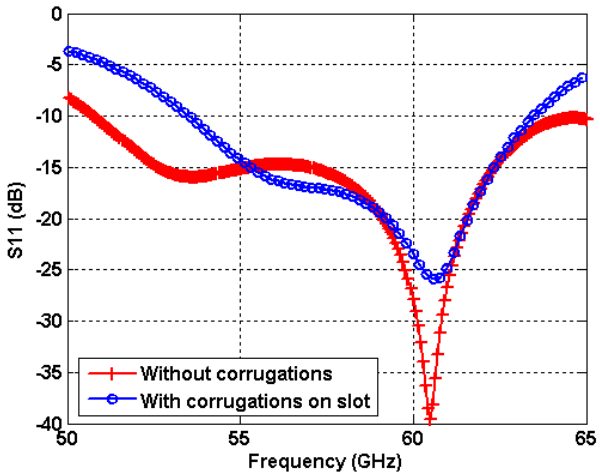

Figure 117. Simulated S_{11} comparison of the H-shaped slot antennas with and without the slot corrugations. The original H-shaped slot antenna has $L1 = 1650\,\mu$m and the miniaturized H-shaped slot antenna has $CL1 = 1150\,\mu$m.

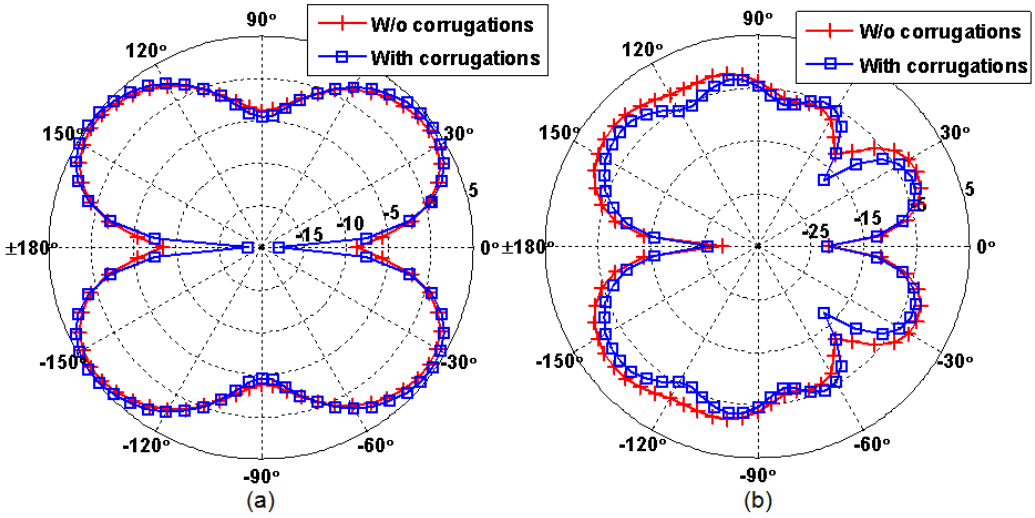

Figure 118. Simulated far field pattern comparison of the H-shaped slot antennas with and without the slot corrugations. (a) $\phi = 90°$**, (b)** $\theta = 90°$**.**

without any corrugations. The peak gain of the antenna decreases slightly from 5.8 dB to 5.3 dB because of the smaller slot size. Although the gain of the antenna is low, it can be improved by using the antenna in an array configuration.

7.3 Eliminating the Effects of the Surface Waves

Conductor-backed dielectric slabs can support wave propagation along the boundary between the dielectric and the free space, which is known as surface wave propagation. Surface waves are guided along the substrate and are responsible for the coupling between multiple elements integrated on the same substrate. Moreover, as these waves reach the edge of the substrate they are reflected and diffracted by the edges, giving rise to a distortion in the far field of the antennas. The power carried by the surface waves increases as the substrate thickness, the dielectric constant and/or the frequency are increased [65].

The surface wave problem is also discussed in Chapter 6 of this thesis. As explained in Chapter 6, the constraint in Eq. (122) should be satisfied to prevent the deterioration in the radiation pattern due to the diffraction of the unwanted higher-order substrate modes. However, Eq. (122) yields impractical thickness values for the relative permittivity of the LCP substrate. Therefore, instead of choosing a thin substrate, the edges of the ground

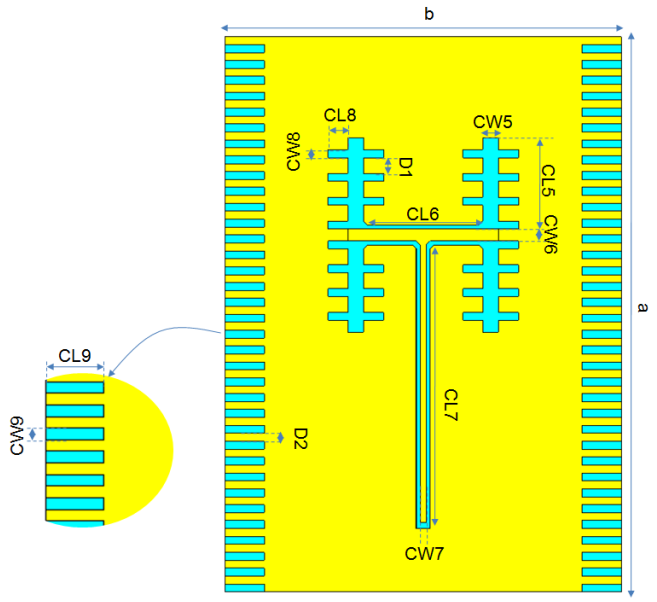

Figure 119. Details of the miniaturized H-shaped slot antenna with ground corrugations.

plane are corrugated to prevent the diffraction of the surface waves, as applied to the linear tapered slot antenna in Chapter 6. The miniaturized H-shaped slot antenna with ground corrugations are shown in Figure 119.

The plots of the surface current distribution on the ground plane at 60 GHz for both the antennas with and without the ground corrugations are displayed in Figure 120. Comparing the current distributions, the effect of the corrugations in preventing the diffraction of the surface waves from the edges of the ground planes can be clearly observed. As seen in the figures, the current distribution around the antennas does not differ considerably in both plots; therefore, the S_{11} of the antenna is not expected to change considerably when the ground corrugations are included. This can be verified with the comparison of the simulated S_{11} of the antennas with and without ground corrugations in Figure 121. However, the far field of the antenna improves with the ground corrugations, as shown in Figure 122. The back-radiation towards the feed-line decreases considerably with the addition of the ground corrugations.

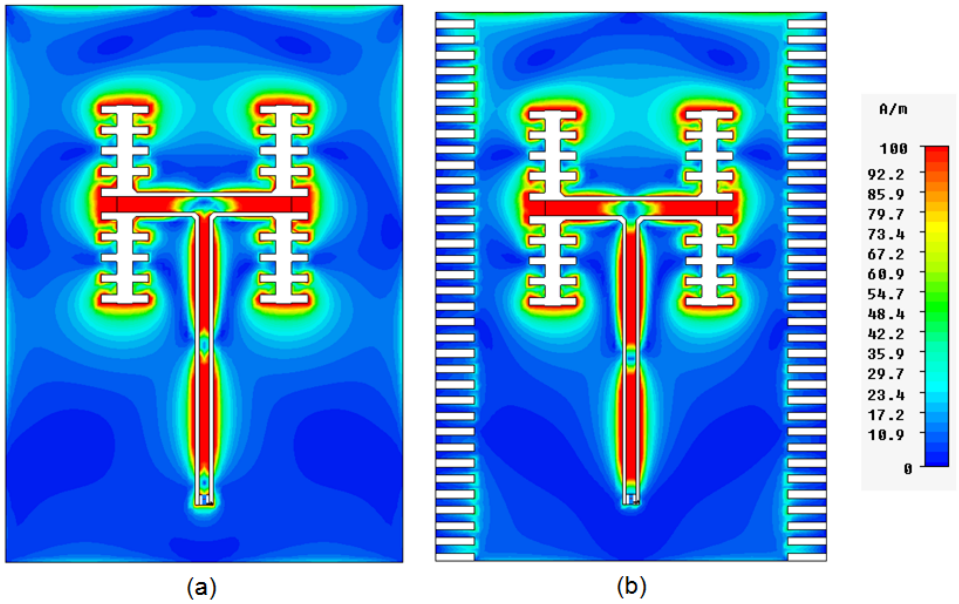

Figure 120. Magnitude of electric current distribution (tangential E-field) on the ground plane. (a) Without ground corrugations, (b) With ground corrugations.

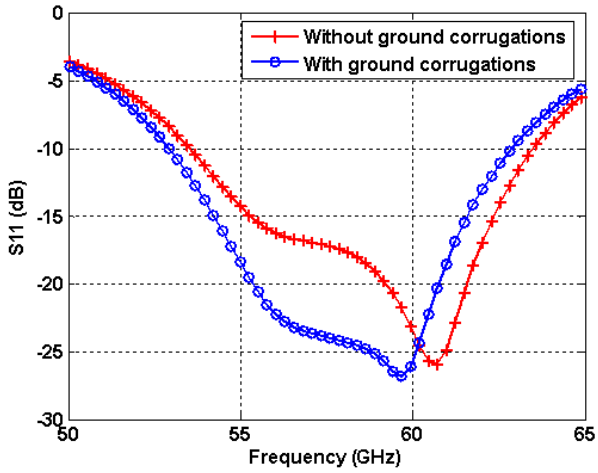

Figure 121. Simulated S_{11} comparison of the H-shaped slot antennas with and without the ground corrugations.

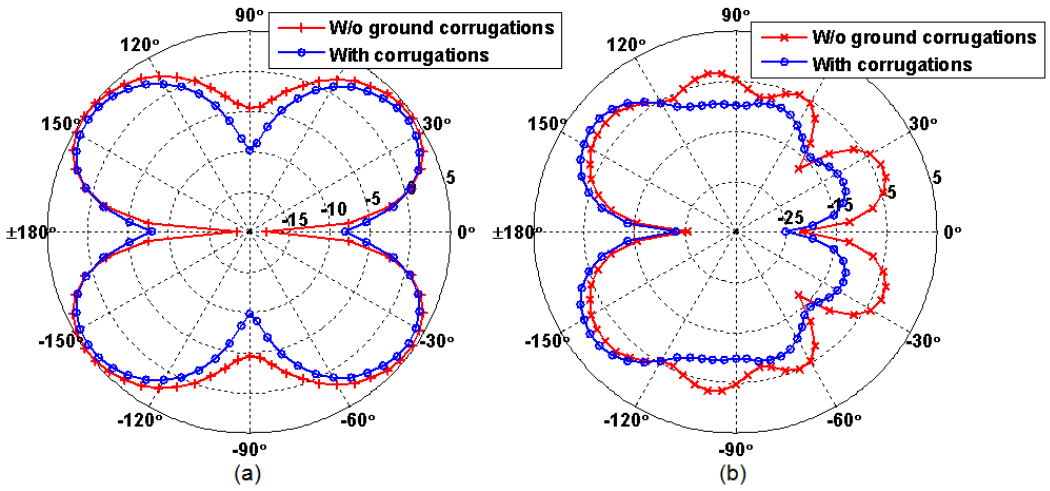

Figure 122. Simulated far field pattern comparison of the H-shaped slot antennas with and without the ground corrugations. (a) $\phi = 90°$**, (b)** $\theta = 90°$**.**

7.4 Simulation Based Design

A miniaturized H-shaped slot antenna was designed with a series of parametric sweeps using the commercially available full-wave electromagnetic field solver, Computer Simulation Technology's Microwave Studio (CST MWS) [58].The antenna was designed according to two measurement scenarios: One depending on using the probe-based setup and the other one based on using the edge-mount GPPO connectors, particularly B010-L13-01 from Corning Gilbert [91]. The antenna designed for the probe-based measurement setup was optimized to use the GBB Probe Industry's Model 67A GSG 250 air coplanar waveguide probes [92]. The antenna designed for the probe-based measurement setup is shown in Figure 119.

The antenna designed for the GPPO-based measurement setup is shown in Figure 123. While designing this H-shaped slot antenna, the connector model was also included in the simulation, as shown in Figure 123b. The connector model used in the simulations was implemented as a 50Ω coaxial connector with a teflon substrate and a gold metal body, according to the dimensions given in the datasheet [91]. Also, the dimensions of the feeding CPW line were adjusted to ensure the proper fitting of the connector.

A series of parametric sweeps was performed using the probe-based H-shaped antenna

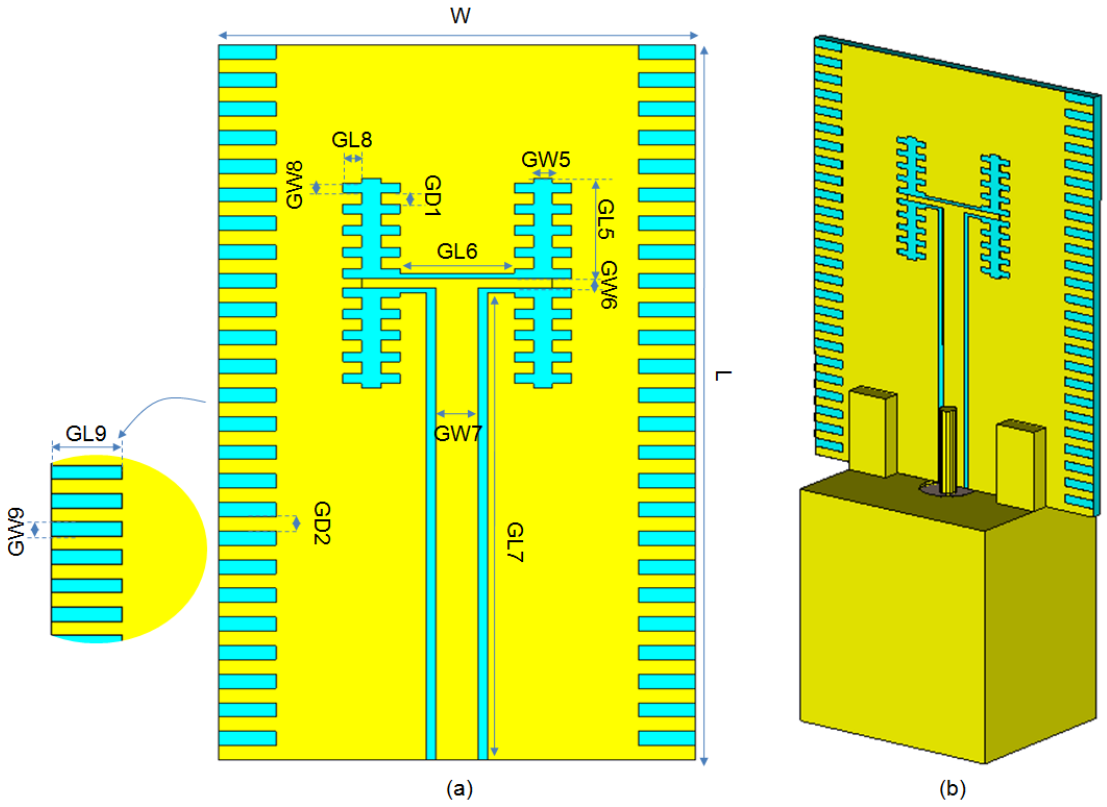

Figure 123. Details of the H-shaped slot antennas designed for the GPPO-based measurement setup. (a) Front view (without the GPPO) (b) Perspective view (with the GPPO).

to study the effects of the design variables. During the parametric sweeps, several design variables were found to be affecting the matching and directivity of the proposed antenna. These main variables are the dimensions of the slot $CL5$ and $CW5$; the dimensions of the slot corrugations $CL8$, $CW8$, and $D1$; and the dimensions of the ground corrugations $CL9$, $CW9$, and $D2$, as shown in Figure 119. It was found through simulations with the GPPO-based antenna that same design variables can be used to optimize the connector-based antenna.

It should be noted that in the following text, the term "**corrugation**" corresponds to the solid rectangles and the term "**slit**" correspond to the gaps between the corrugations.

7.4.1 Slot length, $CL5$

As mentioned before, the slot antenna can be considered as the complementary structure of the dipole antenna. Therefore, the main parameter that determines the resonance frequency of the H-shaped slot antenna proposed in this chapter is the slot length. The slot width affects the input impedance; hence, the matching of the antenna. This is valid for both of the antennas with and without the corrugations.

Figure 124 shows the results obtained from simulating the miniaturized H-shaped slot antenna for different values of $CL5$. As seen in Figure 124a, there are two resonances that merge in the desired frequency band. It was concluded from the parametric sweeps that the first resonance is due to the resonance of the slot, and the second one is due to the mutual coupling between the shorted slots. As the S_{11} graph shows, increasing the slot length decreases both of the resonance frequencies. In all of the cases, there were four slits on each side of the slot arms with $CL8 = 250\,\mu$m, $D1 = 200\,\mu$m and $CW8 = 100\,\mu$m. The steps between the values of $CL5$ were kept as low as $75\,\mu$m to keep the distribution of the corrugations along the slots the same for all the simulated cases.

The effect of the slot length on the directivity pattern of the antenna is also presented in Figure 124b. It was found that a longer slot results in a higher peak gain, similar to the response of a dipole antenna; however, there is a slight difference between the patterns

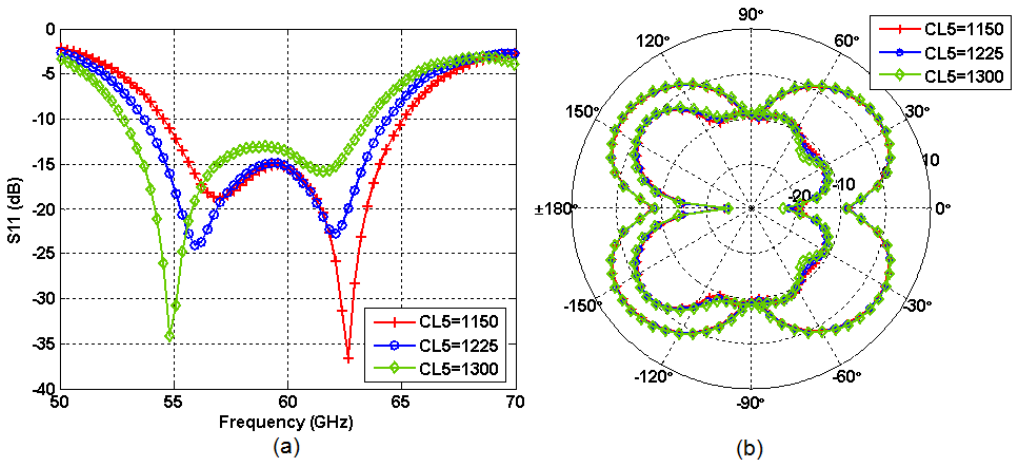

Figure 124. Simulated results for different values of *CL5*. (a) S_{11}, (b) Far field pattern on $\phi = 90°$ and $\theta = 0°$ planes.

shown in Figure 124b due to the small step size between the *CL5* values.

7.4.2 The length of the slits on the slots, *CL8*

Since the slot length determines the resonance length of the antenna, etching slits along the edges of the slots helps to achieve the electrical length with a shorter slot. The length of the slits, labeled as *CL8* in Figure 119, changes both the overall electrical length and width of the slots; hence, it has a strong effect on both the resonance frequency and the matching of the antenna, as shown in Figure 125a. Longer slits result in a lower resonance frequency but also require rematching of the antenna by changing other parameters such as the width and the gap of the feeding CPW lines.

The effect of *CL8* on the directivity pattern of the antennas at 60 GHz is also shown in Figure 125b. The value of *CL8* affects the far field pattern, especially on $\theta = 90°$ plane, since increasing *CL8* decreases the distance between the corrugations along the edge of the ground planes and the ones on the slots. As seen from Figure 125b, the slits should be kept short enough to prevent the coupling to the ground corrugations. If necessary, the width of the ground plane can be increased to eliminate the interaction between the slits on the slots and along the ground edges.

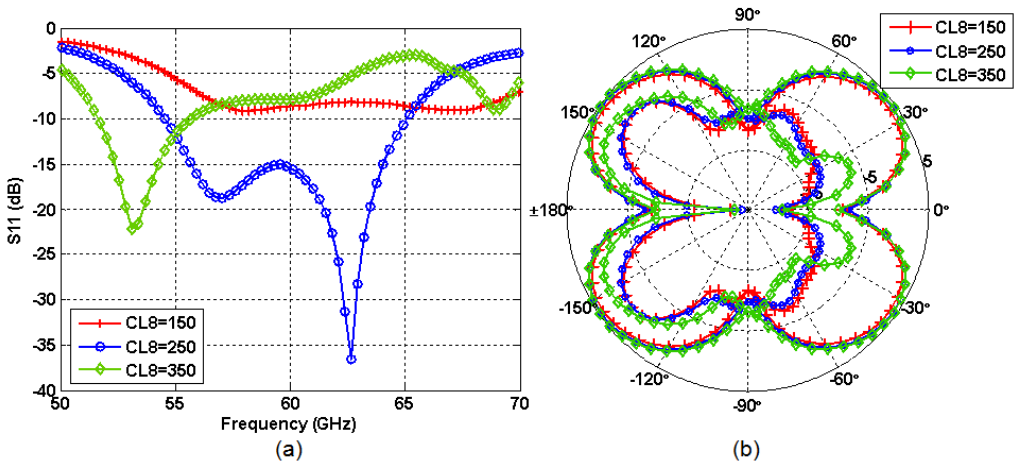

Figure 125. Simulated results for different values of $CL8$. (a) S_{11}, (b) Far field pattern on $\phi = 90°$ and $\theta = 0°$ planes.

7.4.3 Gap between slot corrugations, $D1$

The separation between the slits determines the density of the corrugations on the slots. As expected, decreasing the distance between the slits decreases the resonance frequency, as shown in Figure 126a. In these simulations, the length of the slot arms was kept at $CL5 = 1150\,\mu$m, and the number of the slits were increased as the distance between them was decreased. It can be concluded that more slits with smaller spacing can be used to further decrease the length of the slots. However, it should be kept in mind that decreasing the length of the slots also decreases the gain of the antenna. A rule of thumb can be given as $D1 \approx 2 \times CW8$.

The far field pattern is also presented in Figure 126b. It can be seen that the peak directivity is not affected considerably as the number of slits is increased while making them closer. However, the radiation efficiency was found to decrease from 91% with four slits to 86% with 8 slits.

7.4.4 Width of the slits on the slots, $CW8$

The width of the slits placed on the slots was swept to analyze their effect on the antenna response. In these simulations, the number of slits was kept constant by decreasing the distance between the slits as they were made wider. The effects of varying the width of the

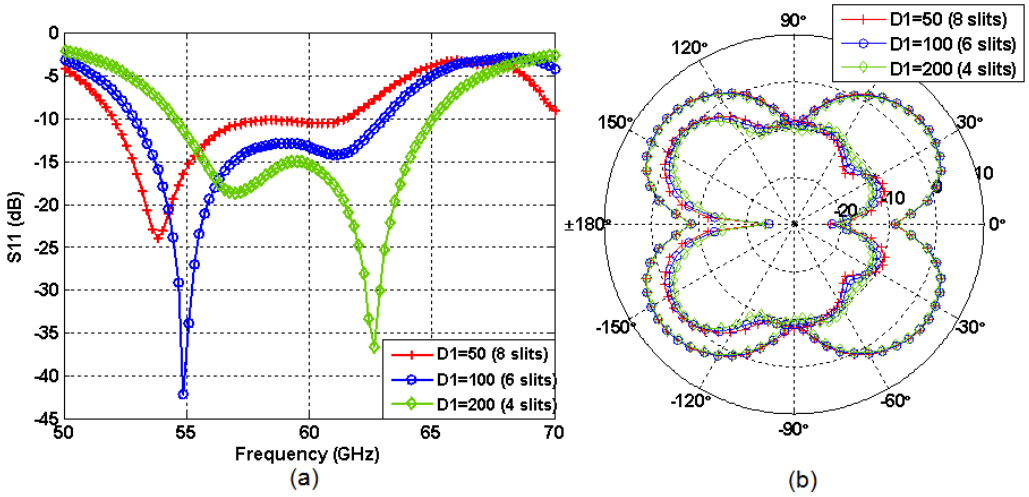

Figure 126. Simulated results for different values of $D1$. (a) S_{11}, (b) Far-field pattern on $\phi = 90°$ and $\theta = 0°$ planes.

slits, $CW8$, along the edges of the slot arms on the S_{11} and the far field of the miniaturized H-shaped slot antenna are shown in Figure 127. As seen in the figure, $CW8$ does not affect the far field pattern of the antenna. On the other hand, creating wider but closer slits along the slots affects the S_{11} of the antenna.

7.4.5 Length of the slits on the edges of grounds, $CL9$

The slits etched along the edges of the ground plane mostly affect the far field pattern of the antenna. However, when the length of the slits forming the corrugations is increased more than a certain value, the S_{11} of the antenna gets distorted, as seen in Figure 128. This is because the current distribution around the slots is altered as the slits on the edges become closer to the antenna. Similarly, the desired effect of the corrugations on decreasing the radiation towards the feed line on $\theta = 90°$ plane starts to disappear when the slits are longer than a certain value. This can be seen in the patterns presented in Figure 128b. A rule of thumb for the length of the ground corrugations is $CL9 \approx \lambda_0 \setminus 10$.

7.4.6 Width of the ground corrugations, $D2$

The width of the corrugations along the edges of the ground plane affects the far field pattern of the antenna. As expected, when the distance between two slits is increased the

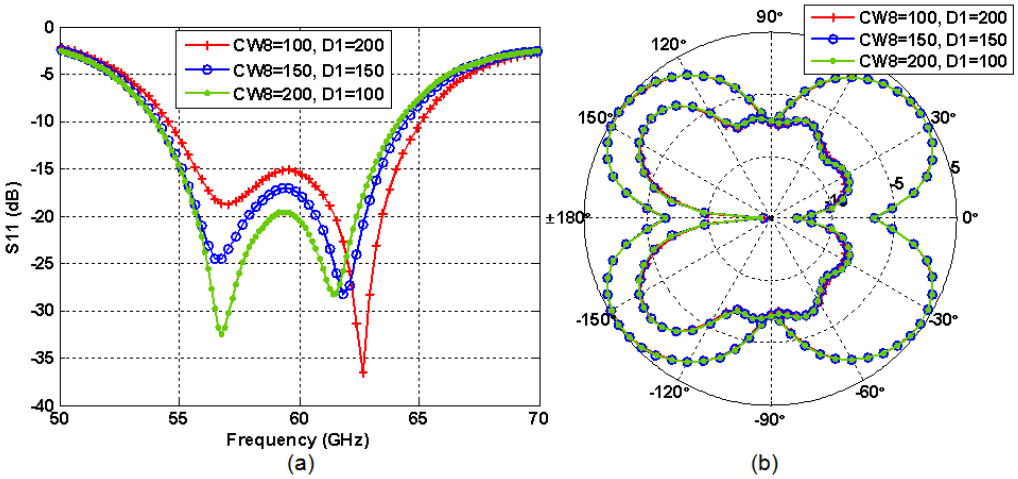

Figure 127. Simulated results for different values of $CW8$. (a) S_{11}, (b) Far-field pattern on $\phi = 90°$ and $\theta = 0°$ planes.

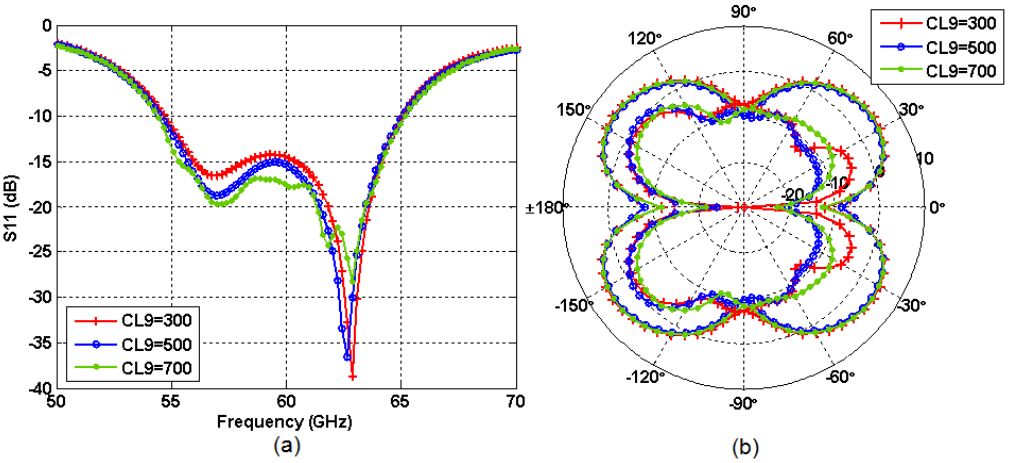

Figure 128. Simulated results for different values of $CL9$. (a) S_{11}, (b) Far-field pattern on $\phi = 90°$ and $\theta = 0°$ planes.

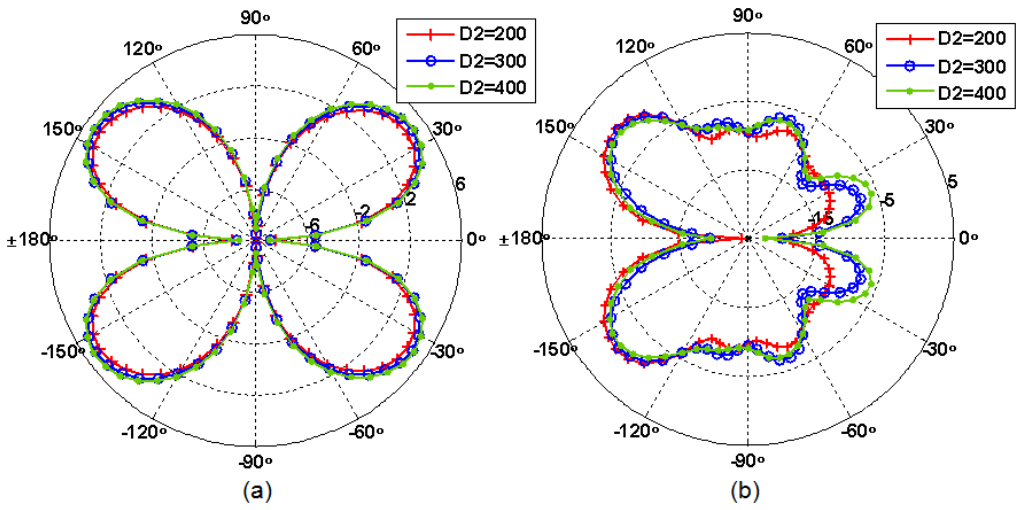

Figure 129. Simulated far field patterns for different values of $D2$. (a)$\phi = 90°$, (b) $\theta = 0°$.

response becomes closer to the case without the corrugations on the ground plane. In other words, the back radiation towards the feedline on $\theta = 90°$ plane increases as $D2$ is increased. The variation of S_{11} with the changes in $D2$ are not included here since S_{11} curves were on top of each other for all $D2$ values simulated.

It should also be noted that the width of the slits along the ground planes, $CW9$, has a similar effect with $D2$ in determining the number of corrugations along the edges of the ground plane. Therefore, the response obtained from $CW9$ sweep is similar to the results presented for $D2$. As $CW9$ is increased the back-radiation of the antenna increases, being similar to the case with no ground corrugations. Also, the S_{11} response is insensitive to the changes in $CW9$.

7.4.7 Distance between the two shorted slot antennas, *CL6*

The distance between the two shorted slot antennas forming the H-shaped slot antenna is labeled as $CL6$ in Figure 119. Figure 130 shows the effects of varying this distance on the S_{11} and the far field pattern of the antenna. As seen from the S_{11} curves in Figure 130a, the second resonance frequency is highly-dependent on this separation while only the matching level of the first resonance is affected. This supports the fact that the second resonance

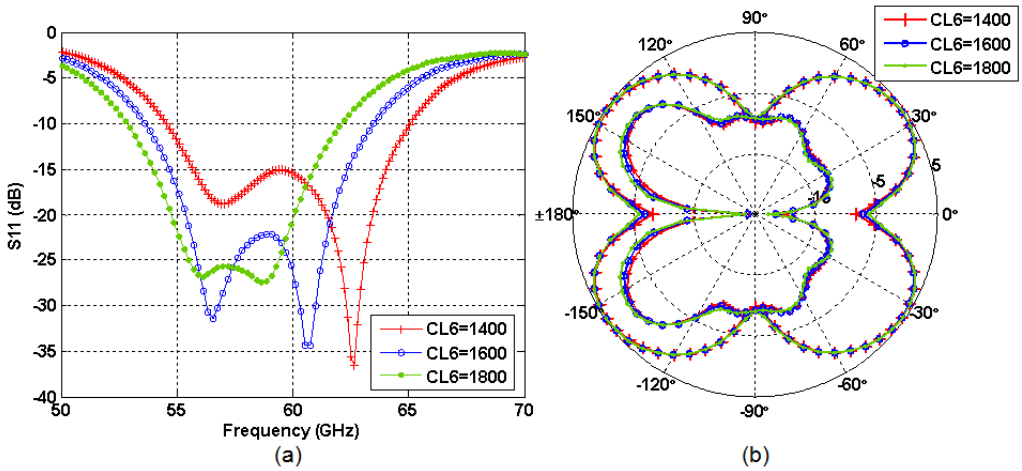

Figure 130. Simulated results for different values of $CL6$. (a) S_{11} , (b) Far-field pattern on $\phi = 90°$ and $\theta = 0°$ planes.

occurs because of the coupling between the two shorted slot antennas comprising the H-shaped slot antenna. The far field pattern is not affected by the value of this separation, as seen in Figure 130b.

7.4.8 Summary of the design guidelines

Although there are many design variables that affect the S_{11} and the far field characteristics of the antenna, the variables can easily be grouped into two categories according to the parameter they affect the most. The effects of the design variables are summarized in Table 7. As expected, the length of the slots $CL5$, the length of the slits $CL8$, the distance between the slits on the slots $D1$, the width of the slits on the slots $CW8$, and the distance between the two shorted H-shaped antennas $CL6$ are the variables that affect the S_{11} and the matching characteristics of the antenna.

The variables determining the dimensions of the corrugations along the edges of the ground planes are the main parameters that affect the far field pattern and back-radiation of the antenna. These variables are the width of the slits $CW9$, the length of the slits $CL9$, and the distance between the slits $D2$. The variables $CL8$ and $CL9$ affect both the S_{11} and the far field pattern of the antenna, especially when the slits are long enough to increase the coupling. For example, when $CL8 > 250\,\mu m$, the slits on the antenna slots become close

Table 7. Summary of the design variables for the H-shaped slot antenna.

	CL5	CL8	D1	CW8	CL9	D2	CW9	CL6
S_{11}	✓	✓	✓	✓	✓	×	×	✓
Pattern	×	✓	×	×	✓	✓	✓	×

to the antenna edges altering the current distribution along the edges of the ground plane, which in turn affects the back-radiation and the far field pattern.

When designing the H-shaped miniaturized antenna, it is recommended first to tune the S_{11} of the antenna to the desired frequency band by adjusting the length of the slots. Next, the slits on the slots can be added and the response can be optimized using the corresponding variables shown in Table 7. Then, the ground corrugations can be added and their dimensions can be tuned to optimize the far field pattern of the antenna. The width and gap of the feeding CPW lines can be used to match the antenna.

7.5 Fabrication

Using the results of parametric sweeps summarized in the previous section, two miniaturized H-shaped slot antennas were designed. As shown in Figures 119 and 123, one of these antennas was designed for the probe-based measurement setup, and the other one was designed based on the connector-based measurement setup. Since the proposed designs are single metal layer structures without any via connections, fabrication process was easy and the antennas were patterned using conventional lithography and etching processes. The fabrication steps can be summarized as follows:

First, a 200 nm Ti and 2 μm Cu layers were deposited on an 8 mil thick bare LCP substrate with a CVC DC sputterer. Then, a Shipley S1828 photoresist was deposited and patterned using a Karl Suss MA-6 mask aligner. Next, the Cu layer was etched with FeCl, and the Ti layer was etched with an HF-based solution to pattern the antennas. Finally, the photoresist was removed using an acetone solution.

The photos of the fabricated designs are shown in Figure 131. The antennas were

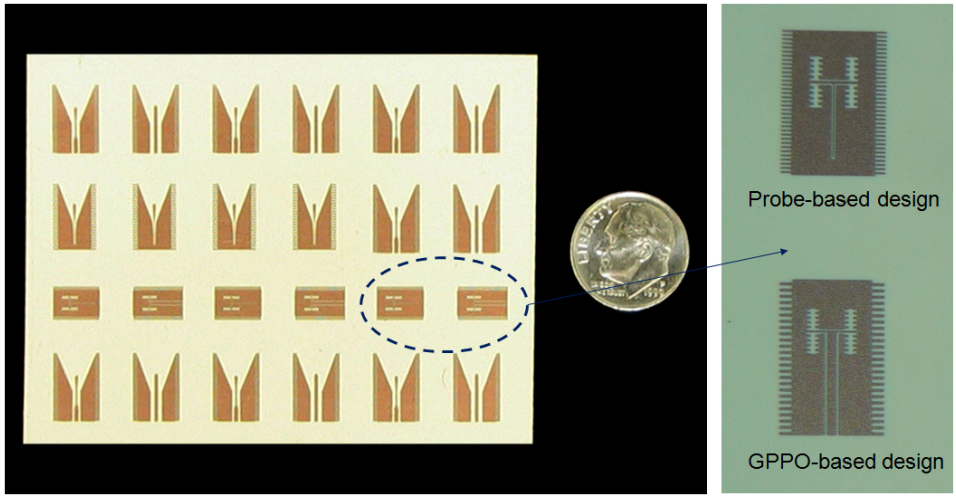

Figure 131. Photos of the fabricated H-shaped antennas compared with 10 cents.

fabricated along with the CPW-fed bi-directional linear tapered slot antennas explained in Chapter 6. The size of the board shown in Figure 131 is 7.5 cm × 5.5 cm.

7.6 Simulation and Measurement Results

Antennas were singulated by cutting the board with scissors. Probe-based and connector-based measurements were performed using an Agilent PNA E8361C. Short Open Load (SOL) calibration was used for both measurement setups.

7.6.1 Probe-based Measurement Setup

Figure 132 shows the setup used for the probe-based measurements. As seen in the photos, the antenna to be measured was placed on a foam substrate since it radiates mainly in the elevation plane.

The measured S_{11} of the antenna is shown in Figure 133 along with the simulated data. As seen in the figure, the measured and simulated results show good agreement but there is a shift in the resonance frequencies. Moreover, the matching level is higher compared to the measurement. The mismatch could be attributed to improper etching of the Ti layer since the gap of the CPW line was only 25 μm for the optimized antenna. The measured 8 dB bandwidth of the antenna was found to be from 52.7 GHz to 66 GHz, covering the band

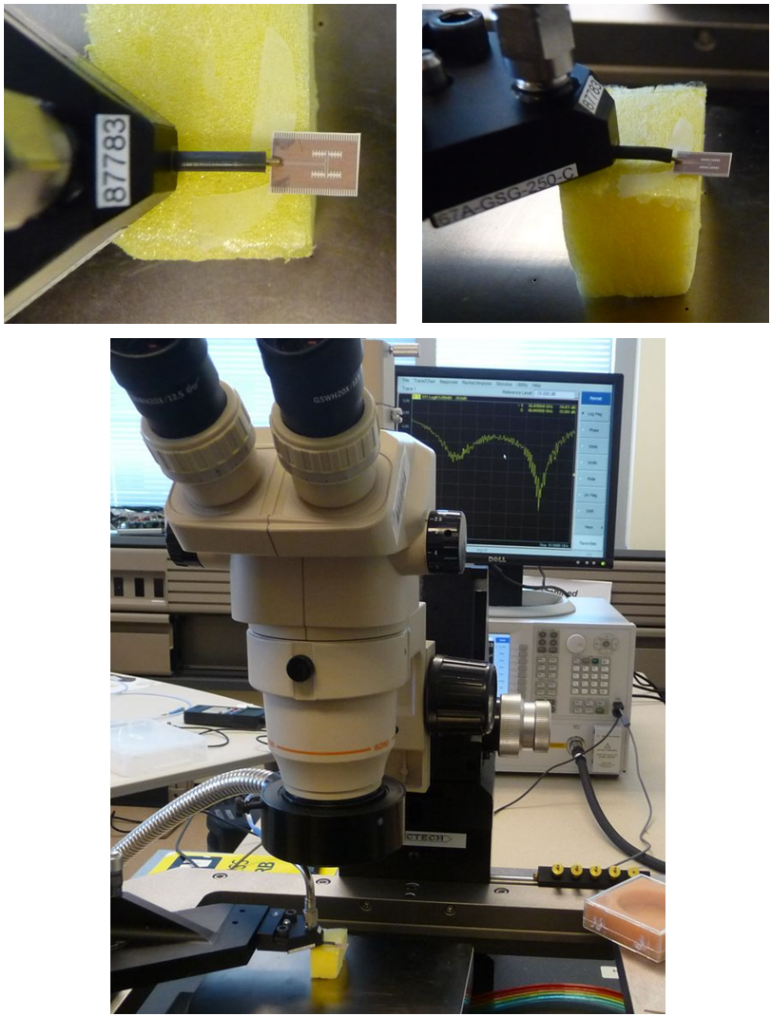

Figure 132. Photos of the probe-based measurement setup.

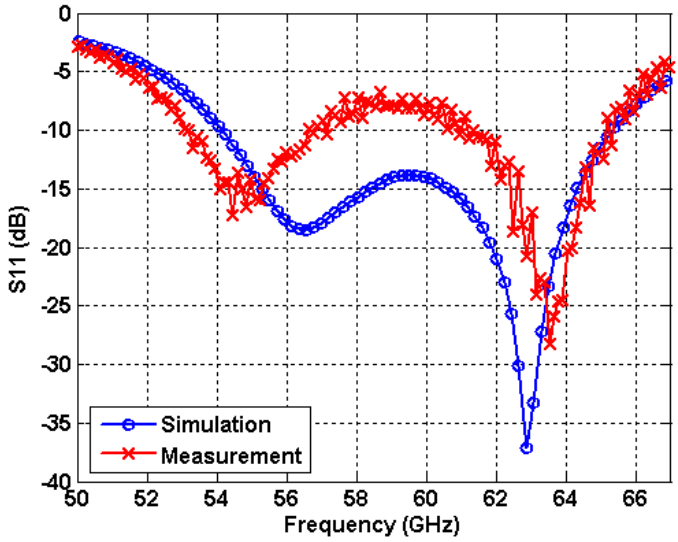

Figure 133. Simulated and measured S_{11} data of the miniaturized H-shaped antenna designed for the probe-based measurement setup.

wider than the desired 7 GHz bandwidth.

Figure 134a shows the simulated 3D gain patterns of the CPW-fed H-shaped antenna designed for the probe-fed setup. The pattern is plotted at 61 GHz. As seen in the figure, the pattern has four beams covering the y-z plane. The simulated directivity patterns of the probe-based antenna at different frequencies are shown in Figure 135. As the figure shows, the antenna pattern is stable over the frequency band, especially on the $\phi = 90°$ plane. The pattern on the $\theta = 90°$ changes slightly with frequency.

Table 7.6.1 summarizes the simulated radiation parameters of the antenna for the probe-based system. The simulated average peak directivity of the antenna is 5.42 dBi in the spectrum from 57 GHz to 64 GHz. The simulated radiation efficiency was found to be around 90% in the whole band. As expected, total efficiency, which includes the effect of the matching of the antenna in addition to the radiation efficiency, is slightly lower and averages to 88% with an average peak gain of 4.9 dB. It should be noted that the gain of the antenna can be increased easily using multiple antennas in an array configuration.

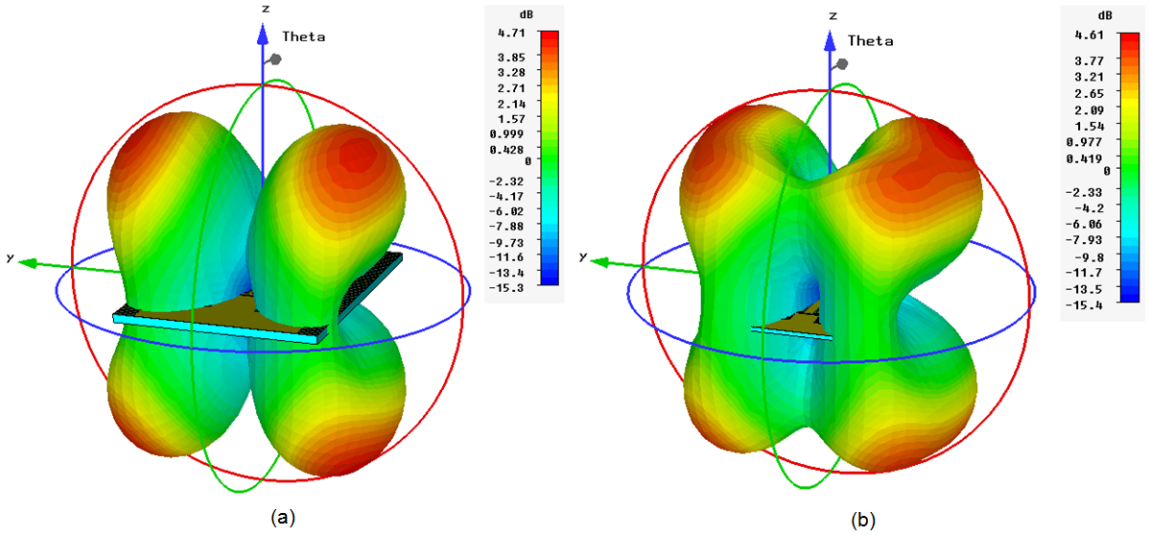

Figure 134. 3D gain pattern of the miniaturized H-shaped slot antenna. (a) Probe-based design, (b) GPPO-based design.

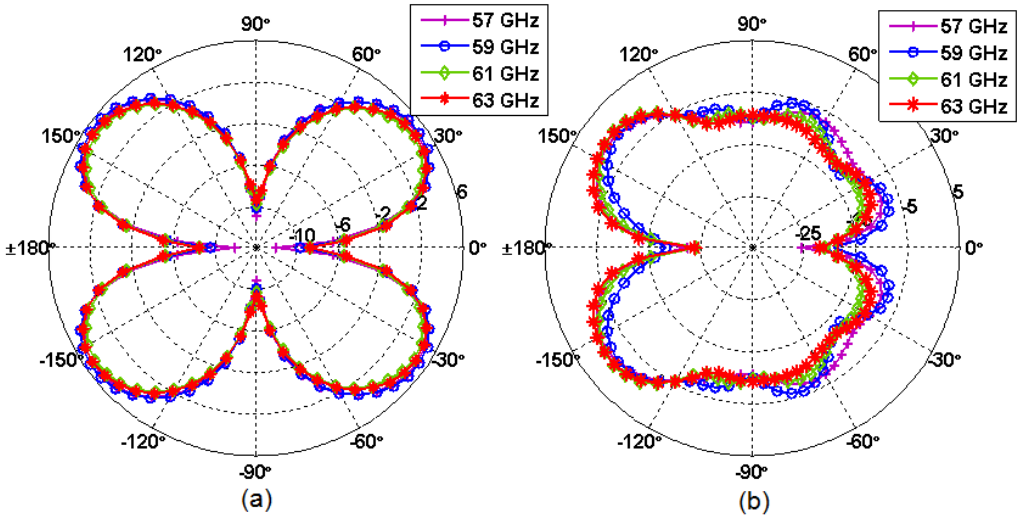

Figure 135. Simulated far field patterns of the miniaturized H-shaped slot antenna for different frequencies. (a)ϕ = 90°, (b) θ = 0°.

Table 8. Summary of the simulated radiation parameters for the probe-fed miniaturized H-shaped slot antenna.

Frequency	Peak directivity	Radiation efficiency	Total efficiency	Peak gain
57 GHz	5.44 dBi	-0.44 dB (90%)	-0.52 dB (89%)	4.92 dB
58 GHz	5.60 dBi	-0.42 dB (91%)	-0.59 dB (87%)	5.1 dB
59 GHz	5.25 dBi	-0.43 dB (91%)	-0.54 dB (88%)	5 dB
60 GHz	5.41 dBi	-0.48 dB (89%)	-0.49 dB (89%)	4.6 dB
61 GHz	5.65 dBi	-0.43 dB (91%)	-0.55 dB (88%)	4.7 dB
62 GHz	5.20 dBi	-0.42 dB (91%)	-0.60 dB (87%)	4.84 dB
63 GHz	5.32 dBi	-0.45 dB (90%)	-0.49 dB (89%)	4.92 dB
64 GHz	5.46 dBi	-0.53 dB (89%)	-0.61 dB (87%)	4.85 dB

Figure 136. Photo of the singulated H-shaped antenna with the GPPO connectors.

7.6.2 Connector-based Measurement Setup

The antennas were also measured with edge-mount millimeter wave connectors, called GPPO connectors. The photos of the antennas fabricated for the connector-based measurement setup are shown in Figures 131 and 136. The GPPO connectors were soldered onto the CPW line feeding the antenna using copper flux. The connectors were soldered only on the ground pads, while the signal pin was left unsoldered to prevent the parasitics due to the solder.

Figure 137 shows the simulated and measured S_{11} of the LTSA designed for the connector based measurement setup. As seen in the figure, the results do not agree well as in the case of probe-based measurement setup. In the figure, the measured S_{11} of the air-loaded cable, i.e. when the cable is not terminated with any structure, is also included. It

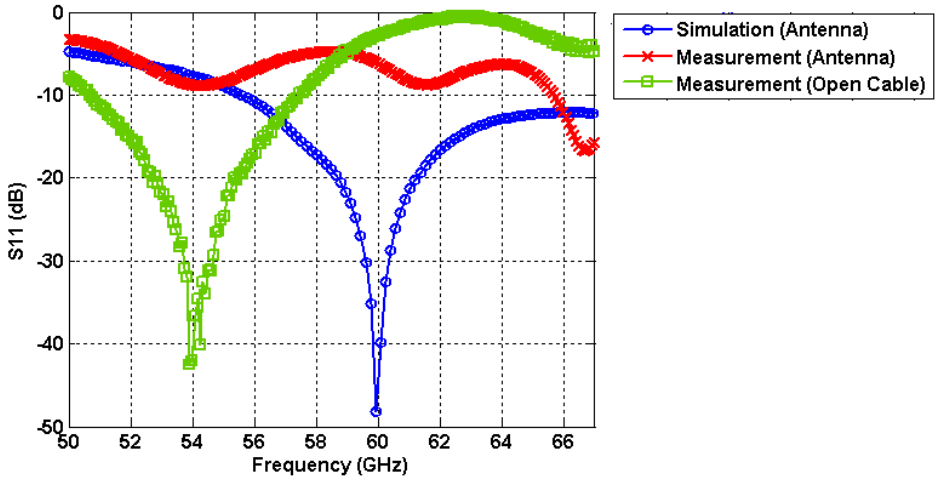

Figure 137. Simulated and measured S_{11} data of the miniaturized H-shaped antenna designed for the GPPO-based measurement setup.

can be seen from the S_{11} of the cable that even after the SOL calibration there is an extra resonance around 55 GHz due to the parasitics of the cable. This resonance is also observed in the antenna S_{11} as a slight resonance. It was also found through simulations that the connector should be flushed to the side of the substrate without any gap and also the signal pin should be touching the signal line to ensure proper connection. Given the tiny size of the connectors, the proper mounting of the connector is difficult to achieve and the disagreement between the measured and the simulated results can be attributed to the aforementioned problems. Moreover, an adapter is used to connect the GPPO connectors to the PNA cables. Since the adapter cannot be calibrated out, the measurement data includes the effect of the adapter as well, which might be another reason for the disagreement between the measured and simulated results.

The simulated 3D gain pattern of the antenna with the GPPO connector at 61 GHz is shown in Figure 134b. Comparing the pattern with the pattern of the probe-based antenna in Figure 134a reveals the distortion in the far field of the antenna due to the radiation of the currents on the connector. Figure 138 shows the directivity patterns of the antenna at different frequencies. As seen in the graphs, the multi-beam pattern is preserved over the desired frequency band. The radiation pattern of the antenna was not measured since the

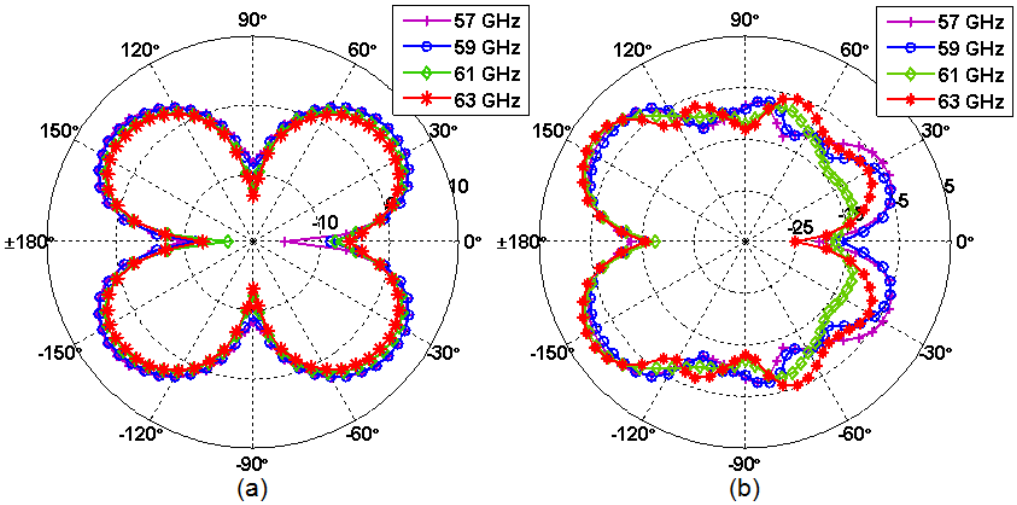

Figure 138. Simulated far field patterns of the miniaturized H-shaped slot antenna designed for the GPPO-based measurement setup. (a)$\phi = 90°$**, (b)** $\theta = 0°$**.**

antenna measured with the GPPO connectors were not matched well, as shown in Figure 137.

The radiation parameters are summarized in Table 7.6.2. The values are similar to the values in Table 7.6.1.

7.7 Conclusions

A novel wireless technology is emerging for the usage of the unlicensed 7 GHz spectrum around 60 GHz for high-throughput short-range wireless communications. Along with the high-speed data transfer capabilities and miniaturized systems, the high carrier frequency brings several challenges, such as increased path loss, material loss and reflections, that require directive, easy-to-fabricate and easy-to-integrate antennas to be used in these systems. Moreover, it is crucial for proper operation and cost issues that the designs selected are insensitive to the fabrication tolerances. Slot antennas have all of the aforementioned advantages along with being low-profile and having the ability to provide wide bandwidth and directive gain operation. In this chapter, a CPW-fed resonant-type H-shaped slot antenna has been presented.

The antenna proposed is a single metal layer structure that can be fabricated easily.

Table 9. Summary of the simulated radiation parameters for the GPPO-fed miniaturized H-shaped slot antenna.

Frequency	Peak directivity	Radiation efficiency	Total efficiency	Peak gain
57 GHz	6 dBi	-0.37 dB (92%)	-0.56 dB (88%)	5.46 dB
58 GHz	6.14 dBi	-0.37 dB (92%)	-0.46 dB (90%)	5.69 dB
59 GHz	5.86 dBi	-0.37 dB (92%)	-0.4 dB (91%)	5.46 dB
60 GHz	5.36 dBi	-0.36 dB (92%)	-0.36 dB (92%)	5 dB
61 GHz	5 dBi	-0.36 dB (92%)	-0.39 dB (91%)	4.6 dB
62 GHz	4.7 dBi	-0.37 dB (92%)	-0.45 dB (90%)	4.26 dB
63 GHz	4.5 dBi	-0.37 dB (92%)	-0.54 dB (88%)	3.99 dB
64 GHz	4.8 dBi	-0.37 dB (92%)	-0.61 dB (87%)	4.2 dB

Moreover, since it is created by combining two CPW-fed shorted slot antennas, the radiation pattern of the antenna has four beams, covering four different directions at the same time. Although, the peak gain of the antenna decreases when the power is divided in multiple directions, the antenna can be used in an array configuration to overcome this problem. The average 6 dB gain of the antenna can be increased approximately to 9 dB by using a two-element array configuration.

Miniaturization of the length of the slots comprising the antenna has also been discussed in this chapter. A method based on etching slits along the edges of the slots has been proposed to achieve the required electrical current length with a shorter slot length. The length of the slots was decreased from $L1 = 1650\ \mu$m to $CL1 = 1150\ \mu$m by incorporating the corrugations on the slots.

In addition to the miniaturization of the slots, the slits were also used to create corrugations along the edges of the ground plane to prevent the diffraction of the surface waves. The method proposed has been shown to eliminate the back-radiation that can cause undesired coupling to the feed elements. The effects of the design variables that can be used to optimize the antenna response have been presented along with some guidelines.

Moreover, the proposed antenna structure was designed for measurement with probe-based and connector-based setups to compare the results obtained from these setups. It was

found that the probe-based measurement setup is more suitable to measure the response of the antenna since the connector requires additional adapters, which introduces discontinuities that are difficult to de-embed. Moreover, the tiny size of the connectors makes it difficult to mount them on the fabricated designs.

CHAPTER 8

STACKED TRIANGLE PATCH ANTENNAS ON MULTILAYER RXP-BASED SUBSTRATES

The internationally available 7 GHz of unlicensed spectrum around 60 GHz promises a wide range of applications that can support multi-gigabits per second throughput. Replacing the high-definition media interface (HDMI) cables with wireless compressed video streaming as part of a wireless personal area network (WPAN) is one example of several desired applications. These applications require compact, low-cost and high-performance wireless systems. Compared to the WLAN/WiMAX applications, the size reduction of these systems is achieved inherently with the miniaturization factor that comes with the high operational frequency. In addition to the miniaturization, efficient integration is critical for designing high-performance systems. Advanced packaging technologies, such as the system-on-package (SOP) technology, have been shown to provide highly-integrated, low-cost solutions using multilayer substrates. However, the need for effective antenna integration with the passive and active circuitries is still a barrier for achieving low-loss and low-noise systems.

Low temperature co-fired ceramic (LTCC) technology has been a popular solution for applying SOP in both the WLAN and V bands. The high-permittivity and low loss tangent of the multilayer LTCC substrates have been advantageous for the miniaturization and integration of RF components. However, LTCC may not provide a cost effective packaging solution due to the higher processing temperature (> 900°C) and the larger manufacturing variations as compared to the multilayer organic technologies (MLO) [19]. Furthermore, organic substrates with a moderate value of dielectric constant provide a better medium to achieve the wide-band matching of the antenna than the LTCC substrate with high dielectric constant.

Therefore, the SOP solution based on liquid crystalline polymer (LCP) has been considered as a promising alternative for RF-system integration due to its superior electrical properties up to millimeter wave frequencies [20]. However, the LCP is based on a relatively high processing temperature (290°C) compared to the FR-4, which creates limitations for low-cost system integration. Recently, a novel ultra-thin organic dielectric material, called RXP, has been introduced which can help to extend the micro-scale SOP to nano-scale SOP. RXP has two variants called RXP-1 and RXP-4. RXP-1 is used as the core material, and RXP-4 is the build-up layer used to replace the bondply layer of the LCP. The RXP technology is more advantageous than the LCP technology in terms of preventing registration errors since the build-up layer is a variant of RXP. Moreover, the RXP technology uses a lower processing temperature (220°C), which has better compatibility with the standard printed circuit board (PCB) manufacturing processes [22]. It also enables building thinner substrates and finer lines/spaces compared to the LCP technology. For instance, 30-50 μm diameter through-vias, 25-40 μm blind vias and 15 μm line/spaces can be fabricated with the RXP technology [21].

Figure 139 captures the integration techniques based on using the multilayer RXP-based substrates. As a first step in integration, RXP-based MLO substrates can be designed as a separate substrate for the antenna and the passive front-end components, as shown in Figure 139a. Next, the integration can be further improved by placing the chip in a cavity constructed in the MLO substrate, as shown in Figure 139b.

In this chapter, stacked triangle patch antenna array configurations based on multilayer RXP-based substrates are presented. These antenna configurations provide the initial step for realizing antenna integration on the RXP-based multilayer substrate for 60 GHz WPAN applications. This chapter starts with a review of the stacked patch antennas in Section 8.1. Next, the first stacked patch antenna array configuration is introduced in Section 8.2. Detailed design analysis is provided along with some design guidelines for the antenna designers. Then, the second configuration, which is achieved with a slight modification

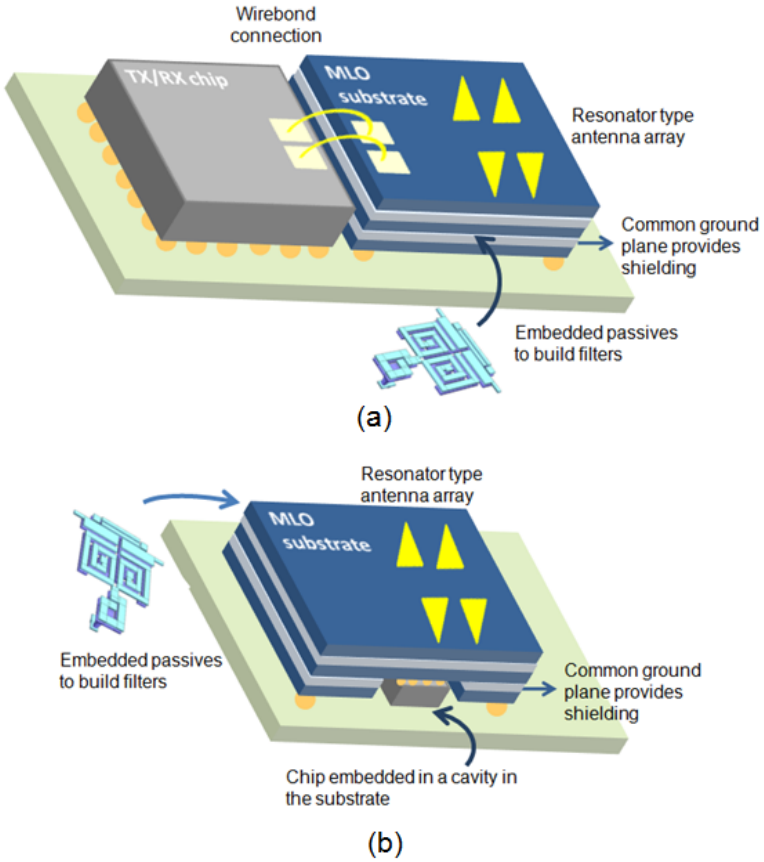

Figure 139. Conceptual integration techniques for RXP-based MLO substrates. (a) MLO as a separate substrate housing the passive components. (b) Chip embedded in a cavity in the MLO substrate.

to the first one, is discussed in Section 8.3. Following this section, the designs optimized for the connector-based measurement setup are presented in Section 8.4. Next, the design optimized for the probe-based measurement setup is presented in Section 8.5. The chapter is concluded with Section 8.6.

8.1 Review of Stacked Patch Antennas

Microstrip patch antennas are resonator-type antennas that consist of a radiating patch printed on a grounded substrate. Microstrip patch antennas have numerous attractive features such as light-weight, low-profile, low-cost, conformability, and easy fabrication [6]. Moreover, their directive radiation pattern and the ability to work with a ground plane are advantageous to achieve vertical integration in multilayer substrates, as suggested for SOP. The primary limiting factor in the use of microstrip patch antennas is their inherently narrow bandwidth, which requires a bandwidth-enhancement technique to be applied along with the antenna design.

Stacked patch configurations implemented on multilayer substrates have been proposed to increase the bandwidth of the patch antennas. The analysis of the aperture-stacked patch antennas has been published in [103], where vertically-stacked rectangular patch antennas were fed by a microstrip line through a resonant aperture. Wide bandwidth was reported in this paper by balancing coupled resonances between the stacked patches and the resonant aperture. A similar stacked patch configuration was studied in [104], where a CPW-fed slot antenna was used to excite the stacked patches. Stacked patch antennas were also designed in LTCC substrates [105], where a probe-feed was used instead of an aperture- or a slot-feed. Recently, a parasitically coupled stacked patch antenna array on a multilayer Teflon substrate was proposed in [106] for V-band applications.

In all the aforementioned papers, thick multilayer substrates were used. For instance, the total thickness of the substrate for the stacked rectangular patch antenna array reported in [106] is 1.1 mm even though the antenna operates at 60 GHz. Although the thickness

of the substrate between the stacked patches is a useful design parameter to optimize the performance of the stacked patch antenna designs, thick substrates suffer from increased surface wave propagation especially at millimeter wave frequencies. Moreover, employing thick substrates does not agree with the aim of miniaturization.

The thickness of the RXP-based multilayer substrates housing the proposed stacked patch antenna arrays presented in this chapter is only 330 μm. Furthermore, triangular patch antennas are used instead of the rectangular patch antennas since triangular patch antennas can provide the same performance in a more compact size compared to the rectangular patch antennas [6]. Moreover, the performance of the triangular patch antennas can easily be tuned using a stub added at the tip or the base of the antenna.

In this chapter, a triangular patch antenna array that utilizes a resonant aperture with parasitically-coupled stacked patches is presented. The 11.67% wide bandwidth requirement for the 60 GHz applications was achieved by merging coupled resonances. The proposed structure using the multilayered configuration is a more compact array solution compared to the single-layer series- or parallel-fed antenna arrays.

8.2 Stacked Triangular Patch Antenna Array (STPAA)

The cross-section of the RXP-based multilayer substrate and the proposed stacked triangular patch antenna array (STPAA) are shown in Figure 140. The substrate is a five-layer balanced stack-up, where a middle 100 μm thick RXP-1 layer is supported by a two-layer stack-up of 20 μm thick and 60 μm thick RXP-4 layers at the top and the bottom. The lateral size of the substrate is 5.5 mm $\times$ 8.5 mm. The dielectric constant and the loss tangent of the layers at 60 GHz are ϵ_r = 3.39 and 0.0038 for the RXP-1 layer, and ϵ_r = 3.01 and 0.0043 for the RXP-4 layers, respectively [22].

Although the five-layer stack-up provides six layers available for metallization, labeled from M1 to M6 in Figure 140, only the metal layers M1, M3, M4, and M6 were employed in the proposed design. The details of the metallization of these layers are shown in Figure

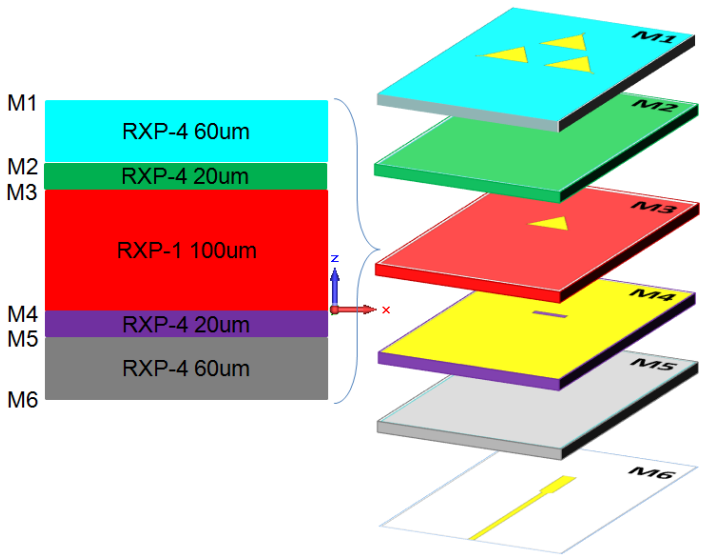

Figure 140. Cross-section of the RXP-based stack-up used for the proposed stacked triangular patch antenna array.

141.

There are four triangular patch antennas in the proposed STPAA. These antennas are labeled as A1, A2, A3, and A4, as illustrated in Figures 141a and b. All of the triangular patches were designed as equilateral triangular patches with side lengths $S1$ for A1, A2, A3; and $S2$ for A4. A4 denotes the centered triangular patch antenna placed on metal layer M3. The antenna A4 is excited by the microstrip line on M6 through the aperture etched on the ground plane occupying M4. The other three triangular patch antennas A1, A2 and A3, are placed on M1 such that the antenna A4 is aligned in the center of these parasitic triangular patches, being equidistant from each patch. The triangular antennas A1, A2, and A3 on M1 are parasitically coupled to A4 on M3.

As seen in the enlarged image of the antenna A1 in Figure 141a, a stub with length $S3$ is placed at the tip of the A1. The parasitic antennas A2 and A3 are rotated images of the antenna A1 by 120° and 240° around the center O shown in Figure 141a. Therefore, the stubs on these antennas are positioned at the outmost tip of each antenna.

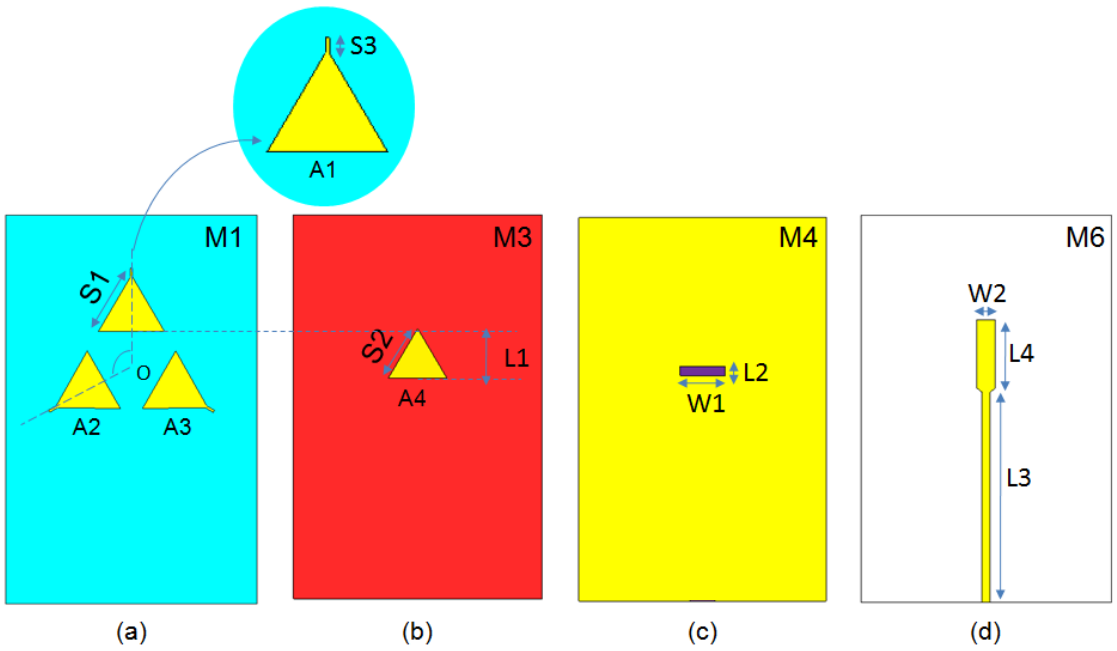

Figure 141. Details of the stacked triangular patch antenna array. (a) Metal layer M1, (b) Metal layer M3, (c) Metal layer M4, (d) Metal layer M6.

Two feeding methods were considered for the initial design. The first method considered was the proximity feed, where the ground plane was placed on M6 and a 50Ω microstrip line was designed on M5, aligned under the antennas. The proximity-feed method enables the use of both the probe-based or the connector-based measurement setups. However, the spurious radiation from the feed lines interferes with the antenna radiation creating distortion in the far field pattern, as seen in the E-field plot in Figure 142a. These E-field plots were obtained by simulating the STPAA model using the commercially available full-wave electromagnetic solver, CST-MWS software [58].

The second, and the preferred, method was the aperture-coupling feed method, where the ground plane is moved to M4, and the microstrip line is placed on M6. Although exposing the microstrip line at the back of the substrate limits the designer to use only the connector-based measurement setup, the aperture coupled feed avoids the coupling of the spurious line radiation with the help of the shielding ground plane, as shown in Figure 142b. Moreover, the aperture can be designed as a nearly-resonant structure, which not only provides coupling of the microstrip line fields but also contributes to the resonance

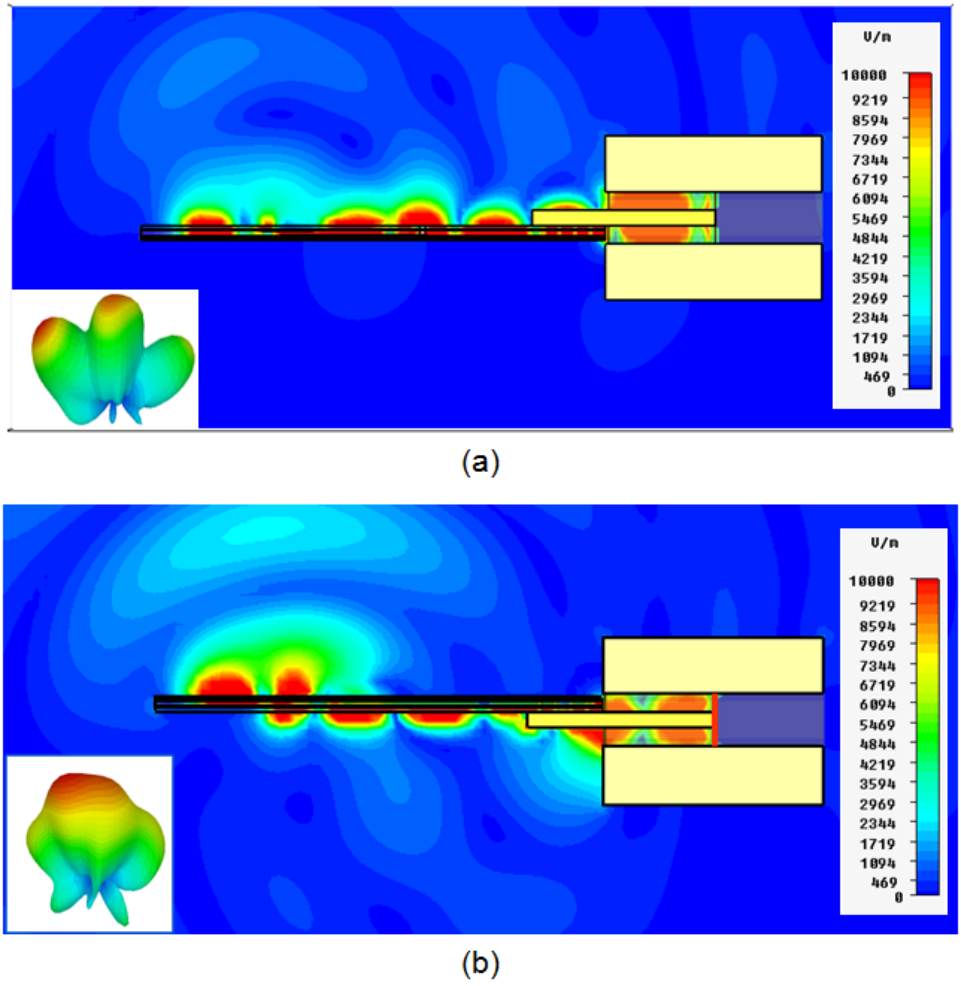

Figure 142. Comparison of the E-field magnitude plots for the proximity- and the aperture-feed cases. The far field patterns for both cases are shown in the inset images. (a) Proximity-coupling feed, (b) Aperture-coupling feed.

[103]. Impedance matching can also be achieved easily for the aperture-coupling feed by terminating the open end of the microstrip line with a lower impedance line to control the coupling through the aperture, as shown in Figure 141d.

8.2.1 Design Based on Simulation

The enhancement in the bandwidth obtained with the aperture-coupled stacked patch antenna configuration is a result of coupled resonances. These resonances are produced by several coupling mechanisms that occur between the aperture and the antenna elements. In general, these resonances produce a resonance loop on the impedance locus when plotted on a Smith chart, where the size of the loop can provide information on the coupling factor. In other words, the larger the radius of such a loop, the greater the coupling factor [103], [104].

There are several coupling mechanisms in the proposed STPAA configuration. Full-wave electromagnetic field solutions obtained through CST-MWS simulations were analyzed to understand these coupling mechanisms and the modes excited in the proposed STPAA. Figure 143 displays the plots of the normal E-field magnitude for the three degenerate modes excited at 59.5 GHz, 62.5 GHz and 65.5 GHz. These frequencies are the three resonances observed in the S_{11} of the antenna. These frequencies can also be found using the Smith chart since the impedance locus of the antenna crosses the real axis of the Smith chart at the frequencies the antenna resonates. In this study, the frequencies to plot the mode fields at are chosen as the ones at which the loops on the impedance locus of the antenna crosses the real axis of the Smith chart second time. It was observed from the Smith chart plots that, the loops on the impedance loci do not cross the real axis for some cases, i.e. the antenna is close to resonance but does not fully resonate. For these cases, the mode frequencies were defined as the frequencies that correspond to the middle points of the loops on the impedance locus of the antenna on the Smith chart.

The fields in Figure 143 are plotted on $z = 50\ \mu$m plane, which is between the antenna A4 and the ground plane, and on $z = 145\ \mu$m plane, which is between the antenna A4 and

the parasitic patches A1, A2, and A3. The orientation of the coordinate system is shown in Figure 140. In all of the field plots presented in the rest of this chapter, these two plane-cuts are displayed. Moreover, in all of the field plots, the phase values are determined such that the top half of the antenna A1 is excited with the peak value of the +z-directed normal field.

It can be seen from Figure 143 that, the patches A1 and A4 are mainly excited in the dominant TM_{10} mode for all frequencies. However, the antennas A2 and A3 are mostly excited with a degenerate TM_{10} mode due to having the stub positioned at the bottom outmost tip of these patches. The coupling between these degenerate modes excited under the antennas A2 and A3 leads to a resonance that would not appear otherwise, which is explained later in this chapter. Analyzing the simulated field plots further reveals that, another coupling mechanism contributing to resonance is the coupling between the aperture and the lower triangular patch A4. The coupling among the lower patch A4, and the upper parasitic patches A1, A2 and A3 also contributes to the resonances.

The interaction of these coupling mechanisms and the resultant mutual resonances lead to a complex design process that depend on several design parameters. To achieve the bandwidth requirements for V-band applications, it is critical to balance these coupling mechanisms such that the loops corresponding to the mutual resonances on the impedance loci become tight loops that are close to each other and in the desired voltage standing wave ratio (VSWR) circle.

To achieve this goal and also gain insight on the effect of the design variables, a systematic parameter study was conducted based on full-wave electromagnetic simulations performed with CST. The effect of the critical design variables were studied extensively using the field plots and Smith chart plots. These parameters are the dimensions of the triangular patches ($S1$ and $S2$), the stub length ($S3$), the relative position of A1 with respect to A4 ($L1$), the dimensions of the aperture ($W1$ and $L2$), and the dimensions of the low impedance line ($L4$ and $W2$). During each sweep, only one variable was altered while the

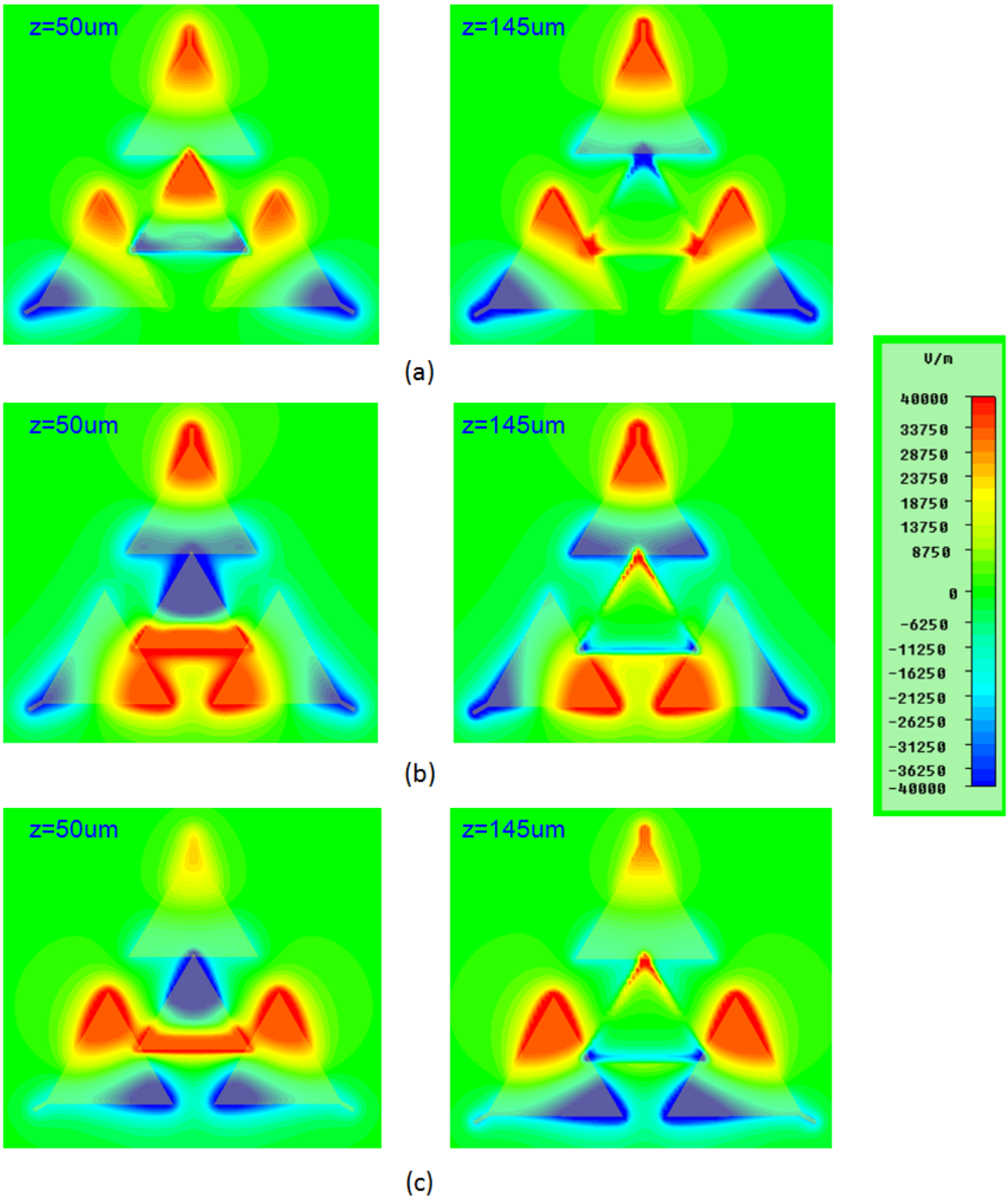

Figure 143. Simulated normal E-field plots for the three modes excited under the stacked triangular patch antenna configuration. The fields are plotted on $z = 50\ \mu$m and $z = 145\ \mu$m. The phase values are determined such that the tip of the A1 is excited at the peak value on all conditions. (a) Mode 1 (at 59.5 GHz), (b) Mode 2 (at 62.5 GHz), (c) Mode 3 (at 65.5 GHz).

others were kept at the following values: $S1 = 1500\,\mu$m, $S2 = 1300\,\mu$m, $S3 = 150\,\mu$m, $L1 = 1125\,\mu$m, $W1 = 1000\,\mu$m, $L2 = 200\,\mu$m, $W2 = 400\,\mu$m, and $L4 = 1500\,\mu$m.

The thicknesses of the substrates between the patches and the ground plane are other critical design variables for the stacked patch antenna configurations. These variables were not used to optimize the final design in this study since the stack-up was predetermined by the fabrication process. However, the effects of these variables are also included in this analysis for the sake of completeness. A set of design guidelines was formulated at the end of this parameter sweep study.

8.2.1.1 L1 Sweep

The distance between the antenna A1 and the antenna A4, labeled as $L1$ in Figure 141b, is one of the main parameters that affects the coupling between the antennas; hence, the resonance frequencies. Increasing $L1$ decreases the overlapped area between the antenna A4 and the parasitic patches A1, A2 and A3.

Figure 144 presents the simulated normal E-field plots for $L1 = 925\,\mu$m case. The fields are plotted on the previously defined cut-planes at 54.5 GHz, as shown in Figure 144a, and at 63.6 GHz, as shown in Figure 144b, which are the resonance frequencies of the two modes excited for this case.

The effect of $L1$ on the coupling between the antennas can be understood by comparing the field plots of Mode 1 for the $L1 = 925\,\mu$m case shown in Figure 144 and the $L1 = 1125\,\mu$m case shown in Figure 143. Comparing the $z = 145\,\mu$m plot in Figure 144a with the corresponding plot in Figure 143a reveals that the fields become stronger as the overlapping area is increased, while decreasing $L1$. Similar result can be concluded from the comparison of the plots for Mode 2 in Figure 144b and 143b, since the antennas A2 and A3 become closer as $L1$ is decreased. Increased field intensity denotes increased coupling, which can also be observed from the Smith chart plots as large loops.

Figure 145 shows the impedance loci for different values of $L1$. The circle corresponding to the desired VSWR value is also included in the graphs. This value was taken as

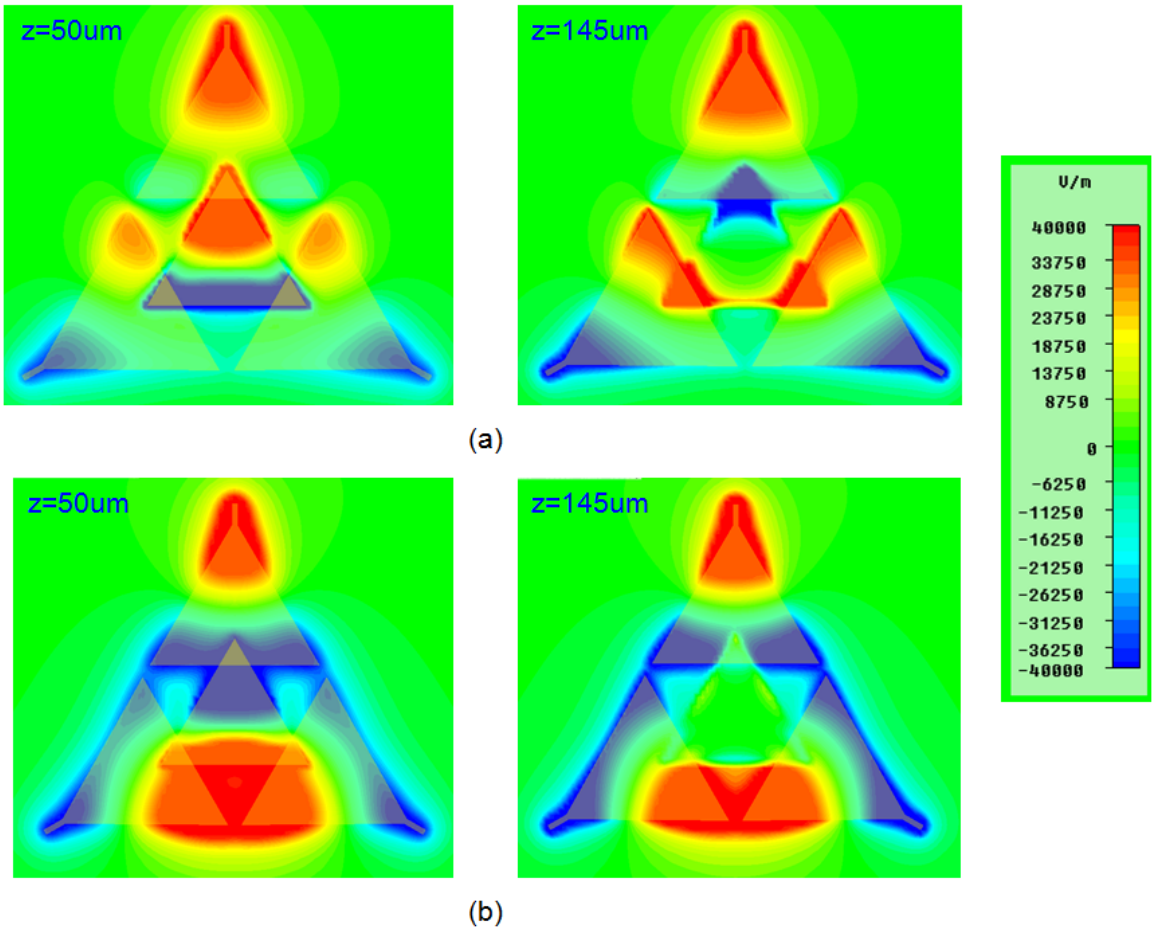

Figure 144. Simulated normal E-field plots for the two modes excited for $L1 = 925\ \mu$m case. The fields are plotted on $z = 50\ \mu$m and $z = 145\ \mu$m. The phase values are determined such that the tip of the A1 is excited at the peak value on all conditions. (a) Mode 1 (at 54.5 GHz), (b) Mode 2 (at 63.6 GHz).

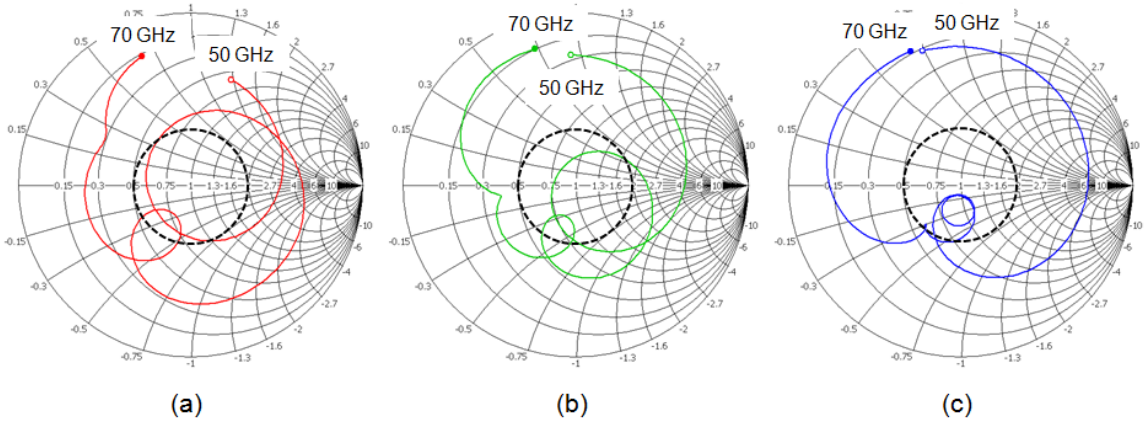

Figure 145. Impedance loci for different values of $L1$. (a) $L1$ = 925 μm, (b) $L1$ = 1025 μm, (c) $L1$ = 1125 μm.

VSWR$\leqslant$2:1, equivalent to S11$\leqslant$-10 dB, for all the cases presented in this chapter. Analyzing the impedance locus from Figure 145a to 145c, it is concluded that the first resonance loop becomes smaller and moves to higher frequencies. Smaller loop size is caused by increasing $L1$ which decreases the vertical coupling between the antennas. This is expected since the overlapping area is decreased with increasing $L1$. Observing the second loop reveals that, the second resonance is not affected as much as the first resonance loop. However, similar to the first resonance, the loop becomes slightly tighter as $L1$ is increased. This is expected since as $L1$ increases, the antennas A2 and A3 move further apart from each other, resulting in weaker coupling. It should also be noted that a third resonance loop appears and moves to lower frequencies as $L1$ is increased. $L1$ = 1125 μm provides the proper balance among the coupling mechanisms, making the resonance loops tighter, closer to each other and inside the 2:1 VSWR circle, as shown in Figure 145c.

The simulated S_{11} data is also shown in Figure 146a on a rectangular plot. Similar conclusions can also be drawn by analyzing this plot; however, the impedance loci provides a better method to understand the strength of the coupling mechanisms. Figure 146b shows the effect of the $L1$ variation on the directivity pattern plotted on the $\phi = 90^\circ$ plane. As the figure shows, $L1$ has a minor effect on the peak directivity. On the other hand, the back radiation increases and the radiation efficiency decreases from 81% to 72% as $L1$ is

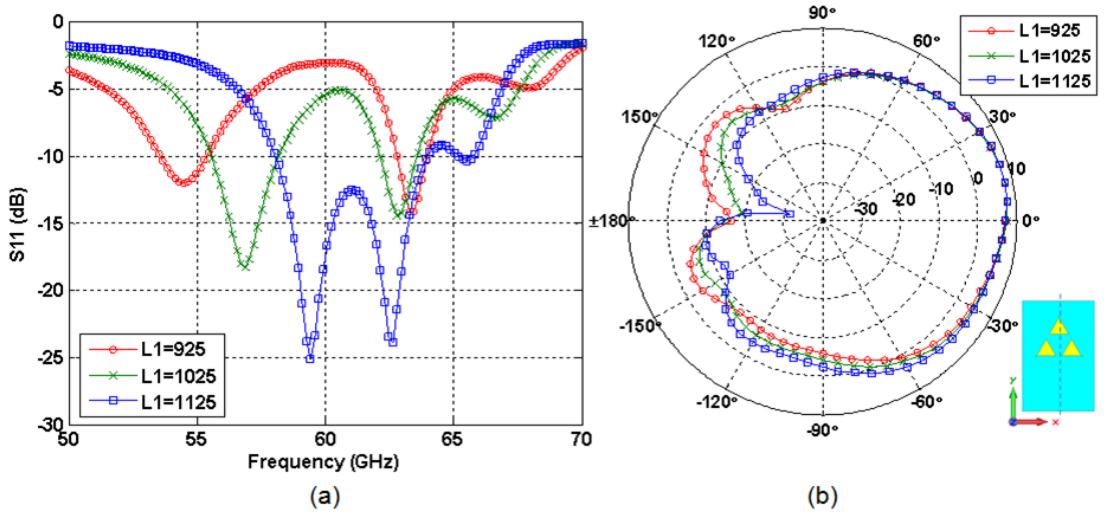

Figure 146. Simulated data for different values of $L1$. (a) S_{11}, (b) Directivity pattern at 58 GHz on the $\phi = 90°$ plane.

decreased from $L1 = 1125$ μm to $L1 = 925$ μm. The far field pattern on $\phi = 0°$ plane is not presented since the patterns on the $\phi = 0°$ and the $\phi = 90°$ planes are similar to each other due to the broadside pattern of the patch antenna.

8.2.1.2 S2 Sweep

In addition to the parameter $L1$, the side length of the antenna A4, $S2$, is another critical parameter that determines the size of the overlapping area between the antenna A4 and the parasitic patches A1, A2, and A3. Therefore, $S2$ also affects the strength of the mutual coupling between these antennas. The effect of $S2$ variation on the impedance loci and S_{11} are shown in Figures 147 and 148a, respectively.

As concluded from the $L1$ sweep, the mutual coupling between the antenna A4 and the parasitic patches increases as the size of the overlapping area between these antennas is increased. This can be seen in the impedance loci as an enlarging first loop that moves counter-clockwise to lower frequencies and onto the inductive region as we move from Figure 147a to 147c thereby increasing the size of A4. It should be noted that the same trend was observed moving from Figure 145c to 145a. This is expected since both directions result in an increased overlapping area. Supporting conclusions can also be drawn from the

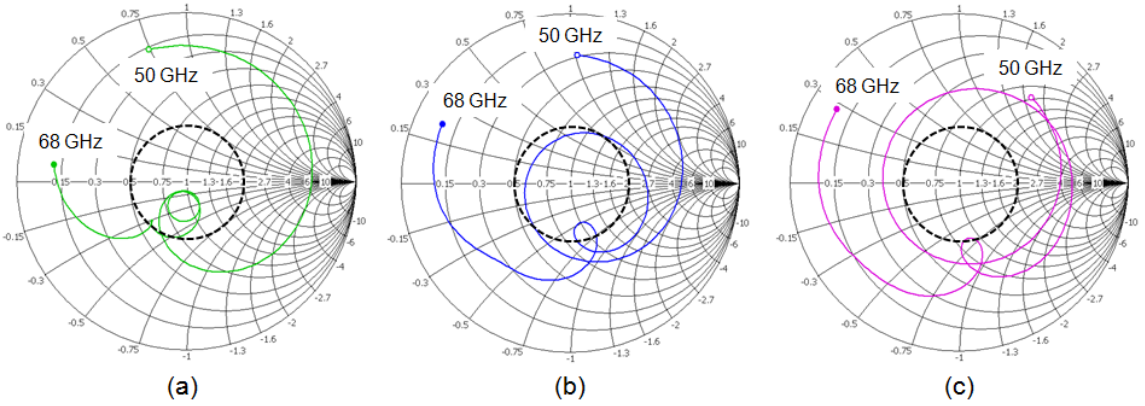

Figure 147. Impedance loci for different values of $S2$. (a) $S2 = 1300\ \mu$m, (b) $S2 = 1400\ \mu$m, (c) $S2 = 1500\ \mu$m.

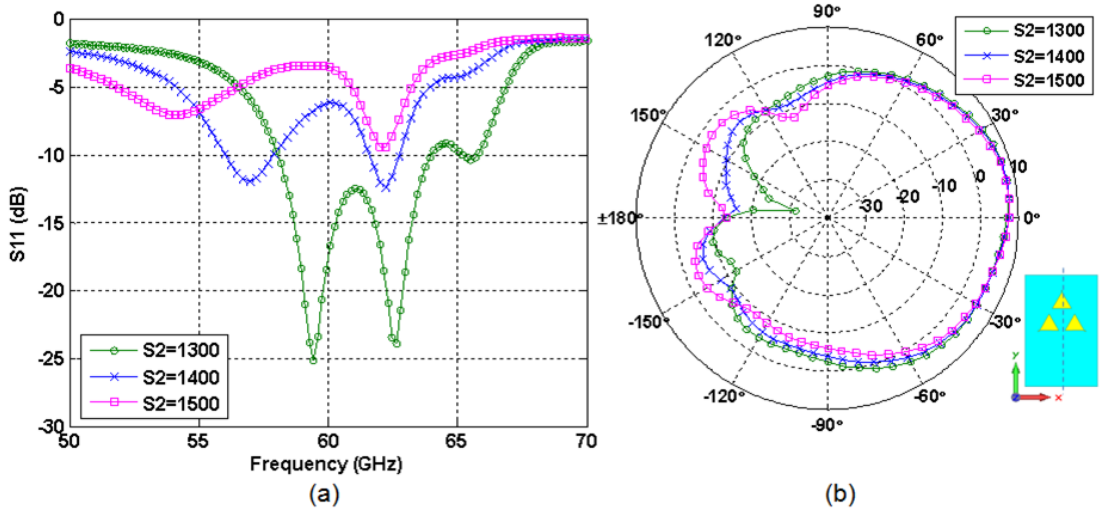

Figure 148. Simulated data for different values of $S2$. (a) S_{11}, (b) Directivity pattern at 58 GHz on the $\phi = 90°$ plane.

S_{11} plots in Figure 148a.

On the contrary to the case with $L1$, Figure 147 shows that the size of the second loop, corresponding to Mode 2, almost stays the same as $S2$ is increased. This is because Mode 2 results from the interaction between the antennas A2 and A3, and the distance between these antennas stays the same as $S2$ is altered, contrary to the case with $L1$. As $S2$ is increased, the second loop moves towards higher capacitive values, shifting out of the 2:1 VSWR circle. This can also be observed in Figure 148a as a second resonance at the same frequency for all cases but with a worsening matching level as $S2$ is increased.

The effect of $S2$ on the third resonance is similar to the effect of $L1$. Increasing the overlapping area has a mitigating effect on the third loop, and the resonance disappears as $S2$ is increased.

The effect of $S2$ variation on the directivity pattern is also shown in Figure 148b. As expected, the pattern plot for $S2$ variation in Figure 148b is similar to the pattern in Figure 146b. Altering $S2$ has a negligible effect on the peak directivity; whereas, the back-radiation increases, and the radiation efficiency decreases, as $S2$ is increased.

8.2.1.3 S1 Sweep

The side length of the antennas A1, A2 and A3, labeled as $S1$ in Figure 141a, has a pronounced effect on all the modes excited. Figure 149 displays the effect of altering $S1$ on the impedance locus. Figure 149a presents the data for $S1 = 1300\,\mu$m, where there is only one resonance loop. This is because the smaller the patches A1, A2 and A3 are, the further apart these patches are from each other. This means A1, A2 and A3 are under-coupled with each other. Figure 150a presents the fields of the single mode excited for $S1 = 1300\,\mu$m at 60 GHz. As seen in the figure, the antenna A4 is strongly coupled to the aperture and the antennas A1, A2, and A3 are too small to excite the dominant TM_{10} mode.

The antennas A1, A2, and A3 become closer to each other, as $S1$ is increased. This creates mutual resonances leading to the appearance of the second and third resonances. Figure 149b shows the appearance of the second resonance loop as the first one becomes smaller and shifts to lower frequencies. As $S1$ is increased from $S1 = 1400\,\mu$m to $S1 = 1500\,\mu$m, the second loop becomes larger, as supported with the Mode 2 field plot shown in Figure 150b for the $S1 = 1500\,\mu$m case. The third resonance loop also appears when $S1$ is increased to $1500\,\mu$m.

Figure 149d displays the impedance locus for the $S1 = 1600\,\mu$m case. It can be seen that, the third resonance becomes larger, indicating a strong coupling mechanism. The strong coupling can be explained looking at the Mode 3 field plot for $S1 = 1600\,\mu$m, shown in Figure 150c. As seen from the field plots, the reduced distance between the antennas A2

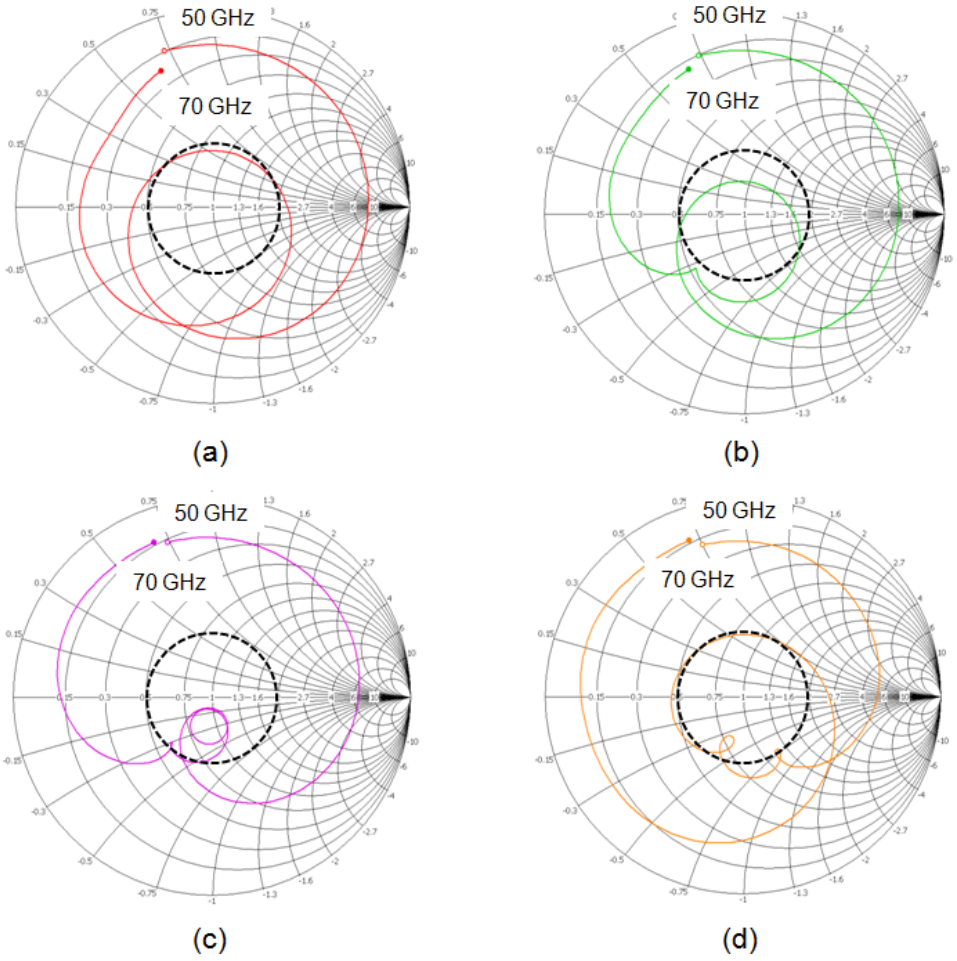

Figure 149. Impedance loci for different values of $S1$. (a) $S1 = 1300\ \mu$m, (b) $S1 = 1400\ \mu$m, (c) $S1 = 1500\ \mu$m (d) $S1 = 1600\ \mu$m.

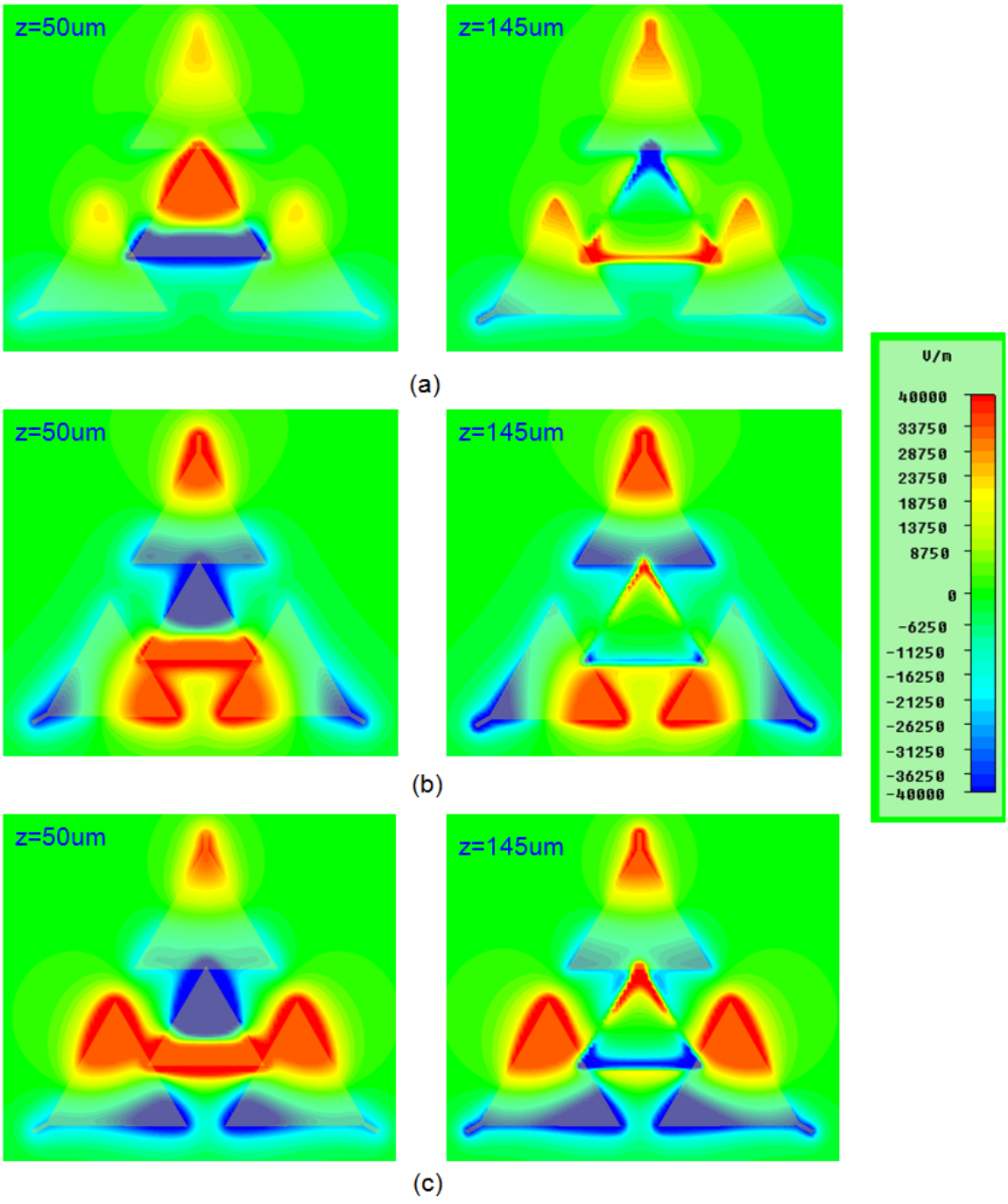

Figure 150. Simulated normal E-field plots for the modes excited for different $S1$ values. The fields are plotted on $z = 50\ \mu$m and $z = 145\ \mu$m planes. The phase values are determined such that the tip of the A1 is excited at the peak value on all conditions. (a) $S1 = 1300\ \mu$m at 60 GHz, (b) $S1 = 1500\ \mu$m at 62.5 GHz (c) $S1 = 1600\ \mu$m at 63.7 GHz.

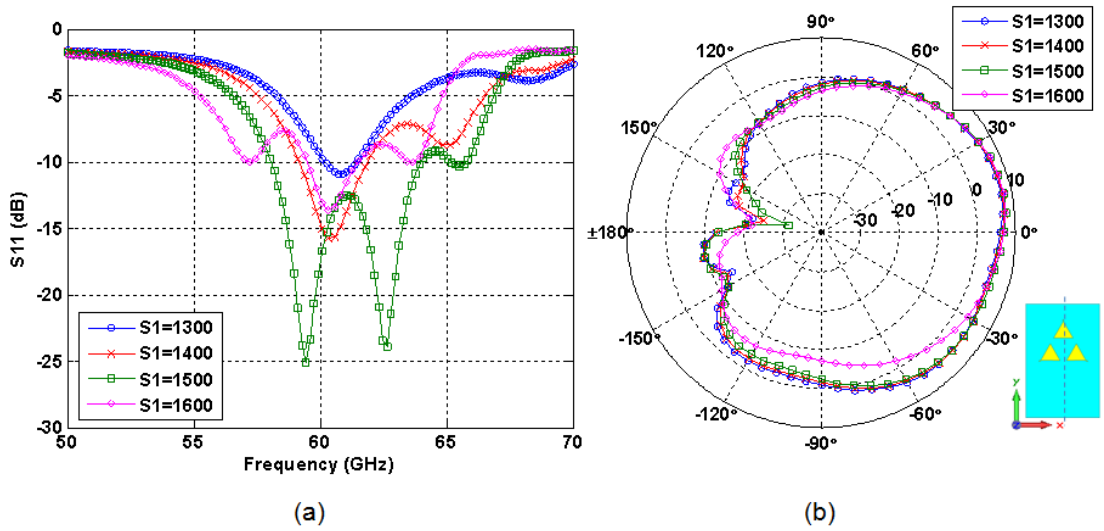

Figure 151. Simulated data for different values of $S1$. (a) S_{11}, (b) Directivity pattern at 58 GHz on the $\phi = 90^\circ$ plane.

and A3 results in increased coupling, similar to the cases for $L1$ and $S2$ sweeps.

Similar observations can be made from S_{11} comparisons shown in Figure 151a. As the graph shows, the second and the third resonances appear as $S1$ is increased. Moreover, all the resonances move to lower frequencies as the patches become larger. The variations in $S1$ also affect the radiation properties of the STPAA. It was found from simulations that increasing $S1$ from 1300 μm to 1500 μm helps to improve the radiation efficiency from 71% to 81%. Moreover, the pattern shape is almost insensitive to the changes in $S1$, as shown in Figure 151b. However, when $S1 > 1500$ μm, the corners of the antennas become too close to each other resulting in a change in the pattern. Therefore, while increasing $S1$, it is important to ensure that the antennas A1, A2 and A3 are not over-coupled.

8.2.1.4 S3 Sweep

A stub placed on the tip or the base of a triangular patch antenna can be used to control the resonance frequency of the antenna [6]. Therefore, three stubs with length $S3$ were placed at the outermost tips of each parasitic patch A1, A2, and A3. Figure 152 shows the impedance loci for different values of $S3$. The field plots for the $S3 = 50$ μm case are also shown in Figure 153.

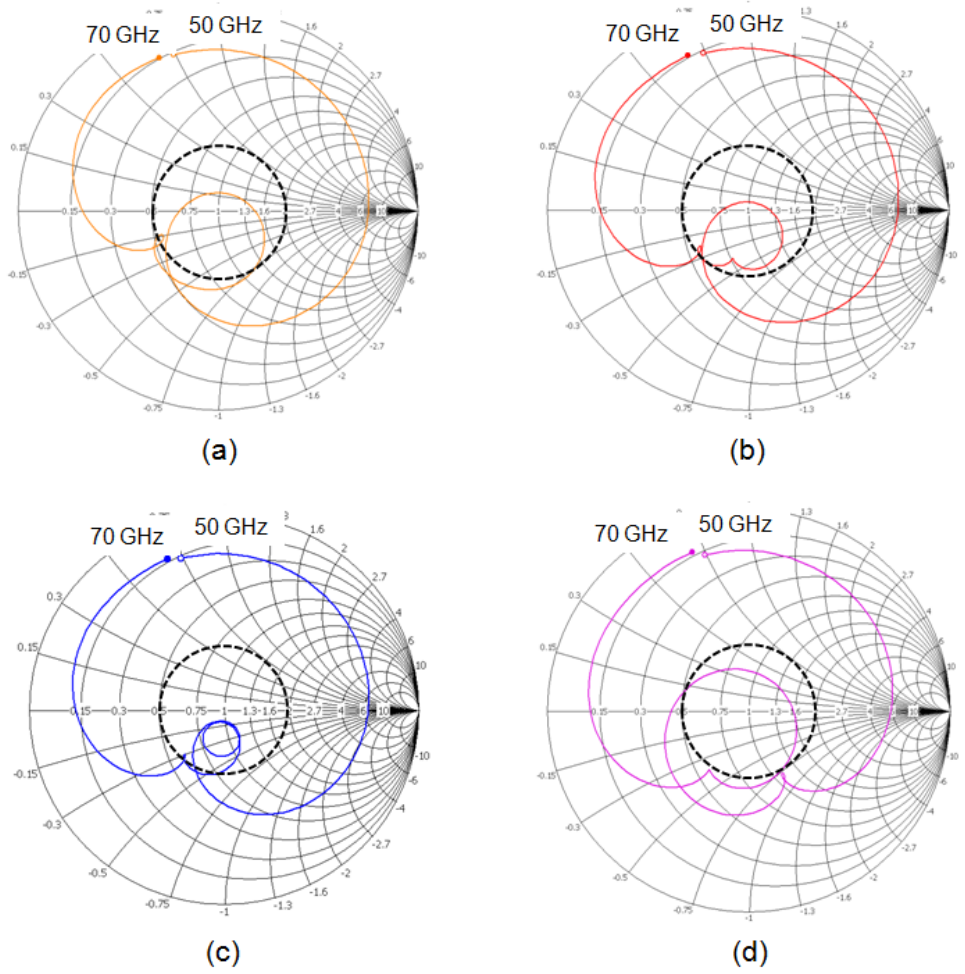

Figure 152. Impedance loci for different values of $S3$. (a) $S3 = 50\ \mu$m, (b) $S3 = 100\ \mu$m, (c) $S3 = 150\ \mu$m (d) $S3 = 250\ \mu$m.

The effect of the stub on the resonances can be found by comparing a short stub case with a long stub case. The impedance locus for the $S3 = 50\ \mu$m case is shown in Figure 152a. As seen in the figure, there are only two resonance loops. Analyzing the fields of the $S3 = 50\ \mu$m case in Figure 153 and comparing these plots with the ones in Figure 143, corresponding to $S3 = 150\ \mu$m, reveal that the modes excited at 60 GHz and 64 GHz for $S3 = 50\ \mu$m case both correspond to Mode 1 while the modes at 66 GHz corresponds to Mode 3. In other words, Mode 2 is not excited when the stub is small or absent.

Figure 152b shows the appearance of the second resonance as stub length is increased to 100 μm. The second loop becomes larger when the stub length is increased further, as

shown in Figure 152c and d. This means the interference between A2 and A3 becomes stronger as the stub length is increased. On the contrary, the first loop becomes smaller and rotates counterclockwise towards lower frequencies, moving out of the VSWR 2:1 circle at $S3 = 250\,\mu$m. The third loop stays almost at the same frequency with the same radius while $S3$ is altered.

Similar results can be concluded by analyzing the simulated S_{11} data on a rectangular plot, as shown in Figure 154a. As seen in the graph, the stub length affects the second resonance the most. The second resonance appears as $S3$ is increased from 50 μm to 100 μm. The first resonance slowly moves to lower frequencies, and it loses the accepted matching level as $S3$ is increased abruptly. The third resonance stays at the same frequency as expected from the conclusions drawn from the impedance loci analysis.

The effect of the $S3$ variation on the far field pattern is negligible until the value is larger than 200 μm, as displayed in Figure 154b. As the stub length is increased further from 200 μm, the pattern shape deteriorates similar to the case for $S1 = 1600\,\mu$m in $S1$ sweep.

8.2.1.5 W1 Sweep

Figure 155 shows the effect of varying the aperture width on the impedance locus. It is seen that the aperture width $W1$ has a pronounced effect on all of the resonance loops. The first loop becomes larger and moves towards the inner part of the 2:1 VSWR circle, indicating a better matching level. The size of the second loop stays the same while changing $W1$; however, the loop moves closer to the center of the Smith chart. Finally, the third resonance diminishes and moves out of the VSWR circle, pointing to a worse matching as $W1$ is increased.

The S_{11} graphs in Figure 156a also support these observations. As seen in the graphs, the first and the second resonances match better with increased $W1$, while the second resonance also moves to lower frequencies. The third resonance slowly disappears, while $W1$ is increased.

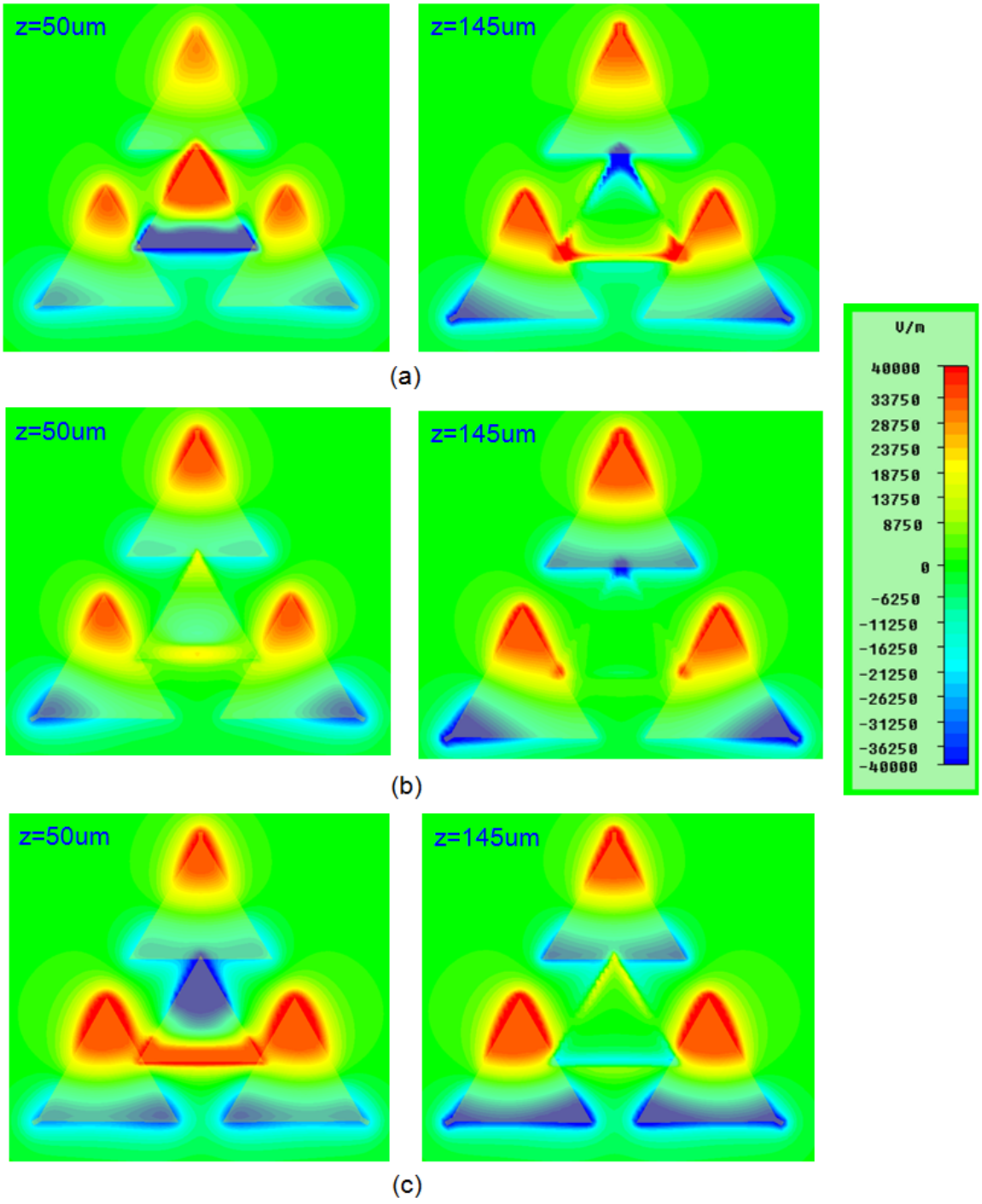

Figure 153. Simulated normal E-field plots for the modes excited for $S3 = 50\ \mu$m. The fields are plotted on $z = 50\ \mu$m and $z = 145\ \mu$m planes. The phase values are determined such that the tip of the A1 is excited at the peak value on all conditions. (a) 60 GHz, (b) 64 GHz (c) 66 GHz.

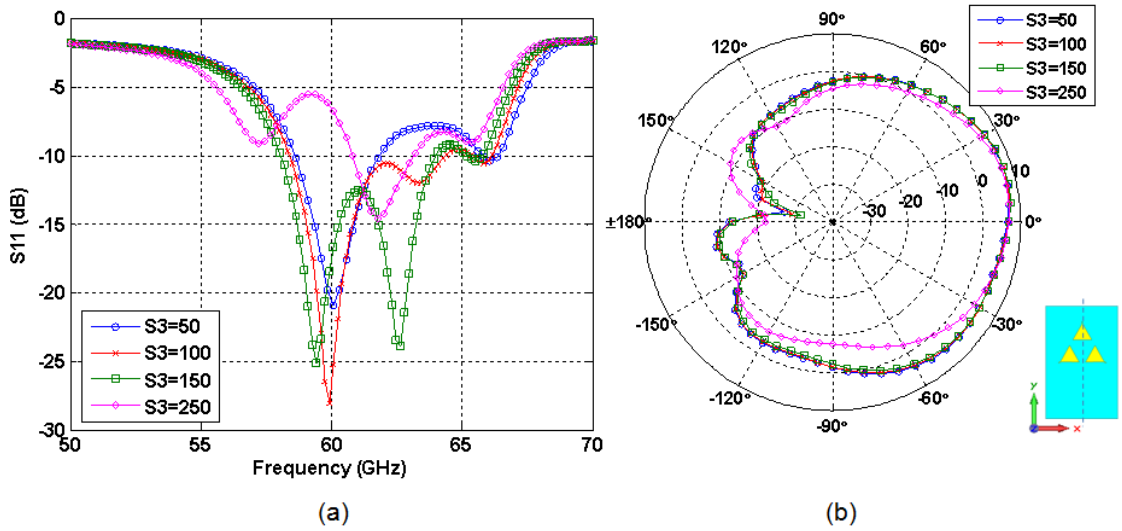

Figure 154. Simulated data for different values of $S3$. (a) S_{11}, (b) Directivity pattern at 58 GHz on $\phi = 90°$.

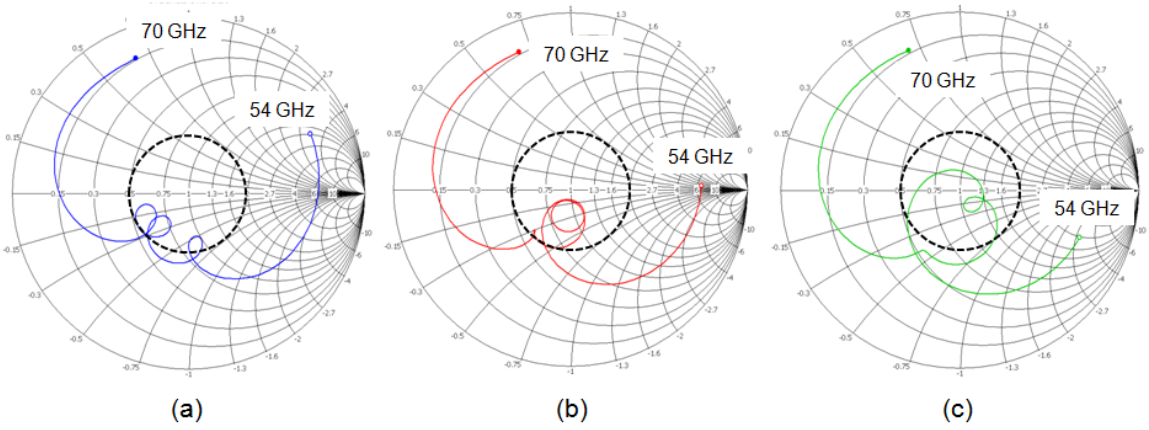

Figure 155. Impedance loci for different values of $W1$. (a) $W1 = 900\,\mu$m, (b) $W1 = 1000\,\mu$m, (c) $W1 = 1100\,\mu$m.

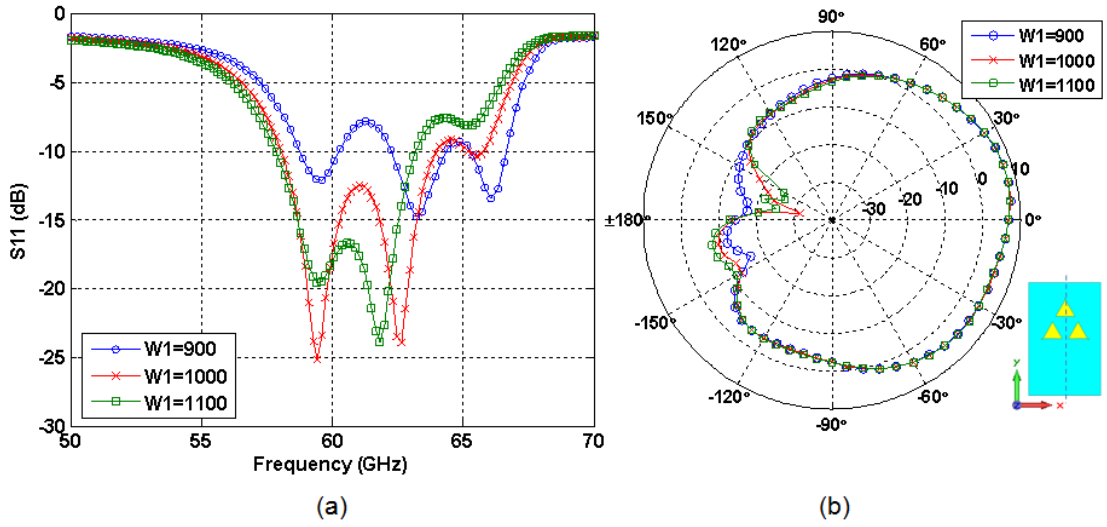

Figure 156. Simulated data for different values of $W1$. (a) S_{11}, (b) Directivity pattern at 58 GHz on $\phi = 90°$.

The far field pattern is also shown in Figure 156b. It can be seen in the graphs that, altering the aperture width has unnoticeable effect on the the peak directivity. Only the back radiation increases gradually as the size of the aperture is increased. The radiation efficiency was also found to stay at the same value of 82% for all simulated width values.

8.2.1.6 L2 sweep

The effect of varying $L2$ on the impedance locus is shown in Figure 157a. $L2$ is another parameter that determines the size of the aperture. Therefore, the variation of $L2$ has the same trend as that of $W1$, and the same conclusions can be drawn.

8.2.1.7 L4 sweep

The 50Ω microstrip line used to feed the antennas was terminated with a low-impedance line to control the coupling. The length of this low-impedance line, $L4$, was another parameter used to meet the bandwidth requirement. Figure 158 shows the effect of $L4$ on the impedance loci from 50 GHz to 70 GHz. It can be observed that the radius of the first resonance loop is smaller for longer lines. The second loop also diminishes with increasing line length. It also moves out of the 2:1 VSWR circle, indicating a worsening matching

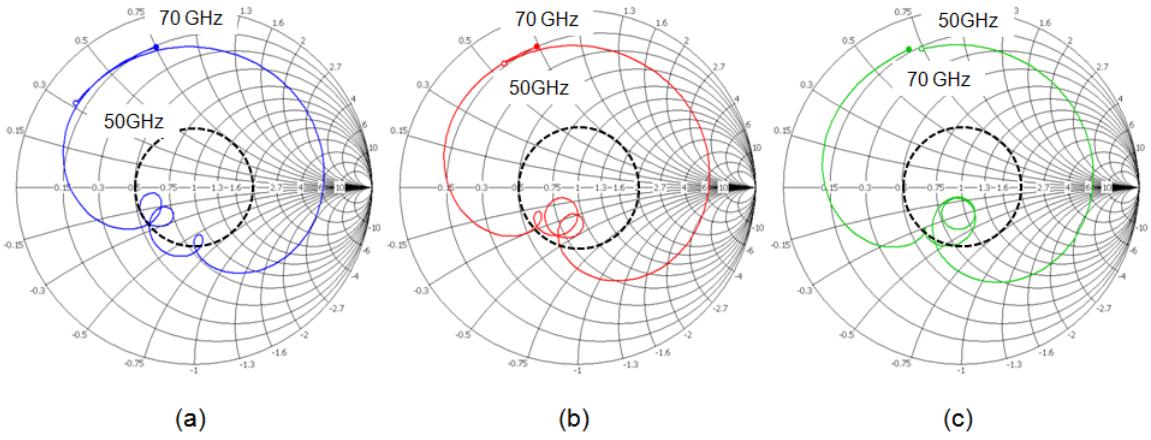

Figure 157. Impedance loci for different values of $L2$**. (a)** $L2 = 50\ \mu$m**, (b)** $L2 = 100\ \mu$m**, (c)** $L2 = 200\ \mu$m**.**

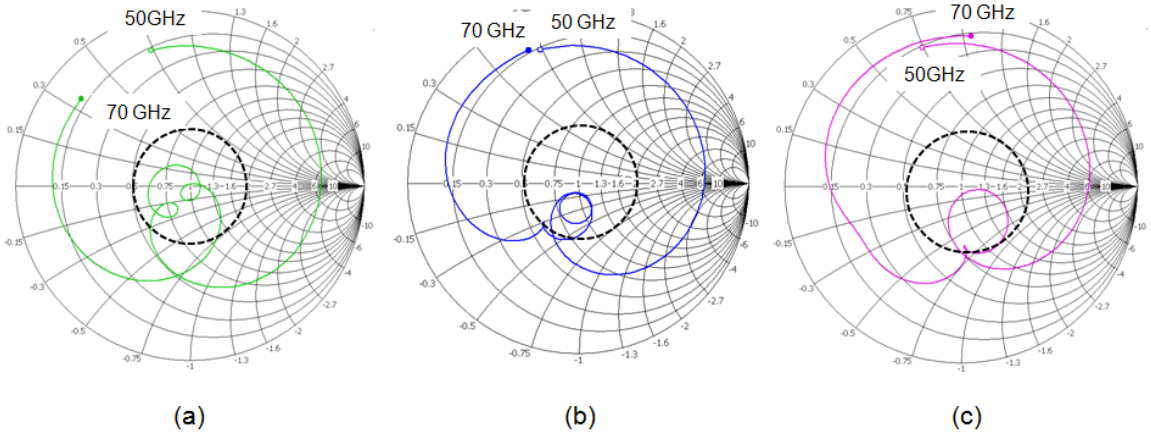

Figure 158. Impedance loci for different values of $L4$**. (a)** $L4 = 1400\ \mu$m**, (b)** $L4 = 1500\ \mu$m**, (c)** $L4 = 1600\ \mu$m**.**

level. The third loop also becomes smaller and almost vanishes for $L4 = 1600\ \mu$m.

The effect of $L4$ variation on the S_{11} and the far field pattern are shown in Figure 159a and b, respectively. As seen in the graphs, the first resonance stays matched but moves to lower frequencies with increasing length; whereas the second and the third resonances diminish gradually. The peak directivity of the antenna is not considerably affected by $L4$ variations. However, the back-radiation and the radiation efficiency increase slightly as the line length is increased.

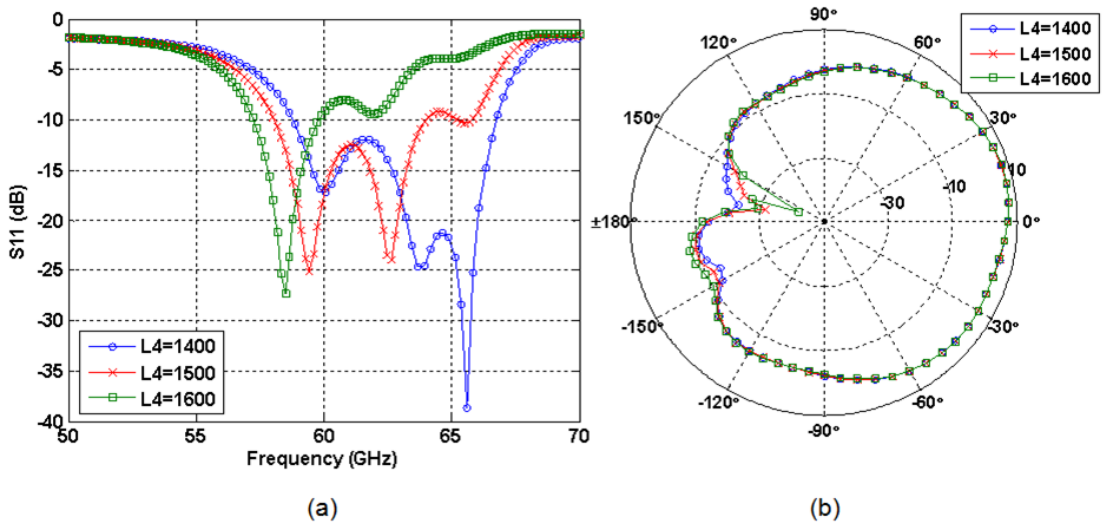

Figure 159. Simulated data for different values of *L4*. (a) S_{11}, (b) Directivity pattern at 58 GHz on $\phi = 90°$.

8.2.1.8 W2 sweep

The width of the low-impedance line terminating the microstrip line is labeled as *W*2 in Figure 141d. *W*2 is mainly used to achieve the desired impedance matching level. It can be seen in Figure 160 that, *W*2 can be used to control the level of coupling and create tight resonance loops that are close to each other.

This can also be supported with the simulated S_{11} data, as shown in Figure 161a. As seen in the figure, adjusting *W*2 helps to match the antenna to the desired S_{11} level. Although the resonance frequencies shift slightly to higher frequencies when *W*2 is increased, the shift in the frequency can be corrected using other variables. Figure 161b presents the far field pattern for different *W*2 values. As seen in the figure, *W*2 variation does not affect the radiation properties of the antenna considerably. However, the total efficiency of the antenna can be improved by adjusting *W*2 since proper impedance matching at the feed-end can be achieved.

8.2.1.9 Thickness Sweep

The thickness of the RXP-layers constructing the stack up were determined by the manufacturer; therefore, they were not used as design variables to optimize the final design.

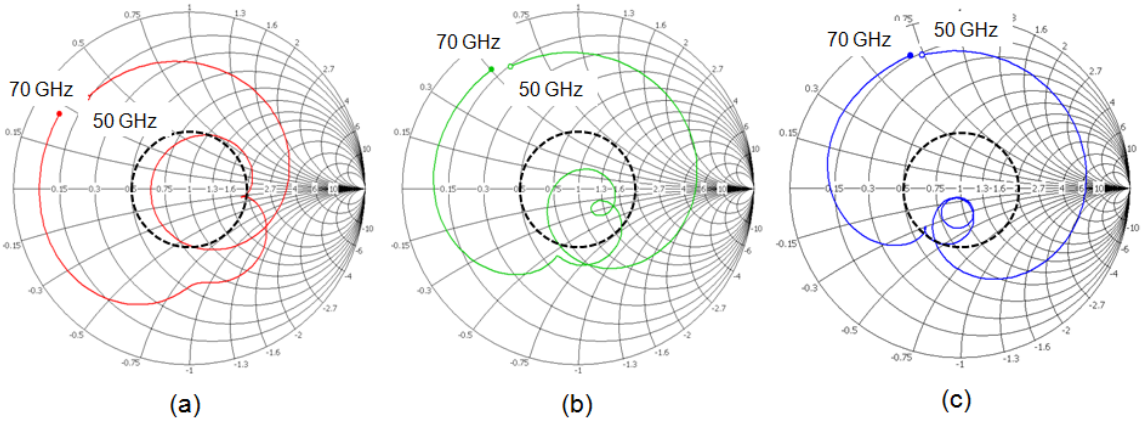

Figure 160. Impedance loci for different values of $W2$. Frequency range is from 50 GHz to 70 GHz. (a) $W2 = 200\ \mu$m, (b) $W2 = 300\ \mu$m, (c) $W2 = 400\ \mu$m.

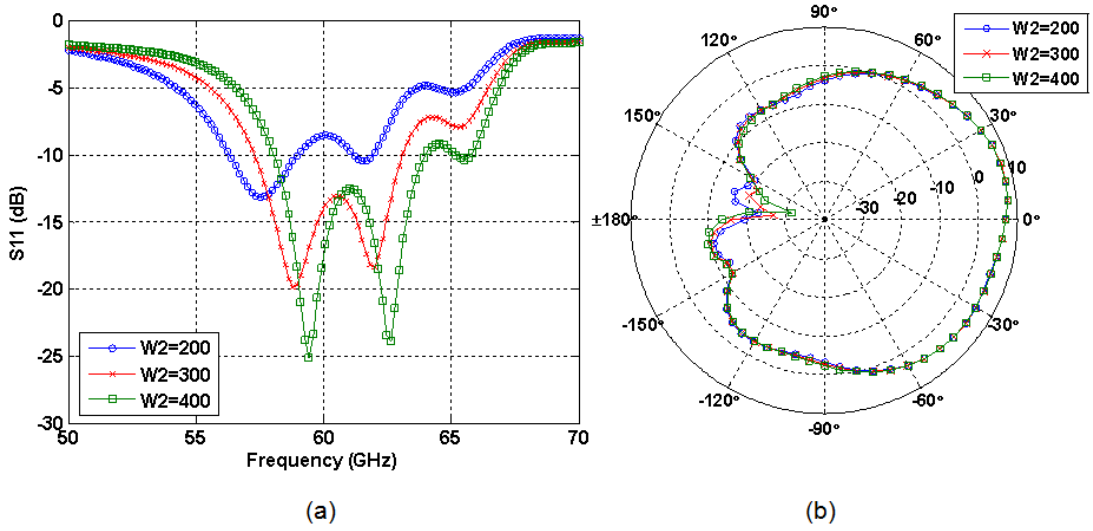

Figure 161. Simulated data for different values of $W2$. (a) S_{11}, (b) Directivity pattern at 58 GHz on $\phi = 90°$.

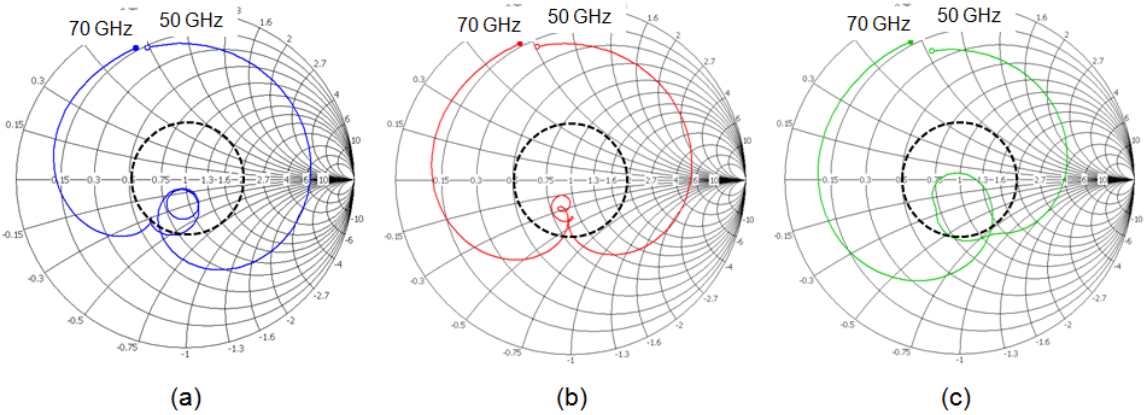

Figure 162. Impedance loci for different values of $H1$. (a) $H1$ = 60 μm, (b) $H1$ = 120 μm, (c) $H1$ = 180 μm.

However, since the thicknesses of the substrates between the aperture and the antenna A4; and between the antenna A4 and the parasitic elements are crucial parameters in the design of the stacked patch antennas, a thickness sweep study is also included in this chapter for the sake of completeness.

The thickness of the substrate is one of the main parameters to control the vertical coupling between the antennas; therefore, even slight changes in the thickness result in a considerable change in the impedance loci. Figure 162 shows the impedance loci for different values of the thickness of the topmost RXP-4 layer, as shown in Figure 140. This RXP-4 layer separates the antenna A4 and the parasitic elements A1, A2 and A3, and the thickness of this layer is labeled as $H1$. As the impedance loci show, increasing $H1$ from 60 μm to 120 μm creates three tight loops that are positioned in the 2:1 VSWR circle. However, two of these resonance loops disappear when the thickness is further increased, as shown in Figure 162c. The S_{11} data in Figure 163a show that, the first and the second resonance loops disappear with increasing $H1$. This is because these resonances are created by the coupling mechanisms between the antenna A4 and the parasitic patches. Making the separation substrate bulky causes the antennas to undercouple and; hence, the resonances to disappear.

The effect of $H1$ variation on the radiation pattern is also shown in Figure 163b. It

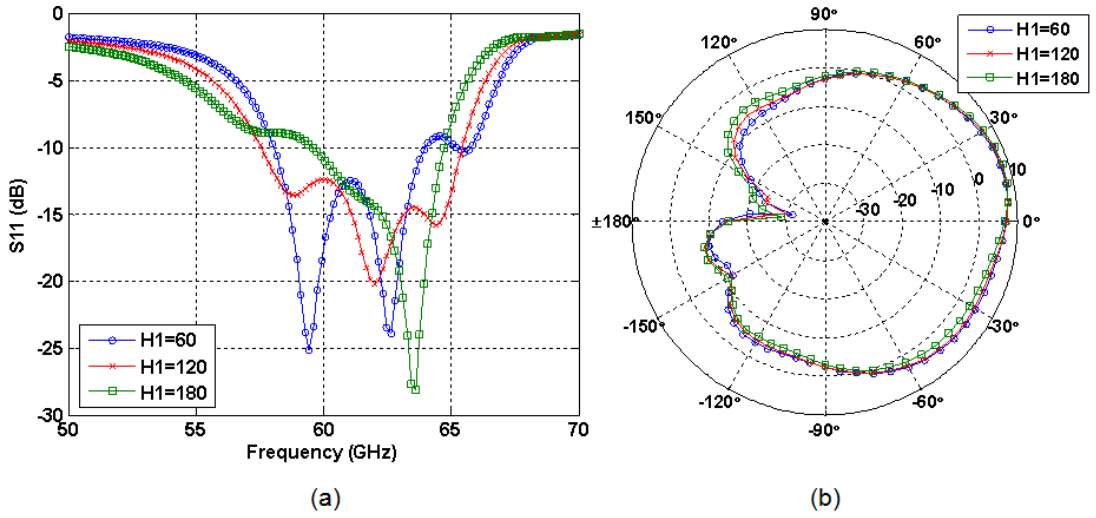

Figure 163. Simulated data for different values of $H1$. (a) S_{11}, (b) Directivity pattern at 58 GHz on $\phi = 90°$.

was found that, the shape and the peak value of the pattern is dependent on the thickness. The back-radiation increases for thicker substrates, which can be explained with increased surface wave propagation.

The effect of the thickness of the substrate between the lower triangular patch, A4, and the ground plane was also studied. The thickness of this separating RXP-1 layer is labeled as $H2$. Figure 164 shows the effect of $H2$ on the impedance loci. As the substrate is thicker, the first and the second resonance loops disappear gradually while the third resonance loop appears to be larger. Moreover, the loops move away from each other as $H2$ is increased. The trend in the simulated S_{11} data, as shown in Figure 165a, also supports these observations. The value of $H2$ has a major effect on the radiation pattern of the antenna as well. It can be seen in Figure 165b that increased surface wave propagation on thicker substrates results in increased back-radiation, similar to the case with increased $H1$.

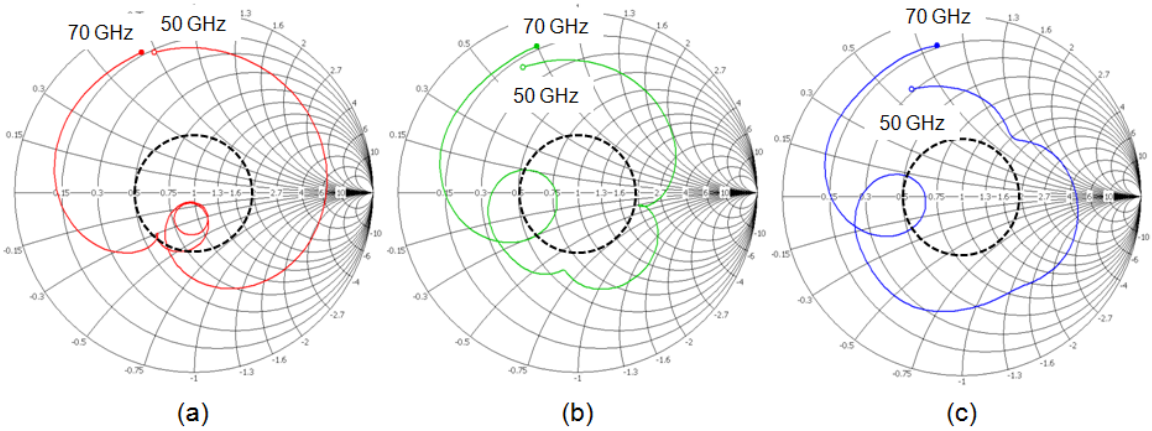

Figure 164. Impedance loci for different values of $H2$. (a) $H2$ = 100 μm, (b) $H2$ = 150 μm, (c) $H2$ = 200 μm.

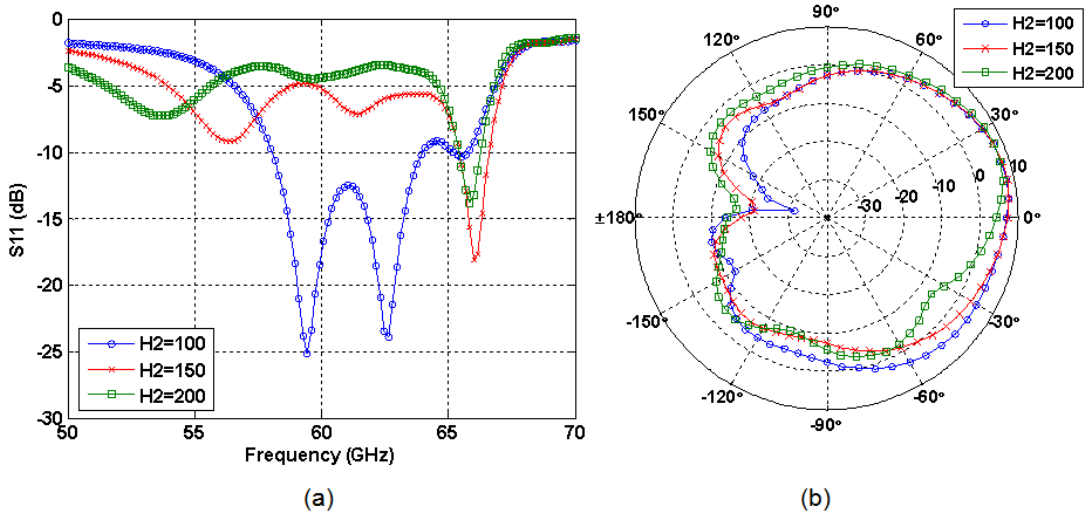

Figure 165. Simulated data for different values of $H2$. (a) S_{11}, (b) Directivity pattern at 58 GHz on ϕ = 90°.

8.2.2 Summary of the Design Guidelines

Table 10 summarizes the effects of the design variables on the three resonance frequencies, the radiation parameters, the peak directivity, the front-to-back ratio (FBR) and the radiation efficiency of the proposed STPAA. The guidelines presented in this table are obtained through the parameter sweep simulations explained in the previous section of this chapter. Antenna designers can use these guidelines to optimize the proposed STPAA to the desired frequency band.

It was found that this configuration excites three modes that lead to three resonances. Although each mode is affected by a number of coupling mechanisms, it can be said that Mode 1 is strongly dependant on the vertical coupling between the antenna A4 and the parasitic patches A1, A2, and A3; whereas, Mode 2 is associated with the coupling of the degenerate modes under the antennas A2 and A3. Mode 3 is a combination of the coupling of all three antennas and the aperture.

The main variables that should be tuned first are the dimensions of the triangular patches, the size of the aperture, and if applicable, the thickness of the dielectric layers. The variables controlling these parameters are labeled as $L1$, $S1$, $S2$, $S3$, $W1$, $H1$ and $H2$. Among these parameters, $S2$ can be used to optimize the first resonance frequency while $W2$ and $S3$ can be used for the second resonance frequency. Then, $L1$ can be used to merge these resonances. The third resonance can be controlled by a number of parameters as shown in Table 10. Finally, $W2$ can be used for optimizing the impedance match.

An important design goal that should be kept in mind during optimization is to make sure that all of the three loops cross the real axis of the Smith chart while they are positioned in the desired VSWR circle. The S_{11} of the antenna may show a good match when the antenna is close to resonance, meaning the loops close to the real axis of the Smith chart but not crossing in the desired band. However, by ensuring that the antennas are not only matched but also resonating the gain of the final design can be increased approximately by 1 dB. It is also important to check the radiation properties of the antenna while optimizing

Table 10. Summary of the design variables for the stacked triangular patch antenna array when the stubs are at the outmost corners. ↑: increase, ↓: decrease, ↗: gradual increase, ↙: gradual decrease, ⟷: no change.

Parameter	f_1	f_2	f_3	Peak directivity	Front-to-back ratio	Radiation efficiency
$L1$ (↑)	↑	↙	↑	⟷	↑	↑
$S2$ (↑)	↓	⟷	⟷ (disappears)	⟷	↓	↗↘
$S1$ (↑)	↓	↓ (appears)	↓ (appears)	↑	⟷	↑
$S3$ (↑)	↓	↓ (appears)	↙	⟷	⟷	↗
$W1$ (↑)	⟷	↓	↙	⟷	↓	⟷
$L2$ (↑)	⟷	↓	↙	⟷	↓	⟷
$L4$ (↑)	↓	↓	⟷	⟷	↗	↗
$W2$ (↑)	↗	↗	↗	⟷	↗	↗
$H1$ (↑)	↙	↙ (disappears)	↙ (disappears)	↗	↗	↗
$H2$ (↑)	↓	↓ (disappears)	↙	↓	↓	↓

the S_{11} of the antenna. The far field of the antenna can be distorted with a low directivity when the antenna elements are over-coupled or under-coupled.

8.3 Stacked Triangular Patch Antenna Array with Parallel Stubs

Small rectangular stubs were placed at the outermost corners of parasitic antenna elements A1, A2 and, A3, as shown in Figure 141a. It was observed during the parameter sweep study that the stub length plays an important role to excite the degenerate TM_{10} modes, as shown in Figure 143b. These modes are responsible for the second resonance seen in the S_{11} data. Therefore, it can be concluded that the position of the stubs affects the coupling mechanisms, which in turn affects the number of the resonances in S_{11}.

To investigate the effect of the position of the stubs, the proposed stacked patch antenna

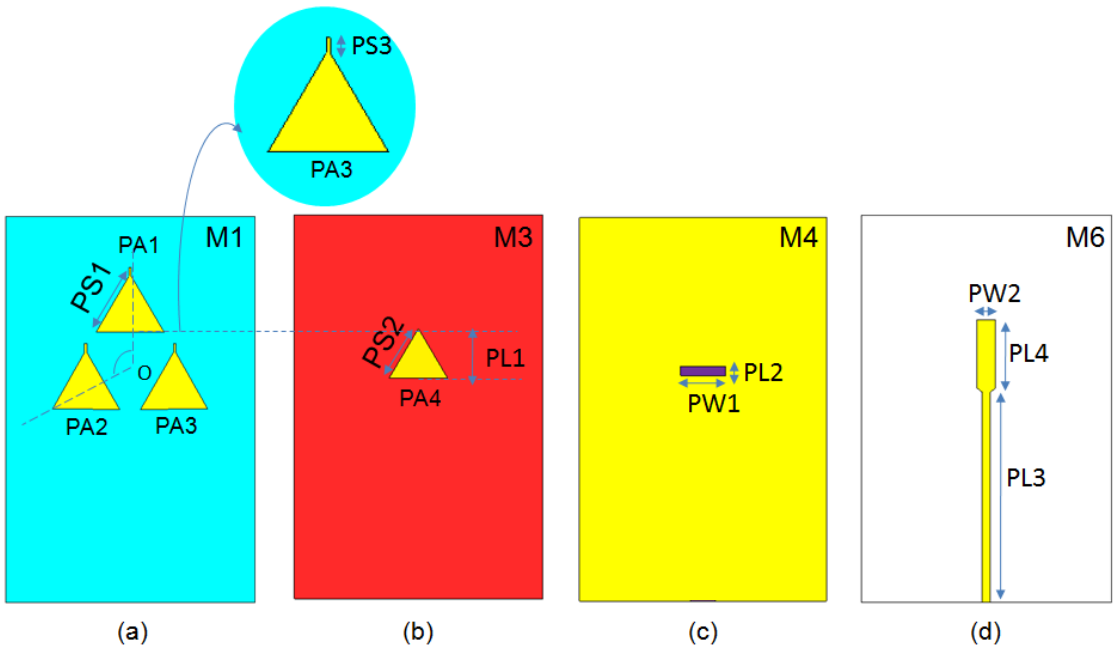

Figure 166. Details of the stacked triangular patch antenna design with the parallel stubs. (a) Metal layer M1, (b) Metal layer M3, (c) Metal layer M4, (d) Metal layer M6.

configuration was simulated when the stubs were placed at the topmost corners of each parasitic triangular patch PA1, PA2, and PA3. This way all three stubs were positioned parallel to each other, as shown in Figure 166a. Figure 166 shows the details of the second antenna configuration, created from the first one presented in the previous section using parallel stubs. All of the variable names were kept similar to the previous stub configuration with a "P" added as a prefix to differentiate between the variables.

Having stubs parallel to each other increases the symmetry of the antennas PA2 and PA3 with the antenna PA1. Therefore, it is expected that the modes excited under the antennas PA2 and PA3 will look similar to the modes under the antenna PA1. Figure 167 shows the two modes excited under the stacked patch configuration with parallel stubs. These modes are labeled as Mode A and Mode B. Comparing this figure with the field plots of the first configuration in Figure 143, it can be concluded that Mode A corresponds to Mode 1 of the previous stub configuration, while Mode B corresponds to Mode 3 of the previous stub configuration. Mode 2 is not excited with this parallel stub configuration. This is because, as seen in Figure 143b, Mode 2 is excited when the antennas A2 and A3 are strongly

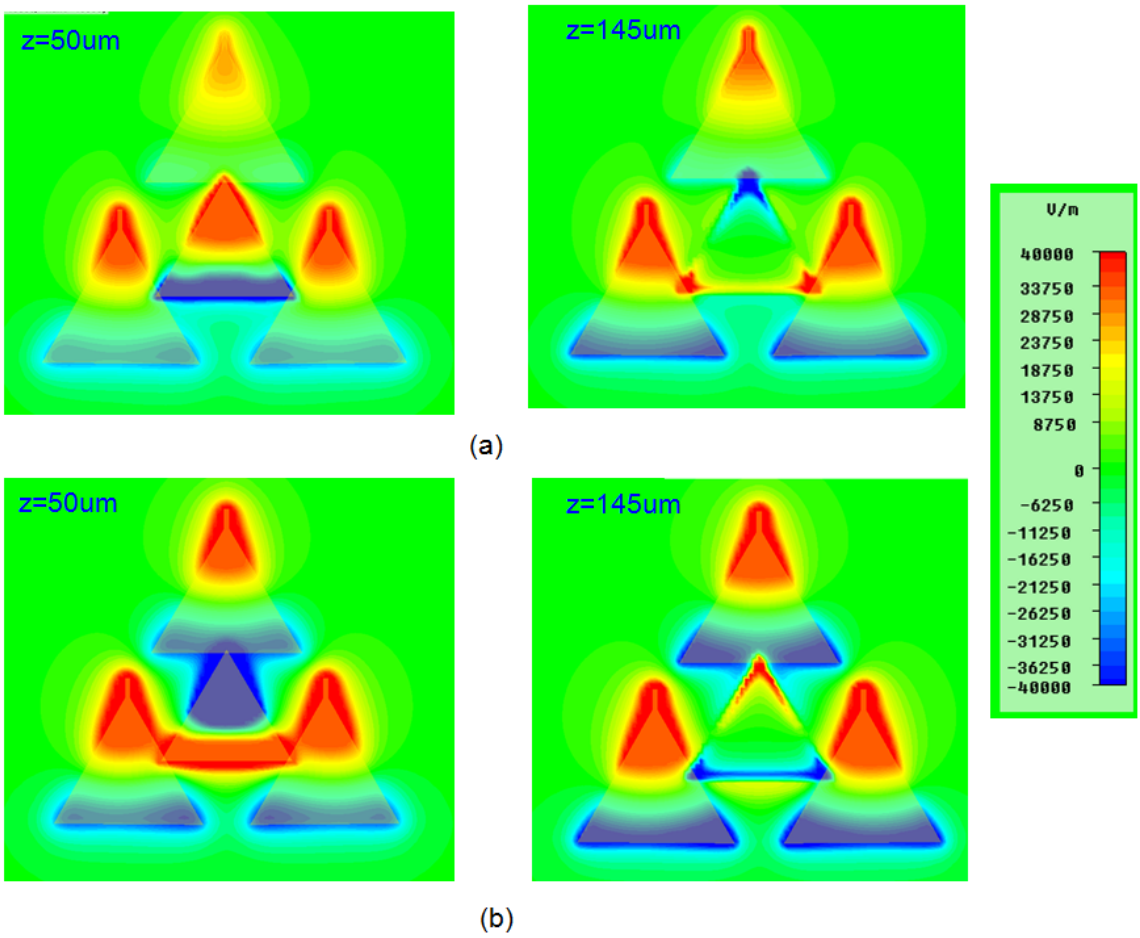

Figure 167. Simulated normal E-field plots for the modes excited when the stubs are placed parallel. The fields are plotted on $z = 50\ \mu$m and $z = 145\ \mu$m planes. The phase values are determined such that the tip of the A1 is excited at the peak value on all conditions. (a) Mode A, 58.7 GHz, (b) Mode B, 63.4 GHz.

coupled with each other and when their fields have a 180° phase difference compared to the fields of the antenna A1. In this new stub configuration; however, the fields under the antennas PA2 and PA3 have the same phase with the fields of the antenna PA1 due to the increased symmetry with the parallel stubs. Therefore, Mode 2 is not excited in the parallel stub configuration.

Figure 168 presents the simulated S_{11} data of the stacked patch antenna array with the new stub configuration. As seen in the figure, the two modes excited under the antenna lead to two resonances in S_{11} and two resonance loops in the impedance locus. The far field pattern of the antenna was also simulated, and it was found to be similar to the previous

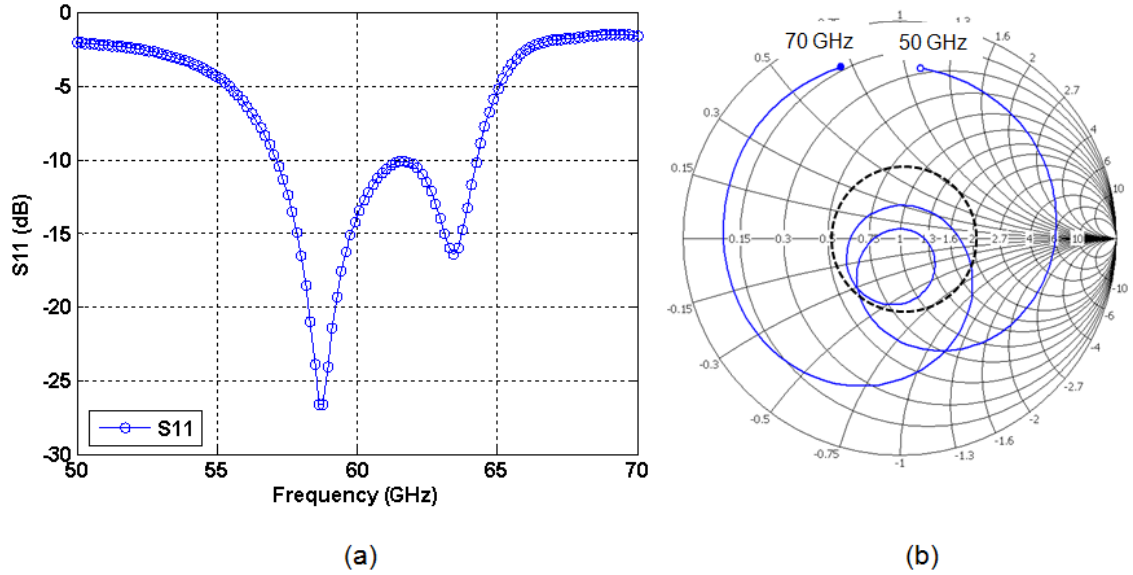

Figure 168. Simulated data when the stubs are placed parallel. (a) S_{11}, (b) Impedance locus from 50 GHz to 70 GHz.

configuration but with almost 1 dB higher gain.

8.3.1 Summary of the Effects of Design Variables

A parameter sweep study was conducted for the new parallel stub configuration as well. The conclusions drawn from this study are summarized in Table 11.

As expected, a close look at both Table 11 and Table 10 reveals considerable resemblance. Mode A creates the first resonance, f_A, and Mode A is found to be equivalent to Mode 1 of the previous configuration which creates the first resonance denoted as f_1 in Table 10. Therefore, the f_A column in Table 11 is expected to be similar to the f_1 column in Table 10. Similarly, Mode B is found to be equivalent to Mode 3. Hence, the f_B column in Table 11 shows the same trend with the f_3 column in Table 10.

The guidelines shown in Table 11 can be used as follows. First, the parameters for the size of the triangular patches and the stub length can be used to create two resonances around 60 GHz, such that the first resonance is at a frequency lower than 60 GHz and the second resonance is at a frequency higher than 60 GHz. The variables controlling these parameters are labeled as $PS\,1$, $PS\,2$, and $PS\,3$ in Figure 166a and 166b. Next, the aperture

Table 11. Summary of the design variables for the stacked triangular patch antenna array when the stubs are placed parallel. ↑: increase, ↓: decrease, ↗: gradual increase, ↙: gradual decrease, ⟷: no change.

Parameter	f_A	f_B	Peak directivity	Front-to-back ratio	Radiation efficiency
$PL1$ (↑)	↓	↑	⟷	↑	⟷
$PS2$ (↑)	↓	↓ (disappears)	⟷	↓	↙
$PS1$ (↑)	↓	↓	↑	⟷	↗ ↘
$PS3$ (↑)	↓	↓	⟷	⟷	⟷
$PW1$ (↑)	⟷	↙	⟷	↓	⟷
$PL2$ (↑)	⟷	↙	⟷	↓	⟷
$PL4$ (↑)	↙	↙	⟷	↓	⟷
$W2$ (↑)	↗	↗	⟷	↗	↗

size can be optimized by using the variables $PW1$ and $PL2$ to tune the second resonance frequency. Then, $PL1$, the distance between the antennas PA1 and PA4, can be used to merge these resonances. Finally $PL4$ and $PW2$ can be used to match the impedance at a desired level. An important design goal that should be kept in mind during optimization is to make sure that all of the three loops cross the real axis of the Smith chart while they are positioned in the VSWR circle. The S_{11} of the antenna may show a good match when the antenna is close to resonance, meaning the loops close to the real axis of the Smith chart but not crossing in the desired band. However, by ensuring that the antennas are not only matched but also resonating the gain of the final design can be increased approximately by 1 dB. Moreover, it is critical to check the radiation parameters of the antenna array during the design process. The far field pattern can be distorted if the antennas are over- or under-coupled.

8.4 Designs for the Connector-based Measurement Setup

8.4.1 GPPO-to-Microstrip Line Transition

Millimeter wave edge-mount GPPO connectors, provided by Corning Gilbert, were considered for exciting the antenna [91] during measurements. The transition from the connector to the microstrip line was optimized separately to decrease the simulation time during the design process.

The GPPO connector was modeled as a 50 Ω coaxial connector with the dimensions given in the data sheet provided by the manufacturer. The transition structure includes GPPO-to-CPW and CPW-to-ML transitions, as shown in Figure 169. The substrate has the same stack-up shown in Figure 140.

First, a CPW-to-ML transition was designed without modeling the GPPO connector. To guarantee a good fit of the GPPO connector onto the designed CPW line, the guidelines provided by the manufacturer were followed. According to the given constraints, the minimum required signal width to fit the GPPO signal pin was found to be much wider than the signal width required for a 50 Ω CPW line. Therefore, a tapered slot was designed to be etched from the ground plane to increase the line impedance. The width of the tapered slot was used as the main design parameter to optimize the transition response. Once the transition from the 50 Ω CPW line to 50 Ω ML was designed, the GPPO connector model was also included in the full-wave simulations. A waveport was setup to excite the transition from inside the GPPO connector model, at the reference plane given in the datasheet of the connector [91]. Another waveport was setup at the termination of the microstrip line.

When the transition was simulated with the GPPO connector, analyzing the simulated field propagation along the transition revealed a field leakage through the dielectric of the connector. This happens because the RXP-stackup is too thin to cover the radius of the dielectric of the connector. The leakage observed is shown in the enlarged image of the E-field plot in Figure 170a. In this figure, the amplitude of the E-field is plotted on the vertical cross-section of the substrate. To prevent the field from leaking and propagating

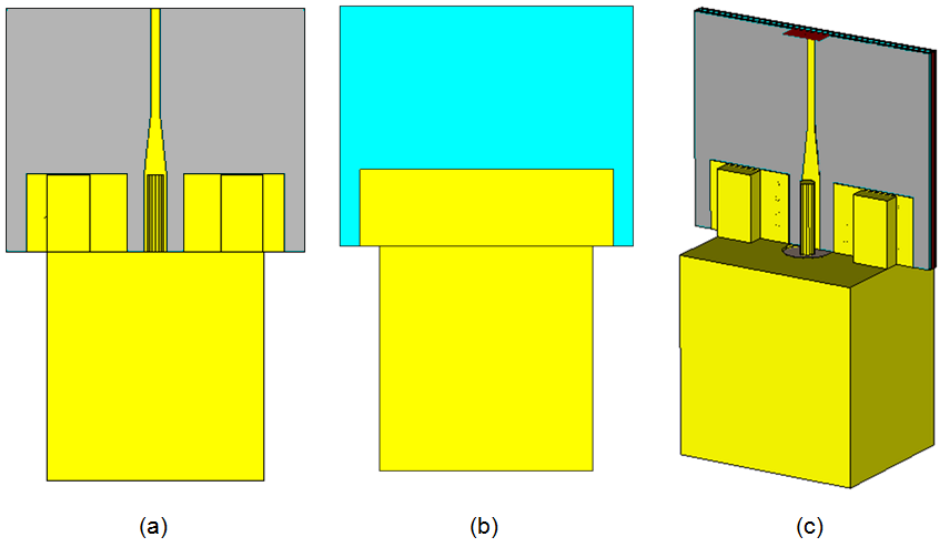

Figure 169. Simulation model of the transition including the GPPO connector. (a) Top view, (b) Bottom view, (c) Perspective view.

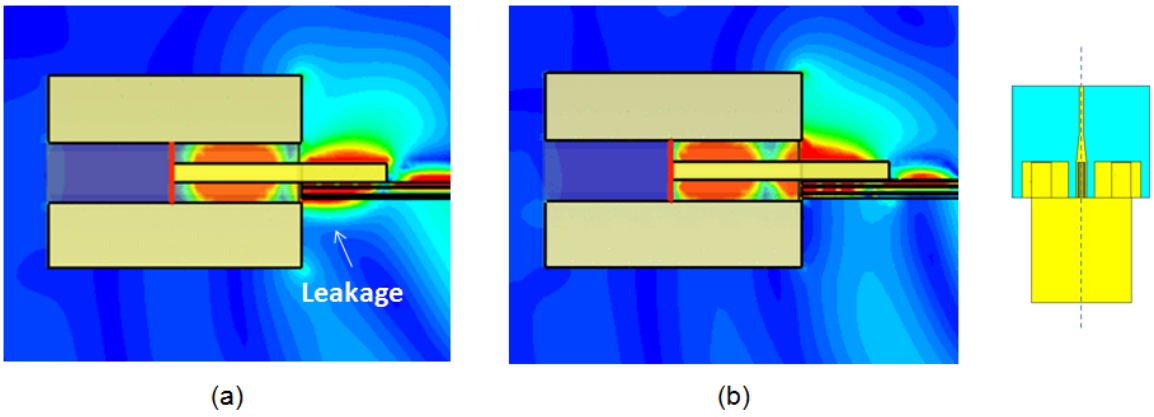

Figure 170. Comparison of absolute value of E-field on yz plane of the transition with and without ground pad on metal layer M1. (a) Without the pad on M1, (b) With the pad on M1.

along the back of the ground plane, an additional ground pad on the metal layer M1 was designed and connected to the ground pad on M6 through vertical via connections. Figure 170b shows the fields when the backing-ground-pad is included. As compared to the non-backing-ground-pad case, it is seen that the leakage is prevented by directing the field into the substrate.

The dimensions of the tapered slot on the ground plane were used as the main parameter to optimize the final design. The details of the optimized transition are shown in Figure 171. The values for the parameters shown in the figure are as follows: $W3 = 4750\,\mu$m, $L5 =$

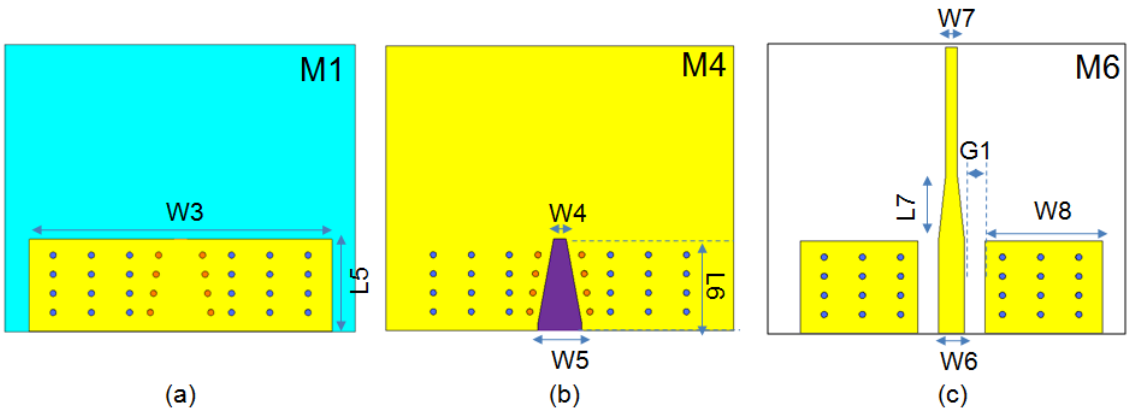

Figure 171. Details of the optimized transition from the GPPO connector to the microstrip line (a) Metal layer M1, (b) Metal layer M4, (c) Metal layer M6.

1450 μm, $W4$ = 200 μm, $W5$ = 700 μm, $W6$ = 400 μm, $L6$ = 1450 μm, $L7$ = 1000 μm, $W7$ = 180 μm, $W8$ = 1850 μm, and $G1$ = 325 μm. The circles show the vias positions in the figure. The types of vias are color-coded such that the blue circles correspond to the thru-holes connecting the metals on M1, M4, and M6. The orange circles correspond to the blind-vias connecting the metal layers M1 and M4.

Simulated S parameters for these given values are presented in Figure 172 from 50 GHz to 70 GHz. As seen in the graph, $|S_{12}|$ was maximized at 60 GHz, and $|S_{12}| \geq$-0.65 dB is satisfied in the entire targeted frequency band around 60 GHz WPAN applications. It should also be noted that the low-loss response was retained from 50 GHz to 70 GHz, while satisfying $|S_{12}| \geq$-0.83 dB. $|S_{11}|$ and $|S_{22}|$ were also optimized for minimized reflections and their values were optimized to be smaller than -15 dB along the targeted frequency band. $|S_{11}|$ and $|S_{22}|$ values are smaller than -10 dB from 50 GHz to 70 GHz.

8.4.2 Stubs Placed at the Outermost Corners

After optimizing the antenna array and the signal transition separately, the optimized GPPO pad transition and the GPPO model were connected with the antenna arrays, as shown in Figure 173. In this section, the proposed STPAA with the first stub configuration, (stubs at the outermost corners of A1, A2 and A3) is presented.

Figure 174 shows the details of the metal layers M1, M3, M4 and M6. The GPPO

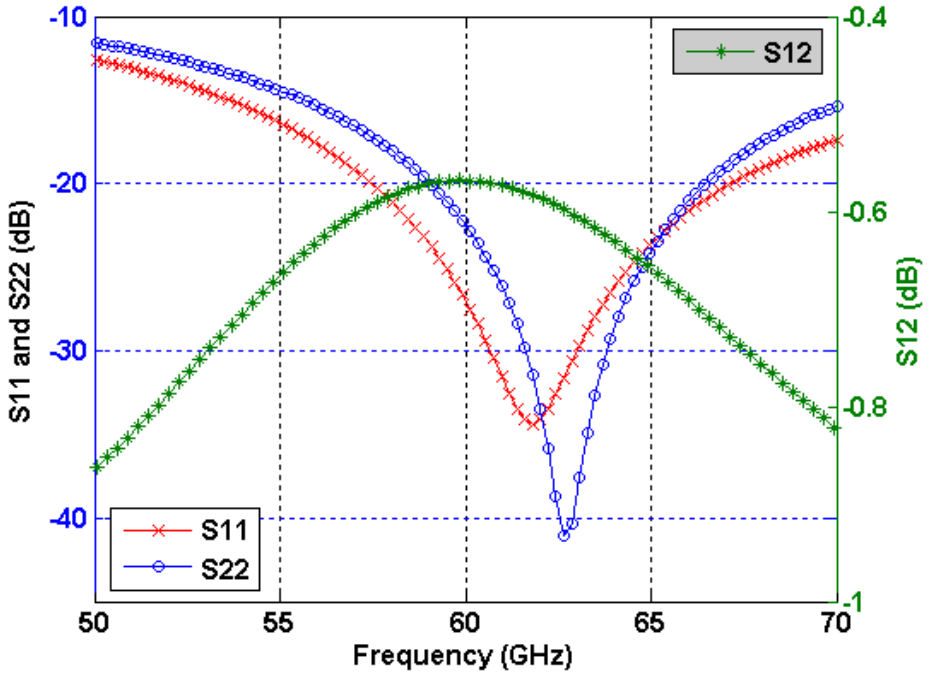

Figure 172. S-parameters of the optimized transition.

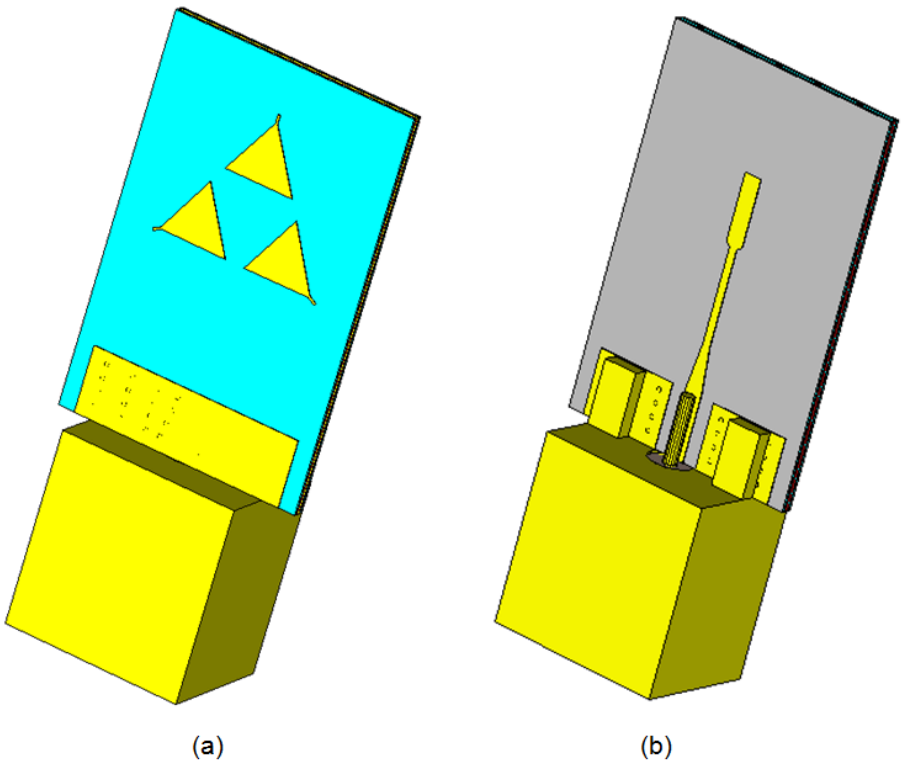

Figure 173. Simulation model of the stacked patch antenna with the GPPO connector model. (a) Perspective view from the top, (b) Perspective view from the bottom.

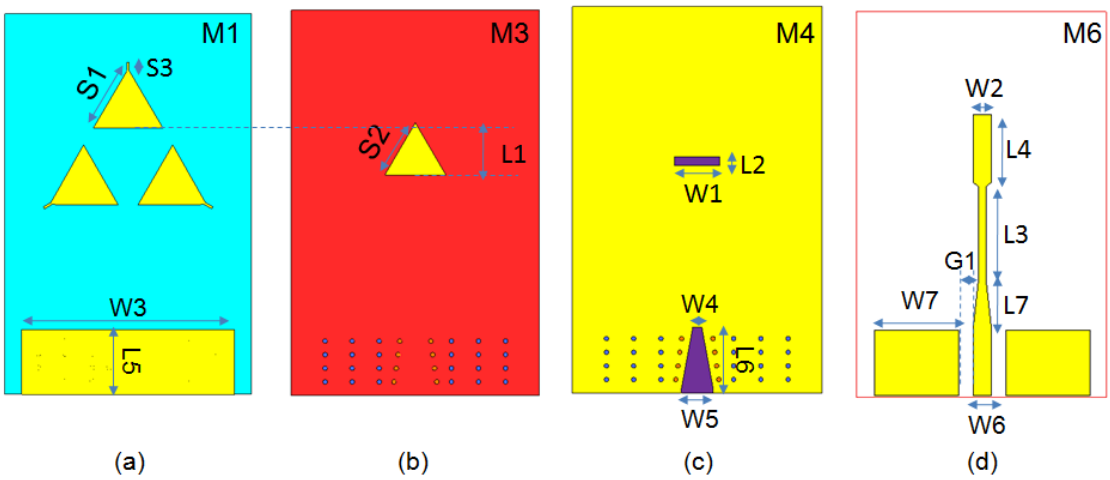

Figure 174. Details of the optimized stacked triangular patch antenna design with the first stub configuration. The GPPO model is made invisible to show the details. (a) Metal layer M1, (b) Metal layer M3, (c) Metal layer M4, (d) Metal layer M6.

connector model is made invisible here to make the figure easier to follow. Since the antenna and the connector transition were both optimized for 50Ω, the final structure required little effort to be optimized. The optimized values for the design variables shown in Figure 174 are as follows: $S1 = 1550\,\mu$m, $S2 = 1350\,\mu$m, $S3 = 150\,\mu$m, $W3 = 4750\,\mu$m, $L5 = 1450\,\mu$m, $G1 = 1050\,\mu$m, $L1 = 1083\,\mu$m, $W4 = 200\,\mu$m, $W5 = 700\,\mu$m, $L6 = 1450\,\mu$m, $W6 = 400\,\mu$m, $W1 = 1000\,\mu$m, $L2 = 200\,\mu$m, $L7 = 1000\,\mu$m, $W2 = 300\,\mu$m, $L4 = 1600\,\mu$m, $L3 = 1916\,\mu$m, $W7 = 1850\,\mu$m, and $G1 = 325\,\mu$m.

The simulated S_{11} data and the impedance locus are presented in Figure 175 for these given values. As seen in the S_{11} graph, three resonances were merged together to cover the desired 11.6% bandwidth around 60 GHz. The impedance locus also shows three tightly coupled loops in the 2:1 VSWR circle. An important design goal that should be kept in mind during optimization is to make sure that all of the three loops cross the real axis of the Smith chart while they are positioned in the VSWR circle. The S_{11} of the antenna may show a good match when the antenna is close to resonance, meaning the loops close to the real axis of the Smith chart but not crossing in the desired band. However, by ensuring that the antennas are not only matched but also resonating, the gain of the final design can be increased by $\sim$ 1 dB.

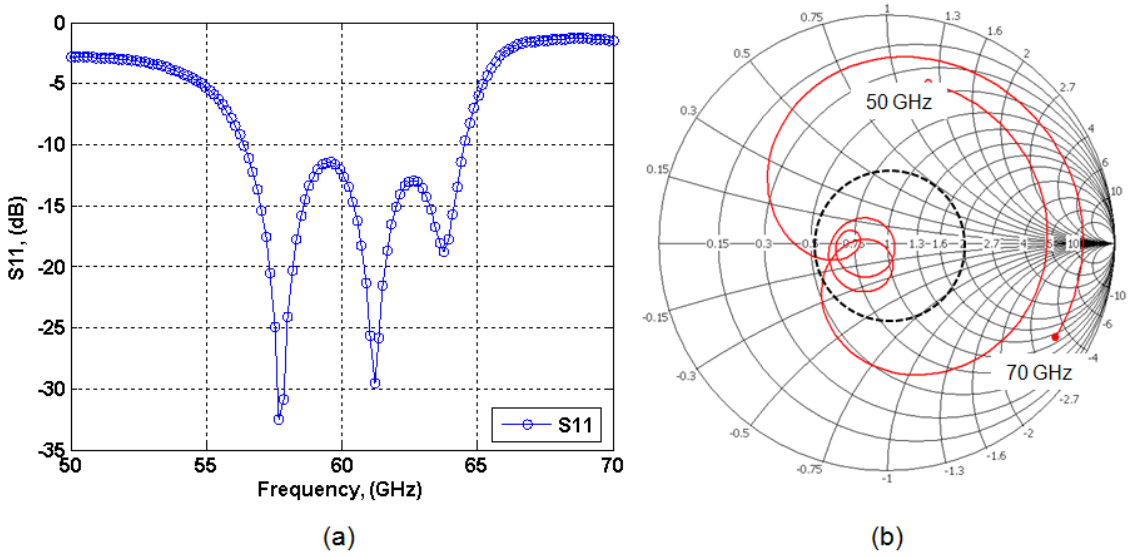

Figure 175. Simulated data for the optimized design with the GPPO model included. (a) S_{11}, (b) Impedance loci from 50 GHz to 70 GHz.

The far field of the optimized design was simulated over the entire desired frequency band. Figure 176 displays the directivity patterns on the E- and H-planes. As seen in the figure, the antenna array has stable characteristics except around 62 GHz, where a null occurs along the $\theta = 30^\circ$ axis towards the GPPO connector. The change in the radiation patterns for different frequencies may be attributed to the fact that different degenerate modes may be radiating at these frequencies since three degenerate modes are excited in the desired frequency band. In Table 12, the simulated values for the peak directivity, the peak gain, and the radiation and total efficiencies are summarized for the frequencies across the desired band. The simulated peak gain averages to 6.7 dB with an average total efficiency of 75%. The difference between the total efficiency and the radiation efficiency is that the effect of the impedance match is included in the total efficiency.

8.4.3 Stubs Placed at the Top Corners (STPAA with Parallel Stubs)

The optimized stacked patch antenna design with parallel stub configuration was also optimized while including the GPPO model and the transition. The details of the final design are shown in Figure 177. The optimized values for the design variables were found

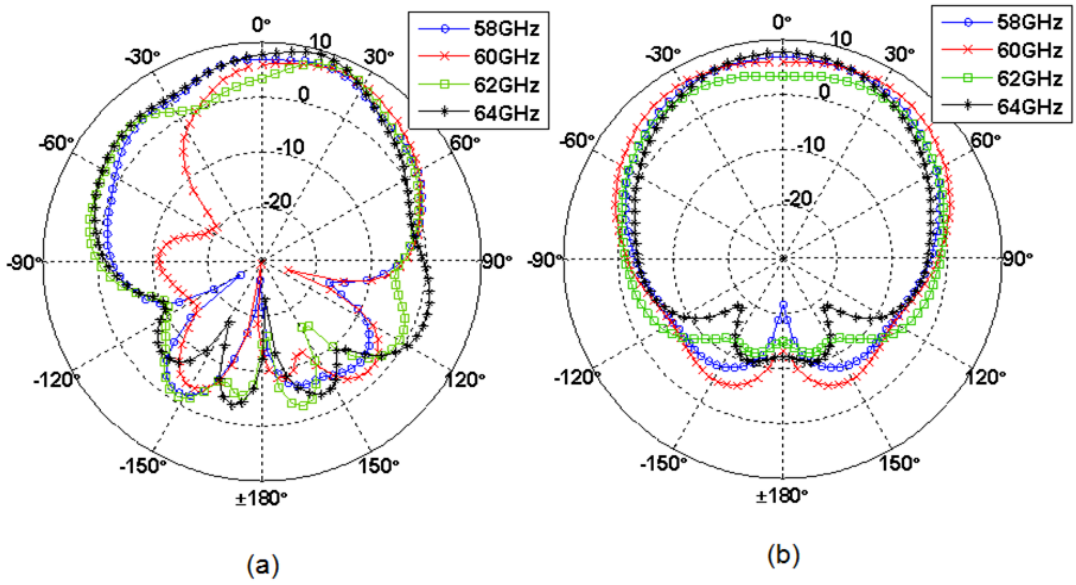

Figure 176. Simulated far field for pattern for different frequencies. (a) $\Phi = 90°$**, (b)** $\Phi = 0°$

Table 12. Summary of the simulated radiation parameters.

Frequency	Peak directivity	Radiation efficiency	Total efficiency	Peak gain
57 GHz	7.71 dBi	-0.95 dB (80.5%)	-1.09 dB (78%)	6.6 dB
58 GHz	7.5 dBi	-0.92 dB (81%)	-0.94 dB (81%)	6.6 dB
59 GHz	7.25 dBi	-0.95 dB (80%)	-1.2 dB (76%)	6.1 dB
60 GHz	7.47 dBi	-1.22 dB (75%)	-1.49 dB (71%)	6 dB
61 GHz	8.3 dBi	-1.30 dB (74%)	-1.32 dB (74%)	7 dB
62 GHz	8.07 dBi	-1.14 dB (77%)	-1.28 dB (75%)	6.8 dB
63 GHz	8.5 dBi	-1.15 dB (77%)	-1.34 dB (74%)	7.15 dB
64 GHz	9.22 dBi	-1.57 dB (70%)	-1.66 dB (68%)	7.6 dB

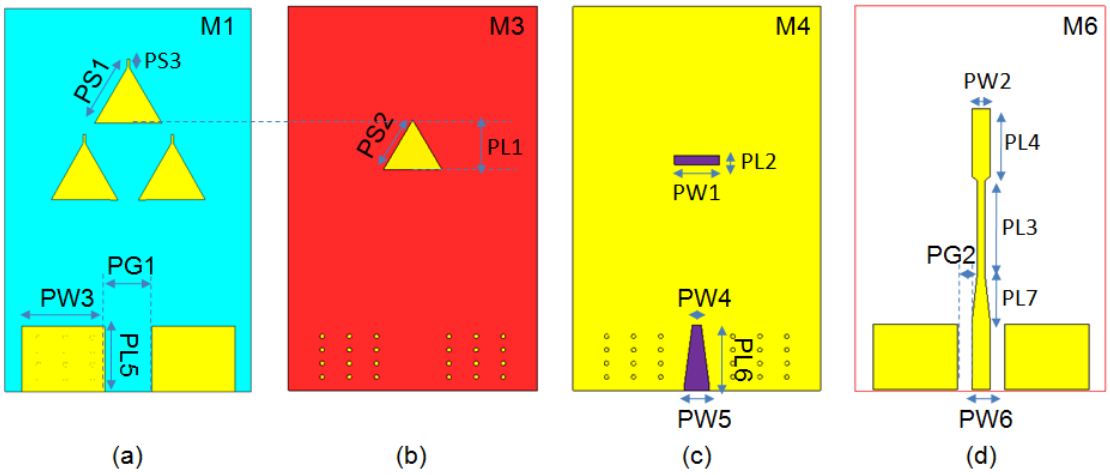

Figure 177. Details of the optimized stacked triangular patch antenna design with parallel stubs. GPPO model is made invisible to show the details. (a) Metal layer M1, (b) Metal layer M3, (c) Metal layer M4, (d) Metal layer M6.

as follows: $PS1 = 1500\,\mu$m, $PS2 = 1300\,\mu$m, $PS3 = 150\,\mu$m, $PW3 = 1850\,\mu$m, $PL5 = 1450\,\mu$m, $PG1 = 1050\,\mu$m, $PL1 = 1125\,\mu$m, $PW4 = 200\,\mu$m, $PW5 = 560\,\mu$m, $PL6 = 1450\,\mu$m, $PW6 = 400\,\mu$m, $PW1 = 1100\,\mu$m, $PL2 = 200\,\mu$m, $PL7 = 1000\,\mu$m, $PW2 = 300\,\mu$m, $PL4 = 1500\,\mu$m, $PL3 = 2116\,\mu$m, and $PG2 = 325\,\mu$m.

Figure 178 shows the simulated S_{11} and the impedance locus for these given values. As seen in the figure, the resonances are successfully merged around 60 GHz to meet the desired bandwidth requirement. The impedance locus also presents two tightly coupled resonating loops positioned in the 2:1 VSWR circle. It should also be noted that the loops cross the real axis, meaning that resonance is achieved instead of being close to the resonance.

Radiation properties of the antenna were also simulated and the obtained far field patterns across the desired band are presented in Figure 179 on the E- and H-planes. As mentioned for the STPAA with the stubs at the outermost corners, the change in the radiation patterns for different frequencies may be attributed to the fact that different degenerate modes may be radiating at these frequencies since two degenerate modes are excited in the desired frequency band. Additionally, the simulated values of the peak directivity, the peak gain, and the radiation and total efficiencies are summarized in Table 13. Compared to the

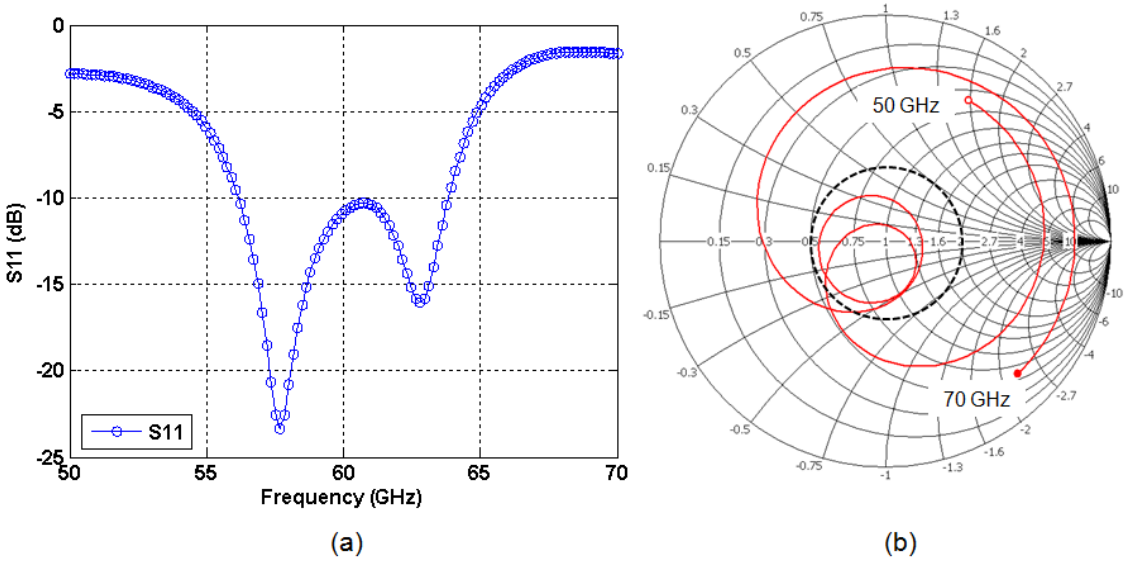

Figure 178. Simulated data for the optimized stacked patch antenna design with the parallel stub configuration including the GPPO model. (a) S_{11}, (b) Impedance loci from 50 GHz to 70 GHz.

results in Table 12, the parallel stub configuration has 0.2 dB to 1 dB higher gain values across the frequency band of interest except at 64 GHz, where the gain is lower for this configuration.

8.5 Design for the Probe-based Measurement Setup

As an alternative to the edge-mount GPPO connectors, GSG air coplanar probes can be used to measure the antenna response. In fact, it was concluded from the measurements of the multi-beam antennas covered in Chapters 6 and 7 of this thesis that the connector-based measurement setup requires advanced calibration and de-embedding methods to remove the effects of the cable, adapter, and the edge-mount connectors; whereas, the probe-based measurements result in accurate S-parameter data even with the basic Short-Open-Load (SOL) calibration method. Therefore, the proposed STPAA was also optimized for the probe-based measurement setup. Moreover, the optimized design was taped-out for fabrication.

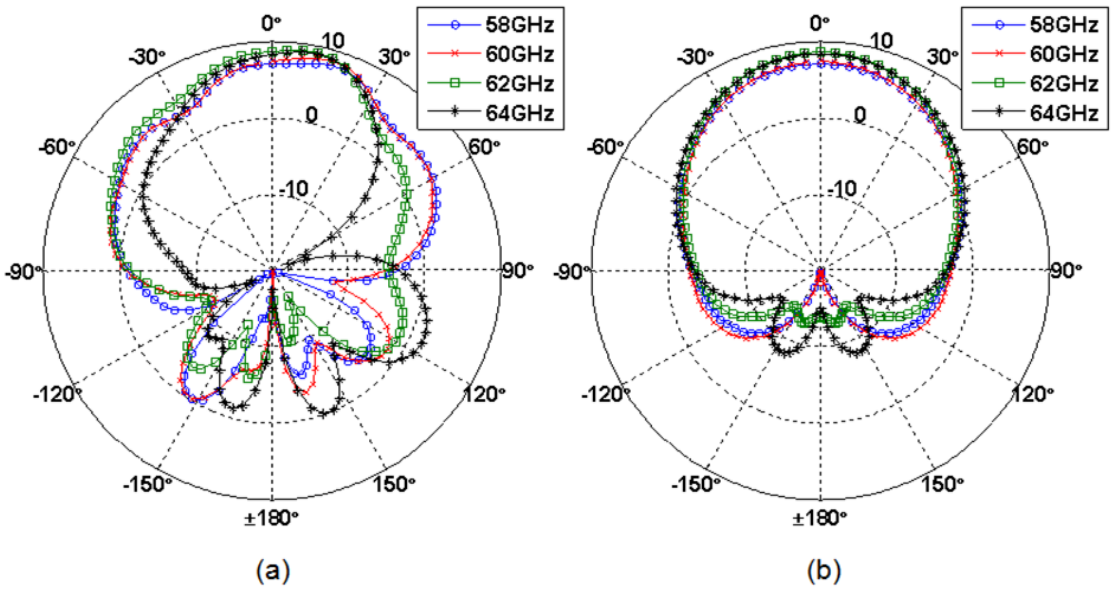

Figure 179. Simulated far field for pattern for different frequencies. (a) $\Phi = 90°$**, (b)** $\Phi = 0°$

Table 13. Summary of the simulated radiation parameters for the STPAA with the parallel stub configuration.

Frequency	Peak directivity	Radiation efficiency	Total efficiency	Peak gain
57 GHz	7.77 dBi	-0.9 dB (81%)	-1.02 dB (79%)	6.75 dB
58 GHz	7.97 dBi	-0.85 dB (82%)	-0.89 dB (82%)	7.1 dB
59 GHz	8.3 dBi	-0.82 dB (83%)	-1.03 dB (79%)	7.25 dB
60 GHz	8.54 dBi	-0.94 dB (81%)	-1.31 dB (74%)	7.2 dB
61 GHz	8.7 dBi	-1.06 dB (78%)	-1.48 dB (71%)	7.2 dB
62 GHz	9.16 dBi	-1.21 dB (76%)	-1.45 dB (72%)	7.7 dB
63 GHz	9.46 dBi	-1.57 dB (70%)	-1.69 dB (68%)	7.77 dB
64 GHz	9 dBi	-2.14 dB (61%)	-2.74 dB (53%)	6.24 dB

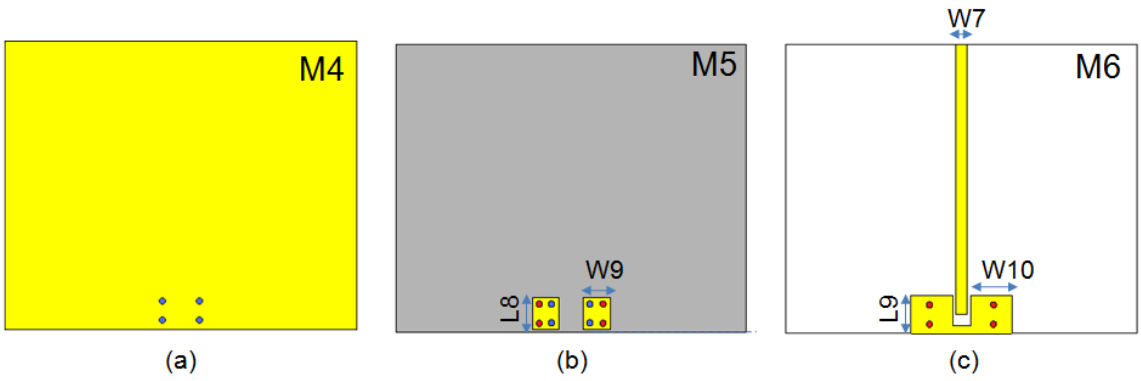

Figure 180. Details of the optimized transition from the GSG probe pad to the microstrip line (a) Metal layer M4, (b) Metal layer M5, (c) Metal layer M6.

8.5.1 CPW-to-Microstrip Line Transition

The proposed STPAA was optimized to measure with the GBB Probe Industry's Model 67A GSG 250 air coplanar waveguide probes [92]. Similar to the case with the GPPO connectors, the transition from the the GSG probe pad to the feeding microstrip line (ML) was optimized separately. Figure 180 shows the details of this transition. As seen in the figure, the transition from the short CPW line to ML was achieved simply by extending the signal line of the short CPW line. The ground pads of the CPW line were electrically connected to the ground layer on metal layer M4. Staggered via configuration was preferred to prevent the registration errors in the via connections. To achieve this configuration additional ground pads were placed on metal layer M5, and the ground pads on metal layer M6 were connected to these additional ground pads on M5 with blue-colored vias in Figure 171. The pads on M5 were also connected to the ground plane on M4 with red-colored vias in Figure 171. It should be noted that blue vias and the red vias are displaced to achieve the staggered via configuration.

The optimized values for the design variables shown in Figure 180 were found as follows: $L8 = 500\,\mu$m, $W9 = 1300\,\mu$m, $L9 = 600\,\mu$m, $W10 = 420\,\mu$m, $W7 = 180\,\mu$m and $50\,\mu$m gap between the signal line and the ground pad of the CPW line. Simulated S parameters for these given values are presented in Figure 181 from 50 GHz to 70 GHz. As seen in the graph, $|S_{12}| \geq$-0.53 dB is satisfied in the entire targeted frequency band for

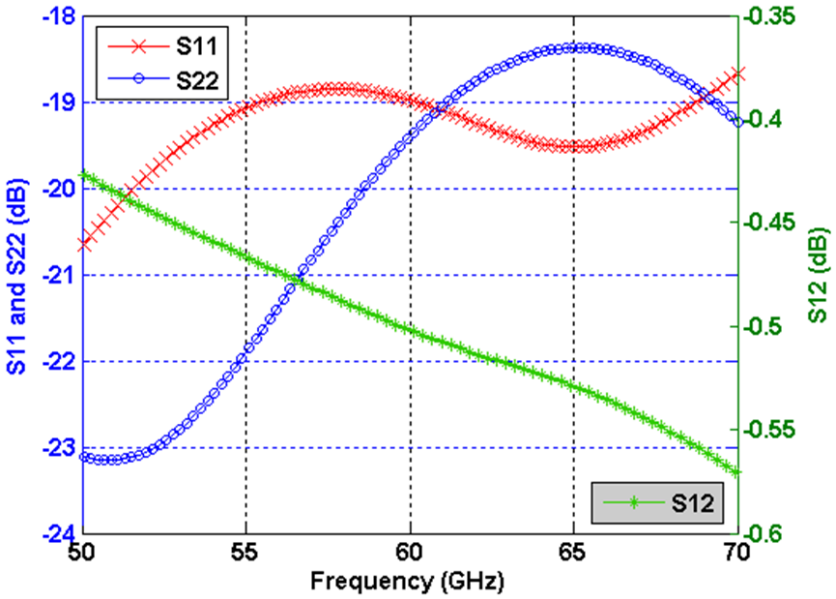

Figure 181. S-parameters of the optimized transition.

the 60 GHz WPAN applications. It should also be noted that the low-loss response was retained from 50 GHz to 70 GHz, while satisfying $|S_{12}| \geq$-0.57 dB. $|S_{11}|$ and $|S_{22}|$ were also optimized for minimized reflections and their values were optimized to be smaller than -18 dB from 50 GHz to 70 GHz.

8.5.2 Stubs Placed at the Outermost Corners

After optimizing the antenna array and the signal transition separately, the optimized pad transition was connected with the antenna array. Only the STPAA with the stubs at the outermost corners was optimized since the allocated area for the antenna design in the taped-out board could fit only single antenna design. In this section, the simulated results for the optimized antenna are presented. The measurements of the antenna will be a part of future work.

Figure 182 shows the details of the metal layers M1, M3, M4, M5 and M6 of the antenna with the optimized signal transition. The optimized values for the design variables shown in Figure 182 are as follows: $S1 = 1550\,\mu$m, $S2 = 1350\,\mu$m, $S3 = 150\,\mu$m, $L1 = 1087\,\mu$m, $W1 = 1000\,\mu$m, $L2 = 200\,\mu$m, $L8 = 500\,\mu$m, $W9 = 1300\,\mu$m, $L9 = 600\,\mu$m,

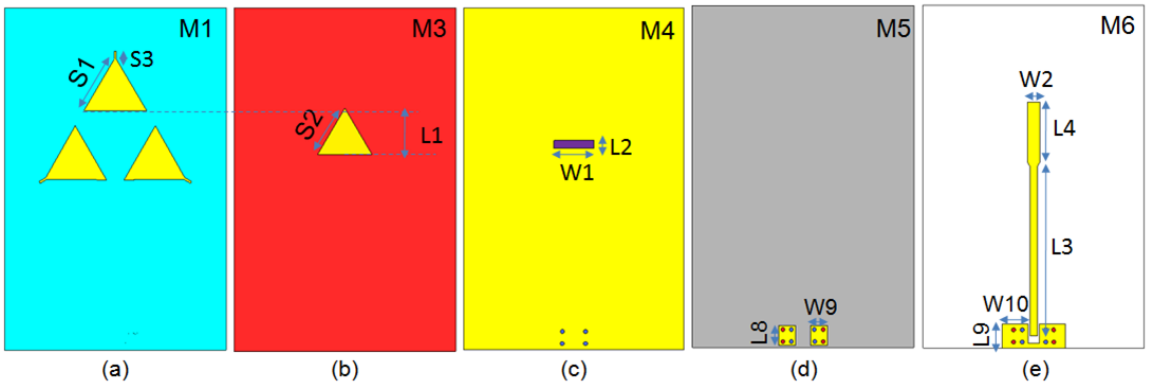

Figure 182. Details of the optimized stacked triangular patch antenna design for the probe-based measurement setup. (a) Metal layer M1, (b) Metal layer M3, (c) Metal layer M4, (d) Metal layer M5, (d) Metal layer M6.

$W10 = 420\ \mu$m, $W2 = 300\ \mu$m, $L4 = 1600\ \mu$m, and $L3 = 4200\ \mu$m.

The simulated S_{11} data and the impedance locus are presented in Figure 183 for these given values. As seen in the S_{11} graph, three resonances were merged together to cover the desired 11.6% bandwidth around 60 GHz. The impedance locus also shows three tightly coupled loops in the 2:1 VSWR circle. It should also be noted that the antenna array resonates in the desired band.

The far field of the optimized design was simulated over the entire desired frequency band. Figure 184 displays the directivity patterns on the E- and H-planes. As seen in the figure, the antenna array has stable characteristics. The slight changes in the radiation patterns for different frequencies may be attributed to the fact that different degenerate modes may be radiating at these frequencies since three degenerate modes are excited in the desired frequency band. The simulated values for the peak directivity, the peak gain, and the radiation and total efficiencies are summarized in Table 14, for the frequencies across the desired band. The simulated peak gain averages to 7.12 dB with an average total efficiency of 79%. The difference between the total efficiency and the radiation efficiency is that the effect of the impedance match is included in the total efficiency.

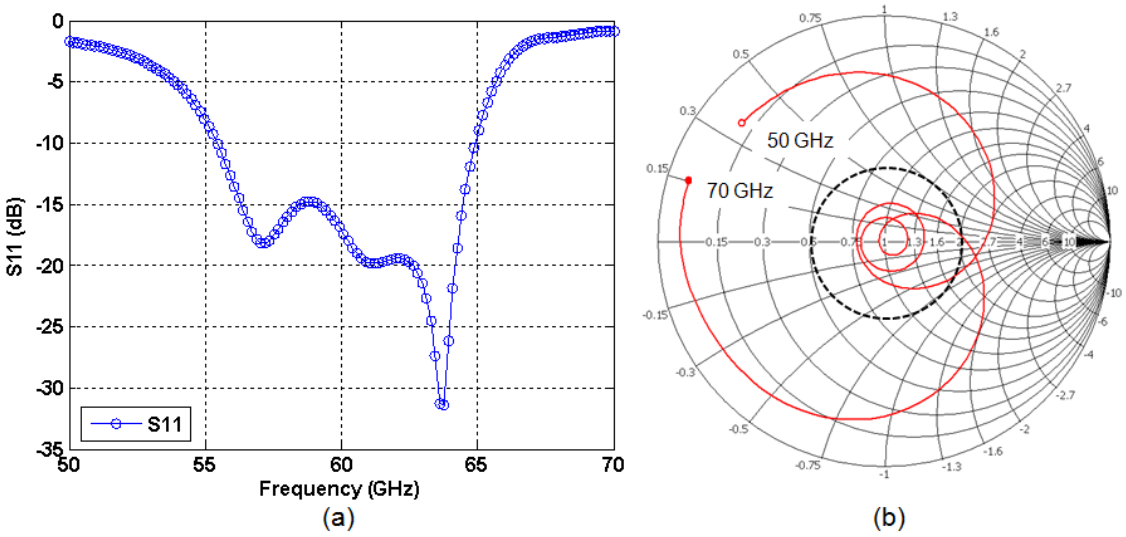

Figure 183. Simulated data for the optimized stacked patch antenna design for the probe-based measurement setup. (a) S_{11}, (b) Impedance loci from 50 GHz to 70 GHz.

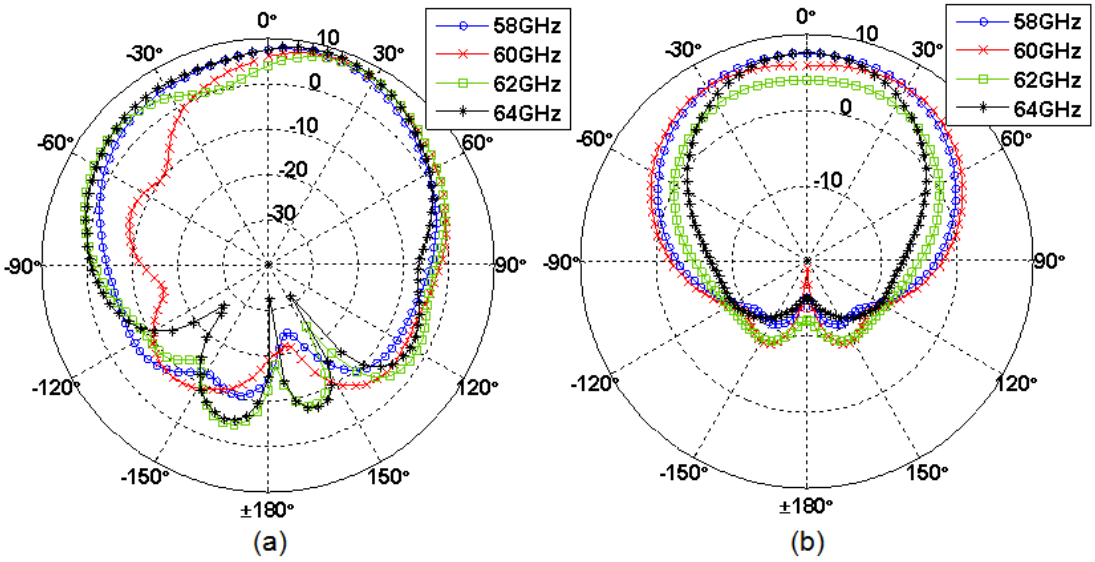

Figure 184. Simulated far field for pattern for different frequencies. (a) Φ = 90°, (b) Φ = 0°

Table 14. Summary of the simulated radiation parameters for the STPAA with the parallel stub configuration.

Frequency	Peak directivity	Radiation efficiency	Total efficiency	Peak gain
57 GHz	8.07 dBi	-0.78 dB (83%)	-0.85 dB (82%)	7.22 dB
58 GHz	8.13 dBi	-0.77 dB (84%)	-0.88 dB (81%)	7.25 dB
59 GHz	8.1 dBi	-0.83 dB (83%)	-0.97 dB (80%)	7.13 dB
60 GHz	7.95 dBi	-1.04 dB (79%)	-1.12 dB (77%)	6.83 dB
61 GHz	7.95 dBi	-1 dB (80%)	-1.48 dB (79%)	6.9 dB
62 GHz	7.85 dBi	-0.91 dB (81%)	-1.04 dB (80%)	6.9 dB
63 GHz	8.17 dBi	-0.95 dB (80%)	-0.98 dB (80%)	7.18 dB
64 GHz	8.75 dBi	-1.16 dB (77%)	-1.18 dB (76%)	7.57 dB

8.6 Conclusions

A new wireless technology has been emerging to enable high-throughput wireless communications using the internationally available 7 GHz spectrum around 60 GHz. The miniaturization factors that can be achieved with the high carrier frequency prevent the antenna miniaturization from being an issue. Furthermore, the SOP technology promises highly-integrated, high-performance, and low-cost RF-systems to design compact front-end modules operating at 60 GHz. However, there is still a need for efficiently integrating the antenna with the passive and active circuitries of the module. A novel material called RXP has been shown to have superior RF performance and mechanical characteristics up to 110 GHz, making RXP-based multilayer substrates an excellent medium to realize SOP-integrated RF systems at 60 GHz.

A novel stacked triangular patch antenna array (STPAA) designed for a low-profile RXP-based multilayer substrate has been proposed in this chapter as a solution to the antenna integration problem at 60 GHz. RXP-based multilayer substrates have been characterized for the antenna applications for the first time with the designs proposed in this dissertation. In addition to the multilayer RXP substrate, the novelty of the proposed stacked patch antenna array comes from the fact that triangular patch antennas with stubs were used

instead of the conventional rectangular patch antennas. Two configurations of the proposed stacked triangular patch antenna array have been presented in this chapter. Mutual resonances between the antenna elements were balanced and merged properly to overcome the narrow bandwidth limitation of the patch antennas. The design process to achieve this goal has been discussed in detail to explain the principles of the proposed STPAA. Moreover, design guidelines are provided for the antenna engineers to simplify and shorten the design process. GPPO connector modeling and the transition design have also been included in this chapter to provide insight on the co-design requirements for the antenna.

Desired bandwidth coverage and the radiation properties necessary for the 60 GHz WPAN applications were achieved with the optimized designs for the both configurations proposed in this chapter. The antennas were designed considering connector-based and probe-based measurement setups. However, due to the size of the prototype board only single antenna design was taped-out for fabrication. The STPAA optimized for the probe-based measurement setup was preferred since the measurements of the antennas covered in Chapters 6 and 7 of this thesis have shown that accurate measurements can be obtained using GSG probes; whereas, connector-based measurements require advanced de-embedding methods to remove the effects of the connector, cable and the adapter. The measurement of the antenna will be done as a part of future work.

The proposed structure using the multilayered configuration presents a more compact array solution compared to the single-layer series- or parallel-feed antenna arrays. The proposed STPAA has a single-beam broadside radiation pattern with an average gain value of 7 dB. It should be noted that although merging resonances help to increase the bandwidth of the antenna, it may also affect the uniformity of the far-field pattern in the desired band since different degenerate modes may be radiating at different frequencies, instead of single mode radiating in the entire band. If pattern reconfigurability or a higher gain value is required, the proposed STPAA configuration can be used in an array configuration. However, optimizing the array configuration using STPAA as the main element may result

in a complex design process since it will require tuning a large number of design variables and also optimizing the mutual coupling between the elements. Analyzing the effects of patch shapes, other than the triangular patches proposed in this dissertation, on the complexity of the design process and the modes radiating in the desired frequency band can be recommended as a part of future work.

CHAPTER 9

CONCLUSIONS

This dissertation primarily focused on designing high-performance antennas along with developing techniques for the miniaturization and system-on-package (SOP) integration of these antennas to achieve fully-integrated SOP systems using advanced multilayer organic substrates and thin-film magneto-dielectrics. The 2.4/5 GHz WLAN/WiMAX and 60 GHz WPAN applications were the targeted applications for the antenna designs. Based on these objectives, the outcome of this research can be summarized as follows:

1. The system-on-package integration of monopole antennas for the 2.4/5 GHz WLAN and WiMAX bands was achieved using a conformal antenna configuration on liquid crystalline polymer based rigid-flex substrates. The integration of flexible antenna substrate with the rigid module package using a single process has been showed the first time with the proposed rigid-flex configuration. The effects of an on-package shielding box was also included during the design of the antennas. The proposed configuration was implemented using single and dual-band prototypes covering the 2.4/5 GHz WLAN and WiMAX bands. The fabricated antennas were also measured and it was found that the requirements were met for the successful operation in the WLAN and WiMAX bands.

2. Magneto-dielectric substrates have been studied for effective miniaturization of antennas and other electromagnetic structures. However, these materials do not exist in nature and are not yet available in the market; hence, they need to be synthesized. There has been research efforts at the Packaging Research Center (PRC) at Georgia Tech to synthesize low-loss magneto-dielectric thin-films. This dissertation supported this material synthesis process in terms of material characterization. In this part of this Ph.D. research, two characterization methods that are based on measuring easy-to-fabricate, -measure, and -analyze two metal layer printed structures

were proposed and applied to the test vehicles of thin magneto-dielectrics synthesized at the PRC. Both methods were verified with the controlled experiments based on simulations and theoretical analysis. Several batches have been synthesized, fabricated and characterized to verify the material synthesis process. Although several boards were characterized to have μ_r values ranging from 1.3 to 1.9 in the low GHz frequencies, some batches with nonmagnetic attributes were also characterized. The fact that not every batch of the materials synthesized in this project showed magnetic properties points to the difficulty of synthesizing magneto-dielectric materials. The reason for the inconsistency in the characterized values of consecutive batches may be attributed to improper alignment of the magnetic dipoles in the synthesized material, oxidation, agglomeration and improper encapsulation of nanoparticles. Advanced synthesis techniques and alternative routes are required to reduce the loss of the substrates and guarantee the consistency and repeatability of the parameters for every fabricated batch.

3. The miniaturization of the conductor-backed planar antennas using magneto-dielectric substrates were investigated both theoretically and experimentally using full-wave electromagnetic simulations. It was concluded that magneto-dielectrics can miniaturize the conductor-backed planar antennas, such as microstrip patch antennas, while improving the bandwidth of the antennas at the expense of increased surface wave power. It was found that when the size of the ground plane is adjusted properly, the surface wave power can be used to improve the gain of the antenna with the constructive addition of diffracted surface waves. Similarly, this method can be used to emulate the radiation pattern of a monopole antenna due to increased back-radiation. However, the antenna may become a poor radiator if the size and the shape of the ground plane are not optimized properly. Therefore, the diffraction of the surface

waves from the edges of the truncated conductor-backed magneto-dielectric substrates may be studied in more detail as a part of future work. Finding design guidelines on the size and the shape of the ground plane (circular, rectangular etc.) to optimize the radiation parameters of the antenna can also be targeted as a part of future work.

4. The efficient miniaturization of the reactive impedance surfaces using the magneto-dielectric substrates was also investigated along with the application of these surfaces to low-profile antenna designs. It was found that magneto-dielectrics are more advantageous in miniaturizing these structures since increasing the permeability of the substrate can miniaturize these surfaces while improving the reflection bandwidth. The antenna performance can be improved by replacing these surfaces with the conductor ground plane of printed planar antennas; however, the size of the reactive impedance surface should be adjusted properly to improve the performance of the antenna.

5. Multi-beam antennas were proposed for mobile 60 GHz WPAN applications as an alternative to pattern-reconfigurable antennas. Two novel slot antenna designs with multi-beam radiation patterns were designed, and fabricated on an 8 mil thick LCP substrate. The effects of the increased surface-wave propagation due to the higher order modes were eliminated using ground corrugations. The designed antennas were measured with probe-based and connector-based measurement setups. It was concluded that probe-based measurement setup is more suitable for return loss measurements since the connectors require adapters whose effect cannot be removed with simple calibration techniques. However, far field pattern of the antenna can be measured easily using the edge-mount millimeter wave connectors. Although the proposed multi-beam radiation pattern is more advantageous compared to the

single-beam directive pattern, the ultimate antenna solution for mobile WPAN applications is a single-element pattern reconfigurable antenna that reconfigures the beam direction to maximize the quality of wireless communications. It is recommended as future work to study the potential of achieving pattern reconfigurability using the proposed multi-beam antennas.

6. An RXP-based multilayer stack-up was characterized for the first time for the antenna applications operating around 60 GHz. A stacked triangular patch antenna array integrated on a RXP-based multilayer stack-up was designed. In addition to the multilayer RXP substrate, the novelty of the proposed stacked patch antenna array comes from the fact that triangular patch antennas with stubs were used instead of the conventional rectangular patch antennas. The wide bandwidth requirement of the 60 GHz band applications was achieved by merging coupled resonances. The multiple resonance mechanisms and the effect of design variables on these resonances have been studied in detail to gain insight in the design process. Design guidelines have been provided to simplify the complicated design process of stacked patch antennas. It should be noted that although merging resonances help to increase the bandwidth of the antenna, it may also affect the uniformity of the far-field pattern in the desired band since different degenerate modes may be radiating at different frequencies. If pattern reconfigurability or a higher gain value is required, the proposed STPAA configuration can be used in an array configuration. However, optimizing the array configuration using STPAA as the main element may result in a complex design process since it will require tuning a large number of design variables and also optimizing the mutual coupling between the elements. Analyzing the effects of patch shapes, other than the triangular patches proposed in this dissertation, on the complexity of the design process and the modes radiating in the desired frequency band can be recommended as a part of future work.

9.1 Publications

1. Nevin Altunyurt, Ralf Rieske, Madhavan Swaminathan, Venkatesh Sundaram, "Conformal antennas on liquid crystalline polymer substrates integrated with front-end module", *IEEE Trans. on Advanced Packaging*, vol. 32, pp. 797-808, Nov. 2009.

2. Nevin Altunyurt, Tae Hong Kim, Madhavan Swaminathan, "Printed monopole antennas with increased bandwidth and gain for Wi-Fi applications," *Proceedings of IEEE International Symposium on Antennas and Propagation*, pp. 237-240, June 2007.

3. Nevin Altunyurt, Madhavan Swaminathan, Venkatesh Sundaram, George White, "Conformal antennas on liquid crystalline polymer substrates for consumer applications," *Proceedings of Asia Pacific Microwave Conference*, pp. 1-4, Dec. 2007.

4. Nevin Altunyurt, Ralf Rieske, Madhavan Swaminathan, Venkatesh Sundaram, "Conformal WLAN/WiMAX antenna on rigid-flex liquid crystalline polymer based substrate," *IEEE Radio Wireless Symposium*, pp. 19-22, Jan. 2009 (Finalist for Student Paper Competition).

5. Nevin Altunyurt, Madhavan Swaminathan, Pulugurtha Raj, Vijay Nair, "Antenna miniaturization using magneto-dielectric substrates," *IEEE Electronic Components and Technology Conference*, pp. 801-808, May 2009.

6. Nevin Altunyurt, Madhavan Swaminathan, Pulugurtha Raj, Vijay Nair, "Magneto-dielectric substrates for antenna miniaturization," *National Radio Science Meeting (URSI)* 2009.

7. Madhavan Swaminathan, Nevin Altunyurt, Seughyun Hwang "Advanced polymers for advanced packaging applications," *submitted to IEEE European Microwave Week*, 2010.

8. Madhavan Swaminathan, Seughyun Hwang, Nevin Altunyurt "RF system integration and miniaturization using advanced polymers," *accepted for IEEE International Microwave Symposium*, 2010.

Invention disclosures:

1. Nevin Altunyurt, Madhavan Swaminathan, Venkatesh Sundaram, "Integration of 3D antennas supporting multiple bands onto liquid crystalline polymer (LCP) based package," Invention Disclosure ID: 3790, March 2006, *Provisional Patent Application filed by Georgia Tech*.

2. Nevin Altunyurt, Madhavan Swaminathan, Tae Hong Kim, Mahadevan Iyer, Rao Tummala, "High gain antennas for mobile MIMO applications," Invention Disclosure ID: 3996, October 2006, *Provisional Patent Application filed by Georgia Tech*.

APPENDIX A

PER UNIT LENGTH PARAMETERS OF MICROSTRIP LINE ON A THIN-FILM MAGNETO-DIELECTRIC SUBSTRATE

A.1 Telegrapher's Equations

A transmission line can be considered as a distributed-parameter network, where voltages and currents can vary in magnitude and phase over its length. Therefore, a piece of a transmission line with an infinitesimal length, dz, can be represented with a lumped-element circuit model as shown in Figure 185 [39]. In this representation, R is a series resistance per unit length, L is a series inductance per unit length, G is a shunt conductance per unit length, and C is a shunt capacitance per unit length. Writing Kirchhoff's voltage and current law for this circuit representation for the sinusoidal steady state condition one can derive:

$$\frac{dV(z)}{dz} = -(R + j\omega L)I(z) \tag{124}$$

$$\frac{dI(z)}{dz} = -(G + j\omega C)V(z) \tag{125}$$

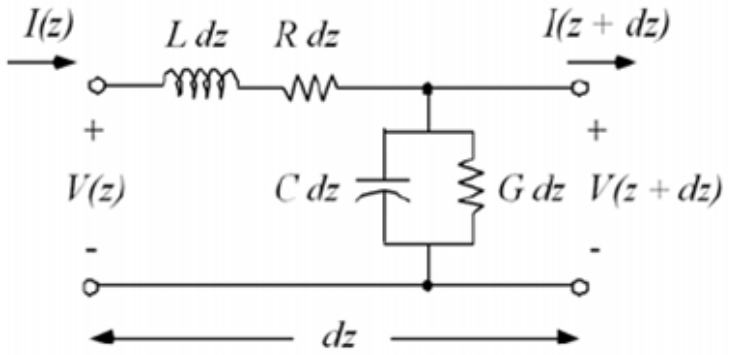

Figure 185. Equivalent circuit for an incremental length of transmission line.

where V(z) and I(z) are cosine-based phasors for voltage and current. Equations (124) and (125) are known as Telegrapher's equations and these equations can be solved simultaneously to give the wave equations for V(z) and I(z):

$$\frac{d^2V(z)}{dz^2} - \gamma^2 I(z) = 0 \tag{126}$$

$$\frac{d^2I(z)}{dz^2} - \gamma^2 V(z) = 0 \tag{127}$$

where

$$\gamma = \alpha + j\beta = \sqrt{(R + j\omega L)(G + j\omega C)} \tag{128}$$

is the complex propagation constant. Solving these wave equations in Equations (126) and (127), traveling wave solutions can be found as

$$V(z) = {V_0}^+ \exp^{-\gamma z} + {V_0}^- \exp^{\gamma z} \tag{129}$$

$$I(z) = {I_0}^+ \exp^{-\gamma z} + {I_0}^- \exp^{\gamma z} \tag{130}$$

Substituting (129) in (124), the characteristic impedance Z_0 can be derived as

$$Z_0 = \sqrt{\frac{(R + j\omega L)}{(G + j\omega C)}} \tag{131}$$

A.2 Deriving Per Unit Length Parameters for a Microstrip Line on a Thin-film Magneto-dielectric Substrate

Per unit length parameters for the microstrip line on a thin-film magneto-dielectric substrate can be obtained by deriving the Telegrapher equations from Maxwell's equations. The geometry of the microstrip line is shown in Figure 186. To ease the problem, it is assumed that microstrip line is embedded in the same magneto-dielectric medium as the substrate. The permittivity and permeability of the material is assumed to be ϵ=ϵ'-jϵ'' and μ=μ'-jμ''. Electric and magnetic field lines are also shown in the figure with red and green arrows, respectively.

A TEM wave propagating along the z-axis on the microstrip line is characterized by E_z=H_z=0; therefore, we are left with E_y(y,z) and H_x(x,z). Furthermore, since the substrate

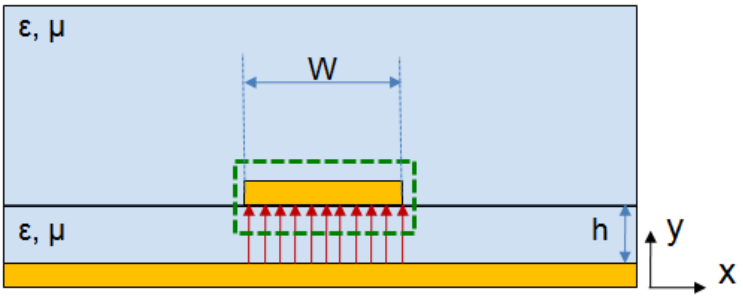

Figure 186. Geometry of the microstrip line on a magneto-dielectric substrate.

is a thin-film material, the thickness of the substrate h is much smaller than the width of the line W, i.e. $h \ll W$. In this case, the fringing fields can be ignored to simplify the problem. In addition, conductor losses are ignored to simplify the analysis. The fields around the microstrip line should satisfy Maxwell's curl equations,

$$\nabla \times \vec{E} = -j\omega\mu\vec{H} \tag{132}$$

$$\nabla \times \vec{H} = j\omega\epsilon\vec{E} \tag{133}$$

Expanding (132) and (133) gives the following vector equations:

$$\nabla \times \vec{E} = -\hat{x}\frac{\partial E_y}{\partial z} + \hat{z}\frac{\partial E_y}{\partial x} = -\hat{x}\, j\omega\mu H_x \tag{134}$$

$$\nabla \times \vec{H} = \hat{y}\frac{\partial H_x}{\partial z} - \hat{z}\frac{\partial H_x}{\partial y} = \hat{y}\, j\omega\epsilon E_y \tag{135}$$

Since the $\hat{z}$ components of these two equations must vanish, it is seen that E_y and H_x should have the forms

$$E_y = f(z) \tag{136}$$

$$H_x = g(z) \tag{137}$$

Then, (134) and (135) can be reduced to

$$\frac{\partial E_y}{\partial z} = j\omega\mu H_x \tag{138}$$

$$\frac{\partial H_x}{\partial z} = j\omega\epsilon E_y \tag{139}$$

Using (136) and (137) in (138) and (139) gives

$$\frac{\partial f(z)}{\partial z} = j\omega\mu g(z) \tag{140}$$

$$\frac{\partial g(z)}{\partial z} = j\omega\epsilon f(z) \tag{141}$$

The voltage and current carried by the TEM waves on the microstrip line can be related to the electromagnetic fields via

$$V(z) = -\int_0^h E_y(z)\,dy = hf(z) \tag{142}$$

$$I(z) = \int_0^W \vec{J}_s \cdot \hat{z}\,dx = \int_0^W \left(-\hat{y} \times \vec{H}\right) \cdot \hat{z}\,dx = Wg(z) \tag{143}$$

Then f(z) and h(z) can be eliminated from Equations (140) and (141) using (142) and (143) to give

$$\frac{\partial V(z)}{\partial z} = j\omega\mu\frac{h}{W}I(z) \tag{144}$$

$$\frac{\partial I(z)}{\partial z} = j\omega\epsilon\frac{W}{h}V(z) \tag{145}$$

Finally, by comparing (144) with (124) and (145) with (125) one can find

$$R + j\omega L = j\omega\frac{(\mu' - j\mu'')h}{W} \tag{146}$$

$$G + j\omega C = j\omega\frac{(\epsilon' - j\epsilon'')W}{h} \tag{147}$$

Equating the real and imaginary parts of each equation, finally R, L, G, and C per unit parameters can be derived as follows:

$$R = \frac{\omega\mu''h}{W} \tag{148}$$

$$L = \frac{\mu'h}{W} \tag{149}$$

$$G = \frac{\omega\epsilon''W}{h} \tag{150}$$

$$C = \frac{\epsilon'W}{h} \tag{151}$$

Although this simplified analysis does not provide the exact solution to the real-case microstrip line problem, it provides the insight on how ϵ', ϵ'', μ' and μ'' affect the per unit line parameters. As can be seen from (148) to (151), magnetic loss of the substrate affects per unit length resistance, R, along with the conductor loss for a lossy metal case. The dielectric loss affects per unit length conductance term, G, while per unit length capacitance, C, depends on ϵ'. Finally, per unit length inductance is directly proportional to μ'.

APPENDIX B

RADIATED FIELDS OF A HERTZIAN MAGNETIC DIPOLE ON A CONDUCTOR-BACKED MAGNETO-DIELECTRIC SUBSTRATE

Calculating the radiated fields of printed antennas on conductor-backed substrates requires using full-wave electromagnetic solvers to calculate these fields. Although accurate results can be obtained through these calculations, there is usually very little insight gained about the radiation mechanism. On the other hand, analytical expressions derived using electric and magnetic Hertzian dipoles can provide accurate results and a clear picture of how the antenna dimensions and the substrate parameters affect the radiated fields of the antenna.

A transmission line method to calculate the far-field radiation of arbitrarily directed Hertzian dipoles in a multilayer substrate has been presented in [67]. In the method presented in this paper, the fields of the Hertzian dipoles are found using the reciprocity theorem, where the radiated fields of the Hertzian dipole in the substrate are calculated using the scattered fields in the substrate due to plane wave incidence. The TM mode plane wave is used to calculate E_θ, and TE mode plane wave is used to calculate E_ϕ. The fields of a magnetic Hertzian dipole on a single layer conductor-backed magneto-dielectric substrate are derived here following the transmission analogy and the method presented in [67].

Figure 187 shows the transmission line circuit used to calculate the radiated fields of a

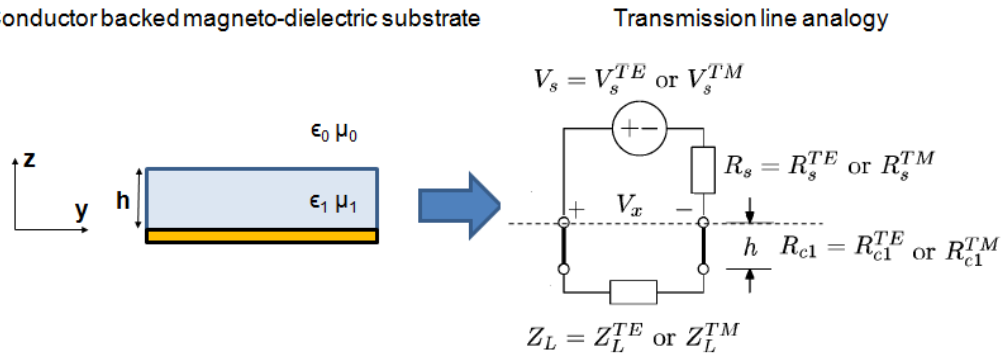

Figure 187. Transmission line circuit used to calculate the horizontal $\vec{E}$ of a magnetic Hertzian dipole.

Hertzian dipole. Assuming the angle of incidence is (θ_i, ϕ_i), the circuit parameters derived for the horizontal magnetic Hertzian dipole can be listed as follows [67]:

$$\begin{aligned} V_s^{TE} &= j\omega\epsilon_0 \frac{\exp -jk_0R}{2\pi R} \\ V_s^{TM} &= V_s^{TE}\cos(\theta_i) \\ R_s^{TE} &= \frac{\sqrt{\epsilon_0/\mu_0}}{\cos(\theta_i)} \\ R_s^{TM} &= \frac{\sqrt{\epsilon_0/\mu_0}}{\cos(\theta_i)} \\ R_c^{TE} &= \frac{\epsilon_1\sqrt{\epsilon_0/\mu_0}}{\sqrt{\mu_1\epsilon_1 - \sin^2\theta_i}} \\ R_c^{TM} &= \frac{\sqrt{\mu_1\epsilon_1 - \sin^2\theta_i}}{\mu_1\sqrt{\mu_0/\epsilon_0}} \\ \beta_1 &= k_0\sqrt{\mu_1\epsilon_1 - \sin^2\theta_i} \end{aligned} \tag{152}$$

Following the steps in [67], and solving for the voltage V_x shown in Figure 187 yields the following the field expressions for the magnetic Hertzian dipole:

$$E_\theta = \frac{j\omega\epsilon_0\exp(-jk_0R)}{2\pi R}F(\theta) \tag{153}$$

$$E_\phi = \frac{j\omega\epsilon_0\exp(-jk_0R)}{2\pi R}G(\theta) \tag{154}$$

where F(θ) and G(θ) are

$$F(\theta) = \frac{\cos\theta\cos\phi\sqrt{\mu_1\epsilon_1 - \sin^2\theta}}{\sqrt{\mu_1\epsilon_1 - \sin^2\theta} + j\mu_1\tan(\beta h)\cos\theta} \tag{155}$$

$$G(\theta) = \frac{\epsilon_1\cos\theta\sin\phi}{j\tan(\beta h)\sqrt{\mu_1\epsilon_1 - \sin^2\theta} + \epsilon_1\cos\theta} \tag{156}$$

As can be seen in (155) and (156), F(θ) and G(θ) are functions of θ and substrate parameters. For thin substrates, using the approximation $\tan(\beta h) \approx \beta h$, the expression in (155) and (156) can be reduced to

$$F(\theta) \approx \cos\theta \tag{157}$$

$$G(\theta) \approx 1 \tag{158}$$

Equations (157) and (158) shows that for thin substrates, the effect of the substrate parameters ϵ_r and μ_r on the radiated fields of a horizontal magnetic Hertzian dipole can be neglected.

APPENDIX C

DERIVATION OF GREEN'S FUNCTIONS IN THE SPECTRAL DOMAIN

A Hertzian electric dipole positioned on top of a conductor-backed magneto-dielectric substrate can be used to derive the electric field Green's function [65]. The dipole can be modeled as an infinitesimal electric current source. If the dipole is located at (x_0, y_0), the x-directed dipole current can be expressed as

$$J_x = \hat{x}\delta(x - x_0)\delta(y - y_0) \tag{159}$$

If the substrate is extended on the x-y plane, the Green's function can be obtained from direct solution of wave equations for E_z and H_z. Starting from following Maxwell's equations for a source-free medium:

$$\nabla \times \bar{E} = -j\omega\mu_r\mu_0\bar{H} \tag{160}$$

$$\nabla \times \bar{H} = -j\omega\epsilon_r\epsilon_0\bar{E} \tag{161}$$

the wave equations for E and H fields can be derived as

$$\nabla^2\bar{E} + \omega^2\mu_r\epsilon_r k_0^2\bar{E} = 0 \tag{162}$$

$$\nabla^2\bar{H} + \omega^2\mu_r\epsilon_r k_0^2\bar{H} = 0 \tag{163}$$

A source-free medium is assumed to simplify the analysis since the effect of J_x can be included in the boundary conditions.

Applying Equations (162) and (163) to the z component gives the wave equations

$$\frac{\partial^2 E_z}{\partial x^2} + \frac{\partial^2 E_z}{\partial y^2} + \frac{\partial^2 E_z}{\partial z^2} + \epsilon_r\mu_r k_0^2 E_z = 0 \tag{164}$$

$$\frac{\partial^2 H_z}{\partial x^2} + \frac{\partial^2 H_z}{\partial y^2} + \frac{\partial^2 H_z}{\partial z^2} + \epsilon_r\mu_r k_0^2 H_z = 0 \tag{165}$$

If we assume an $exp(\pm jk_x x + \pm jk_y y + \pm jk_z)$ behavior, the following relationship can be derived

$$k_x^2 + k_y^2 + k_z^2 = \epsilon_r\mu_r k_0^2 \tag{166}$$

Therefore, the propagation constant k_z is given by

$$k_1^2 = k_z^2 = \epsilon_r \mu_r k_0^2 - \beta^2 \text{ for } 0 \leq z < h \text{ (Region 1)} \tag{167}$$

$$k_2^2 = k_z^2 = k_0^2 - \beta^2 \text{ for } z < h \text{ (Region 2)} \tag{168}$$

where

$$\beta^2 = k_x^2 + k_y^2 \tag{169}$$

Since the analysis is carried out in the Fourier domain, it is convenient to use the Fourier transform of the fields and current densities. If the Fourier transform pair is defined as follows:

$$\psi(x, y, z) = \frac{1}{4\pi^2} \int_{-\infty}^{\infty} \int_{-\infty}^{\infty} \tilde{\psi}(k_x, k_y, z) e^{jk_x x} e^{jk_y y} \, dk_x \, dk_y \tag{170}$$

$$\tilde{\psi}(k_x, k_y, k_z) = \int_{-\infty}^{\infty} \int_{-\infty}^{\infty} \psi(x, y, z) e^{-jk_x x} e^{-jk_y y} \, dx \, dy \tag{171}$$

Maxwell's equations in Equations (160) and (161) can be Fourier transformed using $\partial/\partial x \rightarrow +jk_x$ and $\partial/\partial y \rightarrow +jk_y$ to give

$$\tilde{E}_x = \frac{jk_x}{\beta^2} \frac{\partial \tilde{E}_z}{\partial z} + \frac{\omega \mu_r \mu_0 k_y}{\beta^2} \tilde{H}_z \tag{172}$$

$$\tilde{E}_y = \frac{jk_y}{\beta^2} \frac{\partial \tilde{E}_z}{\partial z} - \frac{\omega \mu_r \mu_0 k_x}{\beta^2} \tilde{H}_z \tag{173}$$

$$\tilde{H}_x = \frac{jk_x}{\beta^2} \frac{\partial \tilde{H}_z}{\partial z} - \frac{\omega \epsilon_r \epsilon_0 k_y}{\beta^2} \tilde{E}_z \tag{174}$$

$$\tilde{H}_y = \frac{jk_y}{\beta^2} \frac{\partial \tilde{H}_z}{\partial z} + \frac{\omega \epsilon_r \epsilon_0 k_x}{\beta^2} \tilde{E}_z \tag{175}$$

The solution for $\tilde{E}_x$ and $\tilde{E}_y$ are obtained by assuming the following general forms for $\tilde{E}_z$ and $\tilde{H}_z$ in region 1 and 2:

$$\tilde{E}_{z2} = Ae^{-jk_2 z} \tag{176}$$

$$\tilde{H}_{z2} = Be^{-jk_2 z} \tag{177}$$

$$\tilde{E}_{z1} = C \cos(k_1 z) + D \sin(k_1 z) \tag{178}$$

$$\tilde{H}_{z1} = E \sin(k_1 z) + F \cos(k_1 z) \tag{179}$$

Boundary conditions can be used to find the constant A to F in the above expressions. The boundary conditions can be summarized as follows:

$$\tilde{E}_x = 0 \text{ at z=0} \tag{180}$$

$$\tilde{E}_y = 0 \text{ at z=0} \tag{181}$$

$$\text{Continuity of } \tilde{E}_x \text{ at z=h, which means } \tilde{E}_{x1} = \tilde{E}_{x2} \tag{182}$$

$$\text{Continuity of } \tilde{E}_y \text{ at z=h, which means } \tilde{E}_{y1} = \tilde{E}_{y2} \tag{183}$$

$$\text{Continuity of } \tilde{H}_x \text{ at z=h, which means } \tilde{H}_{x1} = \tilde{H}_{x2} \tag{184}$$

$$\text{Continuity of } \tilde{H}_y \text{ at z=h-0, which means } \tilde{H}_{y1} - \tilde{H}_{y2} = \tilde{J}_x \tag{185}$$

Substituting Equations (176) to (179) for $\tilde{E}_z$ and $\tilde{H}_z$ for region 1 and 2 in Equations (172) to (175) and solving the equations together with the boundary conditions, the following expressions for $\tilde{E}_z$ and $\tilde{H}_z$ can be found:

$$\tilde{E}_{z2} = \frac{k_x k_1 \sin(k_1 h)}{j\omega\epsilon_0 T_m} e^{-jk_2(z-h)} \tilde{J}_x \tag{186}$$

$$\tilde{H}_{z2} = \frac{-j\mu_r k_y \sin(k_1 h)}{T_e} e^{-jk_2(z-h)} \tilde{J}_x \tag{187}$$

$$\tilde{E}_{z1} = \frac{k_x k_2 \cos(k_1 z)}{\omega\epsilon_0 T_m} \tilde{J}_x \tag{188}$$

$$\tilde{H}_{z1} = \frac{-jk_y \sin(k_1 z)}{T_e} \tilde{J}_x \tag{189}$$

where

$$T_m = \epsilon_r k_2 \cos(k_1 h) + jk_1 \sin(k_1 h) \tag{190}$$

$$T_e = k_1 \cos(k_1 h) + j\mu_r k_2 \sin(k_1 h) \tag{191}$$

Substituting Equations (186) to (189) in Equation (172) yields at z=h ($\partial/\partial z = -jk_2$),

$$\tilde{E}_x(k_x, k_y, k_z) = \frac{-j \sin(k_1 h)}{\omega\epsilon_0 \beta^2} \left[\frac{k_x^2 k_1 k_2}{T_m} + \frac{\mu_r^2 k_0^2 k_y^2}{T_e} \right] \tilde{J}_x \tag{192}$$

Similarly, $\tilde{E}_y$ at z=h can be found using Equation (173) as

$$\tilde{E}_y(k_x, k_y, k_z) = \frac{-jk_y k_x \sin(k_1 h)}{\omega\epsilon_0 \beta^2} \left[\frac{k_1 k_2}{T_m} - \frac{\mu_r^2 k_0^2}{T_e} \right] \tilde{J}_x \tag{193}$$

Equations (192) and (193) are electric field expressions in the spectral domain due to an x-directed current. Similarly, the electric field due to a y-directed current can be obtained. These expressions can be obtained by interchanging $x \leftrightarrow y$ in Equations (192) and (193). This yields

$$\tilde{E}_y(k_x, k_y, k_z) = \frac{-j\sin(k_1 h)}{\omega\epsilon_0\beta^2}\left[\frac{k_y^2 k_1 k_2}{T_m} + \frac{\mu_r^2 k_0^2 k_x^2}{T_e}\right]\tilde{J}_y \tag{194}$$

Similarly, $\tilde{E}_y$ at z=h can be found using Equation 173 as

$$\tilde{E}_x(k_x, k_y, k_z) = \frac{-jk_x k_y \sin(k_1 h)}{\omega\epsilon_0\beta^2}\left[\frac{k_1 k_2}{T_m} - \frac{\mu_r^2 k_0^2}{T_e}\right]\tilde{J}_y \tag{195}$$

Comparing Equation 192 to 195 with following matrix relationship

$$\begin{bmatrix} \tilde{E}_x \\ \tilde{E}_y \end{bmatrix} = \begin{bmatrix} \tilde{Z}_{xx} & \tilde{Z}_{xy} \\ \tilde{Z}_{yx} & \tilde{Z}_{yy} \end{bmatrix}\begin{bmatrix} \tilde{J}_x \\ \tilde{J}_y \end{bmatrix} \tag{196}$$

yields the spectral domain electric field Green's functions.

$$\tilde{Z}_{xx} = \frac{-j\sin(k_1 h)}{\omega\epsilon_0\beta^2}\left[\frac{k_x^2 k_1 k_2}{T_m} + \frac{\mu_r^2 k_0^2 k_y^2}{T_e}\right] \tag{197}$$

$$\tilde{Z}_{xy}\frac{-jk_y k_x \sin(k_1 h)}{\omega\epsilon_0\beta^2}\left[\frac{k_1 k_2}{T_m} - \frac{\mu_r^2 k_0^2}{T_e}\right] \tag{198}$$

$$\tilde{Z}_{yy} = \frac{-j\sin(k_1 h)}{\omega\epsilon_0\beta^2}\left[\frac{k_y^2 k_1 k_2}{T_m} + \frac{\mu_r^2 k_0^2 k_x^2}{T_e}\right] \tag{199}$$

$$\tilde{Z}_{xy} = \tilde{Z}_{yx} \tag{200}$$

The space-domain electric field Green's functions can then be obtained by taking the inverse transform of $\tilde{Z}_{xx}$, $\tilde{Z}_{xy}$ and $\tilde{Z}_{yy}$. The transverse electric Green's functions at (x, y, h) due to the unit strength electric current J_j at (x_0, y_0, h) can then be expressed as

$$E_i(x, y, h) = \frac{1}{4\pi^2}\int_{-\infty}^{\infty}\int_{-\infty}^{\infty}\tilde{Z}_{ij}e^{jk_x(x-x_0)}e^{jk_y(y-y_0)}\,dk_x\,dk_y \text{ i,j=x, y} \tag{201}$$

APPENDIX D

CALCULATION OF THE INTEGRAL FOR SURFACE WAVE POWER

Applying the method in Eq. (106) to the integral in Eq. (105) yields the following integral for the surface wave power:

$$P_{sw} = \frac{-1}{4\pi^2} Re\left\{\int_{\phi=0}^{2\pi}\int_{\beta-\delta_0}^{\beta+\delta_0} Z_{xx}(\phi,\beta)\beta d\beta\, d\phi\right\} \tag{202}$$

where $\delta_0 \sim 0.001k_0$ [73]. The integrand in (202) can be rewritten in the following form

$$I_\delta = \int_{\beta_0-\delta}^{\beta_0+\delta} \left(\frac{f(\beta,\phi)}{T_m(\beta)}\right) d\beta \tag{203}$$

where $T_m(\beta)$ has a pole at $\beta = \beta_0$ and is given in Eq. (95). $f(\beta)$ represents the remaining nonsingular portion of the integrand and given (94) and (104) it can be found as

$$f(\beta,\phi) = \frac{jZ_0 \sin(k_1 h)}{k_0\beta} \frac{T_e k_x^2 k_1 k_2 + T_m \mu_r^2 k_0^2 k_y^2}{T_e} \tag{204}$$

Using the Taylor expansion representation of $T_m(\beta)$ around β_0 yields

$$I_\delta = \frac{-j\pi f(\beta_0,\phi)}{T_m'(\beta_0)}. \tag{205}$$

Applying (205) to (202), one can find

$$P_{sw} = \frac{-1}{4\pi^2} Re\left\{\int_{\phi=0}^{2\pi} -j\pi \frac{-jZ_0 \sin(k_1 h) k_x^2 k_1 k_2}{k_0\beta_0 T_m'(\beta_0)} \cos^2\phi\, d\phi\right\} \tag{206}$$

where using $T_m(\beta_0) = 0$, $T_m'(\beta_0)$ can be shown to be

$$T_m'(\beta_0) = \beta_0\left[h\left(\frac{k_1}{\epsilon_r k_2} + \frac{\epsilon_r k_2}{k_1}\right) + j\left(\frac{-1}{k_1} + \frac{k_1}{k_2^2}\right)\right] \tag{207}$$

If we assume $\beta_0 = x_0 k_0$ (206) can be reduced to

$$P_{sw} = \frac{Z_0 k_0^2}{4} \frac{\epsilon_r(x_0^2-1)}{(k_0 h)\left[1 + \frac{\epsilon_r^2(x_0^2-1)}{(\epsilon_r\mu_r - x_0^2)}\right] + \epsilon_r\left[\frac{\sqrt{x_0^2-1}}{(x_0^2-\epsilon_r\mu_r)} + \frac{1}{\sqrt{x_0^2-1}}\right]} \tag{208}$$

REFERENCES

[1] R. R. Tummala and M. Swaminathan, *Introduction to System-on-Package (SoP)*. New York: McGraw-Hill, 2008.

[2] R. R. Tummala and V. K. Madisetti, "System on chip or system on package," *IEEE Design and Test of Computers*, vol. 16, no. 2, pp. 48–56, 1999.

[3] R. R. Tummala, "Moore's law meets its match (system-on-package)," *IEEE Spectrum Magazine*, vol. 43, pp. 44–49, 2006.

[4] G. E. White, M. Swaminathan, V. Sundaram, and S. Dalmia, "Integrated passive devices fabricated utilizing multilayer organic laminates," *US Patent ID: 6,900,708*, May 2005.

[5] S.Brebels *et al.*, "SOP integration and codesign of antennas," *IEEE Trans. Adv. Packag.*, vol. 27, pp. 341–351, May 2004.

[6] K. L. Wong, *Compact and broadband microstrip antennas*. Hoboken, NJ: J. Wiley & Sons, 2002.

[7] "Dual-Band Patch Antenna for Mobile Phones," *http://www.cst.com/Content/Applications/Article/130*.

[8] "Shangai Universe Communication Electronics Co.," *http://www.suc-universe.com/en/xqitadmin/pic/2007112138657377.JPG*.

[9] K. L. Wong, "Planar antennas for WLAN applications," *http://www.ansoft.com/EMpower/NSYSUniv2.pdf*, Sept. 2002.

[10] C. A. Balanis, *Antenna Theory, Analysis and Design*. Hoboken, NJ: John Wiley and Sons, 2005.

[11] K. L. Wong, *Planar antennas for wireless communications*. Hoboken, NJ: J. Wiley & Sons, 2003.

[12] R.Li *et al.*, "Design of compact stacked-patch antennas in LTCC multilayer packaging modules for wireless applications," *IEEE Trans. Adv. Packag.*, vol. 27, pp. 581–589, Nov. 2004.

[13] Y. P. Zhang, "Integrated circuit ceramic ball grid array package antenna," *IEEE Trans. Antennas Propagat.*, vol. 52, pp. 2538–2544, Oct. 2004.

[14] W. Yun, V. Sundaram, and M. Swaminathan, "High-Q embedded passives on large panel multilayer liquid crystalline polymer-based substrate," *IEEE Trans. Adv. Packag.*, vol. 39, pp. 580–591, Aug. 2007.

[15] A. Bavisi, S. Dalmia, M. Swaminathan, G. White, and V. Sundaram, "Chip-package codesign of integrated voltage-controlled oscillator in LCP substrate," *IEEE Trans. Adv. Packag.*, vol. 29, pp. 390–402, Aug. 2006.

[16] R. Bairavasubramanian and J. Papapolymerou, "Fully canonical pseudo-elliptic bandpass filters on multilayer liquid crystal polymer technology," *IEEE Microwave Wireless Compon. Lett.*, vol. 17, pp. 190–192, 2007.

[17] W. Yun, V. Sundaram, and M. Swaminathan, "A triple balanced mixer in multilayer liquid crystalline polymer (LCP) substrate," in *Proc. IEEE 57th Electron. Compon. Technol. Conf.*, pp. 2000–2005, May 2007.

[18] M. M. Tentzeris *et al.*, "3-D-integrated RF and millimeter wave functions and modules using liquid crystal polymer (LCP) system-on-package technology," *IEEE Trans. Adv. Packag.*, vol. 27, pp. 332–340, May 2004.

[19] M. Swaminathan, A. Bavisi, W. Yun, V. Sundaram, V. Govind, and P. Monajemi, "Design and fabrication of integrated RF modules in liquid crystalline polymer (LCP) substrates," in *31st Annual Conf. of IEEE Industrial Electronics Society*, pp. 2346–2351, Nov. 2005.

[20] D. C. Thompson, O. Tantot, H. Jallageas, G. E. Ponchak, M. M. Tentzeris, and J. Papapolymerou, "Characterization of liquid crystal polymer (LCP) material and transmission lines on LCP substrates from 30 to 110 GHz," *IEEE Trans. Microwave Theory Tech.*, vol. 52, no. 4, pp. 1343–1352, 2004.

[21] V. Sundaram *et al.*, "Super high density two metal layer ultra-thin organic substrates for next generation system-on-package (SOP), SiP and ultra-fine pitch flip-chip packages," in *Pan Pacific Microelectron. Symp.*, pp. 1–10, 2009.

[22] S. Hwang *et al.*, "Characterization of next generation thin low-k and low-loss organic dielectrics from 1 to 110 GHz," *IEEE Trans. Adv. Packag.*, pp. 1–9, 2010.

[23] G. Krishnan *et al.*, "High performance organic dielectrics and high density substrates for next generation system on a package (SOP) technology," in *Proc. IEEE Electrical Components and Technology Conference*, pp. 2101–2104, 2008.

[24] D. Athreya *et al.*, "Ultra high Q embedded inductors in highly miniaturized family of low loss organic substrates," in *Proc. IEEE Electrical Components and Technology Conference*, pp. 2073–2080, 2008.

[25] S. Hwang, S. Min, H. Chan, V. Sundaram, and M. Swaminathan, "A compact third-order 5 GHz bandpass filter with enhanced stopband characteristics in ultra thin organic substrate," in *IEEE Radio and Wireless Symp.*, 2010.

[26] R. C. Hansen and M. Burke, "Antenna with magneto-dielectrics," *Microwave Opt. Technol. Lett.*, vol. 26, pp. 75–78, 2000.

[27] N. Tang, W. Zhong, X. Wu, H. Jiang, W. Liu, and Y. Du, "Synthesis and complex permeability of Co/SiO_2 nanocomposites," *Materials Letters*, vol. 59, pp. 1723–1726, 2005.

[28] N. Tang, W. Zhong, W. Liu, H. Jiang, X. Wu, and Y. Du, "Synthesis and complex permeability of $Ni-SiO_2$ nanocomposite," *Nanotechnology*, vol. 15, pp. 1756–1758, Nov. 2004.

[29] N. Altunyurt, M. Swaminathan, P. Raj, and V. Nair, "Antenna miniaturization using magneto-dielectric substrates," *Proc. of IEEE Elect. Compon. Technol. Conf*, pp. 801–808, May 2009.

[30] M. Rotaru, L. Y. Ying, H. Kuruveettil, Y. Rui, A. P. Popov, and C. C. Parng, "Implementation of packaged integrated antenna with embedded front end for bluetooth applications," *IEEE Trans. Adv. Packag.*, vol. 31, pp. 558–567, Aug. 2008.

[31] K. Brownlee, S. Bhattacharya, K. Shinotani, C. Wong, and R. Tummala, "Liquid crystalline polymers (LCP) for high performance SOP application," in *Proc. 8th Int. Symp. on Advanced Packaging Materials*, pp. 249–253, 2002.

[32] "Nokia, The Morph Concept," *http://www.nokia.com/A4852062*.

[33] "Siemens-BenQ, Future Phones," *http://www.crunchgear.com/2007/02/05/benq-siemens-phones-of-the-future/.*

[34] J. Y. Chen, C. U. Huang, H. J. H. Chen, C. F. Jout, and S. R. S. Huang, "Folded dual-band (2.4/5.2GHz) antenna fabricated on silicon suspended parylene membrane," in *Proc. of IEEE Asia Pacific Microwave Conference*, pp. 2346–2351, Dec. 2005.

[35] S. W. Su, K. L. Wong, C. L. Tang, and S. H. Yeh, "Wideband monopole antenna integrated within the front-end module package," *IEEE Trans. Antennas Propagat.*, vol. 54, pp. 1888–1891, 2006.

[36] N. Altunyurt, M. Swaminathan, V. Sundaram, and G. White, "Conformal antennas on liquid crystalline polymer substrates for consumer applications," in *Proc. of IEEE Asia Pacific Microwave Conference*, pp. 471–474, Dec. 2007.

[37] "High Frequency Structure Simulator," *http://www.ansoft.com*.

[38] W. L. Weeks, "Propagation constants in rectangular waveguide partially filled with dielectric (correspondence)," *IEEE Trans. Microwave Theory Tech.*, vol. 7, pp. 294–294, Apr. 1959.

[39] D. Pozar, *Microwave Engineering*. Hoboken, NJ: J. Wiley & Sons, 2005.

[40] S. I. Maslovski, P. Ikonen, I. A. Kolmakov, S. A. Tretyakov, and M.Kaunisto, "Artificial magnetic materials based on the new magnetic particle: Metasolenoid," *Progress in Electromagn. Res.*, vol. 54, pp. 61–81, 2005.

[41] H. Mossallaei and K. Sarabandi, "Magnetodielectrics in electromagnetics: Concept and applications," *IEEE Trans. Antennas Propagat.*, vol. 52, pp. 1558–1567, 2004.

[42] K. Buell, H. Mosallaei, and K. Sarabandi, "A substrate for small patch antennas providing tunable miniaturization factors," *IEEE Trans. Antennas Propagat.*, vol. 54, pp. 135–146, Jan. 2006.

[43] L. Yousefi and O. M. Ramahi, "Miniaturized wideband antenna using engineered magnetic materials with multi-resonator inclusions," *IEEE Antennas and Propog. Soc. Int. Symp.*, pp. 1885–1888, 2007.

[44] P. M. T. Ikonen, S. I. Maslovski, C. R. Simovski, and S. A. Treyakov, "On artificial magnetodielectric loading for improving the impedance bandwidth properties of microstrip antennas," *IEEE Trans. Antennas Propagat.*, vol. 54, pp. 1654–1662, 2006.

[45] W. Liu, W. Zhong, H. Jiang, N. Tang, X. Wu, and Y. Du, "Highly stable alumina-coated iron nanocomposites synthesized by wet chemistry method," *Surface Coatings and Technology*, vol. 200, pp. 5170–5174, 2006.

[46] Y. Mano and S. Bae, "A small meander antenna by magneto-dielectric material," *IEEE Int. Symp. on Micr., Ant., Propag. and EMC Tech*, pp. 63–66, Aug. 2005.

[47] N. Tang, H. Jiang, W. Zhong, X. Wu, W. Zou, and Y. Du, "Synthesis and magnetic properties of Fe/SiO_2 nanocomposites prepared by a solgel method combined with hydrogen reduction," *Journal of Alloys and Compounds*, vol. 419, pp. 145–148, Nov. 2006.

[48] Y. Li, H. Doo, B. Pan, M. M. Tentzeris, Z. J. Zhang, and J. Papapolymerou, "Novel enhanced-thickness magnetic nanoparticle thin-films for system-on-chip (SOC) wireless applications," in *IEEE MTT-S International Microwave Symposium Digest*, pp. 97–100, 2008.

[49] L. J. Martin, *Flexible magnetic composite for antenna applications in radio frequency identification (RFID).* PhD thesis, Georgia Institute of Technology, 2005.

[50] K. Peng, L. Zhou, A. Hu, Y. Tang, and D. Li, "Synthesis and magnetic properties of Ni/SiO_2 nanocomposites," *Material Chemistry and Physics*, vol. 111, pp. 34–37, Sept. 2008.

[51] Y. Wu, Z. Tang, Y. Xu, and B. Zhang, "An improved measurement configuration for determining the permeability of ferromagnetic thin film materials," *Journal of Electromagn. Waves and Appl.*, vol. 22, pp. 343–352, 2008.

[52] A. T. A. Note, "Solutions for measuring permittivity and permeability with LCR meters and impedance analyzers," 2008.

[53] A. M. Nicholson and G. F. Ross, "Measurement of the intrinsic properties of materials by time-domain techniques,"

[54] K. Saeed, R. D. Pollard, and I. C. Hunter, "Substrate integrated waveguide cavity resonators for complex permittivity characterization of materials," *IEEE Trans. Microwave Theory Tech.*, vol. 56, no. 10, pp. 2340–2347, 2008.

[55] S. N. Prasad and S. Mahapatra, "Triple-mode cavity perturbation method for the characterization of anisotropic media," in *Proc. 38th European Microwave Conf.*, pp. 909–912, 2008.

[56] A. E. Engin, A. Tambawala, M. Swaminathan, S. Bhattacharya, P. Pramanik, and K. Yamazaki, "Frequency-dependent dielectric constant and loss tangent characterization of thin dielectrics using a rapid solver," in *Proc. IEEE Electrical Components and Technology Conference*, pp. 792–797, 2007.

[57] "Sonnet software," *http://www.sonnetsoftware.com*.

[58] "Computer Simulation Technology, Microwave Studio," *http://www.cst.com/*.

[59] A. T. A. Note, "Ultra-low impedance measurements using 2-port measurements," 2008.

[60] T. K. Lo, C.-O. Ho, Y. Hwang, E. K. W. Lam, and B. Lee, "Miniature aperture-coupled microstrip antenna of very high permittivity," *Electronic Letters*, vol. 33, pp. 9–10, Jan. 1997.

[61] J. S. Colburn and Y. Rahmat-Samii, "Patch antennas on externally perforated high dielectric constant substrates," *IEEE Trans. Antennas Propagat.*, vol. 47, pp. 1785–1794, Dec. 1999.

[62] H. Mosallaei and K. Sarabandi, "Design and modeling of patch antenna printed on magneto-dielectric embedded-circuit metasubstrate," *IEEE Trans. Antennas Propagat.*, vol. 55, pp. 45–52, Jan. 2007.

[63] P. M. T. Ikonen, K. M. Rozanov, A. V. Osipov, P. Alitalo, and S. A. Treyakov, "Magnetodielectric substrates in antenna miniaturization:Potential and limitations," *IEEE Trans. Antennas Propagat.*, vol. 54, pp. 3391–3399, Nov. 2006.

[64] E. Wang and S. Fang, "Wideband dual-band microstrip antenna for WLAN application using organic magnetic substrate," *Wireless and Microwave Technology Conference*, pp. 1–3, Dec. 2006.

[65] R. Garg, P. Bhartia, I. Bahl, and A. Ittipiboon, *Microstrip antenna design handbook*. Norwood, MA: Artech House, 2001.

[66] D. R. Jackson and N. G. Alexopoulos, "Simple approximate formulas for input resistance, bandwidth, and efficiency of a resonant rectangular patch," *IEEE Trans. Antennas Propagat.*, vol. 39, no. 3, pp. 407–410, 1991.

[67] X. H. Wu, A. A. Kishk, and A. W. Glisson, "A transmission line method to compute the far-field radiation of arbitrarily directed hertzian dipoles in a multilayer dielectric structure: Theory and applications," *IEEE Trans. Antennas Propagat.*, vol. 54, pp. 2731–2741, Oct. 2006.

[68] D. Thouroude, M. Himdi, and J. Daniel, "CAD-oriented cavity model for rectangular patches," *Electronics Letters*, vol. 26, no. 13, pp. 842–844, 1996.

[69] J. S. McLean, "A re-examination of the fundamental limits on the radiation Q of electrically small antennas," *IEEE Trans. Antennas Propagat.*, vol. 44, pp. 672–676, May 1996.

[70] R. F. Harrington, *Time-Harmonic Electromagnetic Fields*. New York: McGraw-Hill, 1961.

[71] D. M. Pozar, "Rigorous closed-form expressions for the surface wave loss of printed antennas," *Electron. Lett.*, vol. 26, no. 13, pp. 954–956, 1990.

[72] B. Nauwelaers and A. V. D. Capella, "Surface wave losses of rectangular microstrip antennas," *Electron. Lett.*, vol. 25, pp. 696–697, May 1989.

[73] D. M. Pozar, "Input impedance and mutual coupling of rectangular microstrip antennas," *IEEE Trans. Antennas Propagat.*, vol. 30, pp. 1191–1196, Nov. 1982.

[74] D. Sievenpiper, *High impedance electromagnetic surfaces*. PhD thesis, University of California, Los Angeles, 1999.

[75] A. Al-Zoubi, F. Yang, and A. Kishk, "A low-profile dual-band surface wave antenna with a monopole-like pattern," *IEEE Trans. Antennas Propagat.*, vol. 55, pp. 3404–3412, Dec. 2007.

[76] H. Mossallaei and K. Sarabandi, "Antenna miniaturization and bandwidth enhancement using a reactive impedance substrate," *IEEE Trans. Antennas Propagat.*, vol. 52, pp. 2403–2414, Sept. 2004.

[77] F. Yang and Y. Rahmat-Samii, "Reflection phase characterizations of the EBG ground plane for low-profile wire antenna applications," *IEEE Trans. Antennas Propagat.*, vol. 51, pp. 2691–2703, Oct. 2003.

[78] L. Yousefi, B. M. Iravani, and O. M. Ramahi, "Enhanced bandwidth artificial magnetic ground plane for low-profile antennas," *IEEE Antennas and Wireless Propagat. Lett.*, vol. 6, pp. 289–292, Dec. 2007.

[79] K. Sarabandi, M. D. Casciato, and I. S. Koh, "Efficient calculation of the fields of a dipole radiating above an impedance surface," *IEEE Trans. Antennas Propagat.*, vol. 50, pp. 1222–1235, Sept. 2002.

[80] R. C. Daniels and J. R. W. Heath, "60 GHz wireless communications: Emerging requirements and design recommendations," *IEEE Vehicular Technology Magazine*, vol. 22, pp. 41–50, 2007.

[81] P. J. Gibson, "The Vivaldi aerial," in *Proc. 9th European Microwave Conf.*, pp. 101–105, 1979.

[82] S. N. Prasad and S. Mahapatra, "A novel MIC slot line aerial," in *Proc. 9th European Microwave Conf.*, pp. 120–124, 1979.

[83] K. S. Yngvesson, T. L. Korzeniowski, Y.-S. Kim, E. L. Kolberg, and J. F. Johansson, "The tapered slot antenna-a new integrated element for millimeter-wave applications," *IEEE Trans. Microwave Theory Tech.*, vol. 37, pp. 365–374, Feb. 1989.

[84] B. Schoenlinner, X. W. J. P. Ebling, G. V. Eleftheriades, and G. M. Rebeiz, "Wide-scan spherical-lens antennas for automotive radars," *IEEE Trans. Microwave Theory Tech.*, vol. 50, pp. 2166–2175, Sept. 2002.

[85] A. Hirata, H. Ishii, and T. Nagatsuma, "Design and characterization of a 120-GHz millimeter-wave antenna for integrated photonic transmitters," *IEEE Trans. Microwave Theory Tech.*, vol. 49, pp. 2157–2162, Nov. 2001.

[86] N. W. Chen, C. T. Chuang, and J. W. Shi, "A W-band linear tapered slot antenna on rectangular-grooved silicon substrate," *IEEE Antennas and Wireless Propagat. Lett.*, vol. 6, pp. 90–92, 2007.

[87] U. K. Kotthaus and B. Vowinkel, "Investigation of planar antennas for submillimeter receivers," *IEEE Trans. Microwave Theory Tech.*, vol. 37, pp. 375–380, Feb. 1989.

[88] T. G. Lim, H. N. Ang, I. D. Robertson, and B. L. Weiss, "Tapered slot antenna using photonic bandgap structure to reduce substrate effects," *Electron. Lett.*, vol. 41, pp. 393–394, 2005.

[89] J. B. Muldavin and G. M. Rebeiz, "Millimeter-wave tapered slot antenna on synthesized low permittivity substrates," *IEEE Trans. Antennas Propagat.*, vol. 47, pp. 1276–1280, Aug. 1999.

[90] G. H. Huff and J. T. Bernhard, "Improvements in the performance of microstrip antennas on finite ground planes through ground plane edge serrations," *IEEE Microwave Wireless Compon. Lett.*, vol. 12, pp. 308–310, Aug. 2002.

[91] "Corning Gilbert," *http://www.corning.com/WorkArea/showcontent.aspx?id=21645*.

[92] "GGB Probe Industries," *http://www.ggb.com/67a.html*.

[93] K. Kota and L. Shafai, "Parametric study of Vivaldi antenna," in *Antenna Technology and Applied Electromagnetics and the Canadian Radio Sciences Meeting*, pp. 1–4, 2009.

[94] U. Pfeiffer *et al.*, "A 60GHz radio chipset fully-integrated in a low-cost packaging technology," in *Proc. IEEE Electrical Components and Technology Conference*, pp. 1343–1346, 2006.

[95] C. J. Wang, J. J. Lee, and R. B. Huang, "Experimental studies of a miniaturized CPW-fed slot antenna with the dual-frequency operation," *IEEE Antennas and Wireless Propagat. Lett.*, vol. 2, pp. 151–154, 2003.

[96] M. Nesar-Moghadasi, A. Danideh, R. Sadeghifakhr, and M. Reza-Azadi, "CPW-fed ultra wideband slot antenna with arc-shaped stub," *IET Microwaves, Antennas and Propagation*, vol. 3, no. 4, p. 681686, 2009.

[97] E. A. Soliman *et al.*, "Bow-tie slot antenna fed by CPW," *Electron. Lett.*, vol. 35, pp. 514–515, 1999.

[98] C. Chen, E. Yung, and B. Hu, "Miniaturised CPW-fed circularly polarised corrugated slot antenna with meander line loaded," *Electron. Lett.*, vol. 43, pp. 1404–1405, 2007.

[99] D. D. Krishna, M. Gopikrishna, C. K. Anandan, P. Mohanan, and K. Vasudevan, "CPW-fed koch fractal slot antenna for WLAN/WiMAX applications," *IEEE Antennas and Wireless Propagat. Lett.*, vol. 7, pp. 389–392, 2008.

[100] S. P. Natarajan, A. M. Hoff, and T. M. Weller, "Micro coaxial-fed millimeter-wave slot antenna," in *IEEE Radio and Wireless Symp.*, pp. 675–678, 2008.

[101] Y.-F. Lin, P.-C. Liao, P.-S. Cheng, H.-M. Chen, C. Song, and P. Hall, "CPW-fed capacitive H-shaped narrow slot antenna," *Electronics Letters*, vol. 41, pp. 940–942, Aug. 2005.

[102] F. Ohnimus, I. Ndip, S. Guttowski, and H. Reichl, "An efficient and broadband slot antenna for 60 GHz wireless applications," in *Proc. Electrical Design of Advanced Packaging and Systems Symposium*, pp. 69–72, 2008.

[103] S. D. Targonski, R. B. Waterhouse, and D. M. Pozar, "Design of wide-band aperture-stacked patch microstrip antennas," *IEEE Trans. Antennas Propagat.*, vol. 46, pp. 1245–1251, Sept. 1998.

[104] S. Mestdagh, W. D. Raedt, and G. A. E. Vandenbosch, "CPW-fed stacked microstrip antennas," *IEEE Trans. Antennas Propagat.*, vol. 52, pp. 74–83, Jan. 2004.

[105] R. Li *et al.*, "Design of compact stacked-patch antennas in LTCC multilayer packaging modules for wireless applications," *IEEE Trans. Adv. Packag.*, vol. 27, pp. 581–589, Nov. 2004.

[106] T. Seki, N. Honma, K. Nishikawa, and K. Tsunekawa, "Millimeter-wave high-efficiency multilayer parasitic microstrip antenna array on teflon substrate," *IEEE Trans. Microwave Theory Tech.*, vol. 53, no. 6, pp. 2101–2106, 2005.